Application Of Morphometric Analysis And Tissue Engineering To Bioengineering Personalised Autologous Bone Tissues For The Reconstruction Of Congenital Midface Deformities.

Amel El-Kabashi Abdullah Ibrahim

BSc, MBBS, MRCS

Stem Cells and Regenerative Medicine Section

UCL GOS Institute of Child Health

30 Guilford Street

London WC1N 1EH

A dissertation submitted in fulfilment of the requirements for the degree of

Doctor of philosophy

of

University College London.

2017

I, Amel El-Kabashi Abdullah Ibrahim confirm that the work presented in this thesis is my own. Where information has been derived from other sources, I confirm that this has been indicated in the thesis.

……

(Amel El-Kabashi Abdullah Ibrahim)

Abstract

Congenital craniofacial bone deformities frequently occur in conditions such as Craniofacial microsomia (CM) and Treacher Collins Syndrome (TCS). Affected children may suffer from functional impairment and poor self-esteem. Reconstruction aims to restore form and function but often involves multiple invasive surgeries throughout childhood. The reliance on foreign-body implants and autologous tissue-transfer is also associated with morbidity. The aim of this work was to assess whether morphometric analysis and tissue engineering using paediatric adipose derived stem cells could facilitate bioengineering personalised autologous facial bone implants to provide a more accurate and life-long solution for the treatment of midface deformities.

Paediatric facial CT scans (n=70) from control, CM and TCS subjects were used to build a dense surface model of the midface to study normal and dysmorphic postnatal midface development. This enabled relating of soft and skeletal tissue growth, analysis of asymmetry and evaluation of surgical correction. This work also establishes the foundations for developing a surgical planning tool. Paediatric craniofacial bone was also analysed in order to establish a reference for tissue engineering and reverse engineer the bone microenvironment to fabricate biomaterials and culture conditions that enhance osteogenic maturation. It was possible to bioengineer bone tissue using hADSC cultured on a bone biomimetic hybrid POSS-PCL-Fibrin scaffold. Cellularised scaffolds survived subcutaneous implantation in nude mice for 4 months, underwent vascularisation and showed evidence of mature extracellular matrix formation and cellular composition similar to native bone

The results of this work support a multi-faceted approach to bone tissue engineering. Increased understanding of paediatric facial bones permits recreation of the bone microenvironment to enable osteogenic maturation of hADSC. These tissues could eventually be custom-shaped using an operative planning tool based on these computer models. Future work using larger data sets, bioreactors, 3D printing and large animal defect models will seek to build on these promising results.

Acknowledgements

I would like to thank my Principle supervisor Professor Patrizia Ferretti, for giving me the opportunity to undertake this PhD and who has over the years provided me with guidance, inspiration and rigorous training to help me on my journey to becoming an academic surgeon. I also wish to thank my secondary supervisor Professor Peter Hammond for affording me the immense opportunity, challenge and training to include computational biology in my research repertoire. I am also extremely thankful to Mr Neil Bulstrode for his perpetual support, mentorship and encouragement. I am eternally grateful to the Royal College of Surgeons of England for supporting my research firstly through a resreach training fellowship and more recently sponsoring my Fulbright scholarship to enable me to build on my findings and advance my career. A special thank you is also reserved for Mr Martyn Coomer who has consistently mentored, championed and supported me.

This work and my wider research experiences were also enriched and aided by my colleagues. In particular I wish to thank Mr Mike Suttie and Dr Naiara Rodriguez Florez with whom I hope to continue to work with and bring our shared vision of clinically translating our research to alleviate the disability and suffering associated with childhood craniofacial deformity.

I would not have been able to achieve any of this work without the love, support and encouragement of my wonderful family. I will forever be grateful to my partner, Mr Timothy Palmer Edmonds for his strength, friendship and love, which lifted and motivated me even during the toughest times. My sister, Ms Fatin Ibrahim whose intelligence, loyalty, generosity of spirit and wisdom continuously inspire me to be the best version of myself. I am eternally indebted to my late grandmother, Ms Saadia Haridi Mustafa who enthused within us the importance of being fiercely independent and following our dreams. Most of all, I wish to thank my mother, Ms Nadia Mukhtar Ibrahim, for always believing in me and instilling within me the courage, work-ethic and determination to pursue my passions. She has always been my greatest advocate, best critic and role model. It is to her that I dedicate this thesis.

Contents

List of Figures

List of Tables

List of Abbreviations

3D	3-dimensional
AA	Ascorbic acid
AB	Alcian blue
ALP	Alkaline phosphatase
ATF4	Activating transcription factor 4
BCA	Bias-corrected and accelerated
BGP	β-glycerophosphate
BMP	Bone morphogenetic proteins
BMP2	Bone morphogenetic protein 2
BSA	Bovine serum albumin
BSP	Bone sialoprotein
BV:TV	Bone volume fraction
CAM	Chorioallantoic membrane grafting
cDNA	Complimentary DNA
CI	Confidence Interval
CM	Craniofacial microsomia (CM)
COL1	Collagen 1
CT	Computed tomography
DMEM	Dulbecco’s modified Eagle’s medium
DMSO	Dimethyl sulfoxide

DNA	Deoxyribonucleic acid
DNTP	Deoxynucleotide phosphates
DSM	Dense-surface modelling
ECM	Extracellular matrix
FBS	Foetal bovine serum
FGF-2	Fibroblast growth factor 2
GPa	Giga Pascal
H&E	Haematoxylin and Eosin
hADSC	Human adipose-derived stem cells
hAEDSC	Human adipose explant dedifferentiated stem cells
hBMSC	Human bone marrow derived stem cells
HC	Haversian canal
hES	Human embryonic stem cells
hMSC	Human mesenchymal stem cells
hOP	Human osteoblast precursors
HUVEC	Human umbilical vein endothelial cells
IL-11	Interleukin-11
iPSC	Induced pluripotent stem cell
KLF4	Kuppel-like factor 4
L19	60S ribosomal protein 19
LAM	Lamin A/C

LCI	Lower confidence interval
LMN	Laminin
LUT	Look up table
MA	Morphometric analysis
MAPK	Mitogen-activated protein kinase
MSC	Mesenchymal stem cells
NES	Nestin
NFR	Nuclear fast red
OSC	Osteocalcin
OSTP	Osteopontin
OSX	Osterix
PAS	Periodic acid Schiff
PBS	Phosphate buffered saline
PC	Principle component
PCA	Principle component analysis
PCR	Polymerase chain reaction
PFA	Paraformaldehyde
POSS-PCL	Polyhedral oligomeric silsesquioxane-poly(Caprolactone-urea)urethane
POSTOP	Post operative
PREOP	Pre operative
RANK	Receptor activator of nuclear factor k B

RGB	Red-green-blue
RNA	Ribonucleic acid
ROI	Region of interest
RUNX	Runt-related protein 2
SATB2	Special AT-rich sequence-binding protein 2
SEM	Standard error of mean
SHG	Second harmonic generation
SHH	Sonic hedgehog
SOX2	Sex determining region Y-box 2
STD	Standard deviation
STDV	Standard deviation
TCOF1	Treacle Ribosome Biogenesis Factor 1
TCS	Treacher Collins Syndrome
TRAP	Tartrate-resistant acid phosphatase
UCI	Upper confidence interval
VEGF	Vascular endothelial growth factor
VIM	Vimentin
W/W	Wet weight
WNT	Wingless
µCT	Micro computed tomography

Collaborations

All experiments in this thesis were designed, performed, analysed and interpreted by myself. Where collaborative work was undertaken, I have only included the portion of work that was undertaken by myself with the intention of use for this thesis. For clarity, below is a succinct summary of the contributions made by others that is directly relevant to the work presented in this thesis:

The programmes (Facemark, DSMbuilder and DSMexplorer) I used to landmark, build dense surface models and analyse the data were created by Professor Peter Hammond and Mr Mike Suttie who also trained me in the use of these programmes.

The POSS-PCL polymer was created by Professor Seifalian. I used and modified this polymer to fabricate the nanocomposite scaffold.

Paraffin wax embedding and sectioning of the in vivo cellularised scaffolds and calvarial bone samples was performed by the histology department at Great Ormond Street Hospital as a commercial service.

Dr Ciaran Hutchison performed scanning of bone and scaffold samples with the Nikon scanner as part of the conditions of use for this equipment. Preparation, reconstruction, analysis and interpretation of data were performed by myself.

Chapter 1 Introduction

1.1 Anatomy and development of the craniofacial complex

The anatomy of the human head is complex due to the intricate interplay between soft tissue and underlying bone with a direct correlation between form and function (Figure 1.1). The facial skeleton (comprising the frontal, maxillary and mandibular regions) supports the overlying soft tissues by housing the organs of sense and facilitating mechanical functions (Trainor and Andrews, 2013). It also acts as a conduit between the external environment and internal organs through morphology of the face and expressions (Cox et al., 2013).

The craniofacial skeleton is composed of separate but connected components (the neurocranium and the viscerocranium) that are derived from different embryological origins (Sperber et al., 2010, Miloro et al., 2004b). The neurocranium comprises the skull vault (calvaria) and the cranial base. It is derived from mesodermal and neural crest cell origin (Morriss-Kay and Wilkie, 2005, Esteve-Altava and Rasskin-Gutman, 2014). There is a direct relationship between the skull vault and the underlying brain whereby growth of the former is shaped by development of the latter (Richtsmeier and Flaherty, 2013).

The viscerocranium (facial skeleton) houses various organs of sense including taste, smell, vision and hearing as well as the entry into the respiratory and digestive systems. It may be divided into the frontonasal, maxillary and mandibular processes all of which are formed during branchial arch development (Gray et al., 2005). Mechanisms of growth of the viscerocranium are complex due to its attachment to the neurocranium and cranial base as well as the soft tissues it contains and supports. Thus growth of sutures such as the spheno-occipital directs the degree of displacement of the midface whilst the eyes, tongue, teeth, musculature and nasal cavity direct growth of the facial skeleton similar to the relationship between the brain and the neurocranium (McMahon et al., 2013). The shape and direction of growth of the maxilla and mandible, are also influenced by the growth of the teeth (Gray et al., 2005).

Development and growth of the neurocranium and viscerocranium are subject to different cues in the pre and postnatal period. Brain growth exerts internal forces on the craniofacial sutures to stimulate bone growth and remodelling.

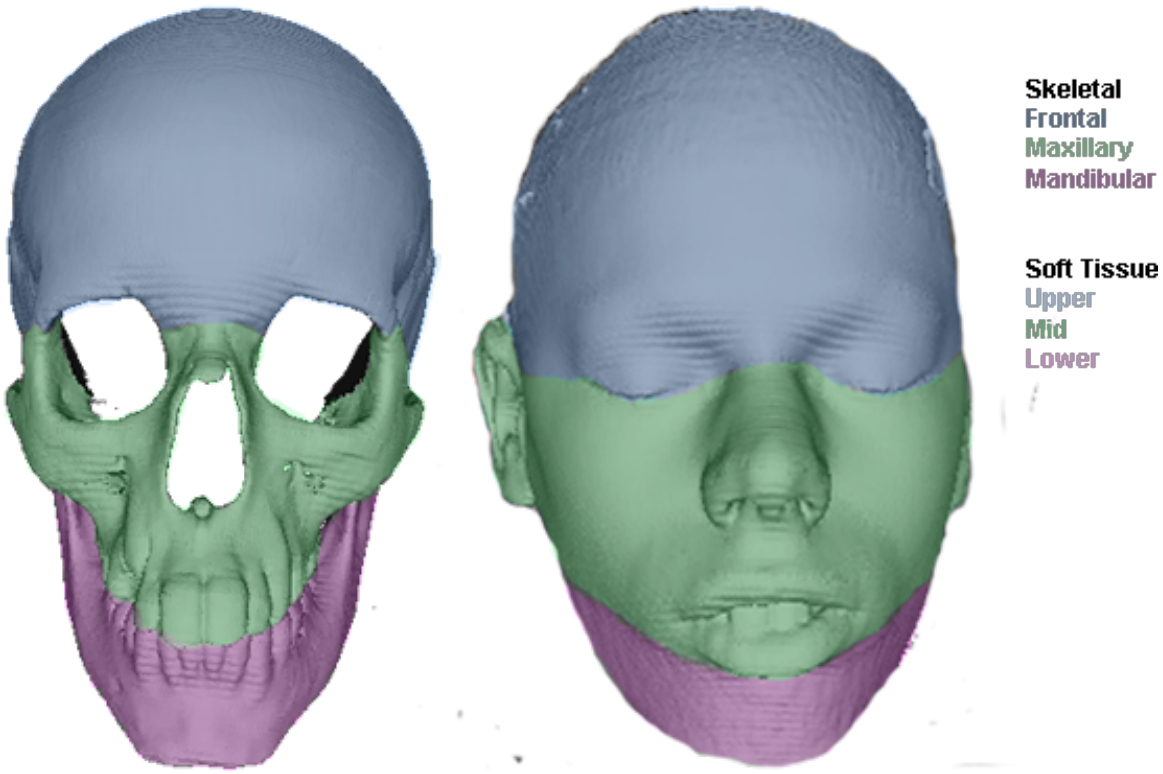

Figure 1.1: Overview of the anatomical compartments of the face.

The facial skeleton is often subdivided into the frontal, maxillary and mandibular components whilst the soft tissue surface is categorised as upper, mid or lower face based on their embryological origins.

Development of the facial skeleton is dictated by multifactorial stimuli including growth of the cranial base and impact of the soft tissues as well as dentition (Sperber et al., 2010, Miloro et al., 2004b). Due to correlation between brain and calvarium, the majority (75%) of skull growth is achieved by 2 years of age in humans (Miloro et al., 2004a). Conversely, the facial skeleton achieves 65% of its growth by age 10 (Sperber et al., 2010).

Facial soft tissue development and growth is affected by the skeletal changes during childhood. The face is divided into a lower, middle and upper portions which, like the components of the facial skeleton, grow separately but are connected (Sperber et al., 2010). The upper third of the face is defined as extending from the hairline to the glabella, the middle (midface) spans the glabella to the subnasale whilst the lower third extends from the subnasale to the menton (Mani, 2010). As with the skeleton, facial growth does not take place at the same rate in the different soft tissue components. Growth of the upper face correlates with brain growth and thus is precocious relative to the rest of the face so that it completes most of its growth by age 12. The rest of the face grows relatively more slowly with the midface completing most of its growth in late puberty whilst the lower third continues to grow into adulthood (Michael Miloro). The direction of growth within each subdivision of the face also displays different growth trajectories creating a sequence of transverse followed by anteroposterior and lastly vertical growth in each component (Michael Miloro).

Pre- and postnatal craniofacial development is an intricate process involving various biochemical, cellular and systemic mechanisms that coordinate the events involved in controlling the growth and morphology of the skeletal and soft tissue components (Sperber et al., 2010). In the early embryo facial morphogenesis is determined by the prosencephalic and rombencephalic organizing centres which, through the actions of the sonic hedgehog (SHH) protein, are responsible for differentiation of the streams of cranial neural crest cells that migrate from the dorsal aspect of the neural folds into the frontonasal mass and branchial arches from which face, neck and upper thoracic region will develop (Berkowitz, 2013, Lieberman, 2011, Delloye-Bourgeois et al., 2014, Odent et al., 1999).

The prosencephalic centre induces mesenchymal differentiation of the neural crest cells to induce development of the upper face, parts of the ear and neurocranium whilst the rombencepahlic centre organizes formation of the viscerocranium, middle and lower parts of the face (Lieberman, 2011). Interactions between the ecto- and endodermal epithelia as well as neural crest cells controls morphogenesis of the face, which develops from five pairs of pharyngeal arches (Pharyngeal arch 1-4 and 6) and the frontonasal prominence (which gives rise to the paired medial and lateral nasal processes) (Berkowitz, 2013, Frisdal and Trainor, 2014). The pharyngeal, or branchial arches, are separated internally by endodermal–lined pharyngeal pouches and externally by ectodermal-lined pharyngeal grooves (Schoenwolf, 2009) with a core of mesoderm and neural crest cells sandwiched between them (Frisdal and Trainor, 2014). These arches are formed around the fourth week and give rise to the skeletal tissues, from neural crest cells, skin which derives from the ectoderm and muscle as well as endothelial cells, which are derived from the mesoderm (Sperber et al., 2010, Frisdal and Trainor, 2014).

Of most importance to morphogenesis of the facial region are the first two pharyngeal arches. The other pharyngeal arches differentiate to form structures of the neck and upper thoracic region. The first pharyngeal arch forms the mandibular and maxillary prominences which give rise to the skeletal (maxillary, zygomatic, petreous portion of the temporal, inner ear and mandibular bones), neural (the trigeminal nerve), muscular (temporalis, masseter, the pterygoids and anterior portion of the digastric) and vasculature (a portion of the maxillary artery) which help form the mid and lower face (Frisdal and Trainor, 2014). Contribution of the second pharyngeal arch to facial development is mainly neural (the facial nerve) and the muscles of facial expression (frontalis, orbicularis oculi, the posterior belly of the digastric, levator labii superius, zygomaticus major and minor, orbicularis oris, buccinators, mentalis and auricularis) (Frisdal and Trainor, 2014). Worthy of mention is that the facial artery, which supplies the superficial structures of the face, develops from the third pharyngeal arch (Kumar, 2014).

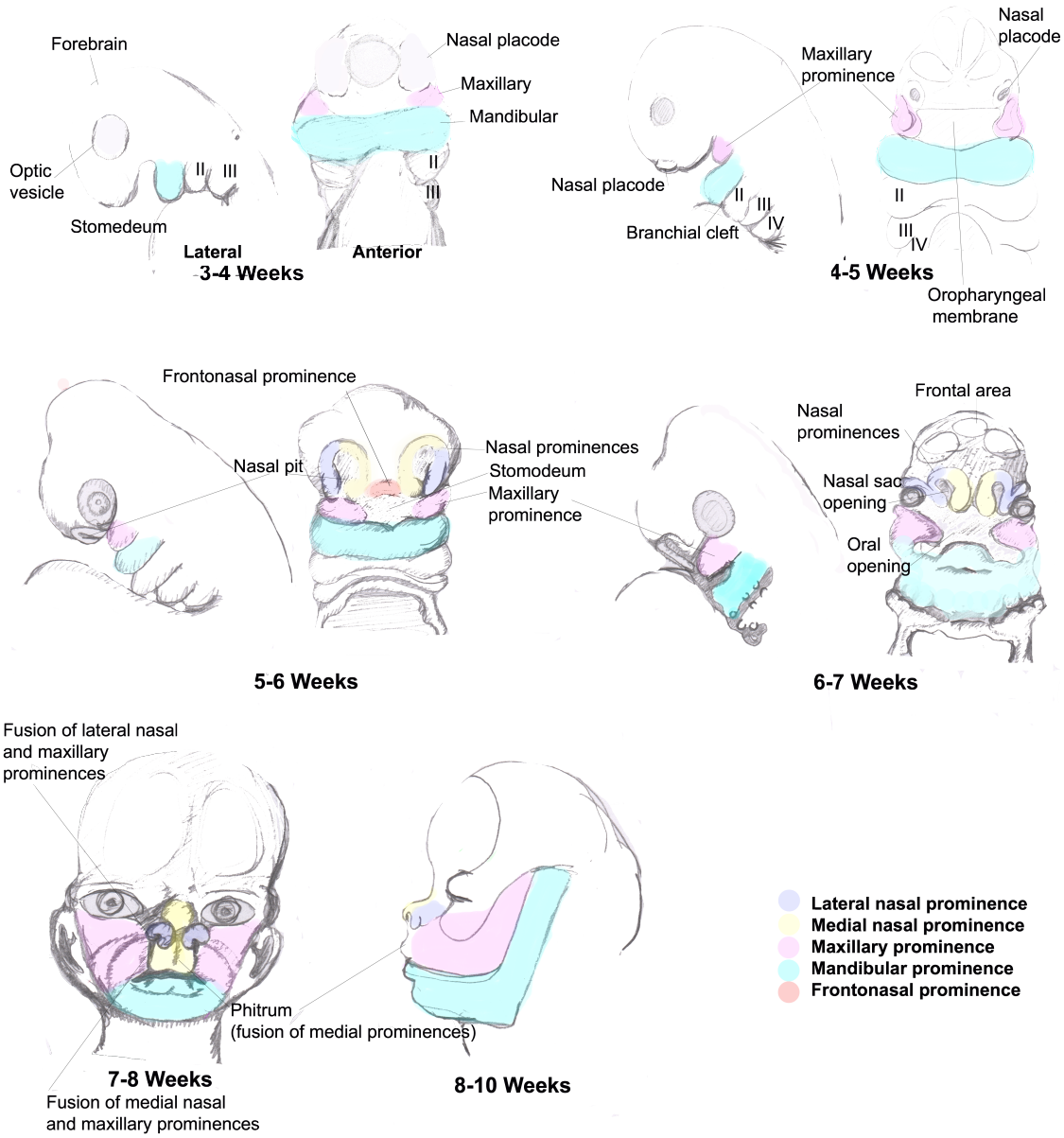

Figure 1.2: Illustrative overview of human prenatal facial development.

The facial complex develops from the first pharyngeal arch (gives rise to the maxillary and mandibular prominences) and the frontonasal prominence (gives rise to the medial and lateral nasal prominences). The frontonasal prominence forms the upper face and nasal bridge whilst the maxillary and mandibular prominences form the mid and lower face. Adapted from (Pansky, 1982).

The upper part of the face and the nasal bridge are formed by the frontonasal prominence (under control of the prosencephalic centre) which comprises an outer layer of ectoderm and inner layer of neural crest and its growth and development are closely related to the forebrain (Moody, 2014, Berkowitz, 2013). Fusion of the frontonasal, maxillary and mandibular prominences around a central depression, which will form the future mouth (the stomodeum), occurs between weeks 5 and 10 of embryonic development to give rise to the morphology of the face (Sperber et al., 2010, Schoenwolf, 2009). The frontonasal prominence forms the forehead, frontal bone and apex of the nose whilst the maxillary prominences fuses with the lateral nasal prominences to give rise to the cheeks, upper jaw and the rest of the nose (Hand and Frank, 2014). The upper jaw is formed by fusion of the maxillary prominence with the medial nasal prominences that form the philtrum, median part of upper lip, nasal septum and the intermaxillary segment whilst the lower jaw (the lips, chin and mandible) is produced by fusion of the mandibular prominence (Hand and Frank, 2014). Continuing face growth is regulated by several signalling pathways including endothelins, fibroblast growth factor (FGF), sonic hedgehog (SHH), wingless (WNT) and bone morphogenetic proteins (BMP), which control the ectomesenchymal interactions that influence survival, apoptosis, proliferation and differentiation of the neural crest cells (Premkumar, 2011). In the foetal and postnatal period, development continues with differential growth of the different structures that constitute the face.

1.1.1 Anatomy, growth and importance of the midface

The skeletal midface is comprised of the zygoma, the maxilla and the inferior portion of the frontal bone. The soft tissue boundaries of the midface extend from the glabella to the top lip vertically and span the pre-auricular distance medially to include the cheeks, nose and upper part of the mouth (Figure 1.1).

The skeletal and soft tissue components develop from the maxillary processes of the first branchial arch and part of the frontonasal prominence (Figure 1.2). The skeletal midface bridges the neurocranium and the rest of the viscerocranium and as such is affected by the growth of both. These bones arise from the neural crest cells within the maxillary prominence and develop through intramembranous ossification (Graber et al., 2011). Development of the soft tissues of the midface occurs simultaneously as the bones through a process of division, cellular proliferation, merging and fusion of the frontonasal and maxillary prominences (Katowitz et al., 2013, Miloro et al., 2004b).

At embryonic week 6, the lateral and medial nasal prominences develop through division of the frontonasal prominence. The medial lateral prominences then merge together in the midline to form the philtrum, tip of the nose and middle segment of the upper jaw whilst fusion laterally of each medial lateral prominence with the paired maxillary prominences completes formation of the upper jaw (cheeks and maxillary area) (Katowitz et al., 2013). The bridge and sides of the nose are formed by the frontonasal prominence and the paired lateral nasal prominences respectively (Katowitz et al., 2013). Differentiation and proliferation of mesenchymal cells in the maxillary prominences causes them to move towards the midline and fuse with the nasal prominences and with each other establishing continuity between the components of the midface (Berkowitz, 2013).

Growth of the skeletal midface is driven by the expansion of the cranial base, enlargement of the brain and development of the eyes which causes displacement resulting in compensatory bone deposition around the metopic, internasal, palatine, maxillary and intermaxillary sutures as well as remodelling of the bones (Burr and Allen, 2013, Graber et al., 2011). The developing teeth,

muscles and enlarging upper airway additionally contribute to driving growth in these bones (Hayward, 2004). The skeletal midface grows most in the anteroposterior dimension, followed by depth and least of all horizontal growth throughout the prenatal period until late adolescence. Postnatal growth of the soft tissues is closely related to that of the skeletal tissues although the correlation is not direct due to the increased subcutaneous fat in children (creating increased thickness of the soft tissue envelope) and projection produced by growth of the nose and lip (Miloro et al., 2004b). Albeit beyond the scope of this thesis, is also the very important role that facial musculature plays in morphogenesis by stimulating bone growth and remodelling as well as directing cartilage growth and connective tissue formation (Hall, 2010, Breitsprecher et al., 1999).

The midface is a complex structure, which is vital for supporting the eyes and contributes to the morphology of the face and upper part of the mouth. It connects the upper and lower face, houses a number of sensory organs, muscles and nerves as well as major blood vessels, which have been discussed earlier. Its complex development, which is related to growth of the brain, can produce devastating clinical manifestations including visual, breathing, feeding, speech and aesthetic problems if impaired. Additionally, deformities can arise from traumatic, infective, iatrogenic and neoplastic causes. Due to its articulations, attachments and neurovascular relations, the midface is an important functional and aesthetic portion of the head.

1.2 Midface dysmorphism in Treacher Collins Syndrome and Craniofacial Microsomia

Congenital defects of the midface can arise due to maldevelopement of all the components such as occurs in the midface hypoplasia (a disorder characterized by midface narrowing, shortening and retrusion) or due to absence or incomplete development of individual structures (e.g. agenesis of the zygomatic bones). It is usually part of a cluster of congenital anomalies in a syndrome and caused by abnormal patterning of the pharyngeal arches and disorders of neural crest cell migration, proliferation or differentiation (Bluestone et al., 2014). Treacher Collins Syndrome (TCS) and Craniofacial microsomia (CM) are

examples of diseases that result in midface dysmorphism due to errors of patterning during branchial arch development and have overlapping phenotypes.

1.2.1 Treacher Collins Syndrome

Treacher Collins Syndrome (TCS), also known as mandibulofacial dysostosis, is a rare genetic disorder of varying penetrance and diverse mutations that causes a spectrum of deformities largely affecting, but not limited to, the craniofacial region. It has a global incidence reported as between 1:10,000-50,000 live births and is predominantly (78-93%) caused by autosomal dominant mutations in the TCOF1 gene which encodes the treacle protein with a smaller proportion of TCS patients (8%) exhibiting autosomal or recessive mutations in POLR1C and POLR1D genes (Conte et al., 2011, Wilkie and Morriss-Kay, 2001, Kadakia et al., 2014, Dauwerse et al., 2011). In a small subset of patients, there may be an atypical mutation in the EFTUD2 gene or chromosome 5q32 deletions (Vincent et al., 2016). Furthermore, 50-60% of TCS cases are caused by de novo sporadic mutations (Trainor, 2010). In animal models of the disease, TCOF1 mutations are associated with neuroepithelial apoptosis, neural crest hypoplasia and abnormal migration of neural crest cells, which are thought to disrupt midface morphogenesis in TCS (Jones et al., 2008).

TCS can lead to a number of skeletal and soft tissue craniofacial deformities including mandibular malformation, midface hypoplasia, lower eyelid coloboma, microtia and cleft palate. Downward slanting palpebral fissures and zygomatic hypoplasia, which result in midface deformity, are the most consistent clinical abnormalities found and give rise to the characteristic “facies” found in TCS (Teber et al., 2004) (Figure 1.3). Patients with TCS rarely suffer intellectual deficit but may have cardiac, gastrointestinal or otolaryngeal problems. So far, a genotype-phenotype association has not been found and extreme clinical variability remains a hallmark of the disease (Vincent et al., 2016).

Diagnosis of TCS usually occurs at birth or even prenatally, if the facial defects are obvious or affect essential functions like breathing. Often, the dysmorphic features trigger an early diagnosis in affected children with radiographic and

genetic testing used to confirm the clinical suspicion, classify disease severity and help formulate a management plan (Kadakia et al., 2014).

A multi-disciplinary approach to management of TCS should be applied in order to deal and optimize with the various clinical and psychological outcomes of the clinical defects. Surgery is often multi-staged with life-threatening problems such as those affecting breathing or feeding addressed in the neonatal period whilst those with a largely aesthetic benefit such as rhinoplasty are often delayed till the child is older (Plomp et al., 2016) (Figure 1.4).

1.2.2 Craniofacial Microsomia

Craniofacial Microsomia (CM) is the second most common cause of congenital craniofacial abnormalities with a global prevalence of 1 in 5600 live births (Birgfeld and Heike, 2012). Aetiology of CM is largely unknown although Chromosomal abnormalities have been discovered in variants of the disease but the clinical significance of these is not clear (Rooryck et al., 2010). A number of mechanisms for pathogenesis have been suggested (through work on animal models) such as stapedial artery haemorrhage, teratogens and abnormalities in neural crest migration, differentiation and proliferation (Poswillo, 1973, Bluestone et al., 2014).

There is a spectrum of craniofacial abnormalities including malformation of the ears, nose, soft palate and lip as well as maxillary and mandibular hypoplasia which arise from abnormal development of the first two branchial arches (Converse et al., 1973). A key feature of the disease is facial asymmetry and the presence of microtia or preauricular ear tags (Keogh et al., 2007). In addition to the craniofacial skeletal and soft tissue deformities, in its broadest sense CM includes a number of clinical abnormalities including nerve palsies, dermoids and extracranial malformations (Heike et al., 2013).

Many of the clinical features of CM overlap with other disorders including TCS, Parry-Romberg and Nager syndromes. As such diagnosis is often after a process of exclusion (Cox et al., 2013). As with TCS, management of CM is multi-disciplinary with surgical procedures undertaken throughout childhood to match the clinical urgency and appropriate developmental stage (Figure 1.4).

Figure 1.3: Male child with Treacher Collins Syndrome.

This child exhibits characteristic facial morphological features. There is malar hypoplasia and down slanting palpebral fissures (black arrows) which are caused by zygomatic bone deficiency (not shown). This child also appears to have bitemporal narrowing, increased intercanthal distance, enlarged forehead, prominent nose and micrognathia that are also dysmorphic features found in TCS.

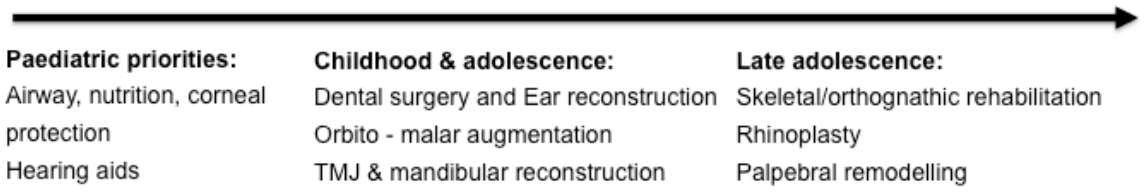

Figure 1.4: Timeline of surgical interventions typically used in Treacher Collins Syndrome and Craniofacial Microsomia.

Priority is given to life threatening and functional problems early on but functional and cosmetic surgery persists throughout childhood.

1.3 Availability and limitations of current reconstructive options for midface deformity

A number of reconstructive methods are available for treatment of midface defects. These are dependent on the nature of the deformity, health and age of the patient as well as resources available. As a general rule, treatment aims to minimize defect, restore function and improve quality of life (Heike et al., 2013).

Autologous fat grafting represents one of the simplest and least invasive techniques for correcting defects and asymmetries caused by soft tissue deficit or minor skeletal hypoplasia. Subcutaneous fat can be harvested (usually from the abdominal or thigh region) in a minimally invasive manner and grafted into deficient compartments with good immediate results and few complications (Pasquale et al., 2015). Limitations of lipofilling include resorption and its use is only appropriate for restoring small volume defects, revision or in primary augmentation prior to more complex reconstructive surgery to optimize results (Guibert et al., 2013, Franchi et al., 2015).

Midface deformities involving significant skeletal hypoplasia often require more complex reconstructive procedures (Brown and Shaw, 2010). Bone grafts, most commonly harvested from the calvarium, can be used to reconstruct skeletal defects although there is a small risk of resorption (Smolka et al., 2005). Osteotomies (with or without bone grafts), distraction-osteogenesis and tissue transfer using flaps represent more complex but effective approaches to correct the skeletal and/or soft tissue deformities (Britto et al., 2014, Tahiri and Taylor, 2014). These procedures are however, not without complications and maybe associated with haemorrhage, infection, neurological events, resorption of bone grafts, donor-site defect and re-operation (Wan et al., 2009, Britto et al., 2014, O'Connell and Futran, 2010). Metals and other alloplastic materials are also used successfully either alone or in combination with autologous tissues to reconstruct complex boney defects (Niechajev, 2012, Brown and Shaw, 2010). Despite good early outcomes, there are concerns regarding extrusion, infection, healing and contour irregularities (Yaremchuk et al., 2011, Curi et al., 2012).

The key limitations of midface reconstruction in children with congenital defects are that often complex invasive surgery is required and repeat procedures are needed to refine the outcome as the child grows. A staged approach to reconstruction is usually applied and some advocate attempting skeletal harmonization first before correcting the soft tissue deformity whilst (Yang et al., 2015a, Cobb et al., 2014, Mitsukawa et al., 2014). Using computer-aided design to plan correction has increased the accuracy of surgery, by enabling preshaping of implants and evaluating outcomes (Herlin et al., 2013b, Watson et al., 2014, Guibert et al., 2013). However, these simulations are often reliant on simple 3D reconstructions of MRI or CT scans and modelling of the skeletal or soft tissue surfaces. Better understanding of the postnatal development of the midface is still needed as it provides improved knowledge of the natural course of the disease, which permits planning of early and long-term management.

The key limitations of current surgical options are that they either involve invasive procedures to reshape and/or reconstruct with autologous tissue, which leaves a donor-site defect, or they use foreign-body implants, which do not grow with the child. Additionally, available methods of operative planning are not able to correlate the skeletal and soft tissues of the face thus final outcome is difficult to predict. As a result, affected children usually need multiple surgeries to fine-tune the initial reconstruction as they grow. This can have an adverse effect on their physical and psychological wellbeing, which can negatively impact their interaction with peers, education and prospects.

1.4 Personalised facial bone implants for midface reconstruction

The morbidity associated with autologous tissue transfer and foreign-body implants could be reduced with the availability of autologous personalised bone implants. Computer modeling can be used to elucidate facial morphology in children during development, compare affected children and plan surgical interventions through virtual normalisation (de Souza et al., 2013) to predict the size and shape of the bone implant needed to accurately reconstruct the defect. If these implants are bioengineered-using cells harvested through minimally invasive surgical methods and induced to undergo bone generation on a biodegradeable scaffold, they could provide an autologous solution to synthetic implants, bone grafts or flaps which is life-long and grows with the child. Combination of these techniques could provide a truly personalised autologous and custom-shaped bone implant.

1.4.1 Morphometric analysis to model postnatal face growth and plan treatment

There is deficiency in the literature for objective quantification of midface growth in both normal and abnormal postnatal development. Additionally, there is a need for characterization of the relationship between the growing bony skeleton and overlying soft tissue envelope. Such information can be used to elucidate facial morphology in children during development, compare dysmorphic children and evaluate surgical interventions through virtual normalization of affected patients. Eventually this data could provide a preoperative planning tool to increase surgical accuracy.

1.4.1.1 Human models of postnatal facial development and reconstruction

Anthropometric studies of the craniofacial region

Traditionally, facial growth and development have been studied using physical measurements of the soft and skeletal tissues. These measurements maybe taken directly from living samples using callipers or indirectly by measuring the distances between landmarks on photographs or in the case of skeletal tissues radiographs. Anthropometry has provided useful information with regards to the dimensions and ratios of the subunits of the face during postnatal development

and comparison between different genders, ethnicities and diagnoses (Mahdi, 2012, Farkas et al., 2004, Kolar et al., 1987). The increasing availability of 3D photography has also allowed 3D anthropometry to be performed using surface modeling thus increasing understanding of soft tissue postnatal development in the craniofacial region (Suttie et al., 2013, Koudelová et al., 2015, de Souza et al., 2013).

Cephalometry, the branch of anthropometry concerned with study of craniofacial bones, may be performed by directly measuring the proportions of cadaveric tissues such as dry skulls or indirectly thorough analysis of the distances between specific landmarks on radiographs, CT scans or ultrasound images. It has increased understanding of the craniofacial growth in normal postnatal development as well as CM and TCS (Ongkosuwito et al., 2013, Posnick et al., 1995). (Mellion et al., 2013, Bergman et al., 2014), computed tomography (CT) scans of dry skulls (Nikkhah et al., 2013, Harnet et al., 2013) or indirectly by extrapolating data from soft tissue to the underlying skeleton (Krimmel et al., 2015). A major limitation of cephalometry is the reliance on plain radiographs, CT scans or other medical imaging outputs. This creates difficulty in finding a suitable control population, as healthy children do not normally undergo diagnostic medical imaging.

Whilst useful information regarding craniofacial growth and development has been gained from anthropometric studies (Farkas et al., 1992), there are several technical challenges which limit its usefulness. The most important is difficulty relating the measurements on 2D images or reconstructions to their corresponding 3D structures on the face (Fernandes et al., 2015, Lisboa et al., 2015) and that shape can not be described using size-based measurements thus form can not be modelled (McIntyre and Mossey, 2003).

Morphometric analysis to model postnatal face development

Both craniofacial shape and size can be described using morphometric analysis (MA). MA allows quantitative analysis of form through a range of methods including voxel-based, deformation and landmarking (Ashburner and Friston, 2000, Rolfe et al., 2011). Craniofacial form is most commonly studied using

geometric morphometrics (GM), which is a landmark-based method of MA. This process involves using 2D or 3D data to generate a set of substitute Cartesian ("shape") coordinates that can undergo multivariate analysis (Schaefer and Bookstein, 2009).

MA has so far been used to study facial characteristics amongst normal and syndromic populations as well as form the basis for classifying non-genetic syndromes (Hopman et al., 2014, de Souza et al., 2013, Hammond et al., 2003). Analysis of the facial skeleton has been undertaken in TCS using GM although this only focused on relatively mild forms of the disease (Nikkhah et al., 2013). Soft tissue analysis in CM has also been studied using 3D surface imaging in a small study (n=3) (Claes et al., 2011). There is however, still paucity in the literature with regards to understanding postnatal development and the relationship between the skeletal and soft tissues during this period in control as well as CM and TCS children's faces.

Computer aided modeling as an to aid surgical management

Computer-aided design has increased the accuracy of operative interventions as it permits 3D reconstructions of the child's face using data from CT or MRI scans to plan surgery. Traditionally, these images have be used to help choose the procedure required to reconstruct the defect or used to generate a prototype using 3D printing in order to simulate and plan the reconstruction (Choi and Kim, 2015). They can also be used to design custom-shaped implants for the procedure (Parthasarathy, 2014).

More recently, MA has been used to generate models of the face in order to virtually simulate surgery with promising early results (Vale et al., 2016, Liebregts et al., 2015a, Liebregts et al., 2015b). These models have also been further developed to propose training and haptic virtual simulation tools in an attempt to increase surgical accuracy (Medellín-Castillo et al., 2016). The outcomes of these studies are promising but are limited by the fact that none have modelled simultaneous skeletal and soft tissue development in paediatric midfaces, severe skeletal defects nor the long-term outcome of the procedures. Thus a method that describes normal postnatal development of the skeletal and

soft tissues, compares dysmorphic children and permits evaluation of surgical outcomes is still needed. This data may eventually allow the development of an accurate virtual simulation tool, which can take into account actual, predicted and desired facial development of children with CM and TCS thus increasing surgical accuracy and reducing repeat procedures.

1.4.2 Bone tissue engineering to generate autologous bone implants

Bone is the second most transplanted tissue (after blood) with 2.2 million bone grafts performed annually (Lewandrowski et al., 2000). Due to the risks and limitations of reconstruction of defects with foreign body implants and autologous bone transfer, tissue engineering provides the promise of generating autologous bone tissue without many of the limitations and morbidities associated with the gold standard treatment.

As a tissue, bone is complex as it has a mechanical, haemopoeitic and metabolic functions. It provides structure and protection to surrounding soft tissues and is necessary for metabolic regulation of calcium and phosphate as well as haemopoeisis. Additionally, the structure and function for each bone is highly site-specific and related to its embryological origin as well as its ability to adapt (e.g. the weight-bearing long bones which are of mesenchymal origin and facilitate locomotion compared with the neural-crest derived flat bones of the face which provide support and structure). Bone is composed of a cellular and acellular component (Rao and Stegemann, 2013). The latter constitutes 80% of the overall bone mass. Osteoprogenitor cells, osteoblasts, osteocytes and osteoclasts constitute the cellular components (Lu et al., 2012). Osteoprogenitor cells are important for proliferation and self-renewal. They differentiate into immature osteoblasts, which further differentiate into osteoblasts, which lay down the bone extracellular matrix and deposit mineral. Osteoblasts eventually mature into osteocytes, which deposit mineral and are needed for mechano-transduction. Osteoclasts are bone-resorbing cells of haematological origin that resorb bone.

There is extensive cross-talk between the bone cells which in concert regulate bone remodelling (Florencio-Silva et al., 2015). Osteoblasts, immature bone

cells found in the periosteum that line the bone and in the endosteum, form bone by depositing the organic and inorganic extracellular matrix and eventually become encased in their lacunae thus forming osteocytes. These are the mature bone cells which act as mechanosensors, control mineral haemostasis and regulate both osteoclast and osteoblast function (Chen et al., 2015). This provides a balance between osteoblast mediated bone formation and osteoclastic resorption in response to the environment. The acellular components are predominantly collagen 1 and extracellular matrix proteins as well as minerals such as hydroxyapatite. The acellular components together provide a scaffold to support cells structurally as well as facilitate their growth, proliferation, differentiation and signalling.

Due to its high metabolic activity, bone is richly vascularised. Any attempt at bone tissue engineering must therefore address the multipurpose nature of bone and its metabolic requirements as well as its complex structure.

To date, many different approaches have been taken to tissue engineer bone using osteoprogenitor cells. In general, the reconstructive principles of finding the optimal cell type scaffold capable of providing biomechanical support as well as perfusion and biochemical environment underpin the basic methodology of most research in this area. A multitude of different options are associated with each of these variables so there is no consensus regarding the optimal method for engineering bone.

1.4.2.1 Sources of Osteoprogenitor Cells

Osteoprogenitor cells are capable of differentiation down the osteogenic lineage into osteoblasts (Rao and Stegemann, 2013) (Figure 1.5). Postnatally, osteoprogenitors can be isolated from mesenchymal stem cells (MSC) present in a variety of tissues including the bone, bone marrow, periosteum and adipose (Corradetti et al., 2015, Rosales-Rocabado et al., 2014, Zielins et al., 2015). Though osteoprogenitors express general markers of pluripotency such as CD44, CD90, CD105 and CD166 (Dominici et al., 2006, Maleki et al., 2014), the sub-populations that have greatest osteoprogenitor potential have been shown to also express STRO-1, SB-10 and HOP-26 (Stewart et al., 2003, Gronthos et

al., 1994, Green et al., 2015). Other potential sources of osteoprogenitor cells include embryonic (Mahmood et al., 2012), amniotic fluid (Si et al., 2015) and induced pluripotent stem cells (de Peppo et al., 2013).

Adipose Derived Stem Cells

The multi-lineage potential of human adipose-derived stem cells (hADSC) has been known for over 10 years (Zuk et al., 2002, Philips et al., 2012). These cells are derived safely and minimally invasively from small amounts of fat available from adult as well as paediatric patients, easily expanded in vitro, capable of self renewal and possess multilineage differentiation potential including osteogenesis (Levi and Longaker, 2011, Guasti et al., 2012). They have also been demonstrated to have immune-modulatory properties and promote vascularization thus making their clinical translation more attractive (Peng et al., 2012, Gao et al., 2014b). In vivo, hADSC have been successfully used to promote critical bone defect repair in rats (Streckbein et al., 2013, Jin et al., 2014). There is also one case report of their use to reconstruct zygomatic hypoplasia in a TCS patient (Taylor, 2010).

Bone Marrow Derived Stem Cells

Another well-studied source of stem cells for bone tissue engineering is human bone marrow derived stem cells (hBMSC). These cells possess multipotency, can self renew, are easily derived from a small amount of donor tissue and can be rapidly expanded (Gao et al., 2014b, Xu et al., 2010). The hBMSC are capable of differentiation along the osteogenic lineage in vitro and when compared with other somatic sources of osteoprogenitor cells, have demonstrated greater osteogenic marker expression and mineralization when differentiated down the osteogenic lineage (Shafiee et al., 2011). Similarly to hADSC, these cells have been shown to promote vessel formation when co-cultured with endothelial cells (Pill et al., 2015). In vivo, hMSC have recently shown promise in repair of sub-acute critical sized long bone defects in a preclinical large animal model and to successfully regenerate a maxillary oral defect in a clinical study of a single patient (Berner et al., 2015, Rajan et al., 2014). Unlike hADSC, the method of harvest is invasive in that a bone marrow

biopsy or bone specimen is required to isolate these cells, which can leave a donor-site defect. This is problematic for children with complex syndromes usually have to undergo several other surgical procedures.

Bone-derived osteoprogenitors

Explant cultures of bone tissue can be used to generate osteoblast-like cells that, when placed in osteoinductive media, upregulate markers of mature bone differentiation and deposit minerals. Human osteoblast precursors (hOP) have been obtained from a variety of bone sources including intraoral and midface tissues (Mailhot and Borke, 1998, Ishino et al., 2003). Traditionally these cells have been considered as being committed to the osteogenic lineage, but recent evidence suggests that they may possess a similar multipotent and proangiogenic profile to hBMSC in children (Jonsson et al., 1999, Wang et al., 2016). Whilst these cells are relatively easy to obtain in the case of trauma or neoplasm where bone debridement/excision is necessary, in correcting congenital defects, harvesting of bone would be associated with a donor site defect and as such their use in reconstruction of defects may be limited.

1.4.2.2 Induction of osteogenic differentiation

In order for new bone formation to occur, osteoprogenitor cells must be recruited through a complex and highly regulated interplay between signalling from the systemic environment and local biomechanical as well as biophysical environment (Ren et al., 2015). These signals co-ordinate activation and maturation of the osteoprogenitor cells giving rise to osteoblasts which in turn produce and lay down the extracellular bone matrix (Chaudhary et al., 2004).

Bone differentiation is characterized by up regulation of genes and protein expression in a sequential manner. Early gene markers of osteogenic differentiation include runt-related protein 2 (*RUNX2*), osterix (*OSX*), collagen 1 (*COL1*) and alkaline phosphatase (*ALP*) whilst maturation of osteoblasts is heralded by expression of late markers such as bone sialoprotein (*BSP*), osteopontin (*OSTP*) and osteocalcin (*OSC*) (Figure 1.6). Also the amount and

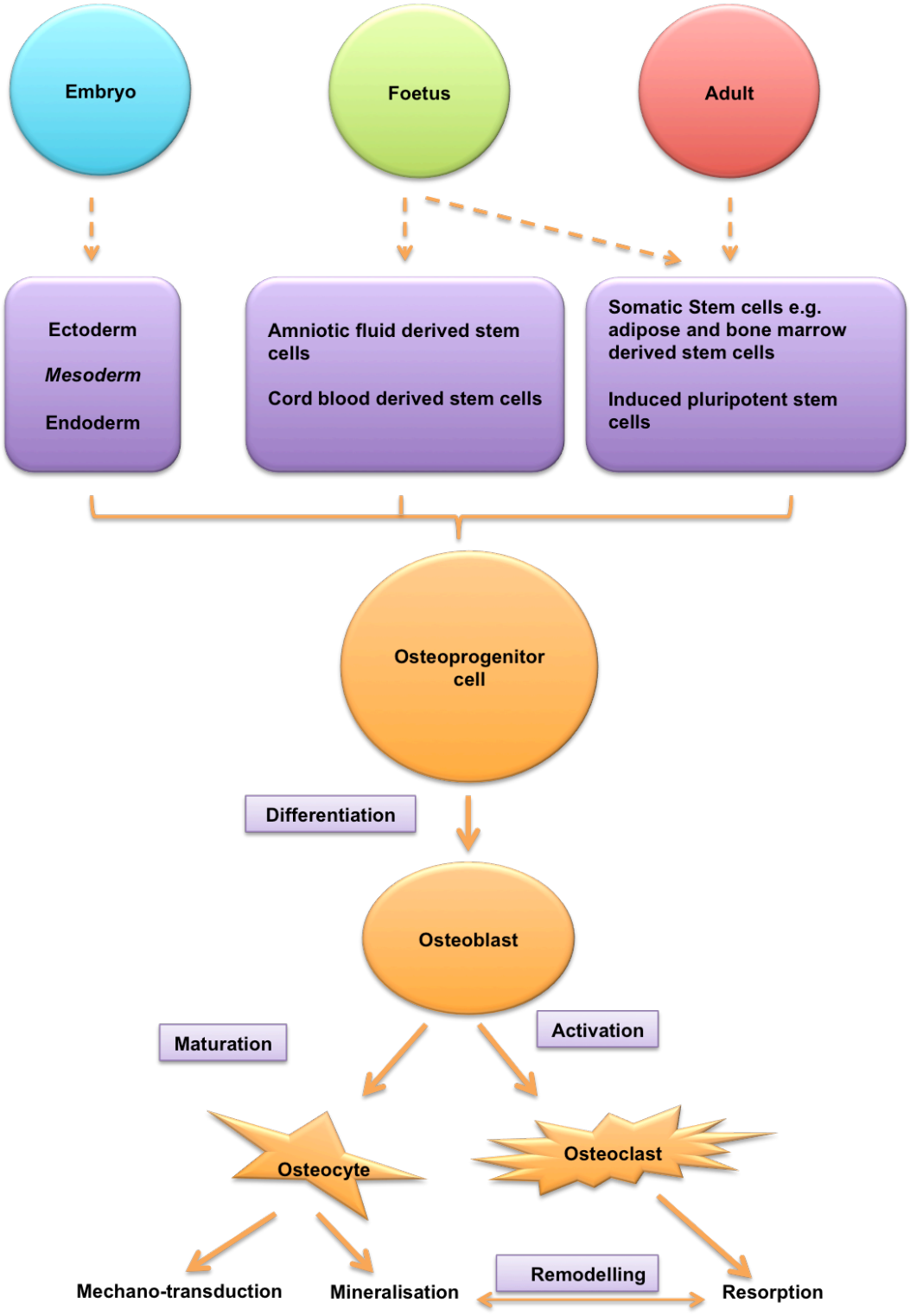

Figure 1.5: Concise overview of osteoprogenitor cell origin and the interplay between bone-related cells.

Osteoprogenitor cells can be embryonic, foetal or adult derived. These cells can differentiate into osteoblasts, which mature into osteocytes. Osteoblasts also activate osteoclasts. Together these cells maintain the balance between mineralisation and resorption.

pattern of calcium deposition (mineralization), extracellular matrix composition and mechanical properties can be used to assess the stage of bone differentiation and maturity.

Bone formed *in vivo* by implanted MSCs is often insufficient to repair defects, thus expansion and osteoinduction of osteoprogenitor cells prior to their implantation into a defect has been postulated to increase bone formation (Siddappa R et al., 2008, Kumar S et al., 2010, Meijer GJ et al., 2007). Many studies have attempted to drive osteogenic differentiation using growth factors such as BMP-2 (Lysdahl et al., 2014), FGF-2 (An et al., 2015, Kwan et al., 2011) and VEGF (Li et al., 2015), genetic modification (Deng et al., 2014), co-culture with other cells (Kim et al., 2014) and using mechanical stimulation such as pulsed electromagnetic fields (Ongaro et al., 2014). Additionally, the role of the musculoskeletal unit (bone-tendon-muscle) provides an important biomechanical stimulus which regulates normal bone development and maintenance (Sartori and Sandri, 2015).

The issue of vascularisation and perfusion is of paramount importance when attempting bone tissue engineering as it not only affects the function of the bone but also the size of tissue that can be generated. Studies have shown that altering the microarchitecture of nanocomposite scaffolds improves vascularisation and enhances MSC osteogenesis when subcutaneously implanted in nude rats. Similarly, 3D co-culture of MSC with endothelial precursors prompted early vascularisation and osteogenic differentiation (Duttenhoefer et al., 2013).

Whilst a number of pathways can be targeted to drive osteogenic differentiation, those activating the canonical Wnt/β-catenin pathway are generally thought to be of greatest importance in driving osteogenic differentiation and mineralisation (Kook et al., 2015). Most differentiation media contain a combination of dexamethasone, ascorbic acid, β-glycerophosphate which are thought to increase *RUNX2* expression, enhance collagen 1 secretion and promote hydroxyapatite formation in vitro, respectively (Langenbach and Handschel, 2013).

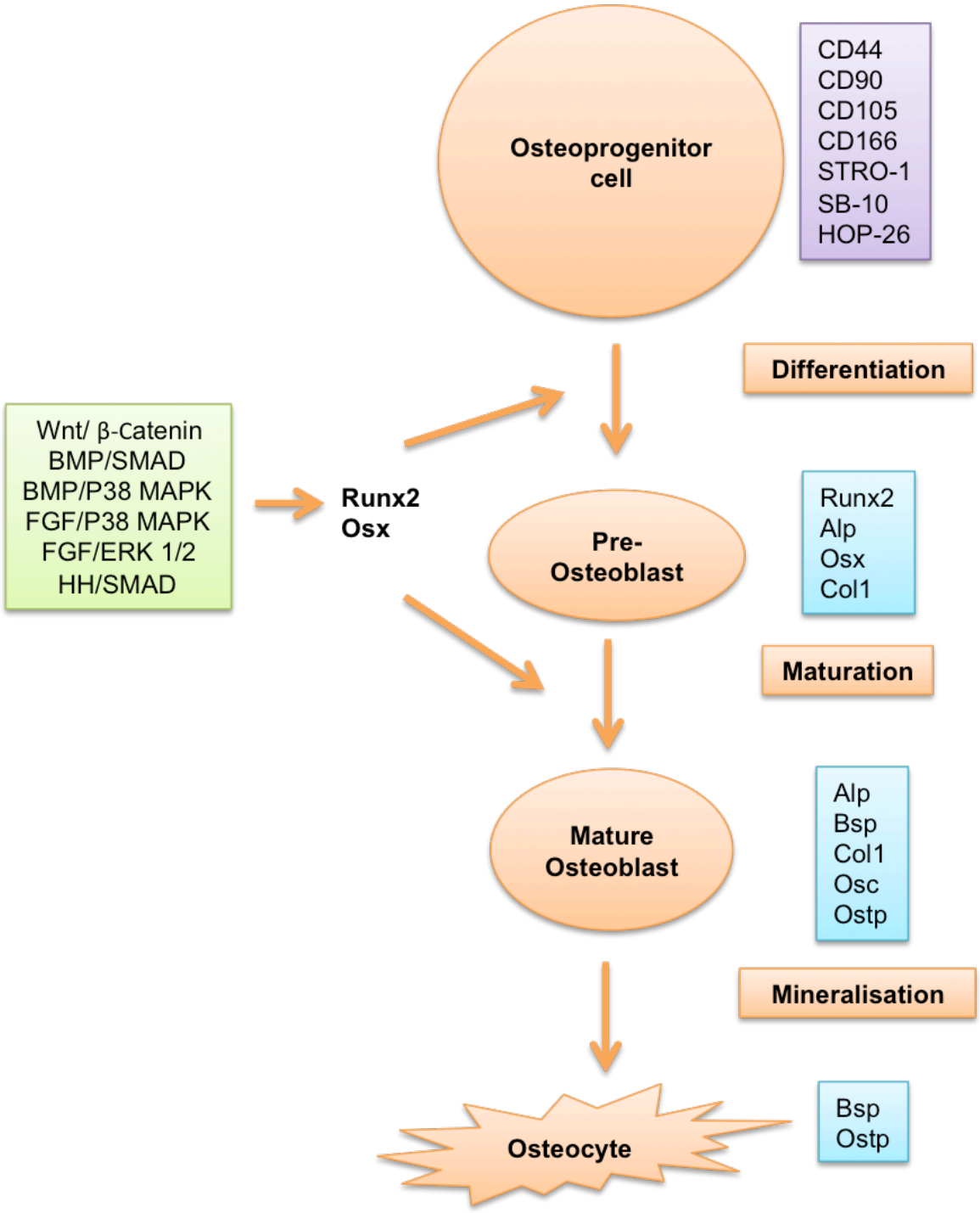

Figure 1.6: Osteogenic differentiation in osteoprogenitor cells.

Osteoprogenitor cells express a number of surface markers (purple box) and can be induced to undergo osteogenic differentiation through several signalling pathways (green box). These pathways lead to RUNX2 and/or osterix (OSX) activation, that generates pre osteoblasts, which upregulate early osteogenic genes (blue box). Further maturation generates mature osteoblasts that are characterised by additional up regulation of later genes. These cells then mineralise and form osteocytes that then express late genes (BSP and OSTP).

Dexamethasone

Dexamethasone has been shown to induce osteogenic differentiation of osteoprogenitors when used at near physiological concentrations in vitro (Walsh et al., 2001). The mechanisms by which this occurs may be due to activation of *RUNX2* expression by WNT/β-catenin signalling or through the mitogen-activated protein kinase (MAPK) phosphatase pathway (Hamidouche et al., 2008, Phillips et al., 2006).

β-glycerophosphate

Osteogenic differentiation is promoted by β-glycerophosphate (BGP) in two ways. Extracellularly, BGP acts as a source of phosphate for the generation of hydroxyapatite mineralization whilst intracellularly it induces bone morphogenetic protein 2 (*BMP2*), a crucial growth factor in mineralization, expression through activation of ERK and cyclic-AMP/protein-kinase-A signaling pathways (Bellows et al., 1992, Langenbach and Handschel, 2013).

Ascorbic Acid

Ascorbic acid (AA) plays an important role in extracellular matrix deposition (ECM). AA is required for the conversion of pro-collagen 1 to collagen 1 as it is a co-factor for the enzymes required for this process (Langenbach and Handschel, 2013). The ECM, and in particular collagen 1 secretion, is a key regulator and promoter of osteoblastic differentiation (Franceschi and Iyer, 1992). ECM-mediated osteogenic differentiation is mediated by MAPK signalling activation as a result of activation from Collagen I and integrin interactions caused by osteoblast binding to the ECM. MAPK signalling leads to *RUNX2* activation resulting in expression of osteogenic markers such as osteocalcin and bone sialoprotein (Xiao et al., 2002, Langenbach and Handschel, 2013).

1.4.2.3 Scaffolds for Bone tissue engineering

In order for bone tissue engineering to succeed, a scaffold which is capable of providing 3D structural support to cells and can mimic the biomechanical environment is required (Rada et al., 2012) (McMahon et al., 2013). In addition,

it should be biocompatible, bioabsorbable, mouldable and able to support vascularisation (Laurencin et al., 2006). The most sophisticated scaffolds attempt to recreate the extracellular matrix and stem-cell niche (Nii et al., 2013, Minardi et al., 2015).

A wide-variety of different scaffolds has been proposed for bone tissue engineering ranging from hydrogels such as collagen and fibrin which have been shown to mimic the extracellular matrix and when impregnated with osteoinductive components repair bone defects in rats (Machado et al., 2015, Quinlan et al., 2015) to synthetic biomaterials in the form of polymers (Rossi et al., 2013) and bioactive ceramics (Baino et al., 2015). Each of these scaffolds has advantages and disadvantage for its use for bone tissue engineering. Due to the complexity of bone with respect to structure, function and metabolic requirements as well as a need to tissue engineer bone rapidly due to the large-scale therapeutic demand, combinations of these scaffolds can yield the best results. Composite scaffolds could provide the biomimetic properties of the extracellular matrix bestowed by natural scaffolds such as hydrogels whilst possessing the mechanical strength, mass production and ease of surface modification that the synthetic scaffolds provide.

Fibrin

Fibrin is readily manufactured using reproducible protocols, easily sterilised, bioabsorbable, already licensed for use in craniofacial surgery and can be 3D printed into a desired shape containing cells (Lee et al., 2010). As a biomaterial, fibrin has repeatedly been shown to promote survival, proliferation and differentiation of osteoprogenitor cells in 3D culture (Gasparotto et al., 2014).

Fibrin is a key constituent of the coagulation cascade and has angiogenic properties which make it a desirable scaffold for bone tissue engineering (Ceccarelli and Putnam, 2014). Due to its low mechanical strength, fibrin has successfully been used either as a cell carrier or combined with a stronger scaffold to regenerate bone defects in animal models (Sagar et al., 2013, Kretlow et al., 2010). It has also been used to deliver osteogenically differentiated hBMSC in combination with bone graft to patients with non-

healing upper limb fractures which were shown to unite on follow-up (Giannotti et al., 2013).

Nanomaterials

Nanomaterials are suited for use as scaffolds in bone tissue engineering as they can provide mechanical strength, biocompatibility, controlled biodegradation and an easily modifiable surface and porous structure which can promote cell proliferation and vascularization (Rossi et al., 2013).

Polyhedral oligomeric silsesquioxane-poly(Caprolactone-urea)urethane (POSS-PCL) is a biodegradeable nanocomposite scaffold that combines a POSS nanocage and a hard PCL tail. POSS nanoparticles are considered to be the smallest silica particles. They comprise an inner inorganic oxygen and silicon layer and an outer organic layer. This structure confers a number of desirable functional and physical properties with respect to scaffold design. These include compatibility with many different polymers, addition of dimensionality to a polymer matrix, and enhancement of mechanical strength as well as enabling surface modification (Ghanbari et al., 2011, Ayandele et al., 2012). Poly(ε-Caprolactone) (PCL) is a nanofibre that has been shown to support osteogenic differentiation including of hADSC (Pereira et al., 2013). Co-polymerisation of POSS with the biodegradeable and biocompatible PCL provides a nanocomposite polymer that combine the properties of the two (POSS-PCL) (Wen Guan and Zhaobin, 2012). This biomaterial can be made into a flat disc-like scaffold (“cast”) which gives rise to sheets of tissue or a porous (“coagulated”) form that can be populated by cells throughout its structure to produce 3D cultures.

1.5 Clinical potential and challenges to bioengineering personalised facial bone implants for paediatric midface reconstruction

Congenital craniofacial deformities of the midface as typified by Treacher Collins Syndrome and Craniofacial microsomia can result in functional and aesthetic deficits, which may cause problems with vision, speech, feeding and psychosocial welfare. Affected children may require treatment in the form of invasive reconstructive surgery using tissue transfer or foreign body implants

which can lead to donor-site defects, do not fully grow or incorporate with the skeleton and may be associated with increased risks of infection and extrusion. Furthermore, reconstruction is currently planned using qualitative analysis of CT scans. As this does not take into account continued growth of the midface, the reconstructive outcome maybe aesthetically unsatisfactory and require further procedures as the child grows. Repeat invasive surgeries can have an adverse effect on the child's physical and psychological wellbeing potentially negatively impacting their interaction with peers, education and prospects.

At present, computer-aided design has advanced the accuracy of preoperative planning in that it provides templates upon which plates and grafts can be shaped on the operating table. Whilst these prefabricated templates have increased reconstructive accuracy, they are still reliant on using autologous bone grafts and/or metallic implants and rely on the shaping of the final implant during the operation (Levine et al., 2012). In addition to the above traditional methods for reconstruction of craniofacial bone defects, there is research on producing bone substitutes using autologous stem cells but it is still at the early stages as an optimal scaffold and differentiation protocols are still under debate (Baskin and Eppell, 2013). It is clear that craniofacial reconstructive surgery would benefit from a better understanding of skull development in children and a minimally invasive approach to yield autologous accurately shaped bone implants.

Reconstructive surgery for craniofacial defects could benefit from an alternative to autologous bone grafts and foreign-body implants through tissue engineering of bone using autologous stem cells and biodegradeable scaffolds. To further increase the accuracy of surgery, these prefabricated implants can be preshaped and sized according to the patient's needs by modeling the skeletal and soft tissues of the face to plan the surgery. Hence, combining computational biology and bone bioengineering holds the potential to generating personalised autologous facial bone implants which could bypass the limitations of current midface reconstructive options in children. These two areas are often studied separately and the aim of bioengineering a custom-shaped facial bone still remains elusive. Fortunately, there are a number of

promising results which can be built on to achieve this but also key limitations that need to be overcome simultaneously.

1.5.1 Modeling normal postnatal development of the midface to establish a normative standard of growth, understand dysmorphology in CM and TCS and build a surgical planning tool

As already discussed, the anatomy of the midface is complex due to the intricate interplay between soft tissue and underlying bone architecture with a direct correlation between form and function. Growth is driven by a number of factors in the prenatal and early postnatal period including development of the brain. The relationship between the skeletal and soft tissues is direct and reciprocal in that growth of craniofacial sutures directs the degree of displacement of the midface whilst the eyes, tongue, teeth, musculature and nasal cavity direct growth of the facial skeleton (McMahon et al., 2013)

The availability of 3D imaging has enabled 3D anthropometry to be performed using surface modelling, thus increasing understanding of postnatal development in the craniofacial region (Suttie et al., 2013, Koudelová et al., 2015, de Souza et al., 2013). Soft tissue facial growth in children has been well studied and most commonly using surface images captured with 3D photogrammetric cameras which have the advantage of being safe, non-invasive and can allow immediate recruitment onto a trial. There have been fewer publications on 3D modelling of facial skeletal development with existing studies predominantly performed using data from CT scans and small patient numbers (Kelly et al., 2017). Where dysmorphology in diseases like TCS was previously modelled, inadequate controls (e.g. use of dry skulls) and modelling only the mild defects has limited the usefulness of these data to generating a surgical planning tool data (Nikkhah et al., 2013).

Until recently, research has traditionally focused on studying hard and soft tissues separately. This is problematic, as accurate surgical planning requires an understanding of how the skeletal and soft tissues correlate with each other in order to plan reconstruction. Studies that have used combined modeling to analyze facial growth are still limited by lack of younger children in the dataset (aged 5 and under for instance) or a very small sample size of dysmorphic

patients (Young et al., 2016, Herlin et al., 2013b, Herlin et al., 2013a, Ibrahim et al., 2016b). Combined models of the face have also been used to recently plan surgery with promising results regarding accuracy (Liebregts et al., 2015b, Liebregts et al., 2015a). Unfortunately, these results are based on data from non-syndromic adults and adolescents.

Whilst the results of pre-existing studies are promising there are still a number of barriers to clinical translation. There is still a need for a combined model of normal and dysmorphic postnatal midface development during childhood. Inclusion of TCS and CM patients before and after surgery would also enable comparison of dysmorphology against normative controls and evaluate efficacy of surgery. This data could help form the basis for developing a preoperative surgical planning tool to design the shape and volume of construct needed to accurately reconstruct the defect.

1.5.2 Recreating the bone microenvironment in order to optimise osteogenic differentiation and maturation of hADSC on a bioabsorbable scaffold to bioengineer bone implants.

A number of different approaches have been investigated bioengineering bone tissues with varying degrees of success although the fabrication of mature functional autologous bone is yet to be achieved. The general principles of finding the optimal osteoprogenitor cell type scaffold capable of providing biomechanical support and recreation of the bone micro-tissue environment form the mainstay of investigation.

Human adipose-derived stem cells (hADSC) have yielded promising results to date due to their ease of culture, self-renewal and multilineage differentiation potential (Levi and Longaker, 2011, Guasti et al., 2012) as well as their ability to confer immune-modulatory effects and promote vascularization (Peng et al., 2012, Gao et al., 2014b). In vivo, hADSC have been successfully used to promote critical bone defect repair in rats (Streckbein et al., 2013, Jin et al., 2014) and there is also one case report of their use to reconstruct zygomatic hypoplasia in a TCS patient (Taylor, 2010). BMSC are also capable of differentiation along the osteogenic lineage in vitro and when compared with other somatic sources of osteoprogenitor cells, have demonstrated enhanced

osteogenic marker expression and mineralization when differentiated down the osteogenic lineage (Shafiee et al., 2011). Similarly to hADSC, these cells have also promoted vascularization in vitro (Pill et al., 2015). In vivo, hBMSC have recently shown promise in repair of sub-acute critical sized long bone defects in a preclinical large animal model and to successfully regenerate a maxillary oral defect in a clinical study of a single patient (Berner et al., 2015, Rajan et al., 2014). Another promising source of MSC for osteogenic differentiation are human osteoblast precursors (hOP) that are capable of forming osteoblast-like cells and have been obtained from a variety of bone sources including intraoral and midface tissues (Mailhot and Borke, 1998, Ishino et al., 2003). Recent evidence suggests that they may possess a similar multipotent and proangiogenic profile to BMSC in children (Jonsson et al., 1999, Wang et al., 2016). Harvesting of hADSC is considerably less invasive than hBMSC or hOP which require a bone biopsy. At present it is however, unclear which of these cell types provides the optimal osteoprogenitor source for producing mature osteoblasts in children. As such, direct comparison of hADSC with hOP and hBMSC is necessary in order to determine the suitability of using hADSC to produce mature bone tissue for children.

Historically, a wide-variety of different scaffolds have been proposed for bone tissue engineering ranging from natural materials such as fibrin (Machado et al., 2015) to synthetic biomaterials in the form of polymers (Rossi et al., 2013), all of which have demonstrated distinct advantages and disadvantages (Ibrahim et al., 2016a). Increasingly, biomaterials that attempt to recreate and stimulate the extracellular matrix and stem cell niche are being generated with the aim of enhancing cell adhesion, proliferation and differentiation (Nii et al., 2013, Minardi et al., 2015).

Fibrin is an attractive biomaterial for bone tissue engineering as it has been repeatedly shown to promote survival, proliferation and ostegenesis of osteoprogenitor cells in 3D culture as well as support vascularization (Gasparotto et al., 2014, Lohse et al., 2012). It can also be decorated with osteoinductive components such as hydroxyapatite crystals or growth factors to stimulate osteogenesis when implanted in rat defects (Machado et al., 2015)

and has also been used to deliver osteogenically differentiated hBMSC in combination with bone graft to patients with non-healing upper limb fractures which were shown to unite on follow-up (Giannotti et al., 2013). It is however limited by poor mechanical strength and thus requires modification in order to replicate the functional and structural material properties of bone.

Nanomaterials have been shown to promote osteoinduction of MSC in vitro (Binulal et al., 2010) (Yang et al., 2015b) (Koroleva et al., 2015). Combination of nanomaterials with natural or synthetic polymers can be used to enhance the biomimetic properties of traditional scaffolds in order to induce osteogenic differentiation and promote mature bone formation in vitro (Nair et al., 2015). (Gandhimathi et al., 2015). The versatility and biocompatibility demonstrated by nanomaterials makes them ideal for designing bone biomimetic scaffolds but further long term in vivo and clinical studies are still required to assess safety and efficacy.

The most basic requirement for a scaffold is to promote cell adhesion, survival and differentiation. In the case of bone, the ability to support vascularization is also critical. Additionally, bioabsorbable scaffolds are more desirable in children whose skeleton continues to grow, as multiple surgeries are required to remove and/or replace permanent implants. Bone tissue engineering is further complicated by the fact that vascularisation is essential for bone survival and maturation. Given that there has not been a single biomaterial to date, which has fulfilled all these requirements, it is likely that a combination of available scaffolds may provide the optimal biomaterial for bone bioengineering.

Despite the many promising achievements in the field of bone 3D bioengineering, this area of research is still in its infancy. There remain a number of critical barriers to engineering clinically appropriate tissues due to the complex structure, metabolic requirements and multi-functional nature of bone. Firstly, none of the studies have so far managed to recreate the multi-cellular composition of bone, which is necessary for the function, growth, and regeneration of native bone tissues. Another major limitation of the studies is that many still use non-human MSC. Most importantly, most studies are still limited to in vitro culture systems and thus the role of vascularisation in

osteogenesis is not fully evaluated nor recreated. To accurately assess the value of these constructs as autologous bone tissues, long-term large animal studies are also necessary to evaluate the efficacy and safety of these bones in reconstructing critical sized defects.

1.6 Aims

The aim of this thesis is to explore whether a combined approach using computational biology and bone tissue engineering could increases the accuracy of midface reconstruction in children. Morphometric analysis will be used to model postnatal midface development in order to improve surgical planning. In parallel, I native bone will also be studied in order to mimic the bone microenvironment and support hADSC osteogenic differentiation on a bioabsorbable scaffold to generate autologous bone implants.

1.7 Hypothesis

Based on the aims and review of the literature, a number of hypotheses were examined in this thesis:

1. Morphometric analysis can be used to relate growth of the skeletal and soft tissues of the midface in order to better understand normal postnatal development

2. The models generated from MA can be used to accurately describe the dysmorphology in TCS and CM patients

3. MA can be used to evaluate current surgical techniques

4. Analysis of calvarial paediatric bones can be used to establish a standard with which bioengineered tissues can be compared

5. Increased knowledge of bone biology and structure can be used to replicate the bone microenvironment by designing biomimetic scaffolds and culture conditions to optimise osteoinduction and osteogenic maturation of hADSC

6. Human adipose derived stem cells from paediatric patients with craniofacial malformations can be induced to undergo mature osteogenic differentiation when compared with hBMSC and hOP using clinically acceptable protocols and are thus a suitable source of MSC for bone tissue engineering

7. Fibrin and POSS-PCL, alone or in combination, can provide a biomimetic scaffold to support hADSC survival and accelerate osteogenic differentiation

8. Vascularisation promotes hADSC osteogenesis and accelerates bone maturation

9. Tissue engineered bone from hADSC cultured on a biomimetic scaffold are biocompatible and capable of vascularization and survival in long term in vivo culture

10. Combining MA and bone bioengineering has the potential to generate personalised facial bone implants for paediatric midface deformities

Chapter 2 Materials And Methods

This chapter describes the materials and methods used in the experiments conducted for this thesis.

2.1 Morphometric analysis

This study used retrospectively anonymised retrospectively acquired computed tomography (CT) scans of the face of control, CM and TCS children from Great Ormond Street Hospital NHS trust (London, United Kingdom).

2.1.1 Ethics

Confirmation was obtained through the National Research Ethics Service that the study did not require Research Ethics Committee approval as it fulfilled their criteria of “projects using non identifiable data that was routinely collected not for research”.

2.1.2 Patient selection and acquisition of CT scans

Suitable patients were identified through clinical codes with the help of the radiology and clinical coding departments. Children with TCS and CM were identified through international diagnostic clinical codes for the diseases and clinic letters cross-checked to ensure that diagnosis was accurate. Controls were patients coded as not having craniofacial defects and had undergone CT scanning of the head for other reasons (e.g. vascular malformation, oncology or otorhinolaryngology). Reports of scans and request forms were crosschecked to ensure that there was not an underlying facial dysmorphology.

Scans were viewed and assessed for suitability (ie correct region and type of scan) then converted and stored as Digital Imaging and Communications in Medicine (DICOM) format using Osirix© v5.5 (Pixmeo SARL, Geneva, Switzerland) open source software (Rosset et al., 2004).

2.1.3 Extraction and preparation of surfaces for model building

2.1.3.1 3-Dimensional reconstruction of CT scans

Using Invesalius© v3.0 (CTI Renato Archer Information Technology Centre, Brazil) open source software (Valeri et al., 2015), each DICOM file was reconstructed as a 3D image of the soft tissue and skeletal tissue using

constant in-built thresholds for volume rendering of bone or soft tissue. Those unsuitable for analysis (e.g. incomplete imaging of the face or its concealment by intubation tubes/dummies/tumour) were excluded from the study. Remaining 3D reconstructions were saved in Stereolithography (STL) format (Figure 2.1).

2.1.3.2 Image preparation

3D files were prepared as a single layer external surface using open source, MeshLab© v.1.3.2 (Visual Computing Lab of ISTI-CNR, Pisa, Italy) (Cignoni et al., 2008) and commercial software, VAM© v1.0 pre18. The selection of mesh and deletion tools were used in Meshlab© to remove subcutaneous tissues on soft tissue surfaces and intracranial structures on the skeletal reconstructions. The paint selection tool was used on VAM© to produce a single layer of each surface (Figure 2.1). The prepared single layer surfaces were saved in STL format in preparation for classification and landmarking.

2.1.4 Classification of deformity in TCS and CM

Standardised scoring of the deformities in TCS and CM was performed using a protocol based on a pictorial Orbit, Mandible, Ear, Nerve, and Soft tissue-Plus (OMENS+) classification which was previously validated on 2D photographs compared with in-person examination (Birgfeld et al., 2016, Birgfeld et al., 2011). This modified OMENS+ was used on the 3D reconstructions of soft tissue and skeletal surfaces of the whole face in TCS and CM patients using a scoring sheet (Birgfeld et al., 2016) (Figure 2.2).

2.1.4.1 Orientation of 3D surfaces

Positioning of the surfaces for landmarking was performed along reference planes. The Frankfurt horizontal plane (FHP) was defined as passing between right to left inferior orbital rims and the superior point of the external auditory meatus for skeletal surfaces. The mid-sagittal plane was used to orientate surfaces vertically and was defined as passing perpendicular to the FHP along the midpoint of the nasion, rhinion and interdentale superius. For soft tissue surfaces, orientation was performed at the same time as the skeletal surfaces (ie with the soft tissue superimposed on to the skeletal as both surfaces were registered in the same space when extracted from the CT scan).

A) 3D reconstruction

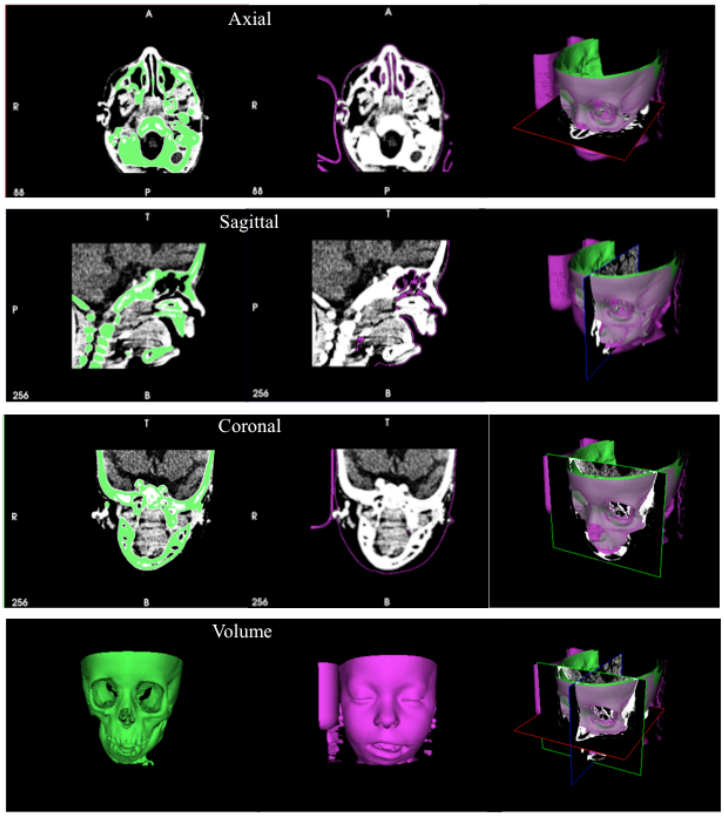

Invesalius

B) Preparation of single surface

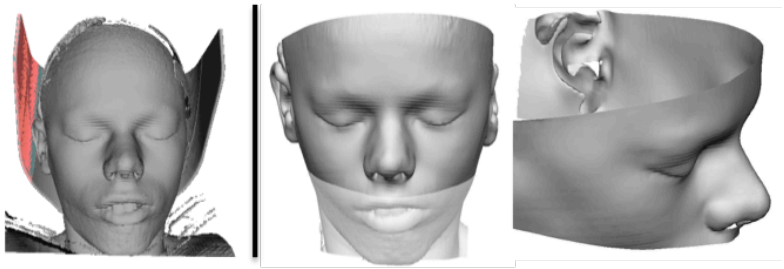

Meshlab **Vam**

Figure 2.1: Preparation of CT scan images for landmarking and model building.

A) CT scans of the craniofacial region were volume rendered using *Invesalius* to extract skeletal and soft tissue surfaces using defined thresholds. Axial, coronal and sagittal sections through the face illustrate the alignment between the skeletal and corresponding soft tissue surfaces. **B)** *Meshlab* was used to remove excess tissue and paraphenalia (e.g. headrests) to isolate the facial region for each individual. The images were further trimmed using *Vam* to contain only the region of interest and a single external surface required.

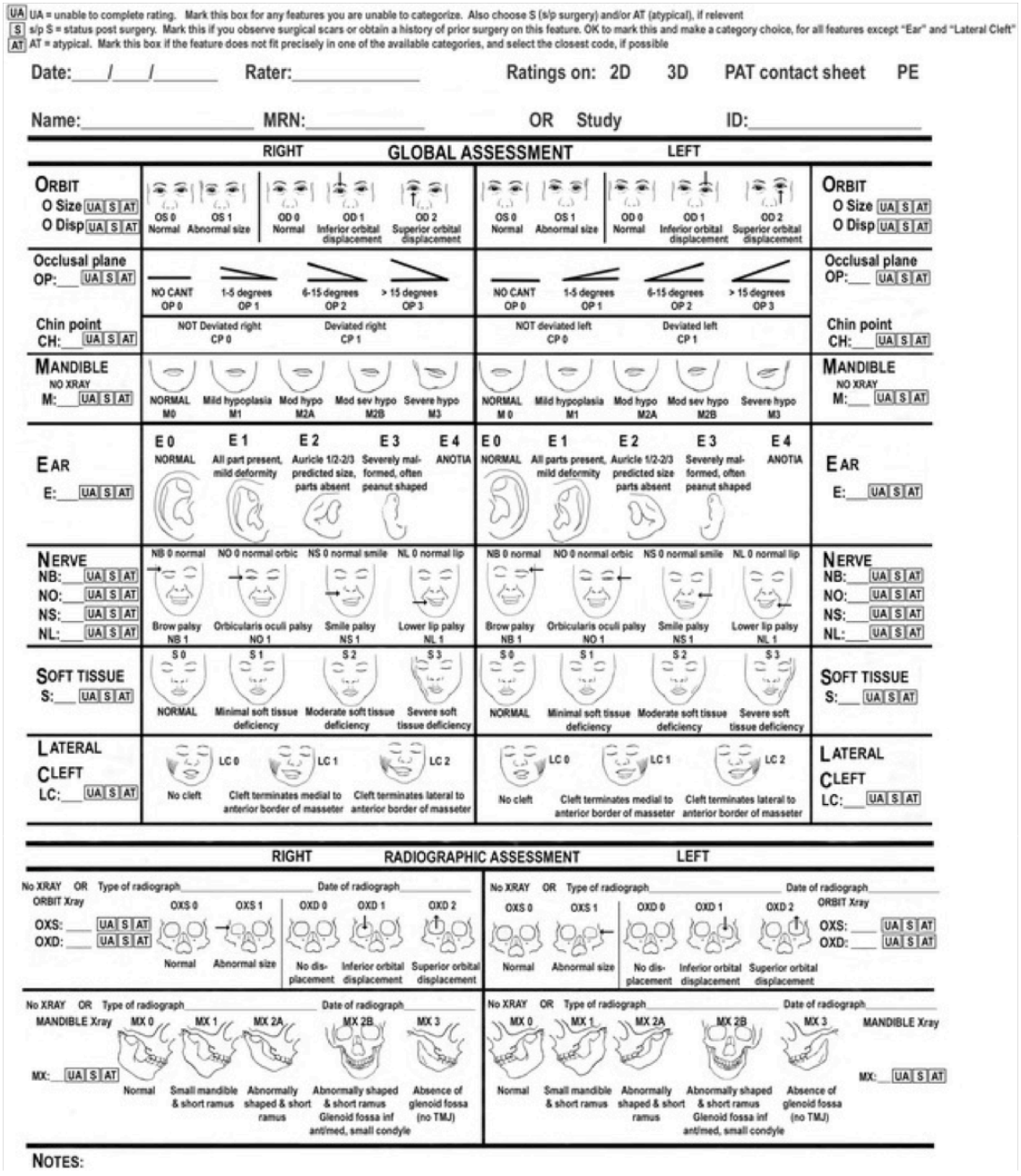

Figure 2.2: Classification protocol for phenotypic severity in TCS and CM.

Adapted from the modified OMENS pictorial classification (Birgfeld et al., 2016).

2.1.5 Landmarking

Anatomically constant landmarks of the skeletal and soft tissue were identified through review of anatomical textbooks (Gray et al., 2005) and from the literature (Hopman et al., 2014, Nikkhah et al., 2013) to ensure chosen landmark reliability and reproducibility.

The majority of soft tissue landmarks used were similar to those described previously (Suttie et al., 2013). In order to ensure that the upper portion of the midface was accurately modelled, a new pair of soft tissue landmarks, right and left temporale, were generated by superimposing soft and skeletal tissue surfaces then selecting the soft tissue point directly overlying the temporal fossa using VAM© then exporting the landmarks. This was to ensure that a detailed model incorporating the whole of the midface was achieved.

Discrete skeletal landmarks for the zygoma and adjacent maxilla as well as lower portion of the frontal bones were identified using direct and indirect landmarks (Farkas et al., 2004, Farkas et al., 2002, Farkas et al., 1999). Identified landmarks were chosen for their reproducibility and easy identification.

Skeletal and soft tissue landmarks were then used to annotate each of the respective surfaces using software and protocols developed in-house (Facemark©) (Suttie et al., 2013).

To ensure further accuracy of landmark positioning, soft tissue landmarks dependent on maximal/minimal depth were plotted by using the “curve” or “groove” features on Facemark©, which generates a topographic heat map of each surface representing concavity and convexity (Figure 2.3**).**

2.1.6 Reliability

Intra-rater reliability was assessed by landmarking a sample of faces (n=5 individuals per category) from the control, TCS and CM group. The skeletal and soft tissue surface for each face was landmarked on 3 different occasions and the x, y and z co-ordinates exported to Microsoft Excel (Microsoft Corp., Redmond, WA, USA).

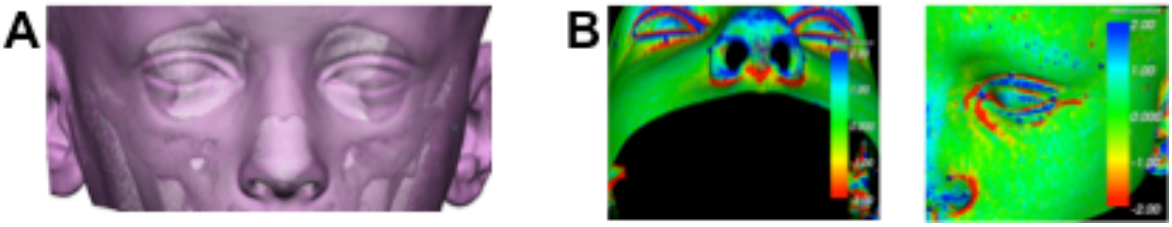

Figure 2.3: Increasing accuracy of landmark positioning using contour and convexity surface representation.

A) Use of skeletal landmarks to determine soft tissue landmarks by superimposing the surfaces. **B)** Contour used to position landmarks defined by curvature.

Landmarking reliability was assessed by using the mean co-ordinates for each landmark for each individual surface as a centroid from which the distribution of landmarks was measured (Schlicher et al., 2012). For each landmark, the Euclidean distance (d) between the triplicate measurements for each individual surface was calculated using the x, y and z co-ordinates (Pittayapat et al., 2015):

$$d = \sqrt{((x_1-x_2-x_3)^2 + (y_1-y_2-y_3)^2 + (z_1-z_2-z_3)^2)}$$

The mean of the measurements of the distance of each landmark from the centroid as well as the standard deviation of these distances were calculated to assess precision. Reliability was analysed by calculating the proportion of precision values <1 mm.

2.1.7 Model building and morphometric analysis

2.1.7.1 Dense-Surface Model building

DSMbuilder© and DSMexplorer© were developed in house. Using the Procrustes algorithm to compute mean landmarks and thin-plate splines, face/skull surfaces were warped to the mean landmarks, which enabled the set of face/skull surfaces to be closely aligned. This allowed points on a selected face/skull to be mapped to closest points on all others to induce a dense surface correspondence of tens of thousands of points enabling computation of the mean midface surface (skeletal or soft).

Position differences between the densely corresponded points on each midface surface and those on the mean midface were subjected to Principal Component Analysis (PCA). Principal Components (PCs) accounting for 99% of face variation were used to build a 3D Dense Surface Model (DSM) for synthesis of midface structures (Hopman et al., 2014) for skeletal and soft tissues.

2.1.7.2 Cephalometric measurements

Indirect (cephalometric) measurements of midface width, depth and length were performed by extracting the Euclidean distance between landmarks identified as representative of these dimensions (Kolar et al., 1985, Budai et al., 2003, Farkas et al., 2002, Farkas et al., 1992) using Facemark© (Figure 2.4**).**

2.1.7.3 Asymmetry modeling

Facial asymmetry analysis was performed by comparing the original surface and its mirrored or reflected form (Hammond et al., 2008). Hence, a reflected form of each surface was generated with relabeling of the left-right landmarks followed by resampling of the surface in Facemark©. This process interpolates a dense set of landmarks on both sides of face surface to enable building a DSM of original and reflected midface surfaces. The Euclidean distance between the DSM representations of the original and reflected faces was then used as an index to measure midface asymmetry (asymmetry index). Calculation of the asymmetry index was performed using the sum of the sum of squares for all PCA values of the original and reflected model for each participant's midface.

2.1.7.4 Virtual simulation of zygomatic reconstruction

The average midface of control and TCS patients was generated by calculating the mean PC values from the skeletal DSM for each group in excel. These average midfaces were then extracted from DSMexplorer© as STL files and superimposed then trimmed as required using VAM.

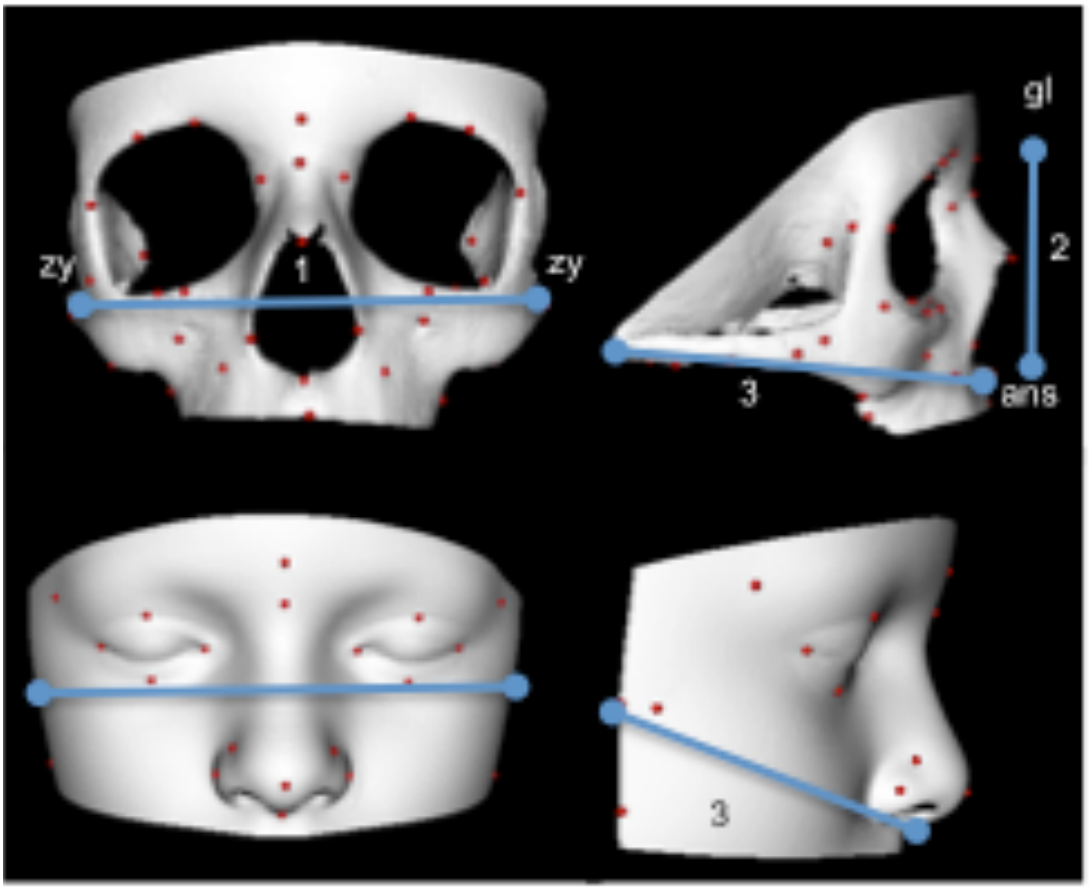

Figure 2.4: Landmarking for cephalometric measurements.

1: width (skeletal and soft tissue: zy-zy). **2:** length (skeletal: gl-ans; soft tissue: gl-sn). **3:** depth (skeletal: ans-m; soft tissue: sn-p).

Ans: anterior nasal spine, gl: glabella, m: mastoidale, na: nasion, p: preaurale, sn: subnasale, zy: zygion.

2.2 Bone Tissue Engineering

All chemicals and reagents were purchased from Sigma-Aldrich (Haverhill, UK) unless otherwise stated. Cells were grown in humidified incubators at 37°C with 5% CO_2.

2.2.1 Ethics

2.2.1.1 Human tissues

All tissues were collected from consented paediatric patients undergoing elective surgical procedures (at Great Ormond Street Hospital for Children) using Professor Ferretti's license under ethical approval from the Camden and Islington Community Local Research Ethics Committee (London, UK).

2.2.1.2 Animal studies

Chick work was performed at the UCL Great Ormond Street Institute of child health under professor Ferretti's project license (PPL70-7339). All mouse work was carried out at the Royal Free hospital under Professor Butler's project license (PPL70/7504) and my personal license (I893881EE).

2.2.2 Human tissue harvest, stem cell isolation, cell culture and differentiation

2.2.2.1 Tissue harvest and processing

Bone tissue harvest and processing

Bone samples were collected from children with non-syndromic sagittal craniosynostosis undergoing sagittal spring insertion whereby a small craniectomy is performed and usually discarded. Samples were retrieved immediately after harvesting from the operating theatre in sterile 50ml falcon tubes containing around 15ml of Liebovitz 15 medium and transferred to the laboratory on ice. Samples were either processed, immediately or occasionally stored in the cold room (4 degrees Celsius) overnight prior to processing, in a sterile container.

Bone samples were handled with sterile forceps and washed in phosphate buffered saline (PBS; PAA Laboratories Ocoid, Basingstoke, UK) until blood

was no longer visible on the surface. Using sterile bone cutters, bone sample were cut into five pieces whose bone marrow cavities were then flushed with sterile PBS until white. The wash from the bone marrow cavities was then set-aside in 50ml sterile Falcon tubes for harvesting of hBMSC. Approximately 1/5 of the bone was reserved for explant culture and 4 pieces set a side for mechanical testing, histology and RNA/protein extraction (Figure 2.5).

Adipose tissue harvest and processing

Surplus lipoaspirates (harvested from the abdominal subcutaneous tissue) were taken from consented patients undergoing lipofilling procedures for reconstruction of craniofacial defects. Samples were transferred in the sterile syringes that they were aspirated into on ice and either processed immediately or left overnight in the cold room in a sterile container. Adipose tissue was processed under sterile conditions in the tissue culture hood. The tissue was decanted into a 50ml falcon tube and washed with PBS several times until visible blood contamination was eliminated then either processed for generation of human adipose derived stem cells (hADSC) or human adipose explant dedifferentiated stem cells (hAEDSC) using previously published protocols (Guasti et al., 2012).

2.2.2.2 Stem cell isolation

The cell lines used for this thesis (Table 2.1) were isolated as detailed below.

Isolation of hBMSC

All the PBS wash from flushing out the bone marrow cavities of bones was collected and placed in a 50ml Falcon tube then centrifuged at 1000rpm for 5 minutes. The supernatant was discarded and the remaining pellet resuspended in expansion medium (high glucose Dulbecco's modified Eagle's medium (DMEM) containing GlutaMAX and supplemented with 10% embryonic stem cell-qualified foetal bovine serum (ES-FBS) and 1% penicillin/streptomycin (all Life Technologies, Warrington, UK) then plated onto a T25 flask and incubated at 37°C in an incubator. Half the media was replaced with fresh medium every 2-3 days.

Isolation of hOP

The bone piece reserved for explant culture was then further split with the bone cutters into smaller pieces (roughly 1x1mm in size) and 2-3 pieces plated onto each well of a 24 or 48 well plate then topped up with expansion media (enough to cover the bone without allowing it to float). Plates were then placed in the incubator with media topped up daily if needed.

Isolation of hAEDSC

Washed fat tissue was then handled with sharp forceps and small pieces (between 1-2mm in size) were plated in groups of 3 in each well of a 24 or 48 well plate. Small volume of expansion medium was pipetted onto each explant to avoid drying but without permitting floating. Plates were placed in an incubator and media was initially topped up every 2-4 hours on the day of explanation then on a daily basis after.

Isolation of hADSC

Washed fat was incubated with equal volume of 0.05% trypsin/1mM ethylenediaminetetra-acetic acid (EDTA) (Life Technologies, Warrington, UK) then placed in a 37 degrees Celsius shaker for one hour. A 1:1 volume of expansion media was added to the tube, which was then centrifuged at 1000rpm for 5 minutes to obtain the stromal vascular fraction. Once the floating adipose tissues, mature adipocytes and media were discarded, the remaining cell pellet was re-suspended in expansion media then re-plated onto a T25 flask. The flask was incubated and half the media was replaced every 2-3 days.

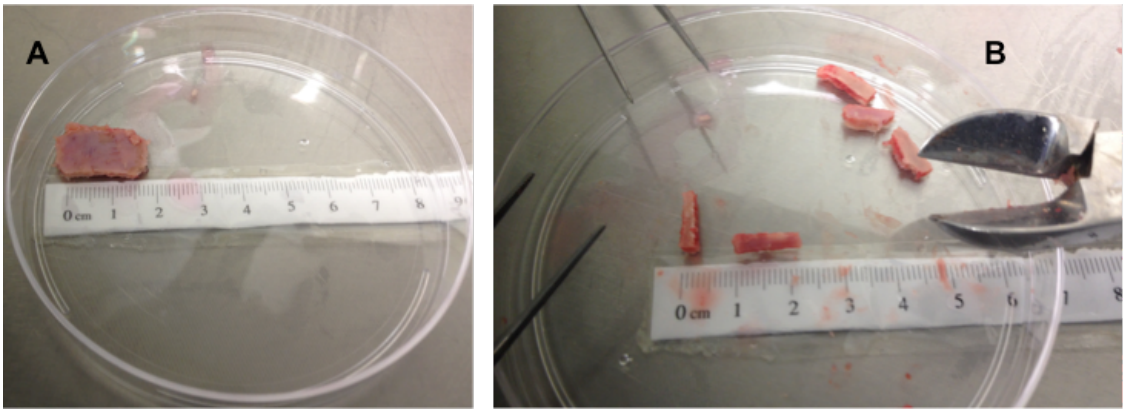

Figure 2.5: Processing of paediatric calvarial bone samples on day of harvest.

A) Freshly collected unprocessed bone sample. **B)** Pieces of bone cut for further analysis or cell extraction.

2.2.2.3 Cell culture

Expansion

All cells were inspected under the light microscope on a daily basis and when required, half the medium aspirated then replaced with fresh expansion medium. Cells were passaged at 75-80% confluence using Trypsin EDTA (TE). This involved removal of medium, x2 washes with PBS and addition of 1ml TE per T25 flask (or 5ml for T75) then incubation till cells detached. Expansion medium was added (x3 the volume of TE) to the flask before transferring all contents into a falcon tube. Cells were spun for 5 minutes at 1000rpm after which the supernatant was discarded. The remaining pellet was re-suspended in 1ml of expansion medium through vigorous pipetting. After counting, cells were split at a ratio of 1:3.

Cell counting

After dissociation, inactivation of TE with medium and centrifugation, cell pellets were re-suspended in 1ml of medium. 20ul of this cell suspension was removed and mixed with Trypan blue (1:10 concentration). 10uL were either loaded onto each chamber of a haemocytometer then counted under a light microscope or onto each end of a counting slide if using the automated Bio-Rad NC20 automated cell counter (Bio-Rad laboratories, Watford, UK).

Freezing and thawing

Long-term storage of cell lines was performed by passaging cells from a T75 or T175 tissue culture flask with TE. Expansion medium in a 1:1 proportion was added to the flask and contents transferred to a falcon tube then centrifuged at 1000rpm for 5 minutes. After counting then centrifuging again at 1000rpm for 5 minutes, cell pellet was re-suspended in 1ml of freezing medium (containing ES-FBS and 10% DMSO) and placed in a cryovial (Life Technologies, Warrington, UK) then transferred to the liquid nitrogen storage container on dry ice.

To use previously cryopreserved cells, cryovials were retrieved from the liquid nitrogen storage container and transferred to the tissue culture hood on dry ice.

1ml of warmed medium was slowly pipetted onto the cryovial contents until thawed. Contents were then transferred to an appropriate flask and topped up with expansion medium then placed in the incubator.

2.2.2.4 Trilineage differentiation

Cells were plated at a constant density of 1000 cells/well in a 24 well plate and left in expansion medium for 48 hours. Medium was then removed and either replaced with fresh expansion medium (control), adipogenic medium (expansion medium containing 1ng/ml insulin, 500μM 3-isobutyl-1-methylxanthine, 1μM dexamethasone and 1μM rosiglitazone), chondrogenic medium (expansion medium with 0.1μM dexamethasone, 10 ng/ml transforming growth factor β1, insulin transferrin selenium and 50μg/ml ascorbate-2-phosphate) or osteogenic differentiation medium (expansion medium, 0.1uM dexamethasone, 100mM β-glycerophosphate and 100μg/ml ascorbate-2-phosphate). Medium was replaced by removing and replacing 50% of the volume of liquid in each well every 2-3 days. Cells were inspected under the microscope on a daily basis and left to differentiate for 3 weeks in total.

Table 2.1: Details of cell lines used in the experiments of this thesis.

Cell line	Cell type	Age	Gender	Patient diagnosis
H11	hADSC	16 years	M	Hemifacial microsomia
H12	hADSC	16 years	M	Gynecomastia
H13	hADSC	17 years	F	Goldenhar syndrome
H20	hADSC	12 years	F	Linear Morphea/Parry Romberg syndrome
H24	hADSC	9 years	F	Hemifacial microsomia
H33	hADSC	15 years	F	Lipoma
H41	hAEDSC	9 years	F	Goldenhar syndrome
H44	hOP/hBMSC	5 months	M	NSSC
H45	hOP/hBMSC	8 months	M	NSSC
H46	hAEDSC	16 years	F	Cavernous haemangioma
H47	hAEDSC	9 years	M	Parry Romberg syndrome
H49	hOP/hBMSC	6 months	M	NSSC
H52	hOP	6 months	M	NSSC
H55	hOP/hBMSC	5 months	M	NSSC
H64	hOP	6 months	F	NSSC
H67	hOP	8 months	F	NSSC
H69	hAEDSC	15 years	M	Goldenhar syndrome
H70	hOP/hBMSC	3 months	M	NSSC
H71	hOP/hBMSC	7 months	M	NSSC
H72	hOP/hBMSC	7 months	F	NSSC
H75	hOP	3 months	M	NSSC
H87	hAEDSC	16 years	M	Parry Romberg
H88	hAEDSC	7 years	F	Parry Romberg

Demographic details of tissue donors. hAEDSC; human adipose explant dedifferentiated stem cells, hADSC; human adipose derived stem cells, hOP; human osteoblast precursors, hBMSC; human bone marrow derived stem cells; M, male; F; female; NSSC; Non syndromic sagittal craniosynostosis.

2.2.3 Biomaterial fabrication, modification, sterilisation

2.2.3.1 Fibrin scaffold fabrication

Fibrin scaffolds were made by combining fibrinogen 10mg/ml with bovine thrombin solution (100iU/ml). Scaffolds were left to polymerise for 30 minutes to allow gelation in a sterile tissue culture hood at room temperature.

2.2.3.2 POSS-PCL fabrication

Aliphatic POSS-PCL discs (both flat and porous forms) were prepared using previously described protocols (Raghunath et al., 2009). The aliphatic polymer solution was manufactured by adding the dry polycaprolactone polydiol (2000 mwt) and POSS nanocages in a reaction flask equipped with a mechanical stirrer and nitrogen gas inlet. This mixture was heated to 135°C to then cooled at 90°C to dissolve the POSS nanocages into the mixture. 4, 4′ methylenebis(cyclohexyl isocyanate) was added to the polyol blend and then reacted, under nitrogen, at 90°C for 120 minutes with bismuth neodecanoate catalyst to form a pre-polymer. Dry DMAc was then added slowly to form a solution which was then cooled to 40°C. A mixture of ethylenediamine and diethylamine in dry DMAc were added drop-wise to the polymer to perform chain extension. Following this, 1-butanol in DMAc was added to the polymer solution to form a POSS-PCL solution.

Cast (monolayer) POSS-PCL:

18% (w/w) solutions of the POSS-PCL polymer in DMAc were cast onto glass or steel moulds then left in an oven at 60°C overnight to evaporate the solvent. Sheets were stored dry in a 50mL falcon tube till needed.

Coagulated (porous) POSS-PCL:

Sodium bicarbonate particles (80% wet weight) were sieved to achieve the desired particle size then dispersed and degassed into an (18% w/w) solution of the POSS-PCL polymer in DMAc containing 2% Tween 80 surfactant using a Thinky AER 250 mixer (Intertonics, Kidlington, UK). The slurry produced was then spread onto a stainless steel/glass mould to achieve a sheet of desired thickness, which was then placed in deionised water for 72 hours with daily

changes of dH2O at room temperature to produce a porous scaffold. Sheets were then stored in sterile deionised water until needed.

Cutting POSS-PCL

Both cast and coagulated sheets of POSS-PCL were cut down to size either using sharp dissections scissors, a 5mm or 2mm biopsy punch or using a metal die to generate 1.5cm discs.

2.2.3.3 Surface modification of POSS-PCL

As described earlier, coagulated aliphatic POSS-PCL scaffolds were prepared using previously described protocols (Raghunath et al., 2009). Porosity was achieved using porogen leaching with sodium bicarbonate particles (80% wet weight) of 105µm size. Surface modification ("sprinkling") was then achieved by sieving 105µm porogens on the seeding surface during the coagulation process.

2.2.3.4 Sterilization of fibrin scaffolds

The reagents required to generate these scaffolds were individually filtered with a syringe filter prior to combining to produce the scaffolds.

2.2.3.5 Sterilisation of POSS-PCL

Cast and coagulated scaffolds were sterilised using either Ultra Violet light ("UV"), 70% ethanol (ETOH), autoclaving ("autoclave") or 10% Decon ("Decon"; Decon laboratories Limited, East Sussex, UK) as detailed below.

Autoclaving

Scaffolds were placed in autoclavable bottles in deionised water (dH_2O) and exposed to saturated steam at 121°C for 15 min at pressures of 115 kPa the allowed to cool for 24 hours before use at room temperature.

Ethanol

Samples were washed in 70% Ethanol for 12 hours then rinsed in serial washes of sterile dH_2O at room temperature.

Ultraviolet (UV)

A UV trans-illuminator was used to sterilize samples by placing them in sealed sterile glass petri dishes for 12 hours.

Decon

Scaffolds were placed in sterile falcon tubes in 10% Decon solution and left for 24 hours then washed repeatedly in sterile dH_2O before use.

2.2.4 3D cell culture on biomaterials

2.2.4.1 3D culture on Fibrin

100uL of fibrinogen 10mg/ml was pipetted onto each well of a 96 well plate to achieve a 100ul thick gel. Freshly passaged cells were suspended in sterile bovine Thrombin solution (100iU/ml) after counting to obtain a final concentration of 10iU thrombin/ml fibrinogen used in a sterile tissue culture hood. Thrombin and cell suspension was divided amongst fibrinogen gels and gently pipetted before gels polymerised taking care to avoid air bubble formation. Cellularised scaffolds were allowed to polymerise for 30 minutes in an incubator before adding expansion medium.

2.2.4.2 3D culture on POSS-PCL

Cast POSS-PCL

Sterile discs were placed into a 24 well plate to achieve a close fit. Discs were kept in expansion medium in an incubator overnight. The following day, the media was removed and cells seeded at desired concentration onto the discs in two steps. For a 1.5 cm sized disc, 50µL of media with half the number of cells needed was placed onto the discs and left for 15 minutes in an incubator. Following this, the remaining cells were plated onto the disc in the same way then left in the incubator for 30 minutes. Discs were then topped up with a further 200µl of expansion medium then incubated. The following day, discs were transferred to a fresh 24 well plate using sterile forceps and topped up with fresh medium.

Coagulated POSS-PCL

After calculating how many cells are required per scaffold, these were suspended in medium equal to half volume of scaffold (multiplied by number of scaffolds). Half the volume of cells required per scaffold were then seeded onto one side of scaffold and left for 30 minutes in the incubator. Then the remaining half volume of cell suspension were seeded onto the other side of the scaffold and left for 30 minutes in the incubator before further expansion medium was added to submerge the scaffolds. The following day, scaffolds were transferred onto a new plate and medium changed every 2-3/7.

Hybrid hydrogel/nanocomposite scaffolds (POSS-PCL-Fibrin)

Fibrin was used as a cell carrier in this combination. Firstly, an approximation of how much Fibrin was needed to make up half the volume of scaffold was made:

Volume of Fibrin (ul) = 0.5 x width of scaffold (mm) x length (mm) x thickness (mm)

From this, calculations of how much thrombin and fibrinogen were made. For instance if volume of scaffold is 100mm^3, or 100ul, then 50ul of Fibrin which is 0.5iU Thrombin and 0.5mg Fibrinogen are needed. Cellularised scaffolds were then left to polymerise for 30 minutes in incubator before adding medium.

2.2.5 Animal studies

2.2.5.1 Chick

Chorioallantoic membrane (CAM) grafting was used to assess early vascularization and biocompatibility of unseeded and cellularised scaffolds. The following protocol was observed for cam grafting:

Day 0

Fertilized brown leghorn eggs (Needle Farm, UK) were incubated on their sides at 38°C in a humidified chamber for 72 hours.

72 hours

Eggshells were sprayed with 70% ethanol and a small piece of adhesive tape was placed on the end of the egg containing the air sac. A small nick was made using the tip of sterile tissue dissection scissors and a large gauge needle and 10ml syringe, were used to withdraw 5ml of albumin. The hole was covered with adhesive tape and egg returned to the incubator.

Day 7

A window was made into the egg by placing adhesive tape over the area required and cutting the shell using tissue-dissecting scissors. If the egg was viable, a small needle was used to cause a minor vascular injury at the site of a bifurcating blood vessel away from the embryo on the CAM.

The specimen intended for grafting was then placed at the site of vascular injury and nestled gently onto the cam. Eggs were labelled with marker pen and windows cover with adhesive tape before replacing eggs in the incubator. Eggs were checked on a daily basis and topped up with deionized water as required.

Day 14 (seven days after grafting)

After imaging the graft in ovo, CAM grafted samples were extracted (with a cuff of cam surrounding the graft) using scissors and forceps with 1% chirocaine anaesthesia. Grafts were washed with sterile PBS then imaged on anterior and posterior surfaces before fixation. Chick embryos were sacrificed using decapitation.

2.2.5.2 Mouse

Female nude mice (athymic strain CD1/Fcxn-1) were purchased at 7-8 weeks old and housed in individually ventilated cages (IVC). On the day of surgery mice were checked to ensure healthy and induced using isoflurane (3%) and full flow oxygen inhalation. Anaesthesia was then maintained using 2.5% Isoflurane and full flow oxygen. After cleaning the area with chlorhexidine, a 1cm incision using loupes magnification was made on each flank. Subcutaneous pockets were made using dissecting scissors and implants were

inserted (3 on each side). Skin was closed using 6/0 monocryl subcuticular sutures and left undressed. All mice were monitored for 60 minutes post operatively then returned to their IVC. Animals were checked regularly to ensure wound healing and general welfare.

2.2.6 Biomolecular analysis of cells and tissues

2.2.6.1 Viability and proliferation (Alamar blue assay)

Cells were plated at 2000 cells/well in 24 well plates and cultured for 4 hours. Culture medium was then removed. Fresh medium containing 20% Resazurin solution (Resazurin sodium salt was dissolved in sterile PBS at a concentration of 1 in 10 for a stock solution) was added to each well. Plates were then incubated for 4 hours. Half the media from each cell was removed and placed in a 96 well plate which was covered with foil then transferred to the plate reader and read at 569 and 595nm. The other half of the media from each well was topped up with fresh medium. This was repeated at 24, 48, 72 and 7 days.

2.2.6.2 Gene expression analysis

RNA Extraction

Samples were harvested by removing medium then processed for RNA isolation using TRizol (Life Technologies)) as per the instructions given by the manufacturer. For adherent monolayer cells (or cells on cast POSS-PCL discs), TRIzol was added at 100uL, 250ul or 500uL per well dependent on whether a 96, 48 or 24 well plate was used. Cells were lysed by pipetting up and down then either stored at -80°C or incubated at room temperature for 5 minutes.

If 3D cultures on scaffolds are used, then 500ul of TRIzol was added per scaffold in a 1.5ml eppendorf tube which was then vortexed briefly then either stored at -80°C or left to incubate for 20 minutes at room temperature. When bone or fat tissues were used, samples were initially wrapped in aluminium foil then snap frozen in liquid nitrogen. Samples were then broken up using a sterile pestle and mortar (on dry ice) then transferred to a 1.5ml eppendorf tube. 500ul of TRIzol were then added, the tube vortexed then either stored at -80°C or left at room temperature for 20 minutes.

After the incubation period, 0.2 mL of chloroform per 1 mL of TRIzol used was added the eppendorf tube that was then shaken vigorously for 15 seconds. Tubes were incubated at room temperature for 3 minutes then centrifuged at 12000 × g for 15 minutes at 4°C. the aqueous phase (colourless top layer) was removed and placed into a sterile eppendorf tube and 0.5 mL of 100% isopropanol per 1 mL of TRIzol used was added to the aqueous phase. After incubation for 10 minutes at room temperature, samples were centrifuged at 12,000 × g for 10 minutes at 4°C.

After centrifugation, the supernatant was discarded and the RNA pellet washed with 1ml of 75% ethanol per ml of TRIzol. After vortexing, the sample was centrifuged at 7500 × g for 5 minutes at 4°C then the wash was discarded. Pellets were then air dried for 10-15 minutes then re-suspended in 20ul of Diethyl pyrocarbonate (DEPC)-treated water by pipetting the solution several times. Samples were then incubated in a heat block set at 60°C for 15 minutes. Samples were either processed or stored at –80°C.

cDNA synthesis

Prior to cDNA synthesis, RNA was quantified using NanoDrop1000 Spectrophotometer (Life Technologies). The device sensor and cover were cleaned with fine tissue paper between each use. At the beginning of a set of measurements, the machine was equilibrated using DEPC-treated water as a blank. 1ul of RNA sample was placed onto specimen pedestal of the NanoDrop 1000 Spectrophotometer. Using the accompanying software (ND1000 v3.5.2,), RNA concentrations and sample purity ratios (260/280 and 260/230) were calculated.

Where possible, cDNA was made using 1ug of RNA as determined by nanodrop. The volume of RNA required to make up 12.5uL (top up with DEPC-treated water if necessary) was added to a sterile Eppendorf tube then mixed with 1ul of random hexamers and left at 80°C for 10 minutes then transferred to ice. RNA was then retro transcribed with Moloney murine leukaemia virus reverse transcriptase (M-MLV; Promega, Madison, USA). A total of 1µl M-MLV reverse transcriptase, 4µl M-MLV 5x buffer, 0.5µl M-MLV reverse transcriptase

inhibitor and 1µl deoxynucleotide triphosphates (dNTPs) were added to each 13.5µl volume of the above RNA containing mixture. This 20µl samples were then placed in a thermal cycler at 37°C for 60 minutes. The resultant cDNA was then diluted with 20ul of DEPC-treated water per sample and either used immediately or stored at -20°C.

Polymerase Chain Reaction (PCR)

Real time PCR (RTPCR) was performed to either detect presence of a gene (traditional gel-based end-point PCR) or to quantify its relative expression through quantitative PCR (qPCR) using a set of primers designed to target genes of interest (Table 2.2).

Primers used where a combination of those previously published (Guasti et al., 2012) and newly designed. All primers were checked using the Blast sequence tool (www. blast.ncbi.nlm.nih.gov) (Maden, 2013 Mar 15), if pre-existing, or designed using Blast and Genecards (http://www.genecards.org). To design a new primer, the FASTA sequence for the required gene was obtained from Genecards and uploaded onto the primer Blast tool. Various parameters were adjusted to ensure quality of primers including setting length at 18-22bp, melting temperature around 52-60°C, G-C content 40-60% and low self-complimentary. Upon receipt primers were spun for a few seconds in the centrifuge then reconstituted with PCR water to achieve a stock concentration of 100µM. Aliquots of these primers were further diluted in PCR water to a working concentration of 10µM and all stored at -20°C. When used in PCR, primers were diluted in reaction volume to achieve a final concentration of 0.5µM.

For gel-based/end-point PCR, GoTaq DNA polymerase kit (Promega, California, USA) was used as per the manufacturer's instructions. Once all cDNA samples were prepared for, the PCR tubes were centrifuged briefly to ensure all contents settled to the bottom of the tube and placed in the thermal cycle with the settings in

Figure 2.6.

Following PCR, 1% agarose gels were made by combining 1g of agarose and 100ml of x1 Tris base acetic acid EDTA (TAE) buffer then heating in the microwave till the agarose dissolved and clear liquid was visible. After cooling, SYBR safe dye (Life technologies) was added to achieve 1X concentration then gel was poured onto an electrophoresis plate with the desired sized comb attached. Once set, more 1X TAE buffer was added and each well of the gel was filled with 15ul of the PCR product. Gels were run at 100V for 60-90 minutes and imaged using the Biorad gel reader.

Real time quantitative PCR (qPCR) was performed using the ABI Prism 7500 sequence detection system (Apllied Biosystems, California, USA) with the Quantitect SYBR Green PCR kit (Qiagen, Hilden, Germany) as per the manufacturer's instructions. All samples were run in technical triplicates in addition to biological and experimental replicates to ensure accuracy for qPCR. Every plate was run with Ribosomal protein 19 (*L19)* or Glyceraldehyde 3-phosphate dehydrogenase ((*GAPDH*) housekeeping gene to allow relative quantification and reduce error that may derive from instrument variation between runs. Prior to qPCR, the plate containing the samples was covered with an adhesive PCR plate seal and vortexed then centrifuged briefly to settle contents. The 7500 Fast system was then used to perform relative quantification with the instrument settings depicted in Figure 1.6. On completion, dissociation was performed with the instrument settings depicted in

Figure 2.8. Data were analysed using the ΔΔCT method to assess relative gene expression..

Table 2.2: Details of primers used for PCR.

Gene	Forward (FW) and Reverse (REV) Primers (5'-3')	Anneal temp (°C)	Cycles	Product size (bp)
ALP	FW CACGGGCACCATGAAGGAAAAG REV TGGCGCAGGGGCACAGGAGACT	59	35	341
CMYC	FW CTTCCCCTACCCTCTCAACG REV AGTGGGCTGTGAGGAGGTTT	56	35	303
COL1 1	FW ATGCCTGGTGAACGTGGT REV AGGAGAGCCATCAGCACCT	56	26	87, 240, 267
DNMTB	FW TACACAGACGTGTCCAACATGGGC REV GGATGCCTTCAGGAATCACACCTC	56	35	195
GAPDH	FW TGATGACATCAAGAAGGTGGTGAAG REV TCCTTGGAGGCCATGTGGGCCAT	56	26	240
KLF-4	FW CCCACACAGGTGAGAAACCT REV TTCTGGCAGTGTGGGTCATA	56	35	220
L19	FW GCGGAAGGGTACAGCCAAT REV CAGGCTGTGATACATGTGGCG	56	32	130
NES	FW CAGCGTTGGAACAGAGGTTGG REV TGGCACAGGTGTCTCAAGGGTAG	56	35	389
NANOG	FW GGATGGTCTCGATCTCCTGA REV CCTCCCAATCCCAAACAATA	56	35	252
OCT4	FW GTACTCCTCGGTCCCTTTCC REV CAAAAACCCTGGCACAAACT	56	35	165
OSC	FW ACACTCCTCGCCCTATTG REV GATGTGGTCAGCCAACTC	56	35	244
OSX	FW CGGGACTCAACAACTCT REV CCATAGGGGTGTGTCAT	56	32	308
RUNX2	FW GCACAGACAGAAGCTTGAT REV CCCAGTTCTGAAGCACCT	56	35	351
SOX2	FW CATGTCCCAGCACTACCAGA REV GTCATTTGCTGTGGGTGATG	56	35	234
VIM	FW GACACTATTGGCCGCCTGCAGGATGAG REV CTGCAGAAAGGCACTTGAAAGC	56	35	418

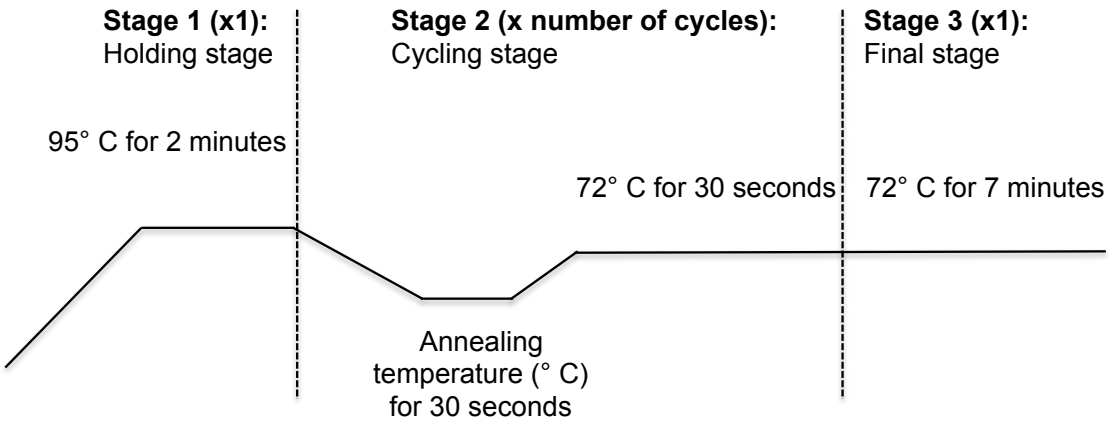

Figure 2.6: Thermal cycler settings for end-point PCR.

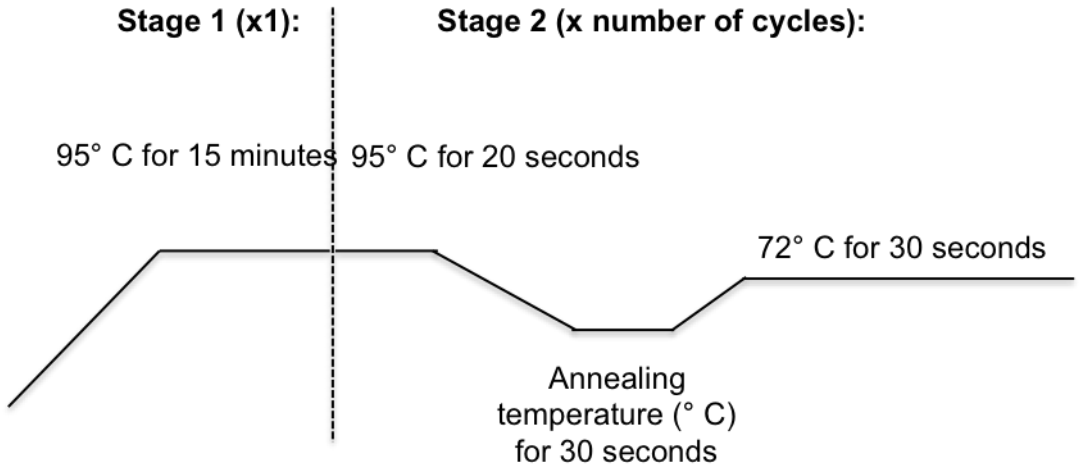

Figure 2.7: Settings for relative quantification on the ABI Prism 7500 sequence detection system.

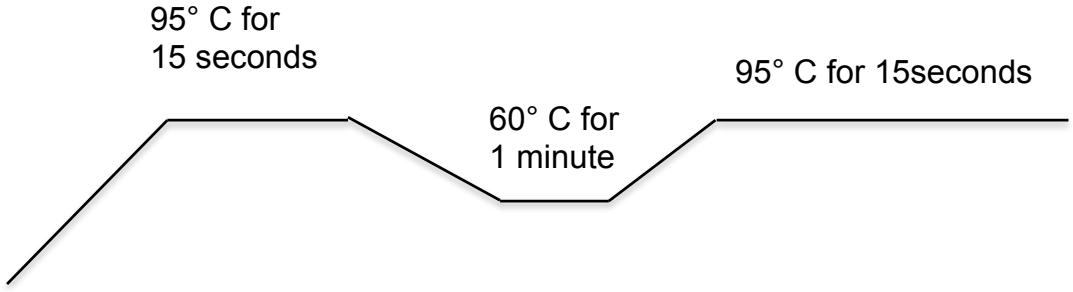

Figure 2.8: Settings for dissociation on the ABI Prism 7500 sequence detection system.

2.2.6.3 Flow cytometry

Characterization of cells using surface markers was conducted using flow cytometry analysis (Table 2.3). Dissociated cells were incubated with blocking solution (2.5% FBS in PBS 1X) for 30 minutes in a 96 well plate. Cells were then incubated with antibodies diluted in blocking solution for 15 minutes at 4ºC then washed in PBS 1X twice. For negative controls cells were incubated with the isotype control. Flow cytometry analysis was performed using FACSCalibur (BD Biosciences, California, USA) and its associated Cell Quest Pro software. Data was analysed using FCS Express 6.0 (De Novo Software, Glendale, USA).

2.2.6.4 Histology and immunoflourescent staining

Cell and tissue fixation

All tissues and cells were fixed in 4% paraformaldehyde (PFA) that was made by adding an amount of PBS equal to 80% of the required volume of PFA. The PBS was heated to 60°C whilst a top a hot plate with a magnetic stirrer. Then the necessary weight of paraformaldehyde powder was mixed into the solution and the sodium hydroxide (NAOH) was added drop-wise until the solution cleared. The solution was cooled and the required total volume was made up by adding 1X PBS. The pH of the solution was checked and adjusted as necessary (to pH 6.9) with hydrochloric acid (HCL). Syringe-driven filters were used to filter and aliquot the PFA which was stored at -20°C till needed.

To fix cells in monolayer, medium was removed from cells that were then fixed by adding 4% Paraformaldehyde solution (4% PFA) for 10 minutes then washed with PBS twice. If not used immediately, fixed cells were stored in PBS at 4°C in the cold room. For tissues and 3D cellularised scaffolds, samples were fixed in 4% PFA overnight in the cold room (4°C) then PFA was removed. Samples were washed x3 times in PBS then frozen, embedded or stored in PBS depending on need.

Table 2.3: Antibodies used in flow cytometry.

Antibody	Fluorophore	Dilution
CD13	PE	1 in 5
CD29	PE	1 in 5
CD44	PE	1 in 5
CD73	PE	1 in 5
CD105	PE	1 in 20
CD166	PE	1 in 5
CD10	FITC	1 in 5
CD14	FITC	1 in 5
CD31	FITC	1 in 5
CD34	FITC	1 in 50
CD45	FITC	1 in 10
CD117	PE	1 in 5
HLA ABC	PE	1 in 5
HLADR	FITC	1 in 5
IgG1	FITC	1 in 5
IgG1	PE	1 in 5
IgG2a	FITC	1 in 5
IgG2b	FITC	1 in 5

All antibodies purchased from BD biosciences.

Cryosectioning

1.5cm moulds were made using aluminium foil and a permanent marker. The optimum cutting temperature (OCT) embedding medium was placed into the mould and samples were orientated then transferred to dry ice. Samples were kept on dry ice for 30 minutes then stored at -80°C till needed.

Samples were transferred at least 2 hours before sectioning to -20°C. The blade and samples were left in the cryostat for 15-20 minutes to equilibrate with regards to temperature. 10-30um sections were taken depending on requirement and placed either onto a super frost slide or as free-floating sections in a 24 well plate with PBS. Slides were stored at -20°C whilst free floating sections were rinsed further in PBS until all OCT was removed then stained in their wells and mounted at a later date.

Paraffin sectioning

Samples were sent to the Great Ormond Street Hospital pathology department for paraffin embedding and microtome sectioning into 4um slices. Sections were deparaffinised using histoclear and rehydrated in descending ethanol concentrations prior to downstream analysis.

2.2.6.5 Immunoflourescent staining

Blocking buffer was made using 3% BSA and 10% FBS in PBS then stored at -20°C till needed. When required for blocking, 0.2% Triton-X was added fresh otherwise the buffer was used to dilute the primary and secondary antibodies (Table 2.4).

Samples were placed in blocking buffer for 60 minutes then incubated with the primary antibody (at the desire concentration) overnight at 4°C. Samples were washed in PBS x3 times (each wash for 5 minutes). Secondary antibody solution (at the desired concentration and containing Hoechst) was added to samples, which were then covered with foil and incubated for 1 hour at room temperature then washed with PBS as before. Samples were then either transferred to a slide (if section) or kept in the well if whole mounting.

Hydromount (1 drop) was added to samples before applying coverslip carefully to avoid any bubble formation. Bone and fat tissue specimens were dehydrated through serial ethanol dilutions (25-100% for 2 hours at a time) then cleared with Xylene before mounting with DPX (one drop) and placing a cover slip.

Table 2.4: Fluorescent markers used in immunoflourescent analysis.

Antibody/Dye	Species	Dilution	Source
Fluorescein Phalloidin (F-Actin)	-	1:400	Thermo Fisher Scientific
Hoechst 33258 (Nuclear counterstaining)	-	1:400	Thermo Fisher Scientific
Anti-Mouse IgG Alexa Fluor 568/594	Goat	1:400	Invitrogen
Anti-Rabbit IgG Alexa Fluor 488	Goat	1:400	Invitrogen
Vimentin	Mouse	1:100	DAKO
Alkaline Phosphatase	Mouse	1:200	Hybridoma bank
Osteopontin	Mouse	1:200	Hybridoma bank
Lamin A/C	Mouse	1:100	Abcam
Laminin	Mouse	1:100	Hybridoma bank
Nestin	Rabbit	1:100	Millipore
Collagen 1	Rabbit	1:100	NOVUS
Von Willebrand Factor	Rabbit	1:5000	DAKO

Antibodies and dyes used for immunocytochemistry and immunohistochemistry.

2.2.6.6 Biological staining and quantification of differentiation

Oil Red O and adipogenic measurement

Samples were washed with 60% Isopropranolol for 5 minutes then stained with filtered Oil Red O for 10 minutes. This was followed by a quick dip (or if not a slide then immersion for 1-2 seconds) in haemotoxylin. Sample was washed with dH2O several times and imaged. Quantification was performed by extracting the dye with 100% isopropranolol for 30 minutes at room temperature then read at OD495.

Alcian Blue and Chondrogenic measurement

Specimens were rinsed with 0.1N HCL for 5 minutes then stained with filtered Alcian Blue (1% in 0.1N HCL) for 30 minutes followed by staining with NFR for 5 minutes. This was washed in dH2O and imaged. Chondrogenic quantification was performed by extracting dye with 6M Guanidine Hydrochloride overnight on a shaker at room temperature then reading using OD595.

Alizarin red and osteogenic measurement

The samples were washed in dH2O then stained with filtered 1% Alizarin for 5 minutes and imaged. Quantification was then performed by incubating samples with 10% acetic acid for 30 minutes at room temperature. The contents were scraped and transferred to 1.5mL Eppendorfs which were heated at 85°C for 10 minutes. Eppendorfs were then centrifuged and the supernatant read at OD405.

Von Kossa Staining

Specimens were stained with 1% Silver Nitrate solution for 20 minutes on a UV transilluminator then rinsed in dH2O x 3 for 1 minute each time. Samples were then incubated with 5% sodium thiosulfate for 5 minutes which was made as below:

- Sodium Thiosulfate 5g
- dH2O 100ml

This was followed by washing in dH2O then staining with NFR for 5 minutes before rinsing with dH2O.

Haemotoxylin and Eosin (H&E)

Samples were immersed in dH2O then stained with haematoxylin for 4 minutes. This was followed by rinsing in tap water then differentiation with 0.3% acid alcohol for a few seconds (until the background disappears). Samples were rinsed with tap water then with Scott's tap water substitute (until blueing is achieved), which was made as follows:

- sodium hydrogen carbonate 1g
- magnesium sulphate 10g
- distilled water 500ml

After rinsing with tap water, samples were stained with eosin for 2 minutes then rinsed again.

Giemsa stain

Slides were brought to methanol for a few seconds then stained with Giemsa's stain for 10-15 minutes. Slides were then moved to a mixture of stain and 6.8 pH phosphate buffer (1:3) for 20-30 minutes. After staining, slides were rinsed in dH2O and air-dried.

MacNeal's Tetrachrome Counterstain

The stain was made up by:

- Adding 2g dye to 100ml dH2O whilst slowly bringing solution to boiling point
- After boiling, heat was turned off and the solution allowed to stir overnight

Samples were rinsed with dH2O for 1 minute. Prior to each use the solution was filtered then samples were stained with McNeal's tetrachrome solution for 10-15 minutes. The samples were then rinsed in distilled water x3 for 1 minute each.

2.2.6.7 Imaging

Live cell imaging

Plates and flasks were imaged using an inverted microscope Olympus IX71 (Zeiss) equipped with a Hamamatsu ORCA-ER digital camera (Hamamatsu Corp) using HCImage processing software.

Time-lapse imaging was performed on 6 well plates using the Zeiss Axiovert 135 live imaging microscope with motorised stage and Hamamatsu Orca R2 monochrome camera and ICY software.

Fluorescence and second harmonic generation scanning

Slides and plates were imaged using an inverted microscope Olympus IX71 (Zeiss) equipped with a Hamamatsu ORCA-ER digital camera (Hamamatsu Corp) using HCImage processing software.

Confocal microscopy of slides and cut samples was performed using the Zeiss LSM 710 upright confocal and accompanying Zen software (Zeiss, Welwyn Garden City, UK). The upright Zeiss LSM 880 multiphoton was used to image whole mount samples (in particular POSS-PCL scaffolds) with accompanying Zen software (Zeiss, Welwyn Garden City, UK). The multiphoton was also used to perform second harmonic generation scanning in order to visualise collagen fibres.

Imaging of collagen either through immunoflourescent staining or SHG processed and interpreted using ImageJ software. All images were post processed equally using the despeckle, background subtraction and Fourier transformation filters. The OrientationJ plugin was then used to analyse collagen fibre orientation.

Colour imaging of biological staining

Images were taken using the Axiovert 135 (Zeiss, Welwyn Garden City, UK) with a ProgRes C14 digital camera using Openlab software (PerkinElmer Life, Wokingham, UK) with a colour digital camera and processed with accompanying manufacture's software.

2.2.6.8 Micro CT (µCT)

Sample scanning and reconstruction

High-resolution uCT scanning of pre and post CAM grafted cellularised fibrin scaffolds was performed using the Skyscan1172 uCT scanner (Bruker, MicroCT, Kontich, Belgium) without a filter. The imaging parameters used were an X-ray tube voltage of 49kV and a current of 200uA, scanning angular rotation of 0 degrees and angular increment of 0.4 degrees for all scans. Median filtering and flat-field correction were also applied to all scans to reduce ring artefacts. Scans were reconstructed with NRecon software (version 1.6.6.0, Skyscan N.V., Kontich Belgium) using the Feldkamp algorithm. All scans were optimised using beam-hardening correction, alignment optimization and ring artefact correction during reconstruction. The resultant image resolution was 3.88um.

The samples that were implanted in nude mice were first fixed in 4% PFA, incubated with iodine for 48 hours, washed then paraffin embedded as described earlier. Prior to sectioning the blocks were scanned using an XTH225 ST microfocus-CT scanner (Nikon Metrology, Tring, United Kingdom) without a filter. All scans used an accelerating voltage of 80kV, a current of 88uA, calibrated centre of rotation of 0 degrees. CT scans were reconstructed with the CTPro3D software (version 5.1.1, Nikon Metrology UK) using a modified Feldkamp filtered back projection. A median filter was applied to all scans during reconstruction to reduce artefacts. The resultant volumes had a voxel size of 12.7um equivalent to an approximate resolution of 13um.

Post processing and segmentation

Post processing of 2D stacks of the reconstructed images was performed using ImageJ freeware. Stacks were converting to 8-bit grey scale then optimised with a Gaussian 3D filter by applying the despeckle filter, background subtraction using a sliding ball algorithm and the 3D Gaussian blur filter to reduce noise. Images were cropped to avoid edge effects, beam hardening and other artefacts. To enable more rapid processing, all stacks were scaled by 50%.

The WEKA trainable segmentation plugin for ImageJ was used to segment the scaffold, blood vessel and mineral components of the samples (Arganda-Carreras et al., 2017). For each stack, an area enclosing the whole scaffold(s) was cropped using a square region of interest (ROI) and pixels were classified as either scaffold, blood vessel, mineral or background as identified by the user to train the classifier. To ensure consistency and comparability, the same machine-learning algorithm was used for related samples by applying the same classifier to each sample. Segmented stacks (the classified images) were then binarised prior to downstream analysis.

Analysis of segmented stacks

The segmented stacks were split into mineral, scaffold and vessel. The 3D viewer was used to build 3D models to visualise mineralisation and vascularisation of the scaffolds by overlaying the segmented stacks onto the original images.

Quantitative analysis of mineralisation was performed using the BoneJ plugin (Doube et al., 2010). Bone volume fraction (BV/TV) was computed as a ratio of the mineral pixels (BV) and total volume of the scaffold pixels (TV). Particle analyser plug in was used to measure the area of mineralised nodules.

Analysis of blood vessels was performed manually on 2D images using the ROI manager and particle analyzer plugin for ImageJ.

Structural assessment of bone controls and scaffolds was also determined using μCT scanning. 3D stacks of constant size (236x236 pixels) were taken

from different parts of the centre of the bone/scaffolds to avoid edge effects, beam hardening and minimize scanning artifacts. Images subsequently were thresholded automatically using Otsu's method and quantitatively analysed using the BoneJ plugin to calculate density and porosimetry.

2.2.6.9 Reflections microscopy

Reflection microscopy (using the Zeiss multiphoton) was used to obtain scans of the surfaces of all scaffolds. Scanning area was limited to the centre of each scaffold to avoid any unintentional changes to the biomaterial's property from cutting or handling with forceps.

All images acquired through reflections microscopy were analysed in grey scale 8-bit mode. ImageJ was used to analyse all data. The plug-in 'Extended Depth of Field' was first used to generate a height profile image, which assigns pixels on each vertical plain a value representing height at that plane. In addition to computing the height map this plugin was also used to represent the height map as a 3D topographic map visualising surface roughness. A second plug-in 'SurfCharJ' as then used to compute surface roughness based on the 32-bit height map. To allow comparison between samples, surface levelling, a sample length of 10um and a Gaussian filter were selected as options on 'SurfCharJ'. Of all the surface characterisation values quantified, the Arithmetical mean deviation (Ra) and Root mean square deviation (Rq) were chosen to evaluate surface roughness based on their common use in this area of research.

2.2.6.10 Mechanical testing

Uniaxial compression testing using the Hounsfield tensile and compression testing machine with a 10kN Load cell to obtain data on deformation and force which were used to derive stress-strain curves for characterisation of the mechanical properties of scaffolds.

Uniaxial compression testing provided raw data of time, displacement and force for each sample. To compare mechanical properties of porous scaffolds common parameters such as the Young's modulus (E), Yield strain (εy), Yield stress (σy) and the material's maximum capacity to elastically absorb energy (U_{el}^{Max}). Where ΔL is the measured displacement and Lo is initial sample length

along a single axis the calculations for stress, strain and Young's modulus were as follows:

Strain $\varepsilon_e = \Delta L/L_o$

Stress $\sigma_e = P/A_o$

Young's Modulus, E (Pa)=σ_e/ε_e

Stress was then plotted against strain for each sample to generate a stress-strain profile. The point on the curve at which linear elastic behavior ceases was used to determine yield strain and yield stress. Based on this, yield strain and yield stress were used to determine the material's maximum capacity to elastically absorb energy was calculated as follows:

$U_{el}^{Max} = 1/2\sigma y \varepsilon y$

2.2.7 Chorioallantoic membrane (CAM) grafting

Paediatric hADSC encapsulated in 2mm fibrin scaffolds were cultured in control or osteogenic differentiation media for 2, 3, 4 or 5 weeks and either harvested then analysed or CAM grafted for an additional 7 days then harvested. Experiments were performed using cells from three different patient lines in at least three experimental replicates for each condition (at least six replicates were used for CAM grafting to account for impaired survival of chick embryos).

2.2.8 In vivo studies

Human ADSC from three different patients were encapsulated in either fibrin or seeded onto POSS-PCL-Fibrin 5mm scaffolds and cultured in control or osteogenic differentiation media for three weeks in experimental triplicates then harvested and analysed as pre in vivo controls. In parallel hADSC from one patient were similarly cultured and then subcutaneously engrafted onto the backs of athymic nude mice (n=6 per experimental condition) for 4 months alongside an unseeded scaffold controls (n=3). In total five mice were used with three scaffolds implanted onto each flank.

2.3 Statistical analysis

2.3.1 Morphometric analysis data (Chapter 3)

GraphPad Prism 6.0 software was used to generate all charts and all graphs apart from 3D scatter plots which were created using SPSS 22.0.

Column statistics were used to test normality of the data using D'Agostino and Pearson omnibus normality test whilst linear regression analysis was used to compare the differences between TCS, CM and control children with respect to the first two PCs in the skeletal and soft tissue DSM as well as the asymmetry index in GraphPad Prism 6.0 for mac (GraphPad software, La Jolla, USA). P values were then calculated to test whether differences between slopes and intercepts of the regression lines of the TCS and Control subgroups were significant different ($p<0.05$).

Bootstrapping was used to generate confidence intervals for the asymmetry index values in SPSS 22.0 (IBM SPSS, Portsmouth, UK). Unpaired two-tailed t-test was used to compare the means of the asymmetry indices and cephalometric measurements between the Control and TCS group whilst comparison between CM and control patients was performed using the Mann-Whitney U test ($p<0.05$).

2.3.2 Tissue engineering data (Chapters 4-6)

All data are presented as the mean ± standard error of mean (SEM). The statistical analysis was performed using GraphPad Prism 7.0 for mac (GraphPad software, La Jolla, USA). Statistical significance was evaluated using ANOVA followed by a Tukey's post-hoc test for multiple comparisons. A p-value equal to or less than 0.05 was considered statistically significant.

Chapter 3 Morphometric Analysis Of Postnatal Midface Development

3.1 Introduction

The midface is the middle portion of the face comprising the orbits, maxilla, nasal and upper mouth areas. The zygoma, maxilla and nasal bones constitute the skeletal components whilst the soft tissues include the malar regions, nose and lips. The skeletal components provide support and protection for the soft tissues, which provide input and output routes for vision, hearing, speaking, breathing and eating. It is also an important contributor to the morphology of the face thus playing a role in social interactions. Due to these functions, malformations of the midface can produce devastating clinical manifestations including sight, respiratory, feeding, speech and psychoscial problems.

3.1.1 Normal postnatal development of the midface

As discussed in section 1.1, the human midface derives from both mesoderm and neural crest origin through a highly complex and regulated activity involving fusion and merging of several processes to produce midface morphogenesis (Suzuki et al., 2016). Continued postnatal growth of the midface is directed by differential growth of the different structures comprising it. Development of the individual components of the midface (e.g. the zygomatic bone or malar region) is independent but also affected by surrounding structures. Thus, development of the bones is also affected by growth of the interconnecting sutures as well as that of soft tissue structures such as the eyes, tongue, musculature and nasal cavity (McMahon et al., 2013, Richtsmeier and Flaherty, 2013). Remodelling, driven by secondary dentition, also affects the shape and direction of maxillary growth (Gray et al., 2005, Brennan et al., 2015).

The skeletal midface grows most in the anteroposterior dimension, followed by depth and least of all horizontal growth throughout the prenatal period until late adolescence. Postnatal growth of the soft tissues is closely related to that of the skeletal tissues although the correlation is not thought to be direct due to increased subcutaneous fat deposition in children and projection produced by growth of the nose and lip (Miloro et al., 2004b).

3.1.2 Dysmorphic development of the midface in Treacher Collins Syndrome and Craniofacial microsomia

Congenital malformations of the midface can be due to maldevelopement of all of the components giving rise to midface hypoplasia (a disorder characterized by midface narrowing, shortening and retrusion) or caused by absence or incomplete development of individual structures. These deformities usually occur as part of a cluster of anomalies in a syndrome. They may also be due to an isolated event causing disruption to development such as a vascular insult. Treacher Collins Syndrome and Craniofacial microsomia are examples of diseases that result in midface dysmorphism due to errors of patterning during branchial arch development. They have overlapping phenotypes but different mechanisms of pathogenesis (Johnson et al., 2011, Tuin et al., 2015).

TCS is a rare autosomal dominant disorder of varying penetrance, which causes a spectrum of craniofacial defects. It has a global incidence of 1:50,000 live births and is mostly caused by mutations in the *TCOF1* gene (Conte et al., 2011, Wilkie and Morriss-Kay, 2001). The characteristic craniofacial abnormalities associated with TCS include midface retrusion and hypoplasia, low set ears and/or microtia/anotia as well as micrognathia. CM on the other hand, has a prevalence of 1 in 5600 live births (Birgfeld and Heike, 2012). The pathogenesis is thought to relate to abnormal development of the first two branchial arches and whilst the aetiology is still unknown, chromosomal abnormalities have been discovered in variants of the disease (Rooryck et al., 2010). There is a spectrum of craniofacial abnormalities including malformation of the ears, nose, soft palate and lip as well as maxillary and mandibular hypoplasia. Another key feature of the disease is facial asymmetry.

3.1.3 Limitations of reconstructive options for midface dysmorphology

The gold standard treatment of the skeletal midface deformities occurring in CM and TCS involves surgery. This aims to reconstruct the deformity by augmenting bone volume, and thus correct the surface morphology to improve. Procedures commonly used include osteotomies and distraction osteogenesis, autologous tissue transfer and foreign-body implants (Sinn et al., 2011, Longaker and Siebert, 1996, Denny et al., 2003, Choung et al., 1991).

3.1.4 Improving accuracy of midface surgical reconstruction

The accuracy of midface surgical reconstruction has been increased through the use of 3-dimensional (3D) reconstructions of computed tomography (CT) scans. This has enabled planning of osteotomy sites as well as to predict the shape and volume of tissue required to reconstruct the deformity. Another use has been in planning autologous flaps or bone grafts whereby the tissue is shaped during surgery or in the fabrication of preshaped synthetic implants (Steinbacher, 2015). These techniques are however still limited with regards to understanding postnatal facial development and relating skeletal to soft tissue growth. This information would enable surgical planning based on projected growth of the entire midface complex and as well as expected growth.

Surprisingly, detailed information on human facial skeletal development after birth is not available. Most work has been on animal models or in looking at the components of the skull separately such as suture fusion or indirectly measuring growth (Martinez-Maza et al., 2013). The limitations of these methods is that animal models may not be generalizable to humans and as growth of the face is complex, analysis of separate regions risks missing out how different regions impact each other's development and the rest of the skull. Craniofacial bone growth has traditionally been assessed using cephalometric studies (Mellion et al., 2013, Bergman et al., 2014), computed tomography (CT) scans of dry skulls (Nikkhah et al., 2013, Harnet et al., 2013) or indirectly by extrapolating data from soft tissue to the underlying skeleton (Krimmel et al., 2015). Reliance on plain radiographs or CT scans has traditionally limited the number of studies that could be undertaken in healthy children who do not normally have such imaging. In contrast, soft tissue growth and morphology has been extensively studied in normal and abnormal development as measurements can be easily and noninvasively obtained through anthropometrics (Farkas et al., 1992, Tutkuviene et al., 2015) or with surface modeling using 3D imaging (Suttie et al., 2013, Koudelová et al., 2015, de Souza et al., 2013).

Craniofacial shape and variation can be quantified using morphometric analysis (MA) which has been widely used to study heterogeneity in soft tissues of the

face, classify non-genetic diseases, demonstrate normal growth and facial asymmetry and link gene expression to facial phenotype (Hopman et al., 2014, de Souza et al., 2013, Hammond et al., 2003). This technique can be used to monitor normal development and variation as well as compare children with congenital craniofacial bone defects. The key advantage of this method is that it provides quantitative assessment of craniofacial shape, which can be statistically analysed. Its use is also well established in the literature (Hopman et al., 2014, de Souza et al., 2013, Hammond et al., 2003).

Whilst quantitative analysis of the facial skeletal tissues for preoperative planning has been undertaken in TCS, it only focused on relatively mild forms of the disease (Nikkhah et al., 2013). Similarly, 3D imaging was used to describe the dysmorphology in CM but this only studied the soft tissues and used three patients with CM (Claes et al., 2011). Furthermore, the relationship between skeletal and soft tissue shape and has similarly not been modelled. This is vital, as it is needed to understand normal and dysmorphic postnatal midface growth and development. This data would permit clinical teams to evaluate the efficacy of surgery and potentially to aid in planning reconstructions.

In this chapter, postnatal development of the skeletal and soft tissue components of the midface will be studied using morphometric analysis based on models built from CT scans of the face. This will be used to understand and compare midface appearance and growth in control, TCS and CM children. Furthermore, morphometric analysis will be used to evaluate the efficacy of surgical correction of midface hypoplasia in TCS and ultimately assess whether this method can eventually help improve the accuracy of surgical reconstruction.

3.2 Results

3.2.1 Sample characteristics

3.2.1.1 Age and gender distribution

A total of 74 CT scans of patients (52 controls, 6 CM, 14 preoperative TCS and 2 postoperative TCS) were used to extract a soft tissue and skeletal tissue surface for each patient in this study. Gender ratio was 28:23 (male:female) in control group, 8:6 in the TCS preoperative group and 4:2 in CM. Age was distributed from 1-16 years in all groups **(**Figure 3.1**).** One TCS male individual had a preoperative (aged 13), immediately postoperative (aged 14) and one year postoperative CT scan (aged 15).

Both control and TCS data passed the D'Agostino & Pearson omnibus normality test whilst the sample size of the CM dataset was too small for such analysis and thus a normal distribution was not assumed for the CM group.

3.2.1.2 Classification of severity of facial dysmorphism

The midface was the focus of this study and soft tissue surface reconstructions reveal a heterogeneous distribution of facial deformity exhibited by the TCS and CM groups (Figure 3.2) (Figure 3.3). To enable validation of the modelling work, skeletal and soft tissue surfaces of the whole face were first scored using a modified OMENS classification form for each unoperated TCS and CM individual (Table 3.1)(Table 3.2). These findings revealed that in both TCS and CM, the abnormalities tended to mainly involve the mandible and orbital displacement (Table 3.3). Soft tissue hypoplasia of the mid and lower face was also a common finding. Overall, according to the classification, where abnormality was found, it was most often bilateral in TCS patients (Table 3.3).

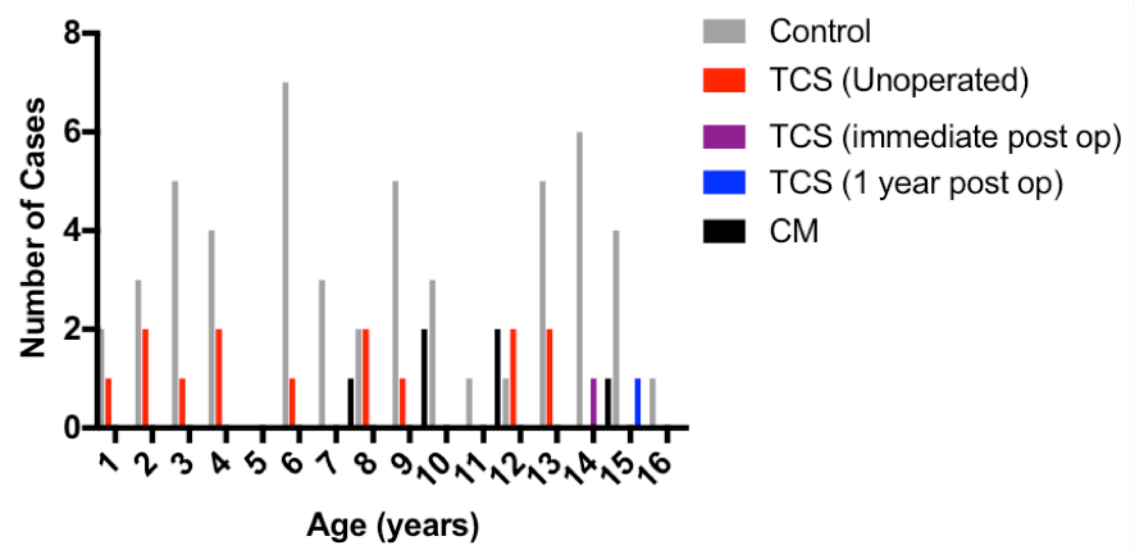

Figure 3.1: Age distribution of participants.

There are 52 controls, 14 unoperated Treacher Collins Syndrome (TCS) cases, 2 postoperative TCS scans (from the same individual; immediately and 1 year on) and. 6 CM cases. *Mean age in years of controls is 8.48 ± 4.55 STD, unoperated TCS is 6.92 ± 4.38 STD and CM is 10.16 ± 2.40 STD.*

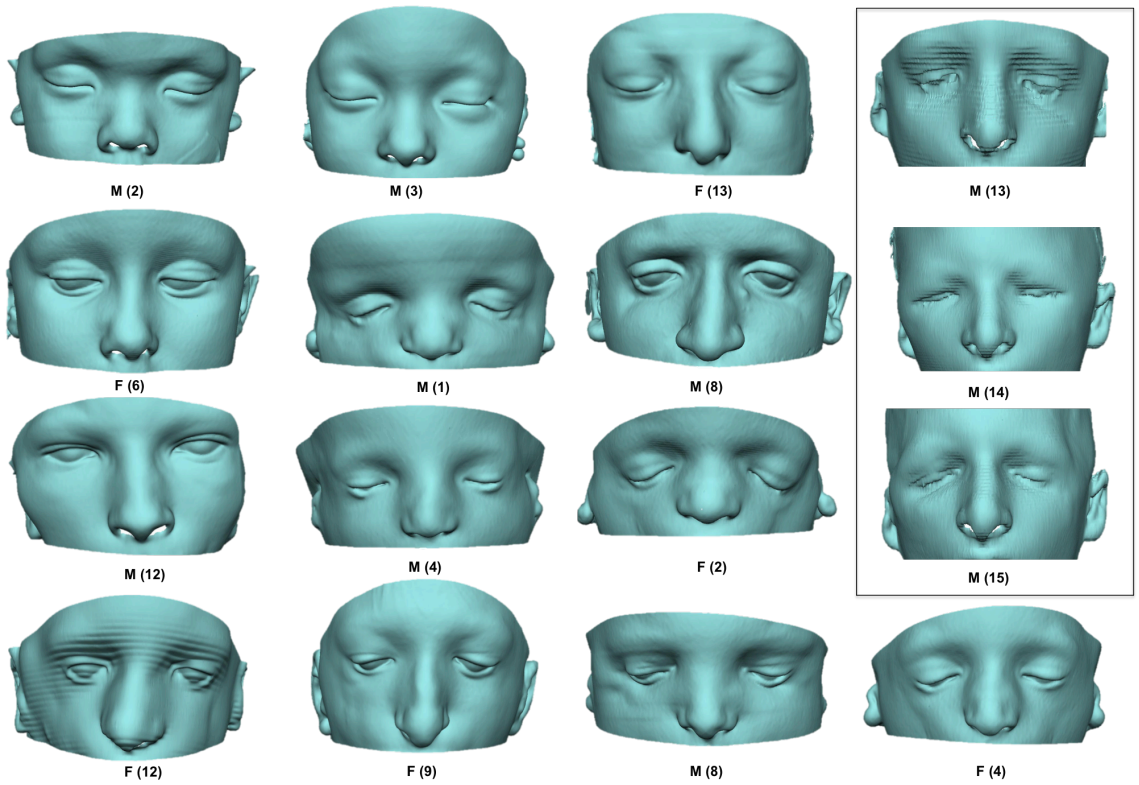

Figure 3.2: Soft tissue surfaces of the midface of the Treacher Collins Syndrome individuals

Midface soft tissue surfaces of all patients with Treacher Collins Syndrome. Coding represents gender (male (M) or female (F)) and age in years. Box encloses TCS individual for whom CT scan was available prior to surgery (M13), immediately following surgery (M14) and one year after surgical correction (M15).

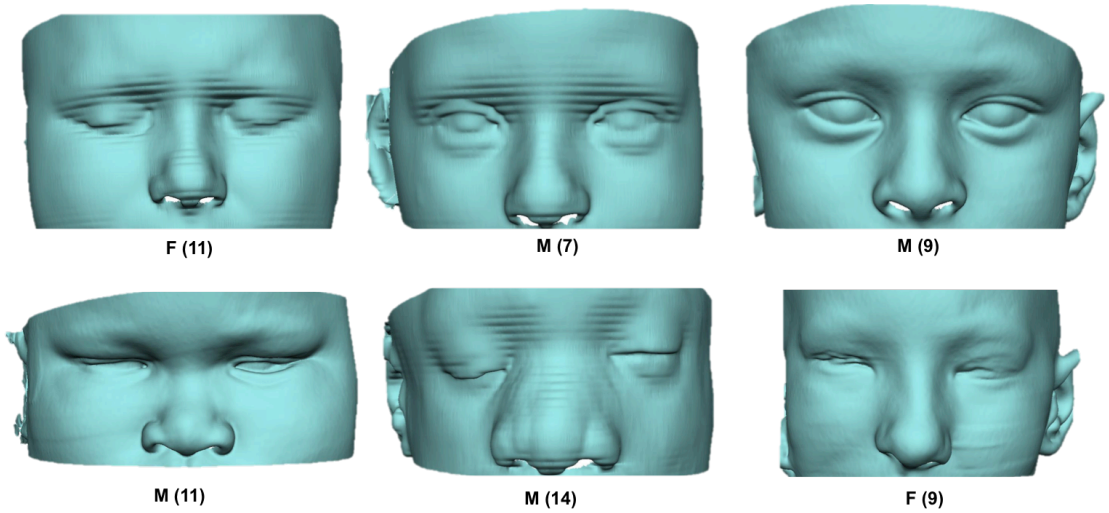

Figure 3.3: Soft tissue surfaces of the midface of the Craniofacial microsomia individuals.

Midface soft tissue surfaces of all individuals with Craniofacial microsomia included in the study. Coding consists of gender (male or female) and age in years.

Table 3.1: Modified OMENS classification of facial deformity in Treacher Collins Syndrome subjects.

	Soft tissue												Skeletal			
	Orbit		Mandible		Ear		Nerve		Soft tissue		Lateral Cleft		Mandible		Orbit	
	Right	Left	Right	Left	Right	Left	Right	Left	Right	Left	Right	Left	Right	Left	Right	Left
M (2)	OS0 OD0 OPUA CHUA	OSO OD1 OPUA CHUA	M0	M1	E0	E1	N0	NB1	S0	S2	LC0	LC0	MX0	MX2B	OXS0 OXD0	OXS0 OXD1
M (3)	OS0 OD0 OPUA CH1	OS1 OD1 OPUA CH0	M3	M0	E2	E3	N0	NO1 NS1 NL1	S2	S0	LC0	LC0	MX0	MX0	OXS0 OXD0	OXS0 OXD1
F (13)	OS0 OD0 OPUA CH1	OSO OD1 OPUA CH0	M2b	M0	EUA	EUA	N0	NB1 NS1	S2	S0	LC0	LC0	MX3	MX3	OXS0 OXD0	OXS0 OXD0
M (13)	OS1 OD1 OPUA CH0	OS0 OD0 OPUA CH0	M0	M0	E3	E3	N0	N0	S0	S0	LC0	LC0	MX3	MX3	OXS0 OXD0	OXS0 OXD1
M (14)	OS0 OD1 OPUA CH0	OS0 OD0 OPUA CH1	M0	M0	E3	E1	N0	N0	S2	S0	LC0	LC0	MX2B	MX2B	OXS0 OXD0	OXS1 OXD0
M (15)	OS0 OD1 OPUA CH0	OS1 OD0 OPUA CH0	M0	M0	E3	E1	N0	N0	S2	S0	LC0	LC0	MX2B	MX2B	OXS0 OXD0	OXS1 OXD1
F (6)	OS0 OD0 OPUA CH0	OS0 OD0 OPUA CH1	M0	M2A	E0	E0	NL1 NS1	N0	S2	S0	LC0	LC0	MX0	MX0	OXS0 OXD0	OXS0 OXD0
M (1)	OS1 OD1 OPUA CH0	OS0 OD0 OPUA CH0	M2A	M0	E3	E3	N0	N0	S3	S2	LC0	LC0	MX3	MX3	OXS0 OXD1	OXS0 OXD1
M (8)	OS0 OD0 OPUA CH0	OS0 OD1 OPUA CH1	M0	M1	E0	E0	N0	N0	S3	S2	LC0	LC0	MX3	MX3	OXS0 OXD1	OXS0 OXD0
M (12)	OS0 OD0 OPUA CH0	OS0 OD0 OPUA CH1	M0	M2A	E3	E3	N0	N0	S2	S1	LC0	LC0	MX3	MX3	OXS1 OXD1	OXS0 OXD0
M (4)	OS0 OD1 OPUA CH0	OS0 OD1 OPUA CH0	M1	M0	E3	E3	N0	N0	S2	S1	LC0	LC0	MX3	MX3	OXS0 OXD1	OXS0 OXD1
F (2)	OS0 OD1 OPUA CH0	OS0 OD1 OPUA CH0	M3	M3	E3	E3	N0	N0	S3	S3	LC0	LC0	MX3	MX3	OXS2 OXD1	OXS0 OXD1
F(12)	OS0 OD1 OPUA CH0	OS0 OD0 OPUA CH1	M0	M2A	E1	E1	N0	N0	S3	S1	LC0	LC0	MX3	MX3	OXS0 OXD1	OXS0 OXD0
F (9)	OS0 OD1 OPUA CH1	OS0 OD0 OPUA CH0	M2A	M1	E1	E1	NB1 NS1	N0	S3	S2	LC0	LC0	MX3	MX3	OXS0 OXD1	OXS0 OXD0
M (8)	OS0 OD0 OPUA CH0	OS0 OD0 OPUA CH0	M2A	M1	E0	E0	N0	N0	S3	S2	LC0	LC0	MX3	MX3	OXS0 OXD0	OXS1 OXD1
F (4)	OS0 OD0 OPUA CH0	OS0 OD0 OPUA CH0	M1	M1	E3	E3	N0	N0	S3	S3	LC0	LC0	MX3	MX3	OXS1 OXD1	OXS0 OXD0

Red box encapsulates the TCS individual (M13) who underwent surgical correction (M14) and had a scan 1 year later (M15). OS/OXS; orbital size, OD/OXD; orbital displacement, OP; occlusional plane, CH; chin position.

Table 3.2: Modified OMENS classification of facial deformity in Craniofacial microsomia subjects.

	Soft tissue												Skeletal			
	Orbit		Mandible		Ear		Nerve		Soft tissue		Lateral Cleft		Mandible		Orbit	
	Right	Left	Right	Left	Right	Left	Right	Left	Right	Left	Right	Left	Right	Left	Right	Left
F(11)	OS0 OD0 OPUA CH1	OS0 OD0 OPUA CH0	M2A	M0	E0	E0	N0	N0	S2	S0	LC0	LC0	MX2B	MX0	OXS0 OXD0	OXS0 OXD0
M(7)	OS0 OD0 OPUA CH0	OS0 OD0 OPUA CH1	M0	M2B	EUA	EUA	N0	N0	S3	S0	LC0	LC0	MX0	MX2B	OXS0 OXD0	OXS0 OXD0
M(9)	OS0 OD0 OPUA CH0	OS0 OD1 OPUA CH1	M0	M2A	EUA	EUA	N0	N0	S2	S0	LC0	LC0	MX1	MX3	OXS0 OXD0	OXS0 OXD0
M(11)	OS0 OD0 OPUA CH1	OS0 OD0 OPUA CH0	M2A	M0	E0	E0	N0	N0	S3	S0	LC0	LC0	MX0	MX2B	OXS1 OXD0	OXS0 OXD0
M(14)	OS0 OD1 OPUA CH0	OS0 OD0 OPUA CH1	M0	M2A	EUA	EUA	N0	LB1	S3	S1	LC0	LC0	MX2B	MX0	OXS1 OXD0	OXS0 OXD0
F(9)	OS0 OD0 OPUA CH1	OS0 OD1 OPUA CH0	M3	M0	EUA	E0	N0	LB1	S0	S2	LC0	LC0	MX3	MX2A	OXS1 OXD0	OXS0 OXD0

Scoring as per sheet detailed in Chapter 2. OS/OXS; orbital size, OD/OXD; orbital displacement, OP; occlusional plane, CH; chin position.

Table 3.3: Comparison of facial deformity in Treacher Collins Syndrome and Craniofacial microsomia using modified OMENS classification.

	Treacher Collins Syndrome (n=14)				Craniofacial Microsomia (n=6)			
Craniofacial feature	Normal (n)	Abnormal (n)	Missing data (n)	Bilateral (n)	Normal (n)	Abnormal (n)	Missing data (n)	Bilateral (n)
Orbital size	11	3	0	0	6	0	0	0
Orbital displacement	4	10	0	1	3	3	0	0
Mandible	3	11	0	5	0	6	0	0
Ear	2	11	1	10	0	2	4	0
Nerve	9	5	0	0	4	2	0	0
Soft tissue	1	13	0	9	0	6	0	1
Lateral Cleft	0	0	0	0	0	0	0	0
Mandible (skeletal)	2	12	0	11	0	6	0	2
Orbital size (skeletal)	10	4	0	0	3	3	0	0
Orbital displacement (skeletal)	2	12	0	3	6	0	0	0

Summary of deformity classification in unoperated TCS and CM faces as detailed in Table 3.1 and Table 3.2.

.

3.2.2 Landmarks used for DSM building

In total 45 skeletal and 24 soft tissue landmarks were identified and used to annotate each skeletal and soft tissue surface respectively (Table 3.4,

Figure 3.4). These were then used to build separate skeletal, soft tissue and combined DSM**.**

3.2.3 Landmarking reliability

In order to evaluate the suitability of the landmarks and resultant models, reliability of the skeletal and soft tissue landmarks was assessed by determining precision of landmark annotation for skeletal and soft tissue surfaces from 5 different patients per group on 3 different landmarking attempts (Table 3.5, Table 3.6).

Reliability with regards to reproducibility of landmark placement was further analysed by categorising the proportion of landmarks, which had a mean precision of <1mm and comparing whether there was a significant difference between groups. For skeletal landmarks there were 18/25, 19/25 and 23/25 of the landmarks in the control, TCS and CM groups respectively had a mean precision <1mm (Table 3.5). The proportion of landmarks with mean precision <1mm in the soft tissue surfaces was 12/14 in the control group, 7/14 in TC faces and 7/14 for CM (Table 3.6).

Precision values for landmarks amongst test groups were compared using ANOVA with Tukey's post-hoc test. The precision for the glabella landmark was significantly different in TCS ($p=0.03$) and CM ($p=0.005$) faces compared with controls in skeletal surfaces. There was also a significant difference in precision for the inferior orbital fissure landmarks between TCS ($p=0.0004$) and CM ($p<0.0001$) compared with controls. Precision for the alare landmark differed between TCS ($p<0.0001$) as well as between CM ($p=0.032$) and controls with regards to the articular tubercle. In the soft tissue surfaces, precision was significantly different between the control and CM groups for the palpebrae superious ($p=0.047$). Precision of palpebrae inferious landmarking was significantly different between TCS and controls ($p=0.006$).

Table 3.4: Description of landmarks used to annotate midface surfaces.

	Skeletal landmark	Definition
Unpaired	1. Glabella	Midway between the supraorbital notches
	2. Nasion	Midpoint of frontonasal suture
	3. Rhinion	Most anterior-inferior point of nasal suture
	4. Anterior nasal spine	Apex of anterior nasal spine of maxilla
	5. Interdentale superius	Between the upper two incisors
Paired	6. Supraorbital foramen	Most concave point of supraorbital notch
	7. Supraorbital margin	Midpoint of the orbital rim
	8. Anterior frontozygomatic	Most anterior point of frontozygomatic suture
	9. Posterior frontozygomatic	Most posterior point of frontozygomatic suture
	10. Lateral frontonasal suture	Most lateral point of frontonasal suture
	11. Orbitale	Most inferior portion of lower orbital rim
	12. Maxillary process	Most superior part of zygomaticomaxillary suture
	13. Infraorbital foramen	Most concave point below infraorbital margin
	14. Ectoconchion	Point of maximum breadth on lateral wall of orbit
	15. Jugale	Junction of the temporal and frontal processes
	16. Infratemporal fossa	Midpoint of cavity deep to Zygommatic arch
	17. Zygomaxillare	Most inferior tip of zygomaticomaxillary suture
	18. Mastoidale	Lowest point on the contour of the mastoid process
	19. Canine fossa	Depression lateral to canine eminence
	20. Tuberosity of maxilla	Lowest part of the infratemporal surface of maxilla
	21. Zygion	Most lateral point on outline of Zygoma
	22. Inferior orbital fissure	Apex of sphenomaxillary suture
	23. Alare	Most lateral point of nasal aperture
	24. Articular tubercle	Inferior and proximal eminence of zygomatic process
	25. Postglenoid tubercle	Inferior distal projection of zygomatic process
	Soft tissue landmark	**Definition**
Unpaired	1. Glabella	Most prominent point of frontal bone in the midline
	2. Nasion*	Midline of frontonasal suture
	3. Pronasale	Most prominent point on nasal tip
	4. Subnasale	Midpoint of columella base
Paired	5. Palpebrae superius	Midpoint of superior aspect of palpebral fissure
	6. Frontotemporale*	Concavity above supraorbital rim
	7. Endocanthion	Most medial point of palpebral fissure
	8. Exocanthion	Most lateral point of palpebral fissure
	9. Palpebrae Inferius	Midpoint of inferior aspect of palpebral fissure
	10. Zygion*	Most lateral extents of zygoma
	11. Subaurale	Most inferior point of the free auricular margin
	12. Preaurale	Most anterior part of the ear
	13. Alare	Lateral extent of alar contour
	14. Lateral pronasale	Most distal point of alar groove

Landmarks were obtained by superimposing soft tissue surface onto skeletal.

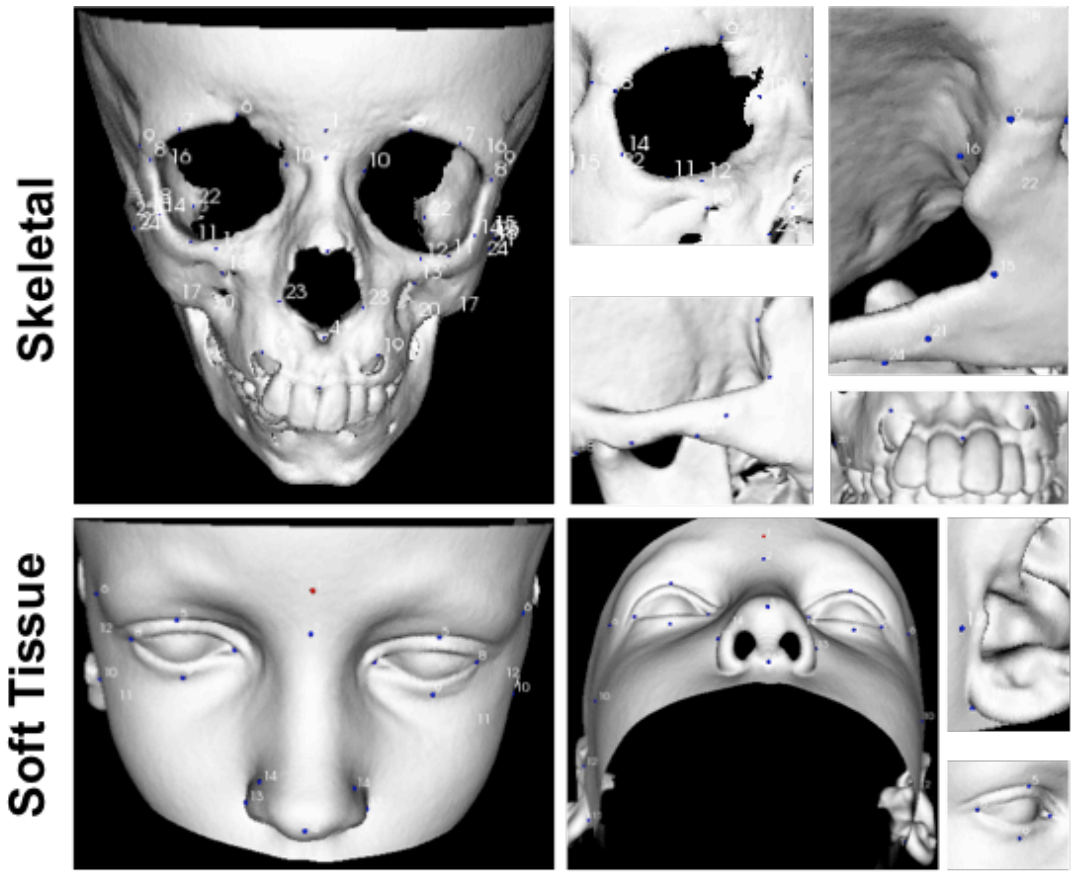

Figure 3.4: Skeletal and soft tissue 3D surfaces annotated with landmarks.

Landmarking of a control skeletal and soft tissue midface surface using points described in Table 3.4.

Table 3.5: Precision of skeletal tissue landmarks.

Landmark	Control	Treacher Collins Syndrome	Craniofacial microsomia
Glabella	1.46 ± 1.31	1.65 ± 1.28	0.66 ± 0.44*
Nasion	0.50 ± 0.42	0.59 ± 0.39	0.34 ± 0.20
Rhinion	0.66 ± 0.62	0.41 ± 0.34	0.80 ± 0.57
Anterior nasal spine	0.59 ± 0.42	0.43 ± 0.36	0.35 ± 0.25
Interdentale superious	0.31 ± 0.32	0.91 ± 1.22	0.67 ± 0.45
Supraorbital foramen	0.66 ± 0.61	0.83 ± 0.68	0.57 ± 0.58
Supraorbital margin	1.15 ± 0.95	1.03 ± 0.85	0.66 ± 0.67
Anterior frontozygomatic	0.70 ± 0.68	0.61 ± 0.51	0.75 ± 0.79
Posterior frontozygomatic	0.90 ± 0.80	0.89 ± 0.72	0.74 ± 0.92
Lateral frontonasal suture	0.52 ± 0.46	0.87 ± 0.87	0.76 ± 0.68
Orbitale	0.72 ± 0.85	0.88 ± 1.32	0.56 ± 0.71
Maxillary process	0.61 ± 0.55	0.31 ± 0.31	0.39 ± 0.46
Infraorbital foramen	0.69 ± 0.57	0.67 ± 0.57	0.46 ± 0.42
Ectochonchion	0.74 ± 0.63	0.68 ± 0.49	0.67 ± 0.78
Jugale	0.34 ± 0.35	0.75 ± 0.66	0.57 ± 0.52
Infratemporal fossa	1.15 ± 0.76	1.08 ± 0.92	1.11 ± 0.94
Zygomaxillare	0.97 ± 1.02	0.72 ± 0.77	0.65 ± 0.60
Mastoidale	1.13 ± 0.97	1.18 ± 1.12	1.42 ± 1.47
Canine fossa	1.04 ± 1.06	1.51 v1.56	0.85 ± 0.92
Tuberosity of maxilla	0.71 ± 0.45	0.84 ± 0.60	0.90 ± 0.70
Zygion	0.62 ± 0.52	0.62 ± 0.68	0.74 ± 0.66
Inferior orbital fissure	1.63 ± 3.22	0.74 ± 0.78***	0.45 ± 0.34****
Alare	0.58 ± 0.39	1.72 ± 1.55****	0.96 ± 0.72
Articular tubercle	1.09 ± 1.24	0.85 ± 0.85	0.53 ± 0.64*
Postglenoid tubercle	0.85 ± 0.88	0.60 ± 0.68	0.82 ± 0.90

Landmark precision expressed as mean and standard deviation on 3 attempts per patient (n=5 different patients per group). *p<0.05, ***p<0.001, ***p<0.0001.

Table 3.6: Precision of soft tissue landmarks.

Landmark	Control	Treacher Collins Syndrome	Craniofacial microsomia
Glabella	0.49 ± 0.49	1.03 ± 0.48	1.01 ± 0.61
Nasion	0.71 ± 0.50	0.61 ± 0.54	0.99 ± 0.72
Pronasale	0.22 ± 0.12	0.42 ± 0.43	0.46 ± 0.43
Subnasale	0.22 ± 0.14	0.74 ± 0.43	0.87 ± 0.75
Palpebrae superious	0.54 ± 0.55	0.82 ± 0.8	1.19 ± 1.02*
Frontotemporale	1.54 ± 1.62	1.28 ± 1.01	1.58 ± 1.23
Endocanthion	0.47 ± 0.56	0.52 ± 0.47	0.48 ± 0.45
Exocanthion	0.75 ± 0.85	1.26 ± 1.09	0.66 ± 0.60
Palpebrae inferious	0.53 ± 0.50	1.38 ± 1.07**	0.69 ± 0.70
Zygion	2.13 ± 2.08	1.91 ± 2.06	2.01 ± 3.01
Subaurale	0.73 ± 0.84	0.99 ± 0.91	1.14 ± 1.29
Preaurale	0.90 ± 0.79	1.03 ± 1.22	1.02 ± 1.00
Alare	0.74 ± 0.53	1.03 ± 1.28	0.83 ± 0.67
Lateral pronasale	0.76 ± 0.83	0.83 ± 0.45	1.06 ± 0.82

Landmark precision expressed as mean and standard deviation on 3 attempts per patient (n=5 different patients per group). *p<0.05, **p<0.01.

3.2.4 Combined modeling reveals close alignment between skeletal and soft tissue morphology

3.2.4.1 The first Principal Component (PC1)

The first Principle Component was responsible for 53%, 56% and 52% of variation in the skeletal, soft tissue and combined models respectively. When plotted against age, PC1 corresponds to overall midface growth (length and width) **(**Figure 3.5**,** Appendix I, Video 1).

In the skeletal model, the PC1-age regression line has a significantly non-zero slope in controls (slope=0.1857 ± 0.01079; $p<0.0001$) and TCS (slope=0.1781 ± 0.04054; $p=0.0009$) indicating a linear relationship between age and PC1. The difference in slopes is not significant ($p=0.7999$) suggesting similar rates of growth for both groups whilst difference in the intercepts ($p<0.0001$) reflects reduced midface size in TCS. The PC1-age regression line also has a significantly non zero slope for CM (slope= 0.1676 ± 0.01930; $p=0.001$) but when compared with controls does not have a significantly different slope ($p=0.7783$) or intercept ($p=0.4819$) implying similar rates of growth and sizes of the midfaces of CM and controls.

In the soft tissue model, there is also a linear relationship between age and PC1 (slope=0.1917 ± 0.01027; $p< 0.0001$) in controls and TCS (slope=0.1357 ± 0.05402; $p=0.0273$) with a difference in slopes ($p<0.0001$) of the two groups but not intercepts ($p=0.1033$). This is also demonstrated by the CM dataset whereby there is a significantly non-zero slope (slope= 0.2583 ± 0.04361; $p=0.0041$) but there is no significant difference in the slopes ($p=0.2859$) or intercepts ($p=0.9223$) when compared with controls.

The combined model echoes the findings of the individual skeletal and soft tissue DSM. PC1 is also related to age in controls (slope= 0.1917 ± 0.009300; $p<0.0001$) and TCS (slope= 0.1650 ± 0.04608; $p=0.0038$) with lack of difference in the slopes ($p=0.3693$) and significant difference in intercepts ($p<0.0001$). This is also the case for the CM patients (slope= 0.2220 ± 0.01468; $p=0.0001$). There is however, no difference in slopes ($p=0.584$) or intercepts ($p=0.6385$) when compared with controls.

Overall, these results reveal correlation between all 3 DSM and that PC1 relates to age in control, TCS and CM children. Whilst rate of growth is the same, it is likely that children with TCS have smaller faces compared with controls.

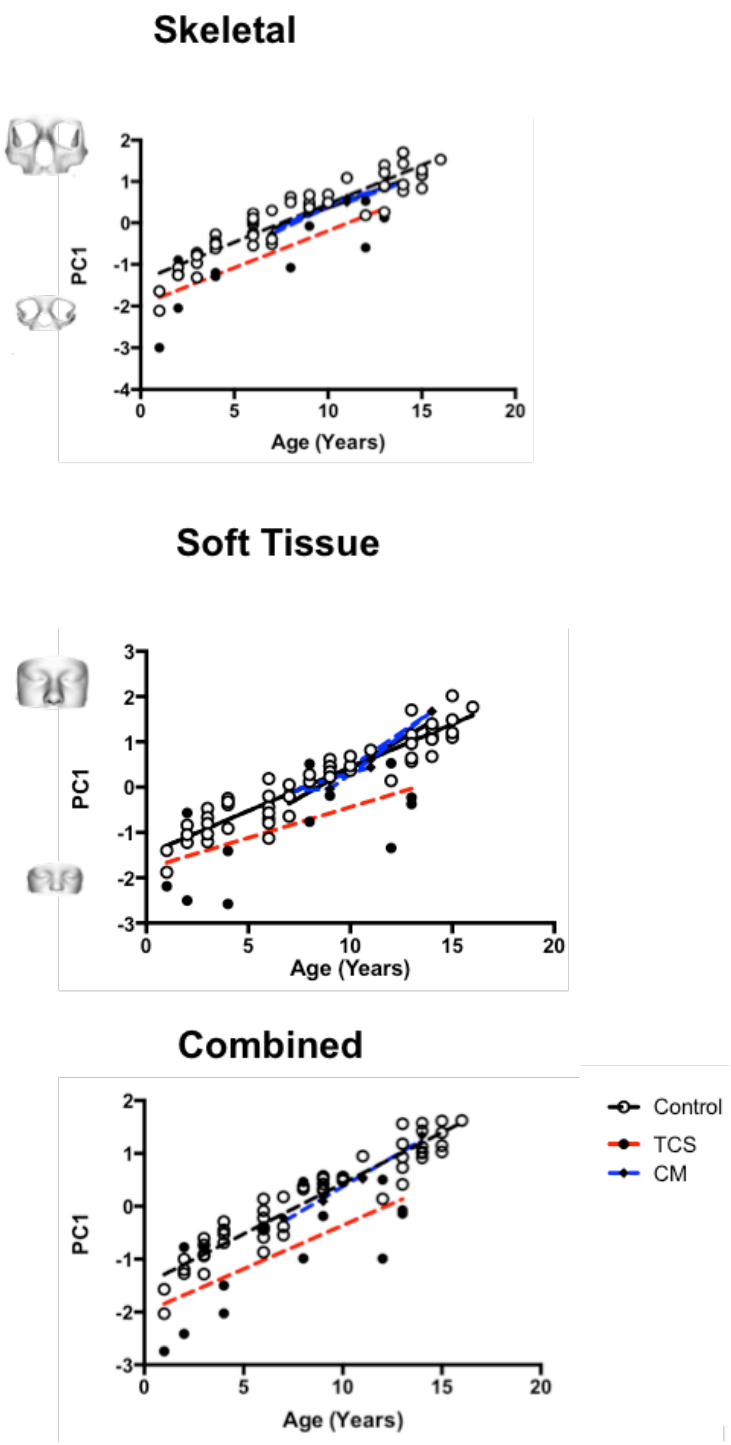

Figure 3.5: Midface growth with respect to the first Principal Component (PC1).

There is a significant relationship between age and PC1 in controls, TCS and CM in the skeletal, soft tissue and combined DSM ($p<0.01$). Growth is reduced in TCS on skeletal ($p<0.0001$), soft tissue ($p=0.0003$) and combined ($p<0.0001$) DSM. In contrast, there is no difference between CM and controls with regards to PC1 in the skeletal ($p=0.7783$), soft tissue ($p=0.2859$) or combined ($p=0.584$) DSM.

3.2.4.2 The second Principal Component (PC2)

The second Principle Component mainly relates to midface width and depth (Figure 3.6, Appendix I, Video 2) and accounts for 11%, 11% and 10% of variation in the skeletal, soft tissue and combined models respectively.

In the skeletal model, the linear regression line for controls has a significantly non-zero slope (slope=-0.05998 ± 0.01143, $p<0.0001$) indicating a direct relationship between age and PC2 which is not the case for TCS (slope=-0.03227 ± 0.08364, $p=0.7064$) or CM (slope=-0.03045 ± 0.02869; $p=0.3484$). Controls and TCS do not show significant difference in regression line slope ($p=0.5591$) but do so for intercept ($p<0.0001$) likely due to the narrower and shallower midface in TCS. There is no difference in the slopes ($p=0.6656$) and intercepts ($p=0.4155$) between controls and CM suggesting similar sizes and rates of growth of the skulls of both groups.

The soft tissue DSM reveals a significant relationship between age and PC2 for controls (slope=-0.06855 ± 0.01825; $p=0.0005$) but not for TCS (slope=-0.1194 ± 0.05613; $p=0.0548$) or CM (slope=-0.03526 ± 0.3290; $p=0.9198$). Comparison of controls with TCS midfaces reveals similar slopes ($p=0.2784$) but different intercepts ($p<0.0001$). In CM there is no significant difference in slopes ($p=0.8141$) or intercepts ($p=0.7561$) compared with controls.

The combined DSM is consistent with the skeletal and soft tissue models demonstrating a linear relationship between age and PC2 in controls (slope-0.07041 ± 0.01383; $p< 0.0001$) but not TCS (slope-0.08226 ± 0.07500; $p=0.2942$) without significant difference between TCS and control slopes ($p=0.7993$) and significant difference in intercepts ($p<0.0001$). Again, the data from the CM cases mirrors that in the individual models whereby there is no significant relationship between PC2 and age (slope=-0.04897 ± 0.1412; p=07462) and no significant difference in the slopes ($p=0.8136$) or intercepts ($p=0.6817$) of the linear regression line as compared to controls.

The findings of the three DSM suggest that PC2 is related to age in controls but not TCS or CM affected midfaces. There is no difference in rate of growth between controls and dysmorphic children but there a difference in the size and

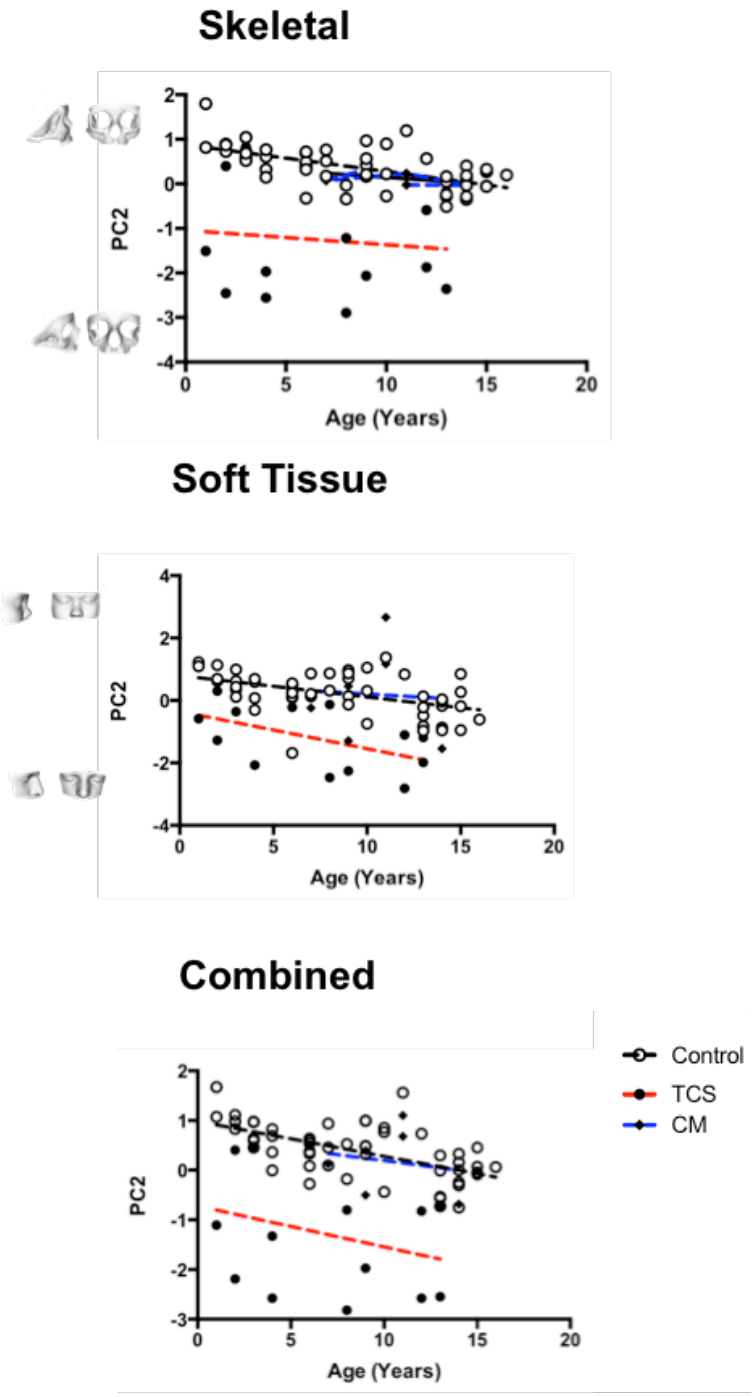

Figure 3.6: Midface growth with respect to the second Principal Component (PC2).

There is a relationship between age and PC2 in the control group in skeletal ($p<0.0001$), soft tissue ($p=0.0005$) and combined ($p<0.0001$) models. Width and depth as described by PC2 are reduced in TCS on skeletal ($p<0.0001$), soft tissue ($p<0.0001$) and combined ($p<0.0001$) DSM. In contrast, there is no difference between CM and controls with regards to PC2 in the skeletal ($p=0.4155$), soft tissue ($p=0.7561$) or combined ($p=0.6817$) DSM.

shape of midfaces (as evidenced by PC2) in TCS but not in CM when compared with controls.

3.2.4.3 Bivariate analysis of the first two Principal Components

To analyse the relationship between skeletal and soft tissue postnatal development, bivariate analysis was performed using PC1 and PC2 values for control, TCS and CM subjects (Figure 3.7). Bivariate analysis of the first two PCs supports the relationship described by the DSM between skeletal and soft tissue growth and morphology (Figure 3.5, Figure 3.6).

There is a significantly non-zero slope between the skeletal and soft tissue PC1 values for controls (slope=0.9575 ± 0.05015; $p<0.0001$) and TCS (slope=0.8652 ± 0.1555; $p=0.0001$) but not CM (slope=-0.6978 ± 0.7118; $p=0.3824$). Although the slopes between controls and CM differ significantly ($p=0.0001$), there is no significant difference between the slopes ($p=0.4156$) and intercepts ($p=0.2663$) of the control and TCS groups.

Bivariate analysis of the skeletal and soft tissue PC2 values similarly illustrates significantly non-zero slopes in control (slope=0.8054 ± 0.1709; $p<0.0001$) and TCS (slope=0.5445 ± 0.1623; $p=0.0057$) groups. Again, this is not the case with CM (slope=-6.169 ± 4.026; $p=0.2002$). Furthermore, neither the slopes ($p=0.2507$) nor intercepts ($p=0.1587$) show difference between controls and TCS whilst there is significant difference between the slopes of the control and CM datasets ($p=0.0006$).

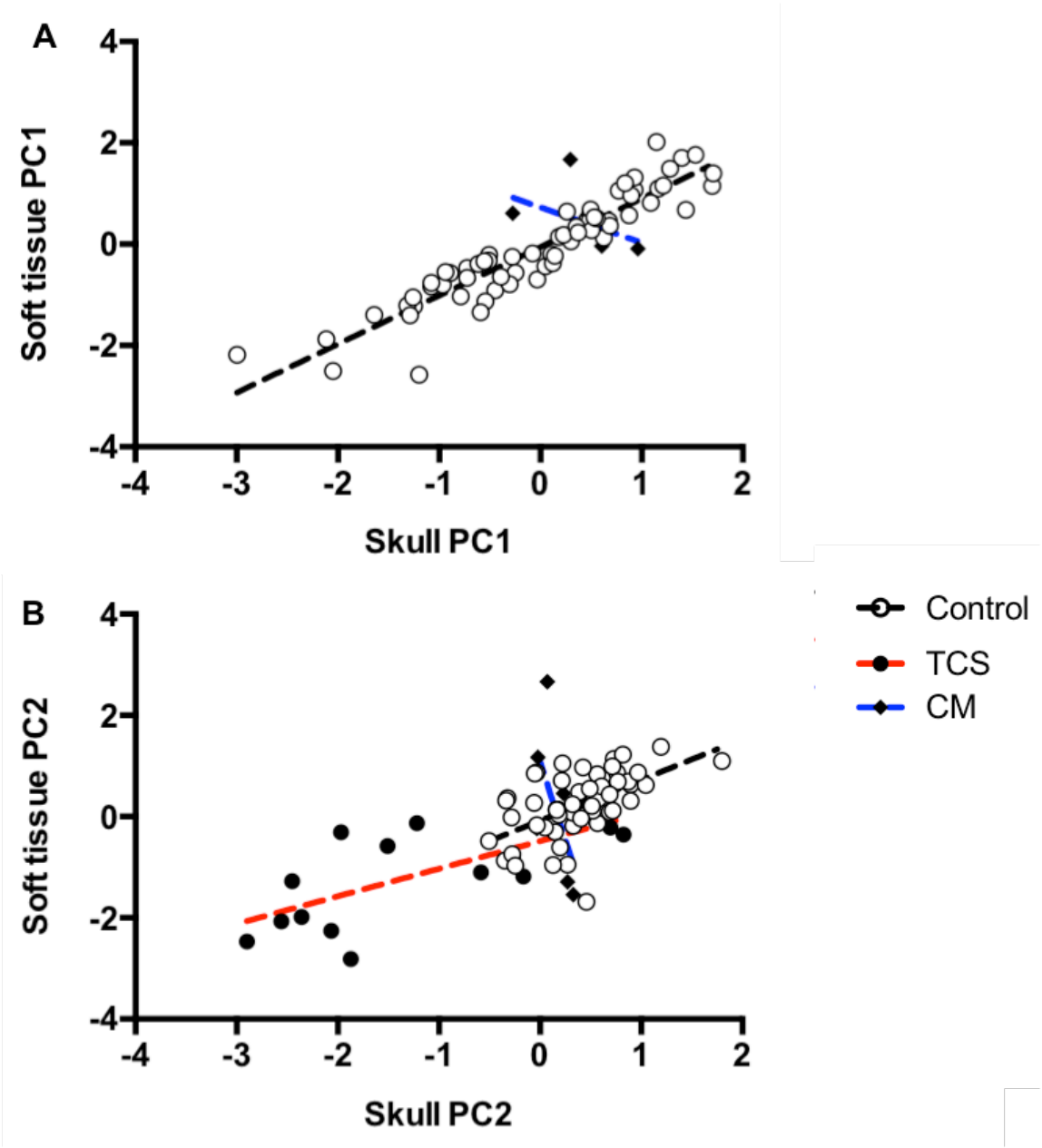

Figure 3.7: Bivariate analysis of the first two Principal Components.

This analysis supports the relationship between skeletal and soft tissue growth and morphology shown by the DSM. **A)** Plotting skeletal against soft tissue PC1 reveals a significantly non-zero slope in controls (slope=0.9575 ± 0.05015; p<0.0001), TCS (slope=0.8652 ± 0.1555; p=0.0001) but not CM (slope=-0.6978 ± 0.7118; p=0.3824). There is no significant difference between the slopes (p=0.4156) and intercepts (p=0.2663) of the control and TCS groups whilst the slopes between controls and CM differ significantly (p=0.0001). **B)** With regards to PC2, bivariate analysis demonstrates significantly non-zero slopes in control (slope=0.8054 ± 0.1709; p<0.0001), TCS (slope=0.5445 ± 0.1623; p=0.0057) but not CM (slope=-6.169 ± 4.026; p=0.2002). Neither the slopes (p=0.2507) nor intercepts (p=0.1587) show difference between controls and CM. Comparison of the slopes of control and CM patients reveals significant difference (p=0.0006).

3.2.4.4 Analysis of the first three Principal Components (PCs)

PC3 mainly describes midface width and length (Appendix I, Video 3) and represents 4%, 8% and 6% of all variation in the skeletal, soft tissue and combined models. Together, the first three PCs account for 68%, 75% and 68% of all shape variation in the skeletal, soft tissue and combined models.

A 3-D scatter plot (Figure 3.8) of PC1-3 shows largely separate clustering of controls and TCS individuals. There are 6 CM and 5 TCS individuals who are located within or close to the control data set. This reiterates the differences seen in the linear regression analysis and bivariate analysis whereby there was generally a difference between controls and TCS but not CM (Figure 3.5, Figure 3.6, Figure 3.7). The variation in distribution of TCS individuals likely represents the phenotypic heterogeneity found in the disease. The appearance of the scatter plots of all three DSM are similar suggesting that skeletal and soft tissues midface morphology is closely aligned with respect to PC1-3.

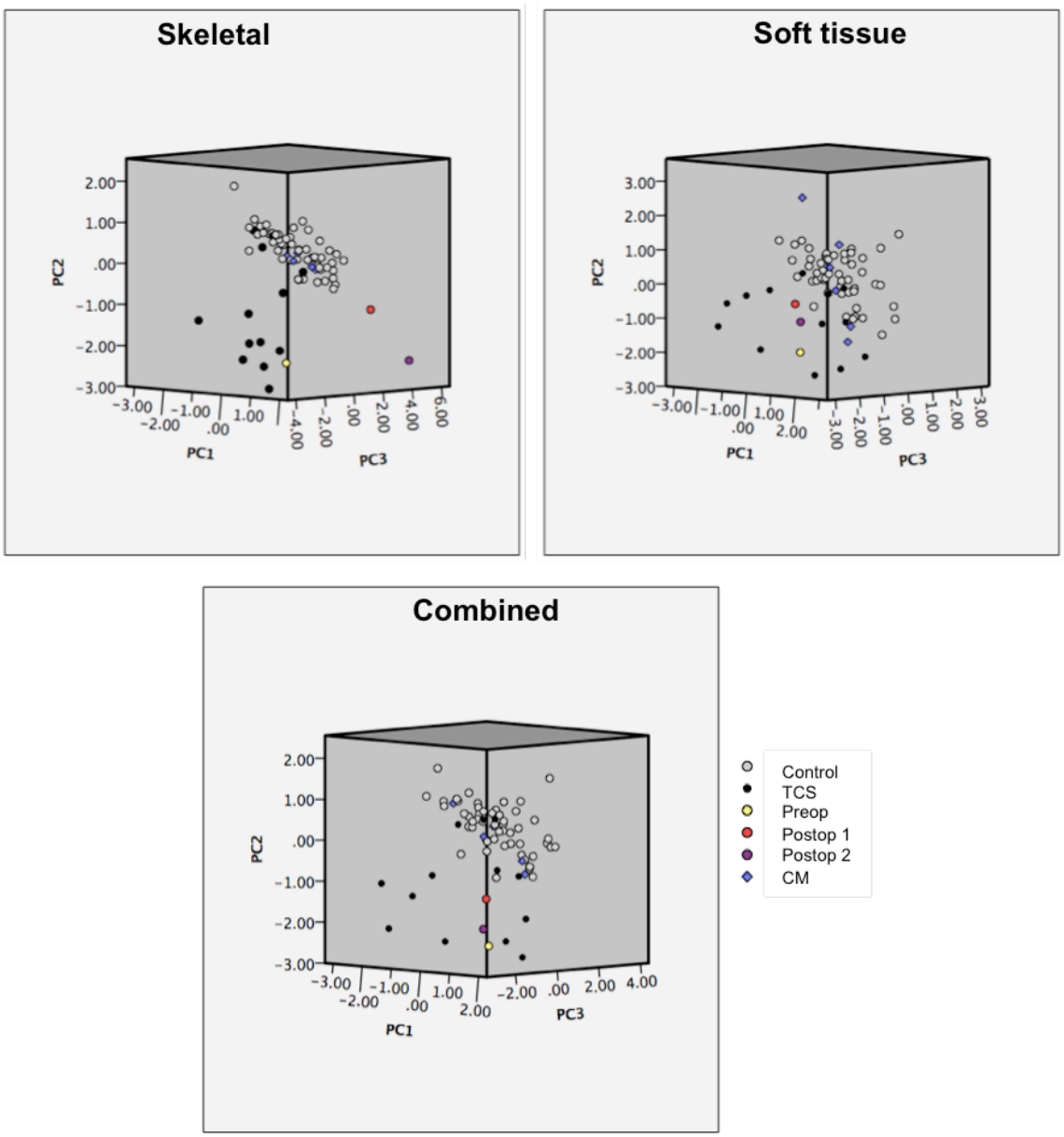

Figure 3.8: Comparison of Control, TCS and CM midfaces using the first 3 Principle Components.

There is separate clustering of TCS individuals (black dot) compared with control groups (grey dot) whilst the CM (blue diamond) dataset is largely distributed amongst the control set. The preoperative TCS (preop; yellow dot) patient (initially located amongst TCS group) moves closer to the controls postoperatively (red dot; Postop 1) but regresses to the TCS cluster 1 year postoperatively (purple dot; Postop 2).

3.2.5 Heat map representation of midface shape differences

3.2.5.1 Representation of the midface in Treacher Collins Syndrome

Heat maps were used to compare a 4 year old with TCS to age-sex-ethnicity-matched controls (n=20) and visually represent the differences described by the DSM (Figure 3.9 A). In the surface normal comparison, the zygomatic and temporal bone regions in the skeletal model and corresponding soft tissue areas (malar and bitemporal) demonstrate malar hypoplasia and bitemporal narrowing (red in Figure 3.9 A) whilst frontal and nasal regions in both models illustrate prominence of the nose (blue in Figure 3.9 A) and relatively (compared with malar region) enlarged forehead which are characteristic of TCS (Kolar et al., 1985). In the lateral (X-axis) and vertical (Y-axis) comparisons there is midface narrowing and shortening respectively (red in Figure 3.9 A). Along the depth (Z-axis), the fronto-nasal region shows reduction in depth (red in Figure 3.9 A). As a whole, this individual exhibits midfacial, orbital and zygomatic hypoplasia that is typical of TCS dysmorphism (Kolar et al., 1987, Kolar et al., 1985). The average TCS midface was generated using the means of the PC values for all of the TCS models (n=14) and compared with age-sex-ethnicity-matched controls (n=20) to generate a heat map (Figure 3.9 B). The corresponding soft tissue areas reflect malar hypoplasia in the surface comparison (red-yellow in Figure 3.9 B). Enlargement of the fronto-nasal area in the skeletal model corresponds with the relative enlargement of the forehead and prominent nose (blue in Figure 3.9 B) in the soft tissue heat map. Along the X-axis, there is zygomatic narrowing in the skeletal model whilst both skeletal and soft tissue models reveal shortening (red in Figure 3.9 B) along the Y-axis.

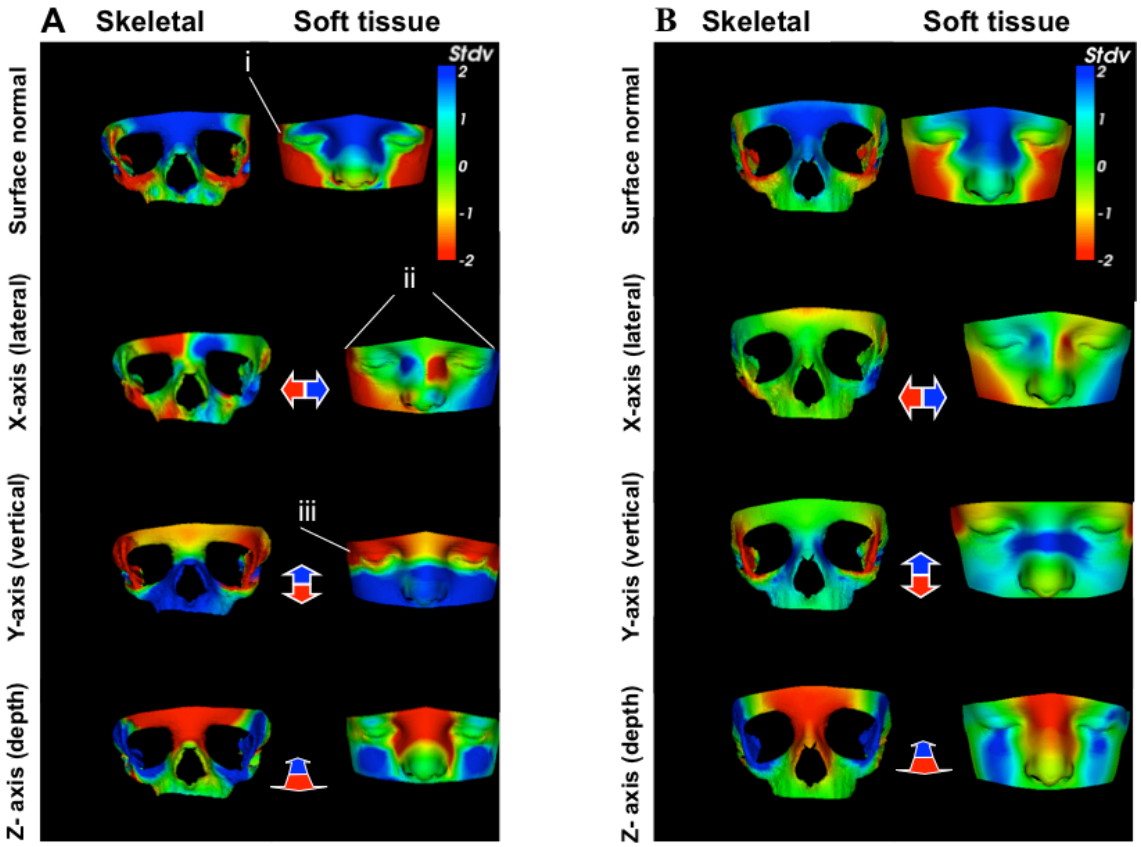

Figure 3.9: Heat maps of skeletal and soft tissue Treacher Collins Syndrome midfaces.

A) Dysmorphology in a 4-year old with TCS compared with age-sex-ethnicity-matched controls (n=20) reveals zygomatic and malar hypoplasia (red-yellow), bitemporal narrowing (red on surface normal (i); red-blue on lateral (ii)) and down-slanting palpebral fissures (red on vertical (iii)). **B)** The average TCS midface (n=14) exhibits narrowing and shortening of the zygoma (X and Y-axes) and reduction in fronto-nasal depth (Z-axis). Surface normal shows malar and zygomatic hypoplasia (yellow-red), increased inter-orbital distance (blue) and nasal bridge prominence (blue) when compared age-sex-ethnicity-matched controls (n=20). Heat maps demonstrate difference between TCS and controls on surface normal comparison and along the X, Y and Z-axes. Red-green-blue scale indicates a contraction-coincidence-expansion of 2 standard deviations (Stdv) from the mean in the surface-normal comparison.

3.2.5.2 Representation of the midface in Craniofacial microsomia

A 9-year old female with CM was compared with age-sex-matched controls (n=30) through virtual normalisation (Figure 3.10 A). Red patches on the malar and orbital region demonstrate bitemporal and malar hypoplasia, which is predominantly on the right side of the midface in both the skeletal and soft tissue models along the surface normal comparison. She also exhibits shortening and reduced nasal projection as evidenced by red-yellow patches on the vertical and depth axes. The left side demonstrates increased malar and zygomatic depth as compared with the right along the Z-axis, which is demonstrated by blue patches.

The average CM midface was also generated using the means of the PC values for all of the CM models (n=6) and compared with age-sex-ethnicity-matched controls (n=30) to generate a heat map (Figure 3.10 B). There is overall a similar face size between both groups as shown by predominance of green on the skeletal and soft tissue surfaces. Unilateral zygomatic hypoplasia (yellow patches) on the right side on the skeletal model contrasts with relative malar hypertrophy (blue) on the left side of the soft tissue DSM along the surface normal comparison. Shortening of the malar and zygomatic regions is delineated by yellow/red patches on the left side of the midface along the Y-axis on both models. There is also reduction in midface depth (yellow on the fronto-orbital and maxillary regions) on the soft tissue DSM along the Z-axis.

The difference in midface heat maps is not as stark between CM and control cases as when TCS midfaces are compared with controls. There are however fewer CM cases (n=6) than TCS (n=14).

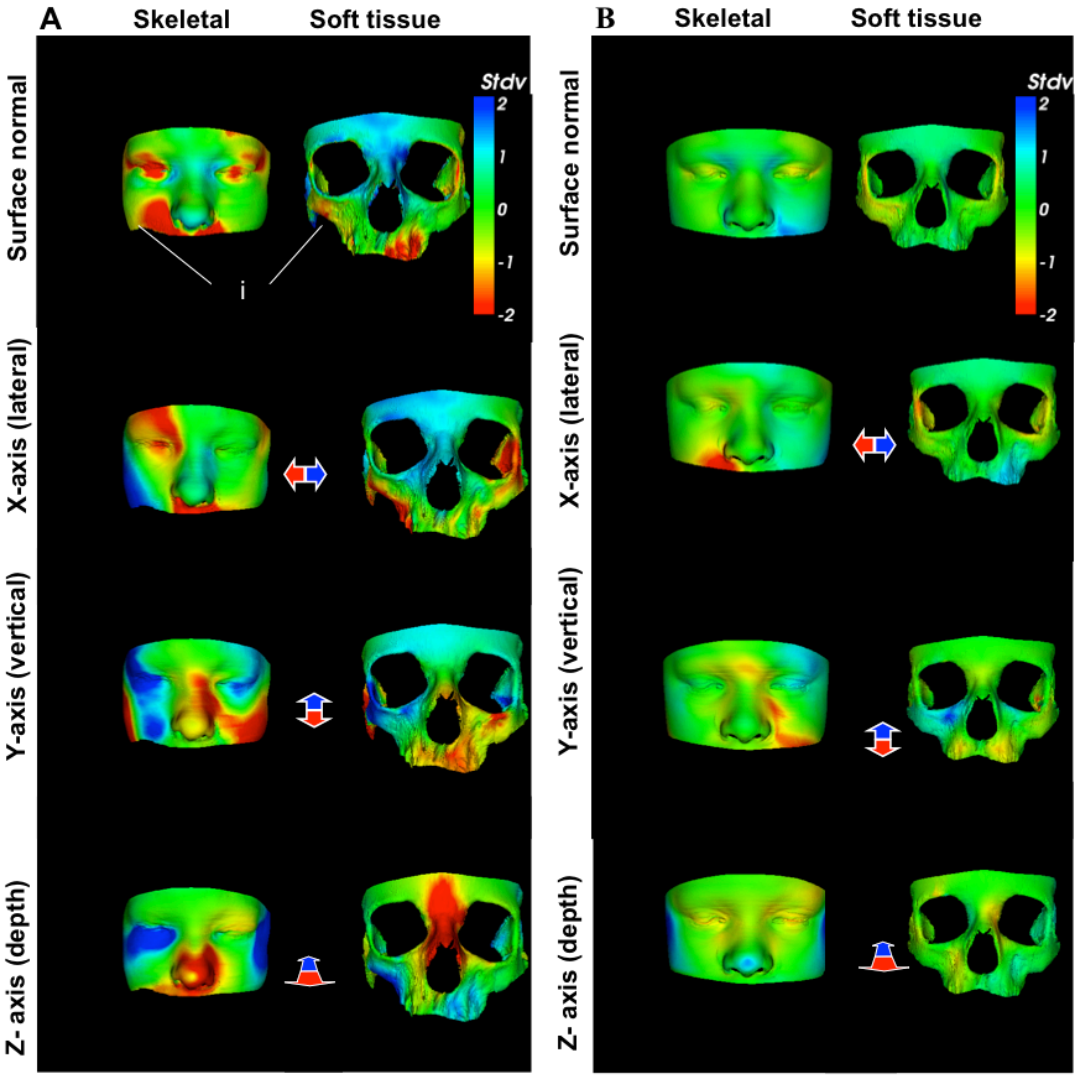

Figure 3.10: Heat maps of the Craniofacial Microsomia midface.

A) Comparison of a 9-year old female with CM with age-sex-matched controls (n=30) reveals bitemporal and malar hypoplasia on the right side along the surface normal comparison (i). There is also shortening and reduced nasal projection on the vertical and depth axes. The left side demonstrates increased malar and zygomatic depth along the Z-axis. **B)** The average CM midface (n=6) compared with age-sex-matched controls (n=30) exhibits an overall similar face size. There is some zygomatic hypoplasia on the right side on the skeletal model with contrasting malar hypertrophy on the left side of the soft tissue DSM along the surface normal comparison. Shortening of the malar and zygomatic regions is demonstrated along the Y-axis.

Heat maps demonstrate difference between TCS and controls on surface normal comparison and along the X, Y and Z-axes. Red-green-blue scale indicates a contraction-coincidence-expansion of 2 standard deviations (Stdv) from the mean in the surface-normal comparison.

3.2.6 Cephalometric analysis of midface soft and skeletal tissue surfaces

To validate these models, analysis of cephalometric measurements of midface size (width, length and depth) (Table 3.7) was undertaken. These were derived from calculating the Euclidean distance between set landmarks using Facemark as described in the methods section.

Analysis demonstrates reduction in width in unoperated TCS midfaces compared with controls in both skeletal ($p=0.0033$) and soft tissue surfaces ($p=0.0009$). Midface depth is also significantly reduced in TCS in both skeletal and soft tissue ($p<0.0001$) measurements whilst there is no significant difference in length in both the skeletal ($p=0.167$) and soft tissue ($p=0.262$) surfaces (Table 3.7). This corresponds with the findings of the heat maps of the average and individual TCS midface (Figure 3.9).

In CM, there is no significant difference between the width of the midface in the skeletal ($p=0.931$) and soft tissue ($p=0.852$) surfaces when compared with the control group (Table 3.7). The same is true for the differences midface length between control and CM patients in the skeletal and soft tissue surfaces ($p=0.718$). This is also the case for CM midface depth in the skeletal ($p=0.089$) and soft tissue ($p=0.202$) surfaces when compared with unaffected children. Again, this is similar to the findings of the heat maps (Figure 3.10).

Table 3.7: Differences in Euclidean distances from cephalometric measurements of control, Treacher Collins Syndrome (TCS) and Craniofacial Microsomia (CM) midface 3D reconstructed surfaces.

	Skeletal			Soft tissue		
Measurements (corresponding landmarks)	Controls (n=52)	TCS (n=14)	CM (n=6)	Controls (n=52)	TCS (n=14)	CM (n=6)
Midface width (zy-zy)	106.8 ± 1.279	90.55 ± 4.475*	106.9 ± 2.336	125.0 ± 2.828	102.1 ± 5.194*	124.9 ± 4.957
Midface length (Soft tissue: gl-sn; Skeletal: gl-ans)	51.83 ± 0.9531	48.46 ± 2.116	53.44 ± 2.137	58.08 ± 1.199	54.75 ± 2.682	59.61 ± 2.937
Midface depth† (Soft tissue: sn-p; Skeletal: ans-m)	91.24 ± 1.018	81.09 ± 1.939*	96.33 ± 1.360	109.3 ± 1.176	92.13 ± 2.056*	120.1 ± 7.734

†For depth both left and right-sided measurements were analysed. The landmarks are as defined in Table 1 (**ans**: anterior nasal spine, **gl**: glabella, **m**: mastoidale, **na**: nasion, **p**: preaurale, **sn**: subnasale, **zy**: zygion). Values shown are means ± SEM. * statistically significant.

3.2.7 Comparison of midface asymmetry

The difference of the PCA representations of original and reflected forms was used to visualize and measure asymmetry of the midface in each individual as represented by the Asymmetry Index (AI) (Figure 3.11). Linear regression analysis shows a relationship between the asymmetry index (AI) and age in controls as demonstrated by a significantly non-zero line in the skeletal (slope= 4.098 ± 0.9957; p=0.0001) and soft tissue (slope= 1.988 ± 0.8961; p=0.0311) DSM. This is also the case for TCS in the soft tissue (slope= 5.767 ± 2.021; p=0.0145) but not skeletal (slope= 6.710 ± 4.949; p=0.2001) DSM. The AI CM dataset does not demonstrate any correlation with age in neither the skeletal (slope= 11.88 ± 11.99; p=0.3779) nor the soft tissue (slope= 1.145 ± 13.37; p=0.9359) DSM.

Comparison of the linear regression lines between controls and TCS shows no difference in slopes (p=0.4132) but significant difference in intercepts (p<0.0001) in the skeletal model. This is also the case for the soft tissue model whereby the slopes are not significantly different (p=0.0756) whilst the intercepts are (p<0.0001). Comparison of the lines of the controls with the CM dataset does reveal a significant difference between the intercepts (p=0.0254) but not the slopes (p=0.2538) in the skeletal model. The soft tissue model also does not describe any significant difference in the slopes of the lines of control and CM data (p=0.8965) but there is a difference in intercepts (p<0.0001).

The mean asymmetry index of controls (skeletal=133.7 ± 5.143, Soft tissue=86.95 ± 4.19) was compared with that of TCS (skeletal=212.3 ± 21.53, soft tissue=127.4 ± 10.61) and demonstrated significant differences in both skeletal (p=0.0031) and soft tissue (p=0.0024) models (Table 3.8). There was however, no significant difference in mean AI between controls and CM in the skeletal (176.8 ± 26.24; p=0.076) model. With regards to soft tissue, there was a difference in mean AI between CM and controls (152.0 ± 26.25; p=0.0053).

Bootstrap confidence intervals for these comparisons did not show any possible correlation within the intervals for TCS and controls (Table 3.9).

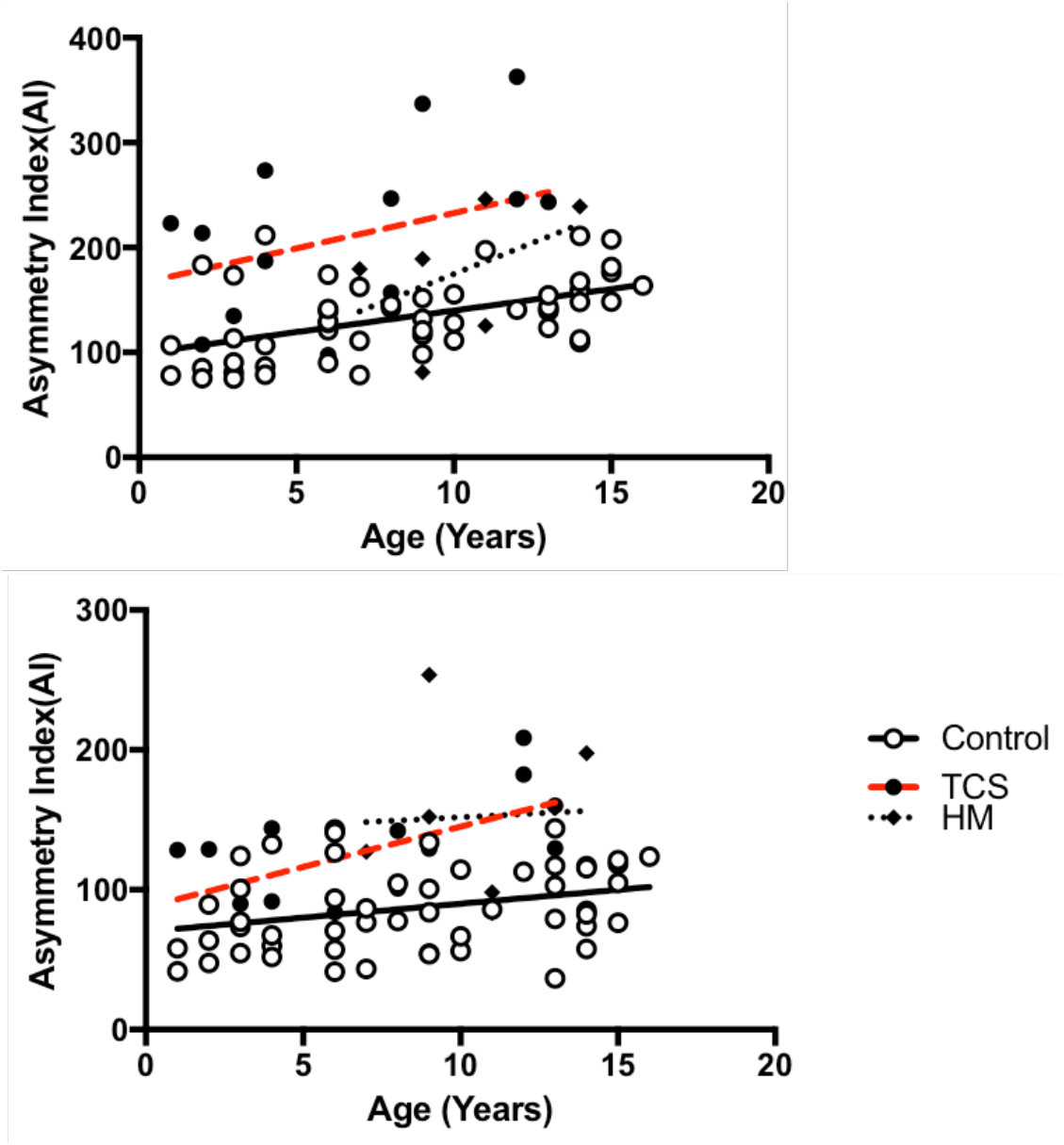

Figure 3.11: Comparison of midface asymmetry between controls, Treacher Collins Syndrome (TCS) and Craniofacial Microsomia (CM) using linear regression analysis of the Asymmetry index (AI).

There is increased AI in TCS ($p<0.0001$) skeletal and soft tissues ($p<0.0001$). AI is increased in CM soft tissue models ($p<0.0001$) but not skeletal ($p=0.0254$). AI is related to age in both skeletal and soft tissue models in control subjects ($p<0.05$).

Table 3.8: Comparison of the mean asymmetry index (AI) of the control, Treacher Collins Syndrome (TCS) and Craniofacial Microsomia (CM) groups in the skeletal and soft tissue models.

	Skeletal			Soft tissue		
	Controls (n=52)	TCS (n=14)	CM (n=6)	Controls (n=52)	TCS (n=14)	CM (n=6)
Mean AI ± SEM	133.7 ± 5.14	212.3 ± 21.53*	176.8 ± 26.24	86.95 ± 4.19	127.4 ± 10.61*	152.0 ± 26.25*
Lower 95% CI ± STD	119.67 ± 18.01	173.76 ± 52.07	128.66 ± 25.73	87.43 ± 28.20	86.8 ± 32.18	87.04 ± 32.68
Upper 95% CI ± STD	154.81 ± 45.29	252.75 ± 100.15	223.63 ± 80.34	116.09 ± 27.04	137.14 ± 42.46	186.25 ± 55.11

SEM: Standard Error of the Mean; CI: Confidence Interval; STD: Standard deviation. * Statistically significant.

Table 3.9: Bootstrap analysis of the mean asymmetry index (AI) of the control, Treacher Collins Syndrome and Craniofacial Microsomia (CM) groups in the skeletal and soft tissue models.

	Skeletal			Soft tissue		
	Controls (n=52)	TCS (n=14)	CM (n=6)	Controls (n=52)	TCS (n=14)	CM (n=6)
Mean AI ± SEM	133.7 ± 5.16	212.25 ± 20.14	176.75 ± 24.03	86.95 ± 4.02	127.40 ± 9.89	152.0 ± 23.57
Bias ± STD	-0.23 ± -0.55	-0.16 ± -3.52	0.33 ± -8.14	0.25 ± -0.34	-0.24 ± -1.93	-1.56 ± -8.12
BCa 95% LCI ± STD	124.18 ± 31.55	173.50 ± 58.28	132.44 ± 44.09	78.62 ± 26.69	110.32 ± 27.94	105.27 ± 37.56
BCa 95% UCI ± STD	142.24 ± 41.49	252.94 ± 94.14	216.54 ± 68.70	95.17 ± 33.16	145.86 ± 46.72	201.16 ± 73.43

SEM: Standard Error of the Mean; Bca: Bias-corrected and accelerated; LCI: Lower Confidence Interval; UCI: Upper Confidence Interval; STD: standard deviation.

3.2.8 Comparison of preoperative, immediate postoperative and one year postoperative TCS

Heat maps of a male individual with Treacher Collins syndrome reveal zygomatic hypoplasia preoperatively with corresponding loss of soft tissue volume in the malar region (red in Figure 3.12 A) compared with age-sex-ethnicity-matched controls (n=20). This patient underwent reconstruction with bone grafts and immediate results show improvement in the skeletal and soft tissue hypoplasia (blue-green in Figure 3.12 B). A year later, the zygomatic bones appear hyperplastic (blue in Figure 3.12 C) but the overlying soft tissue appears hypoplastic (red in Figure 3.12 C).

This reversion of midface morphology is also reflected in the 3D scatterplots of PC1-3 (Figure 3.8). The preoperative TCS individual is initially located amongst the TCS cluster of patients in all 3 scatterplots. Immediately postoperatively, this individual moves closer to the normal dataset within the plot but one year later, he regresses towards the TCS cluster.

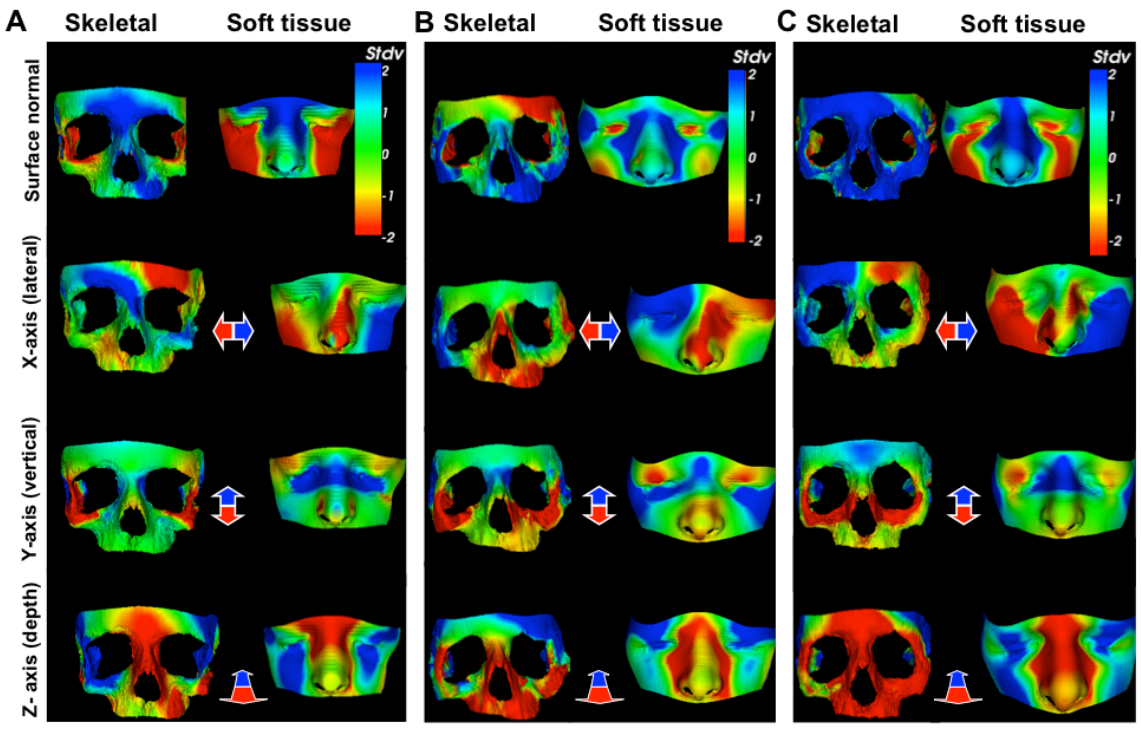

Figure 3.12: Evaluating postoperative outcomes in a 13-year-old male child with Treacher Collins Syndrome (TCS).

A) Preoperatively there is zygomatic (skeletal), malar, orbital and bitemporal (soft tissue) hypoplasia. **B)** Dysmorphology reduces after surgery. **C)** One year postoperatively there is soft tissue malar and bitemporal hypoplasia compared with (B) but improved overall compared with preop (A). Controls (n=20).

Heat maps demonstrate difference between TCS and controls on surface normal comparison and along the X, Y and Z-axes. Red-green-blue scale indicates a contraction-coincidence-expansion of 2 standard deviations (Stdv) from the mean in the surface-normal comparison.

3.2.9 Simulation of zygomatic reconstruction in Treacher Collins Syndrome

The average skeletal and soft tissue midface of unoperated TCS (n=14) and age-matched controls (n=10) was generated using the mean PC values. Superimposing the average matched control skull or soft tissue midface onto the average TCS midface revealed which regions were deficient when compared with age-matched controls (Figure 3.13 A i). Most obviously affected was the zygomatic complex (zygoma and zygomatic process of the temporal bone) (Figure 3.13 A ii). Trimming of the control midface allowed prediction of the shape and size of the Zygomatic complex which would be needed to normalize the average TCS skull to the average control (Figure 3.13 A iii). The same methods were used to extract an age-matched control midface (n=10) for the preoperative TCS individual previously analysed in Figure 3.12 (Figure 3.13 B). Superimposition of the control midface permitted retrospective simulation of what skeletal correction was required to normalize the patient and the potential ensuing soft tissue correction (Figure 3.13 B iii). The large TCS frontonasal region described by the model is also evident using this technique.

The same patient's postoperative midface was then overlaid onto the preoperative and matched-control surfaces (Figure 3.14). Comparison of the skeletal and soft tissue surfaces shows good correspondence in general. There is however, reduced height of the zygomatic bone when comparing the postoperative correction with the simulated correction (Figure 3.14 A). The soft tissue comparison shows malar hypoplasia of the postoperative midface when compared with the predicted outcome (Figure 3.14 B) which may reflect the fact that TCS patients have reduced subcutaneous fat compared with controls (Herlin et al., 2013a).

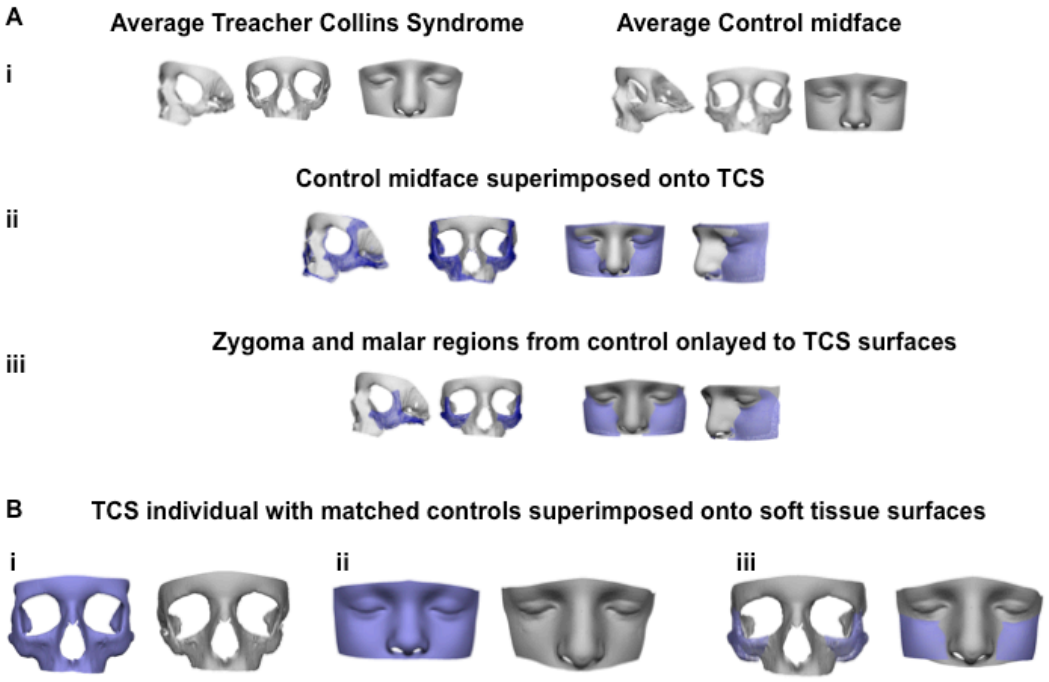

Figure 3.13: Simulated zygomatic complex reconstruction using age-matched controls.

A) i) The average TCS and control midfaces were generated using the mean principal components of their respective datasets. There is zygo-maxillary hypoplasia evident in the average TCS skull compared with controls. **ii)** Superimposition of the average control midface shape onto the TCS reveals the areas deficient in the TCS skull and the shape that can be used to normalize this (lilac mesh). **iii)** The deficient areas are trimmed to the zygomatic complex only (lilac mesh) which could be used as templates to plan surgical reconstruction. The predicted soft tissue correction can also be seen (lilac). **) B) i-ii)** 13-year old male TCS individual's skeletal and soft tissue midface models (grey) and corresponding age-matched controls (n=10) (lilac). **iii)** Predicted shape of zygoma and corresponding soft tissue malar area generated by superimposing the age-matched controls (lilac) onto TCS individual's midface (grey).

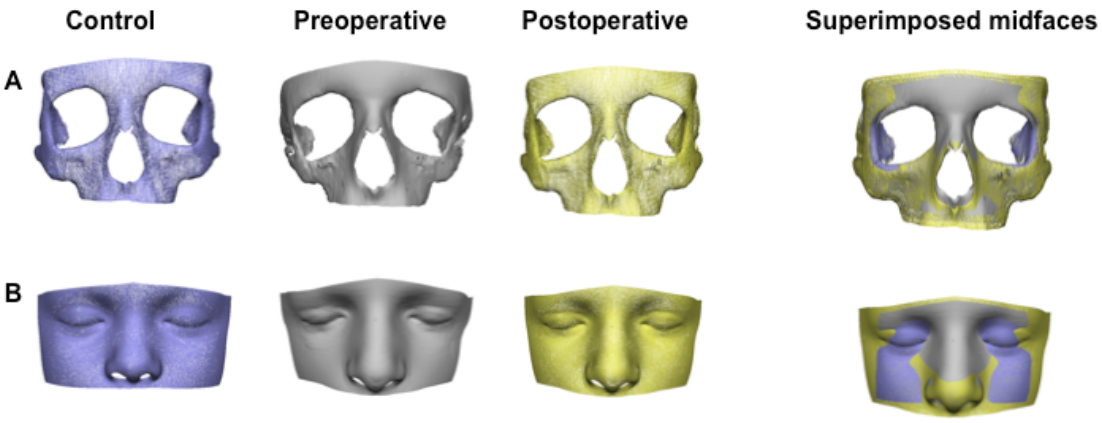

Figure 3.14: Comparison of simulated reconstruction against immediate postoperative outcome of TCS patient.

A) Age-matched control skeletal midface (lilac) superimposed onto preoperative (grey) and immediate postoperative (yellow) models demonstrating differences between the three. **B)** Comparison of soft tissue correction post operatively (yellow) with predicted soft tissue correction from matched-controls (lilac) and preoperative midface (grey).

3.3 Discussion

This study is the first to describe facial growth and morphology in healthy and syndromic paediatric populations using combined skeletal and soft tissue modeling. Dense surface modeling was then used to evaluate the effects of surgery on an individual with TCS immediately then after a year. This simplified approach to virtual simulation of surgery was applied using the outputs of the model to plan midface reconstruction in the same TCS individual and compare with the postoperative outcome. This provides proof of concept for use of the model for evaluation and lays the basis for future development of an operative planning tool.

3.3.1 Describing postnatal midface development using combined modelling

Young et al have previously used CT images to extract soft tissue and skeletal 3D surfaces of the face in patients aged 7-58 (n=175) (Young et al., 2016). Using geometric morphometrics, they analysed skeletal and soft tissue shape to show significant covariation suggesting that skeletal shape can be predicted using soft tissue morphology. The models in this chapter were also built using 3D CT reconstructions of skeletal and soft tissue surfaces and show close alignment between morphology of the midface skeleton and its overlying soft tissue envelope using individual and combined DSM for normal, TCS and CM midface postnatal development.

Changes in midface width, depth and size were quantified and used to describe the skeletal and soft tissue defects in TCS and to some extent CM. The models developed also revealed evidence of significant midfacial asymmetry in TCS (Figure 3.11, Table 3.8, Table 3.9) not previously reported (Dixon, 1996) but did not demonstrate any difference in asymmetry between controls and CM. These results are supported by the findings of anthropometric studies of the face by Kolar et al (Kolar et al., 1985) who demonstrated reduced face width, reduced depth and normal length in TCS. Whilst they concisely described the dysmorphism in TCS using well-established protocols, their study only included 6 children and was restricted to soft tissue morphology. Skeletal dysmorphism in TCS was previously analysed by Nikkhah et al (Nikkhah et al., 2013) who

used cephalometric measures on preoperative CT scans of TCS and control (dry) skulls which were then compared using PCA to quantify the dysmorphism in TCS and attempt virtual normalization. Their study only analysed skeletal models and excluded severe defects. An attempt at correlating skeletal and soft tissue findings in TCS was made by Herlin et al (Herlin et al., 2013b) who used CT reconstructions for skeletal analysis and Magnetic Resonance Imaging (MRI) for the soft tissue study (Herlin et al., 2013a) to perform surgical simulation. Whilst this presented the first quantitative analysis of subcutaneous soft tissue volume in TCS, limitations included a small sample size on the MRI study (n=2 TCS) and methodology that disallowed direct correlation between skeletal and soft tissue analysis. The fact that the models did not show much difference between the CM group and controls is unsurprising as CM is also a disease of varying severity with previous studies demonstrating that the extent of defects and asymmetry depends on the severity of disease and that mildly affected individuals may have similar references to controls (Claes et al., 2011, Ongkosuwito et al., 2013, Tuin et al., 2015). The small CM sample size does however make it difficult to draw any conclusions regarding this.

3.3.2 Development of a postoperative evaluation model

The models were used to compare a pre and postoperative TCS patient against controls to evaluate the efficacy of surgery. This demonstrated immediate correction but changes were not maintained in the long-term which may be due to the type of surgery performed, growth arrest secondary to skeletal surgery or limitation in current preoperative planning tools. This again supports current understanding of the limitation of using on lay bone grafts, which ultimately leads to resorption (Fan et al., 2012).

3.3.3 Virtual simulation of surgery

This work builds on that of Liebregts et al who showed that surfaces acquired from pre and postoperative cone-beam computed tomography images can be used to plan mandibular advancement surgery (Liebregts et al., 2015b). Their study accurately predicted soft tissue changes post surgery and was validated in another study published by the same group that used this technique to plan bimaxillary correction (Liebregts et al., 2015b, Liebregts et al., 2015a). These

papers provide important evidence supporting virtual planning of surgery but are limited to non-syndromic adults and adolescents. The models built do not at present have the capability of virtually planning surgical correction. However, in generating age-matched controls for the average TCS midface and a preoperative TCS individual, a crude attempt was made at predicting skeletal reconstruction by superimposing the controls onto the TCS midfaces. This simple approach which was previously used by other groups to simulate the shape of implant needed to reconstruct the zygomatic complex (Nikkhah et al., 2013). Comparison of this predicted shape with the actual postoperative result of the same TCS patient reveals that the zygomatic shape would have been slightly larger using planning based on the age-matched controls (Figure 3.14). Interestingly, the soft tissue prediction reveals a much larger (depth) malar region would be required to normalize the area then what was achieved by surgery. This maybe due to the fact that TCS children tend to have reduced subcutaneous fat which is not corrected simply by skeletal reconstruction and that this should be considered in any model of midface reconstruction (Herlin et al., 2013a).

This study is limited by the relatively small sample size especially with regards to CM cases (n=6) and the postoperative evaluation patient (n=1). These limit the generalization possible with regards to the postoperative evaluation results and any statistical analysis made on the CM dataset due to the very low numbers. It could also explain the lack of difference between CM and controls with regards to PC1-2, asymmetry and cephalometric measurements (Figure 3.5, Figure 3.6, Figure 3.11, Table 3.7) as CM has a heterogeneous phenotype and thus inclusion of mild forms in a small sample may have affected the outcome of this study.

An increased sample size, different surgical procedures and most importantly repeat CT scan data for each individual over a prolonged period of time are needed to build a tool which can model growth trajectories for each child. This would allow identification of the most variable regions in face growth and shape and correlation between the dependent variables. The combined model needs further analysis to accurately assess how it correlates with the individual DSM to enable modelling of how changes in skeletal tissue affects soft tissues and

the reverse. This could potentially permit development of a surgical planning tool with adequate predictive capabilities so that immediate and long-term morphology and growth can be simulated. The increase in sample size and longitudinal data collection is more easily achievable in the TCS cohort who often have repeat scans but may be difficult with regards to controls and CM, thus a multi-centre study will be necessary in future.

3.4 Conclusions

This study shows that a combined model can be generated to relate skeletal and soft tissue changes during normal and TCS midface postnatal development. Heat maps and PCA were used to describe the dysmorphism in TCS and evaluate the impact of a common surgical procedure revealing that whilst correction maybe achieved in the short term, it may not be maintained long term. This combined approach has the potential to eventually be used to develop a surgical planning tool and extended to other parts of the face using similar protocols.

Chapter 4 Paediatric Osteoprogenitor Cell Sources

4.1 Introduction

Reconstruction of craniofacial bone deformities such as those occurring in midface hypoplasia associated with Treacher Collins Syndrome or acquired skeletal defects (e.g. due to trauma or neoplastic) usually requires invasive transfer of bone tissue (usually calvarial bone grafts) with/without associated vascular or soft tissue. This is associated with risk of absorption and donor-site morbidity. Alternatives for correction of these deformities include foreign-body implants (either used as a prosthesis or as a scaffold to stimulate bone growth) that do not resorb nor produce a secondary defect at the donor-site. These implants are however associated with an increased risk of infection, extrusion and are unable to grow or fully integrate with the rest of the child's skeleton. Due to the risks and limitations of reconstruction of hypoplasia or defects with foreign body implants and autologous bone transfer, tissue engineering provides the promise of generating autologous bone tissue without many of the limitations and morbidities associated with the gold standard treatments. One of the most important considerations is which cell type to use for bone bioengineering.

4.1.1 Facial bone development and remodelling

The biological properties and functions of bone have been described in detail in Chapter 1 of this thesis. Facial bone and more specifically that found in the midface (such as the Zygoma and Maxilla) develop through a process of intramembranous ossification (Figure 4.1). During this, neural crest derived stem cells proliferate then condense into nodules to differentiate into either capillary vessels or osteoprecursor (osteoblast precursor) cells (Paiva and Granjeiro, 2014).

The osteoprecursor cells are recruited through a complex and highly regulated local and systemic signalling pathways (Ren et al., 2015) involving the bone morphogenetic proteins as well as the runt related transcription factor 2 and osterix pathways. These genes co-ordinate activation and maturation of osteoprecursor cells to differentiate in to osteoblasts which in turn generate and lay down the extracellular bone matrix (Chaudhary et al., 2004). This collagen-proteoglycan matrix binds calcium crystals to permit calcification. Osteoblasts

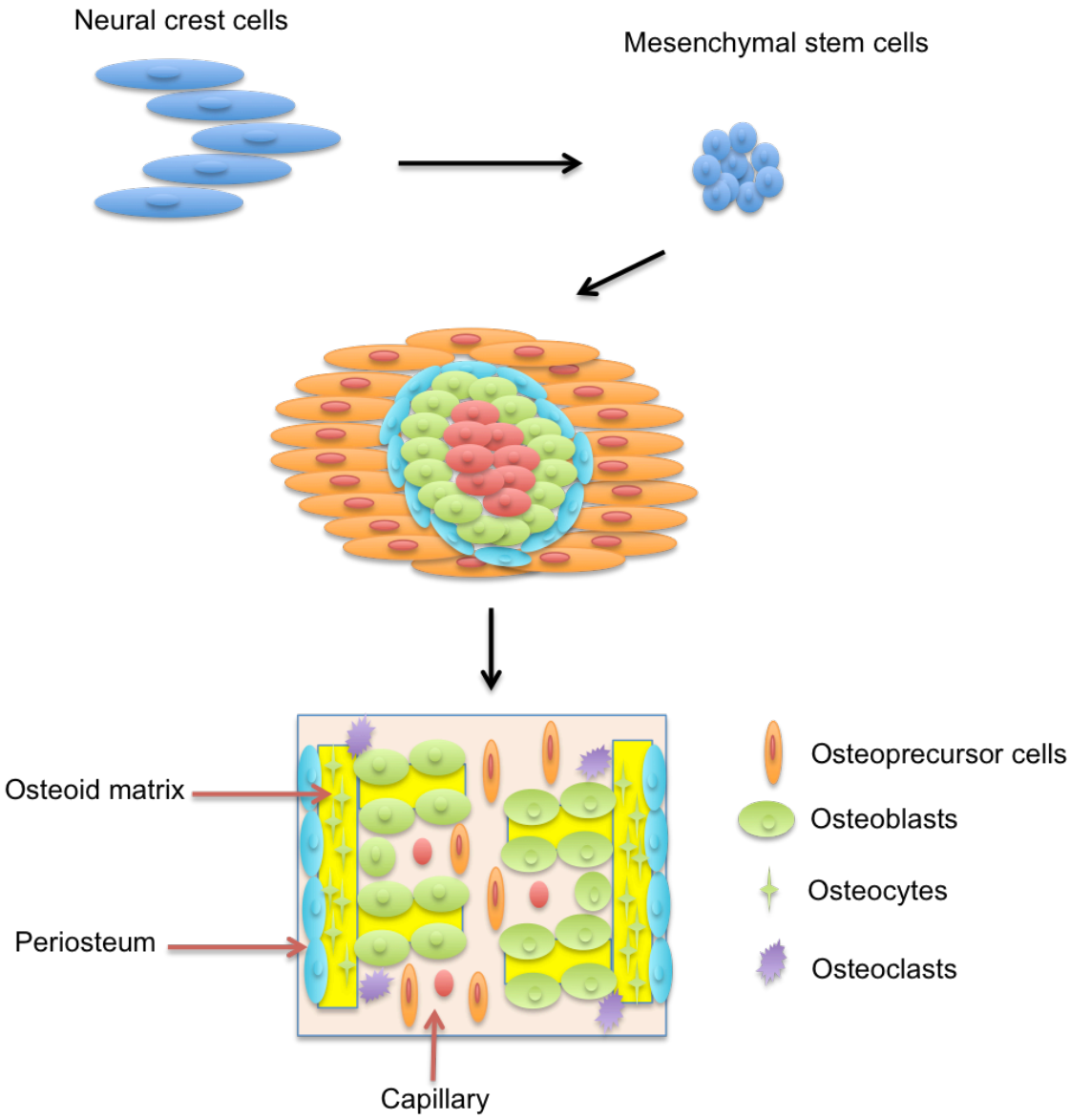

Figure 4.1: Facial bone development through intramembranous ossification.

Migrating neural crest cells proliferate to become mesenchymal stem cells (MSC), which undergo aggregation and condensation. Osteoinduction causes differentiation of MSC into capillaries or osteoprecursor cells. The latter further differentiate into osteoblasts that lay down osteoid matrix and periosteum before becoming buried in their own calcified matrix and maturing into osteocytes. Osteoclasts contribute to bone remodelling through break down of the extracellular matrix. Adapted from “Bone tissue remodelling and development: Focus on matrix metalloproteinase functions” by Paiva et al (Paiva and Granjeiro, 2014).

are separated from this region of calcification by the osteoid matrix that they continually produce although eventually around 15% become buried in their own matrix and form osteocytes.

On-going ossification eventually results in the formation of bone spicules, which are then surrounded by mesenchymal cells forming a membrane (the periosteum). The cells on the inner surface of the periosteum then become osteoblasts and begin depositing osteoid matrix in parallel to the pre-existing boney spicules.

Osteoclasts, alongside osteoblasts and matrix metalloproteinases (MMPs), play an important role in bone turnover and remodelling (Paiva and Granjeiro, 2014). These cells are widely thought to share a common precursor to macrophages and regulate bone turnover through matrix degradation using a hydrogen ion pump mechanism. This allows control of new bone formation and even shaping by creating cavities required for vasculature or bone marrow. Osteoblast signalling plays a key role in stimulating osteoclast recruitment and differentiation (Figure 4.2).

4.1.2 Stages of bone formation and maturation

As discussed in Chapter 1, a number of genes are associated with osteogenesis and intramembranous bone formation. Runt-related transcription factor 2 activation leads to differentiation of osteoprogenitor cells into a “preosteoblast” phenotype. During osteogenesis, these cells express genes such as *COL1*, *ALP*, *OSTP*, *OSX*, *BSP* and *OCN* in a pattern dependent on stage of maturation (Stein et al., 2004). Most of these genes are down regulated in late osteogenesis with osteocytes predominantly expressing *OSP* and *OCN*. Calcium deposition (mineralization) and extracellular matrix are also key characteristics of bone formation and maturity (Rutkovskiy et al., 2016). Late stage bone development can also be assessed by mechanical and architectural properties whilst remodelling can signify fully mature and functioning bone.

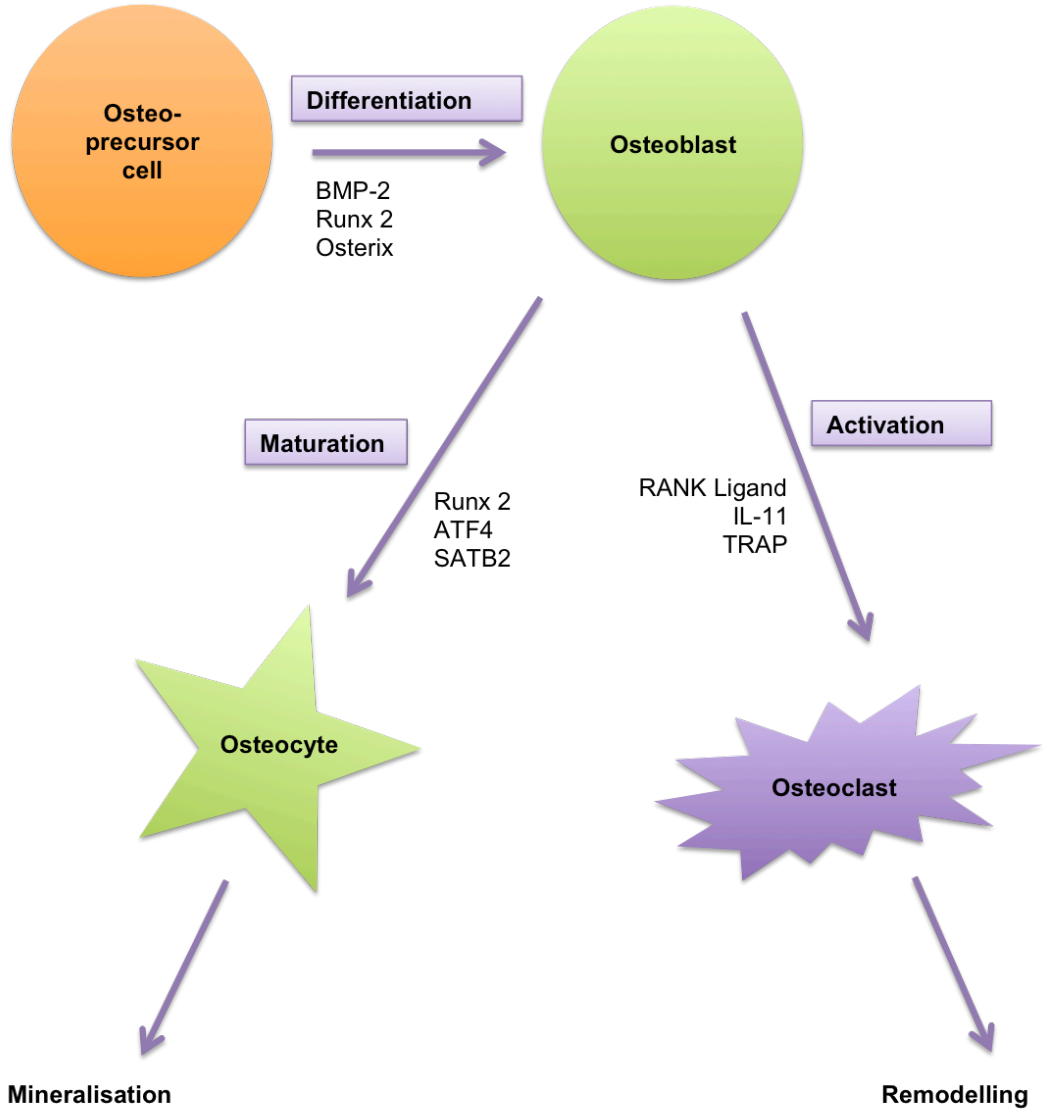

Figure 4.2: A concise overview of osteogenic differentiation.

Osteoprecursor cells of mesenchymal origin are induced to differentiate into osteoblasts under stimulation by bone morphogenetic protein 2 (*BMP2*), Runt related transcription factor 2 (*RUNX2*) and Osterix signalling. Osteoblasts may then mature into osteocytes which deposit mineral or activate osteoclasts, which drive bone resorption.

4.1.3 Osteoprogenitor cell sources

A number of tissues, including bone and fat, have been shown to contain mesenchymal stem cells which possess osteoprogenitor potential (Rao and Stegemann, 2013). These cells express general markers of pluripotency such as CD44, CD90, CD105 and CD166 (Dominici et al., 2006, Maleki et al., 2014). There is also evidence that the sub-populations that have greatest osteoprogenitor potential additionally express STRO-1, SB-10 and HOP-26 (Stewart et al., 2003, Gronthos et al., 1994, Green et al., 2015)

In this chapter, structural, molecular, and histological evaluation of calvarial bone grafts will be undertaken to characterize non-syndromic paediatric bone and establish a reference against which bone bioengineering protocols can be assessed. Three commonly used and easily harvested osteoprogenitor cell sources (human osteoprecursor cells (hOP), bone marrow derived stem cells (hBMSC) and human adipose derived stem cells (hADSC)) will be compared for their osteogenic differentiation potential and suitability in bone tissue engineering as a clinical stem cell therapy.

4.2 Results

4.2.1 Histological and molecular characterisation of calvarial bone samples

Calvarial bone tissues (from 11 different patients, 1 individual bone graft retrieved per patient analysed using at least 3 samples from each bone) were analysed for histological composition, mineralization in addition to gene and protein expression to define criteria through which bone tissue engineering for craniofacial reconstruction could be measured against.

4.2.1.1 Analysing the distribution patterns of extracellular collagen

Collagen 1 comprises 80% of all proteins found in bone matrix and regulates the mechanical properties of bone. Collagen 1 alone, imparts the ability of bone to absorb energy (toughness) and balances the stiffness generated by osteoblast mediated crystal deposition in and around the collagen fibrils (Viguet-Carrin et al., 2006). Immunoflourescent staining for collagen 1 revealed widespread collagen deposition in the bone spicules (islands of bone) and the osteoid layer, which is the extracellular matrix freshly deposited by the osteoblasts (Figure 4.3 A a-b).

Collagen fibril orientation and details of architecture were further demonstrated using second harmonic generation (SHG) scanning. In the paediatric calvarial samples, the collagen meshwork appeared abundant in the extracellular matrix. Fibrils appear tightly packed and aligned in parallel to the long axis of the bone at the osteoid matrix whereas the density appears looser and the orientation less polarized at the spicule. This heterogeneity in collagen fibril orientation has previously been detected using polarized Ramen spectroscopy in human femoral bone (Schrof et al., 2014) but not calvarial or other intramembranous bone.

Quantitative and qualitative analysis of collagen fibre orientation was performed on SHG images using the OrientationJ plugin (Figure 4.3 B). Quantitatively, 50 regions of interest (ROI) were selected in sequence per bone section (a total of n=3 bone sections were used from each patient sample) were analysed using a uniform weighting which provided the coherency which is a measure of isotropy

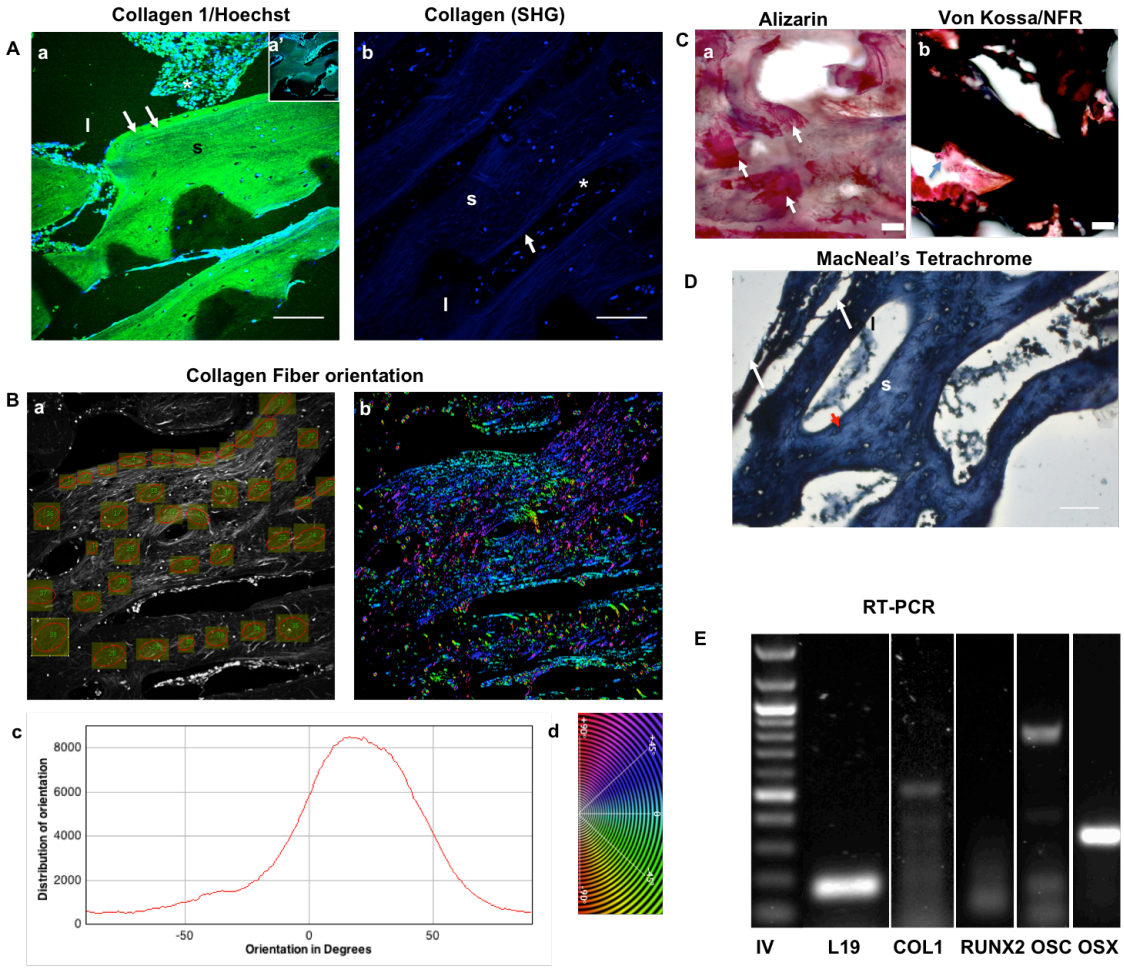

Figure 4.3: Characterisation of paediatric human calvarial bone tissue using histological and gene expression analysis.

A) Collagen 1 fluorescent staining (a) and SHG imaging (b) for collagen on boney spicules (s), osteoid (arrows) and osteoblast containing matrix (*). **B)** Analysis of SHG images showing collagen networks in grey scale overlaid with fibre orientation of user-defined ROI (a), colour map of local fibre orientation in degrees (-90° to 90°) (b), histogram of distribution of fibre orientations (c) and fibre orientation colour wheel (d). **C)** Staining of calcified sections for mineral deposition with Alizarin (arrows) (a) and Von Kossa (black) (b). **D)** MacNeal's tetrachrome staining of decalcified sections for osteoid (blue, arrows) with Von Kossa counterstain for mineralised bone (black). **E)** Osteogenic gene expression. l; lacuna, s; spicule, L19; ribosomal protein 19, COL1; collagen 1, Runx2; runt-related transcription factor 2; OSC; Osteocalcin, OSX, Osterix; negative antibody controls; alexa 488nm anti rabbit (a'); scale bars=100um.

and orientation of the collagen fibres in that area and a visual representation of this as an oval window (Figure 4.3 B a). Coherency ranges from 0 (anisotropic or disorganised fibres) to 1 (isotropic or parallel arranged). In the ROI over the osteoid region, coherency was higher (0.37 ± 0.018) than in the spicules (0.25 ± 0.018) confirming a difference in collagen arrangement ($p<0.0001$). Orientation was visualised as a colour map with osteoid fibres predominantly aligned between 0-90° whilst collagen orientation in the spicules was more heterogeneous (Figure 4.3 B b). The histogram of orientation throughout the sample suggests that orientation is skewed more positively (0-90°) (Figure 4.3 C c).

4.2.1.2 Visualisation of mineralisation in paediatric calvarial bone

The inorganic component of bone matrix is largely comprised of hydroxyapatite crystal which are deposited as plates within and around the collagen fibrils (Liu et al., 2016b). This process is regulated by alkaline phosphatase, which is secreted by osteoblasts under the regulation of phosphate and calcium and results in mineralization (Anh et al., 1998, Farley et al., 1994). Alizarin red complexes with calcium and is thus an indirect marker of calcium deposition. Calcified calvarial sections revealed widespread patchy calcification of the tissues on Alizarin red staining whilst Von Kossa staining which reacts with phosphates and carbonates (not calcium) was more widespread (Figure 4.3 C a-b). This lack of specificity in Von Kossa staining was previously described in murine cells where positive staining was associated with dystrophic mineralization (Bonewald et al., 2003).

4.2.1.3 Assessment of paediatric calvarial bone maturity

Differentiation between osteoid and more mature bone can be achieved using MacNeal's tetrachrome stain in which immature bone (osteoid) stains blue and more mature bone stains red (Bonewald et al., 2003). Staining of the calvarial decalcified sections exhibited blue staining in the peripheries of the spicules and the matrix encasing osteoblasts in the lacunae (Figure 4.3 D). This is in the expected location of the osteoblast layer and corresponds with SHG staining pattern for collagen 1 in the osteoid matrix (Figure 4.3 A).

4.2.1.4 Osteogenic gene expression by paediatric calvarial bone tissue

Gene expression is frequently used in bone tissue engineering studies to assess osteogenic potential and differentiation. To establish a reference for gene expression, calvarial bone samples were assessed for genes most commonly used to verify osteogenesis (n=11 individual patient samples, analysis performed in triplicates) (Figure 4.3 E).

RUNX2 expression is required to promote osteogenesis in mesenchymal cells through BMP2 regulation (Liao et al., 2014, Zhou et al., 2016a). Calvarial bone samples did not express RUNX2 (Appendix II). Canonical Wnt signalling is also important in osteoblast differentiation and leads to transcription of RUNX2 which promotes expression of osteogenic matrix protein genes such as *COL1*, *ALP* and *OSC* (Zhou et al., 2016a). Both *COL1* and *OSC* were expressed by bone samples (Figure 4.3 E) but not ALP (Appendix II). Osterix is an important marker of osteoprogenitor cell differentiation. It facilitates osteoblast lineage commitment in osteoprecursor cells and has been shown to promote calcium deposition and *ALP* up regulation through β-catenin signalling (Liu et al., 2015). Furthermore, knockout mice lacking *OSX* demonstrated premature bone formation with reduction in *OSC* expression (a late marker of osteogenic differentiation) (Baek et al., 2009). As expected, the bone samples expressed *OSX*.

4.2.2 Analysis of cellular composition of paediatric calvarial bone through histomorphometry

The composition of bone was determined through staining of paraffin fixed decalcified sections of bone from individual patients (n=4) with H&E (Figure 4.4). Bone sections demonstrated islands of boney spicules with cells suspended within them and extracellular matrix encasing more nuclei surrounding the spicules and within the lacunae (Figure 4.4 A). Morphology of the three main cellular constituents of bone (osteoblasts, osteoclasts and osteocytes) was defined using known histological criteria (Florencio-Silva et al., 2015). Large cells were found in the lacunae which appeared large, multinucleated, had an abundant cytoplasm and an irregular shaped membrane (Figure 4.4 B). These cells fitted published descriptions of osteoclasts. Small cuboidal shaped cells with round nuclei were found on the surface of the bone spicules in keeping with known osteoblast morphology whilst oval shaped cells embedded in the bone matrix were characteristic of osteocytes (Figure 4.4 C).

Areas between 53.76-959.33 um^2 were selected in sections of bone from individual patients (n=7). The regions chosen were representative of the overall bone (the region with spicules lacunae and extracellular matrix). To ensure reproducibility (some samples had pericranium attached and others did not), the fibrotic membrane covering the surface of some bones was not included in the analysis (Figure 4.4 A). The different cell types were quantified using the counting tool on ImageJ and revealed an overall average cell density of 2.82 (± 0.25) cells per um^2 of bone tissue of bone with osteoblasts and osteocytes each making up an average of 56% and 41% of the total cell density respectively (Figure 4.4 D). Osteoclasts made a significantly smaller contribution to overall cell mass of 3% on average compared with osteoblasts and osteocytes (Figure 4.4 D). Whilst, the density of osteoblasts is considered an important indicator of osteogenesis in the presence of osteogenic supplements in vitro and in vivo (Yassin et al., 2015), this type of analysis has not been previously performed on paediatric calvarial bone. It is however potentially important when generating and evaluating tissue engineered bone.

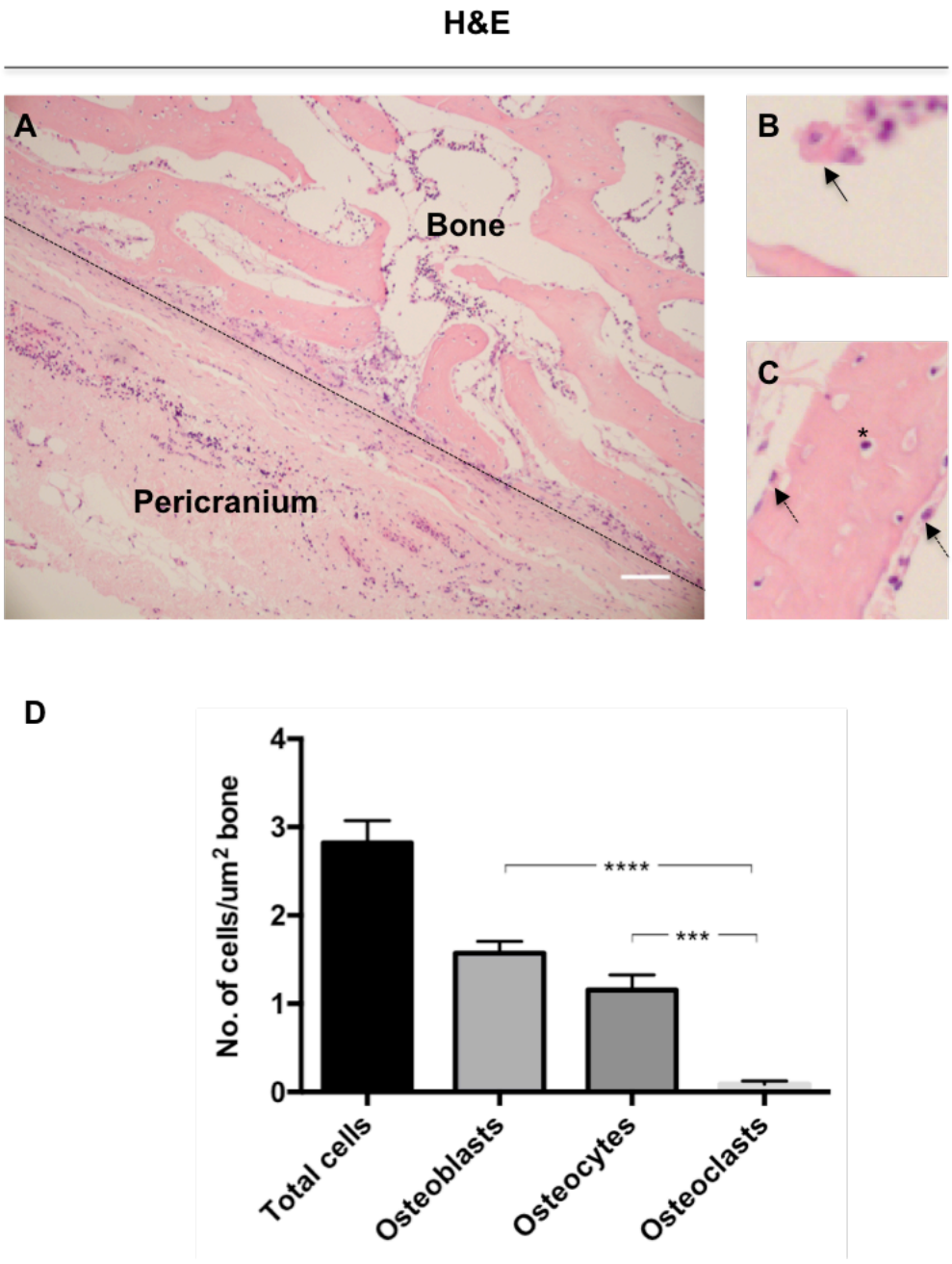

Figure 4.4: Analysis of cellular constituents of paediatric human calvarial bone using Haematoxylin and Eosin (H&E) staining.

A) Representative section of bone and attached pericranium. The dotted line demarcates exclusion zone for analysis. **B)** Large irregular shaped cells identified as osteoclasts. **C)** Osteoblasts appeared small and cuboidal (arrow) whilst osteocytes were located within the bone mass (*). **D)** Cells counted on H&E sections from different patients (n=7) with average 2.82 (± 0.25) cells per um2 of bone tissue. There is no significant difference between osteoblast (1.57 ± 1.28) and osteocyte (1.16 ± 0.17) density (p=0.34). Osteoclast density (0.088 ± 0.04) is significantly less than that of osteoblasts (p<0.0001) and osteocytes (p=0.0003). Data expressed as mean number of cells/um2 area of tissue ± SEM; Scale bars = 100um; ***p<0.001; ****p<0.0001.

4.2.3 Analysis of mineralisation density in paediatric calvarial bone

Fixed samples (n=11 individual patient samples) were imaged using a uCT scanner then analysed in ImageJ using the BoneJ plugin to quantify bone structure (Figure 4.5). 3D reconstructions of the uCT slices were used to visualize the extracellular matrix structure of bone (Figure 4.5 A) and a colour thermal LUT (look up table) was applied to visually represent the gradient of mineralization density in calcified samples (Figure 4.5 B). The surfaces (cortices of bone) were red-green on the red-green-blue (RGB) scale that represents greater density whilst the middle portion of the bone tended to be more green-blue suggesting lower mineralisation density. This corresponds with the distribution of collagen seen previously (Figure 4.5 B) whereby the cortex contained densely packed fibres of collagen compared with the middle. The possibility of collagen fibril orientation determining mineralisation and mechanical properties has been previously suggested in a study on human cortical bone (Granke et al., 2013).

The uCT stacks of bone were thresholded on ImageJ to isolate the mineralized tissue and generate a binarized image (black and white). Randomly selected samples containing the cortex and medulla of the bone were then extracted and BoneJ was used to establish bone volume (mineralised matrix), total volume (mineral and organic components) and the ratio between these two (Figure 4.5 C). The bone volume to total volume ratio (BV/TV), also known as the bone fraction volume, is a measure of mineralized bone density. BV/TV is on average 48.3% in the dataset of calvarial bone from children aged 3.7-7.4 months (n=11) (Figure 4.5 C). Plotting these values against age (Figure 4.5 D) did not demonstrate any correlation between age and bone density as described by BV/TV ($p=0.3568$).

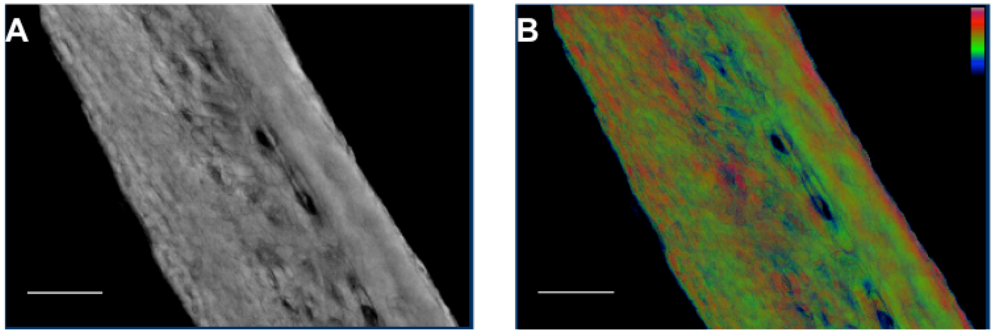

C

Age (months)	Bone Volume (BV) (mm^3)	Total Volume (TV) (mm^3)	BV/TV (%)
5.54 ± 0.34	1.60 ± 0.40	3.49 ± 0.80	48.3 3 ± 3.01

D

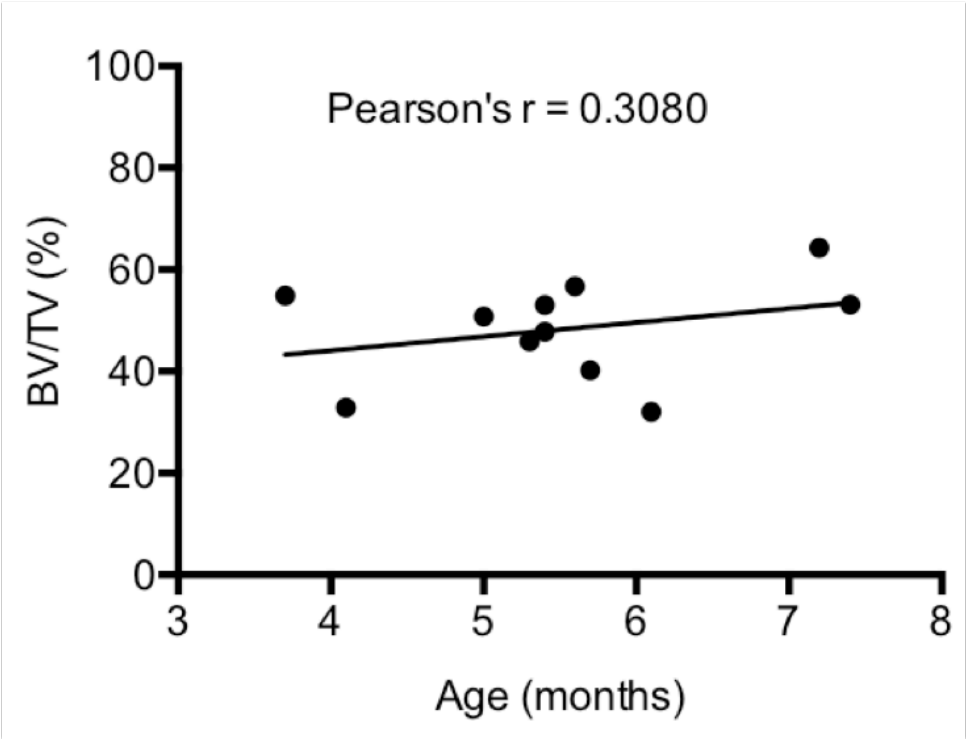

Figure 4.5: Micro CT (uCT) analysis of mineralisation density in paediatric calvarial bone tissues

A) uCT imaging reveals structure and grey values of bone tissue. **B)** Thermal colour filter visually represents gradient of mineral density with red correlating with increased mineral density and blue coinciding with reduced mineral density. **C)** Quantification of bone fraction volume (BV/TV) of specimens from different patients (n=11). **D)** Relationship between bone fraction volume (BV:TV) and age of patient (p=0.3568). BV; bone volume, TV; total volume, scale bars; 0.5mm, statistical significance; $p<0.05$.

4.2.4 Comparison of different sources of osteoprogenitor cell type for osteogenic potential and mature bone formation

4.2.4.1 Isolation of osteoprogenitor cells

Fat samples collected from abdominal lipoaspirates (n=13 individual patient samples) were enzymatically digested to produce hADSC or plated onto cell culture dishes to isolate hAEDSC. The latter were always obtained even from small fat samples and so were used most frequently. Occasionally, hADSC were used in place of hAEDSC as both these cell types were previously shown to exhibit similar pluripotency and skeletogenic differentiation properties (Guasti et al., 2012). Where this occurred, the other two lines in the biological triplicate were always hAEDSC.

Histologically (samples from n=13 patients analysed in triplicates), fat samples demonstrated typical appearance (Parlee et al., 2014) with adipocytes displaying large fat vacuoles and small peripheral nuclei (Figure 4.6 A). Cells were seen to migrate from the fat explant within 5-8 days (B). Cells closer to the explant had a more adipocyte-like morphology whilst those further away appeared more spindle-shaped.

Calvarial bone samples were analysed histologically (samples from n=11 patients analysed in triplicates) revealing typical structure of bone islands with bone marrow dwelling in the lacunar regions (Figure 4.6 C). Bone samples (samples from n=11 patients) were used to directly generate human osteoprecursor cells through explant culture of fragments (Figure 4.6 D). This resulted in migration of cells from the explant within 5-8 days that became more elongated and spindle-like in appearance as they moved further away.

Histologically, the bone cavities contained a large number of cells, which were heterogeneous in appearance and consistent with bone marrow as verified by Giemsa staining (Figure 4.6 C). Bone marrow was isolated from bones using serial PBS washes and verified using Giemsa staining (Figure 4.6 E). Human BMSC subconfluent monolayers were visible within 7 days after plating and appeared elongated in morphology (Figure 4.6 F).

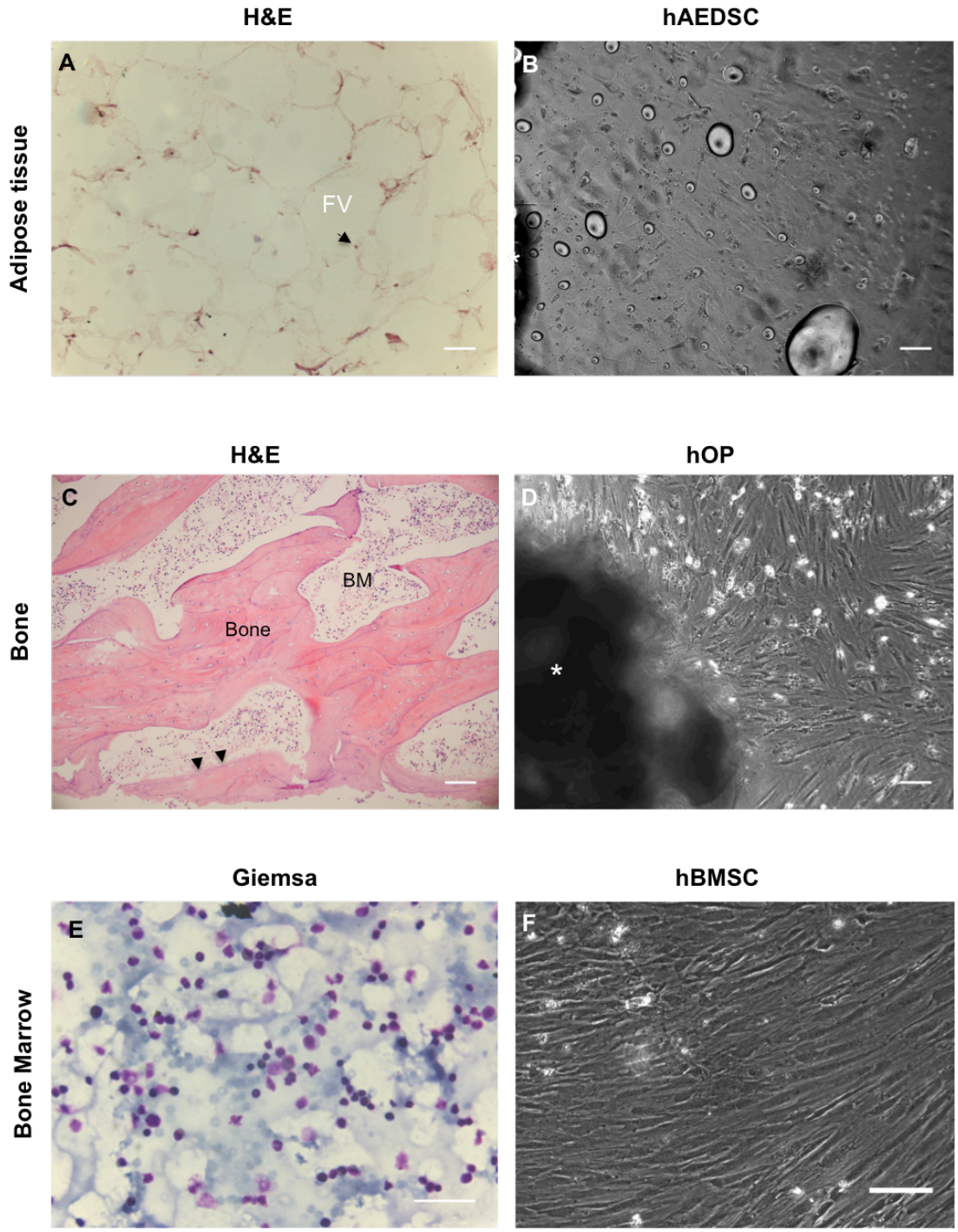

Figure 4.6: Appearance of different tissue sources of osteoprogenitor cells.

A) Adipose tissue displaying cobblestone arrangement of adipocytes with large fat vacuoles (FV) and peripheral nuclei (arrow). **B)** Explant culture of fat tissue (*) with cells migrating from explant. **C)** Bone histology demonstrating bone tissue with osteoblasts lining the surface (arrows) and bone marrow (BM) filling the lacunar spaces. **D)** Bone explant (*) with cells migrating from tissue. **E)** Giemsa staining to visualise bone marrow collected from flushing cavities. **F)** Appearance of cells cultured from bone marrow flushes after 7 days. BM; bone marrow, scale bars; 100um.

All fat and bone explant samples could be replanted several times (maximum of 7 times replanted and stopped due to time limitation). For consistency, only the first migrating population of cells were studied to ensure consistency and because a previous study suggested these cells represented a more heterogeneous population than later replants in bovine trabecular bone explant samples (Chan et al., 2009).

4.2.4.2 Cell behaviour and expansion potential

hAEDSC (n=6 cell lines) displayed a more heterogeneous morphology after two passages moving from a uniform population of spindle-shaped cells to a mixture of mostly fibroblastic and some flatter and polyhedral shaped cells (Figure 4.7 A a). The hOP (n=11 cell lines) tended to cluster on plastic once confluent and whilst cells appeared flatter, they varied greatly in shape and degree of elongation (Figure 4.7 A b). The appearance of hBMSC (n=7 cell lines) was similarly heterogeneous but overall appeared to predominantly contain spindle-shaped cells, which did not cluster on confluence (Figure 4.7 A c).

The cell cytoskeleton is important in determining cell behaviour including adhesion, migration and differentiation (Yourek et al., 2007, Sonowal et al., 2013). Cytoskeletal appearance was assessed using F-actin (Phalloidin) staining which revealed elongated and organized distribution of the intracellular actin in hAEDSC (Figure 4.7 A d). F-actin was similarly organized with fibres arranged in parallel within the cell cytoskeleton in hOP and hBMSC (Figure 4.7 A e-f). These findings are in keeping with previous studies that actin fibres are arranged in thin parallel bundles which span the cytoplasm in undifferentiated MSC (Rodríguez et al., 2004).

Comparison of potential cell yield from each tissue source was performed by counting the number of cells that could be retrieved per wet weight of explanted tissue (Figure 4.7 B). The hAEDSC (n=3 different cell lines) provided an average of 603970 (± 293610) cells per gram of adipose tissue; hOP yield was 2042000 (± 580825) cells per gram of bone (n=5 different cell lines) whilst 468114 (± 160122) hBMSC were obtained per gram of bone (n=4 different cell lines). The number of hOP cells derived per gram of tissue was not significantly more than hAEDSC ($p=0.0552$) and hBMSC ($p=0.0870$) nor was there a difference between number of hAEDSC and hBMSC ($p=0.9778$). Proliferative capacity of osteoprogenitor cells was compared using the Alamar blue assay (Figure 4.7 C). There is no significant difference in cell viability in the first 72 hours although hBMSC showed increased proliferation at 168 hours compared with hAEDSC ($p=0.0268$) and hOP ($p=0.0317$).

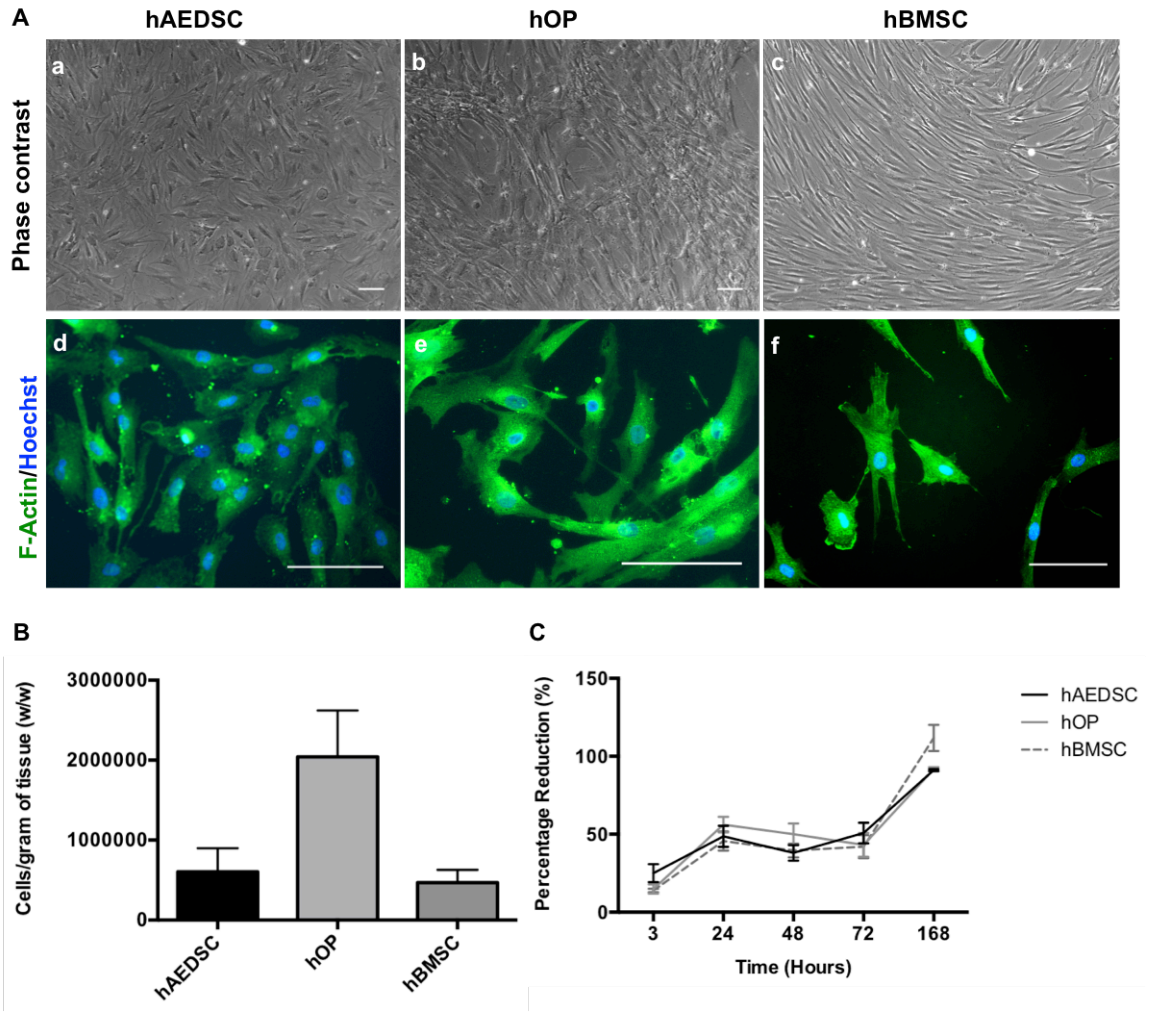

Figure 4.7: Morphology and proliferative capacity of different osteoprogenitor cell types.

A) Typical appearance of confluent monolayer cultures on plastic of hAEDSC (a), hOP (b) and hBMSC (c). **B)** F-actin (green) and Hoechst nuclear dye (blue) staining of cells showing cytoskeletal structure of hAEDSC (d), hOP (e) and hBMSC (f). **B)** Cells yielded per gram (wet weight) of tissue to obtain hAEDSC (603970 ± 293610), hOP (2042000 ± 580825) and hBMSC (468114 ± 160122). **C)** Proliferation of osteoprogenitor cell types using Alamar blue assay reveals a significant difference in proliferation rate of hBMSC between 72-168 hours compared with hAEDSC ($p=0.0268$) and hOP ($p=0.0317$). Scale bars; 100um, data expressed as mean ± SEM.

4.2.4.3 Comparative characterization of different osteoprogenitor cell types using surface markers

Flow cytometry was performed to assess mesenchymal and non-mesenchymal markers (Table 4.1). Different cell lines of hAEDSC (n=3), hOP (n=5) and hBMSC (n=5) expanded in culture media at passages 3-8 were compared.

Mesenchymal markers CD13 (aminopeptidase N), CD29 (integrin B1), CD44 (hyaluronic acid receptor) and CD73 (ecto-5'-nucleotidase), CD90 (Thy1), CD105 (endoglin), CD166 (activated leucocyte cell adhesion molecule) were positively detected in all three osteoprogenitor cell types. There was no significant difference in the positive staining for these markers.

Expression of the non-mesenchymal markers CD10 (neprilysin), CD14 (monocyte differentiation antigen), CD34 (hematopoietic progenitor cell antigen), and CD45 (lymphocyte common antigen) was low in all groups. CD117 (c-kit) is considered a non-mesenchymal marker and was detected in low levels in all cell types with higher proportion of hAEDSC positive cells than hBMSC ($p=0.0488$). Recently, c-kit positive populations of BMSC and ADCS were shown to possess multi-lineage differentiation potential, which in the case of ADSC was independent of CD105 (Ding et al., 2015, Kubo et al., 2009, Blazquez-Martinez et al., 2014). Similarly, whilst CD31 (platelet endothelial cell adhesion molecule-1) positive cells were low, there were more of these cells in hBMSC compared with hOP ($p=0.0119$). Recent analysis of CD31 positive cells in bone marrow reveals a distinct subpopulation (mesodermal progenitor cells) with proangiogenic properties (Pacini et al., 2016, Pacini and Petrini, 2014).

Immunophenotype profile was compared using HLA ABC and HLA DR surface markers. HLA ABC was expressed at a level in hBMSC (64.48 ± 15.46), which was not significantly different compared with hAEDSC (69.76 ± 15.37, $p=0.84$) and hOP (66.23 ± 10.77, $p=0.97$). There was also no significant difference in HLA DR expression between hAEDSC (9.32 ± 5.74) and hOP (6.03 ± 5.14) ($p=0.77$) or hBMSC (15.8 ± 10.19) ($p=0.45$). Previous studies have shown that HLA expression is similar in ADSC and BMSC (Niemeyer et al., 2007). There have not been any published reports on HLA expression in human calvarial bone explant derived cells.

Table 4.1: Comparison of osteoprogenitor cells using flow cytometry.

		hAEDSC	hOP	hBMSC
Mesenchymal	**CD13**	98.41 ± 0.59	93.18 ± 1.89	98.05 ± 0.62
	CD29	99.40 ± 0.33	97.68 ± 0.67	99.46 ± 0.14
	CD44	98.94 ± 0.58	97.46 ± 1.08	97.30 ± 1.69
	CD73	98.65 ± 1.00	92.05 ± 3.58	95.58 ± 2.38
	CD90	93.75 ± 5.43	83.36 ± 3.90	88.16 ± 4.69
	CD105	98.47 ± 0.51	92.54 ± 3.65	92.58 ± 4.42
	CD166	92.21 ± 4.47	89.17 ± 4.53	87.49 ± 6.08
Non-mesenchymal	**CD10**	7.61 ± 3.34	2.16 ± 1.16	6.46 ± 3.74
	CD14	4.16 ± 1.93	3.01 ± 1.78	7.83 ± 4.70
	CD31	4.62 ± 4.38	1.45 ± 1.25*	24.78 ± 15.51
	CD34	2.05 ± 1.75	1.45 ± 1.14	4.55 ± 2.83
	CD45	5.65 ± 2.30	2.89 ± 1.82	8.33 ± 5.13
	CD117	96.76 ± 3.00*	79.64 ± 5.79	74.68 ± 10.33
	HLA ABC	69.76 ± 15.37	66.23 ± 10.77	64.48 ± 15.46
	HLA DR	2.05 ± 1.75	6.03 ± 5.14	15.80 ± 10.19

Panel of mesenchymal and non-mesenchymal markers used to analyse cell lines from different patients to compare hAEDSC (n=3), hOP (n=5) and hBMSC (n=5). Data are represented as mean ± standard error of mean (SEM). Comparison of hAEDSC vs. hOP, hAEDSC vs hBMSC or hOP vs hBMSC; *p< 0.05.

4.2.4.4 Pluripotent potential of different osteoprogenitor cell types

Pluripotent potential of hADSC, hOP and hBMSC was assessed using gene expression for known markers of pluripotency with human embryonic stem cells and induced pluripotent stem cells as positive controls for comparison (Figure 4.8).

OCT4 and *DNMT3B* were expressed by hES (n=1 patient) (A). Whilst *OCT4* was expressed by hBMSC (n=3), it was not detected by PCR in neither hAEDSC (n=2) nor hOP (n=3). None of the osteprogenitor cells expressed *DNMT3B*. Whilst these transcripts were previously detected in our research group by quantitative PCR in paediatric hADSC and hAEDSC using the same primer sequences (Guasti et al., 2012) but is in keeping with a recent study comparing hADSC and hBMSC from adults (Heo et al., 2016a).

Relative quantification PCR analysis demonstrated that *CMYC*, *SOX2*, *KLF4* and *NANOG* were expressed by hAEDSC (n=3), hOP (n=5) and hBMSC (n=5) (B-D). There was no significant difference in *CMYC* fold change between hAEDSC (p=0.9608), hOP (p=0.8706) or hBMSC (p=0.9783) when compared with positive iPSC controls (n=2). On the other hand, *SOX2* expression was significantly lower in hAEDSC (p=0.0280), hOP (p=0.0119) and hBMSC (p=0.0031) compared with iPSC (C). *KLF4* expression did not significantly differ between iPSC and hAEDSC (p=0.9983), hOP (p=0.8699) or hBMSC (p=0.8764). There was also no significant difference in *NANOG* between iPSC and hAEDSC (p=0.9914), hOP (p=0.9730) or hBMSC (p=0.9984).

Nestin is an intermediate filament protein found in neuroepithelial cells that is found in mesenchymal stem cells. It is increasingly used as a marker of multi-lineage potential (Roson-Burgo et al., 2014, New et al., 2015). All cell types similarly expressed Nestin but at significantly reduced levels ($p<0.0001$) compared with iPSC (Figure 4.8 F). Interestingly, a previous study demonstrated that Nestin was expressed in hBMSC of calvarial bone origin only and not those from iliac crest bone (Shinagawa et al., 2015).

Vimentin expression is associated with fibroblastic phenotype although it is also expressed by mesenchymal stem cells (Alt et al., 2011). Expression of vimentin

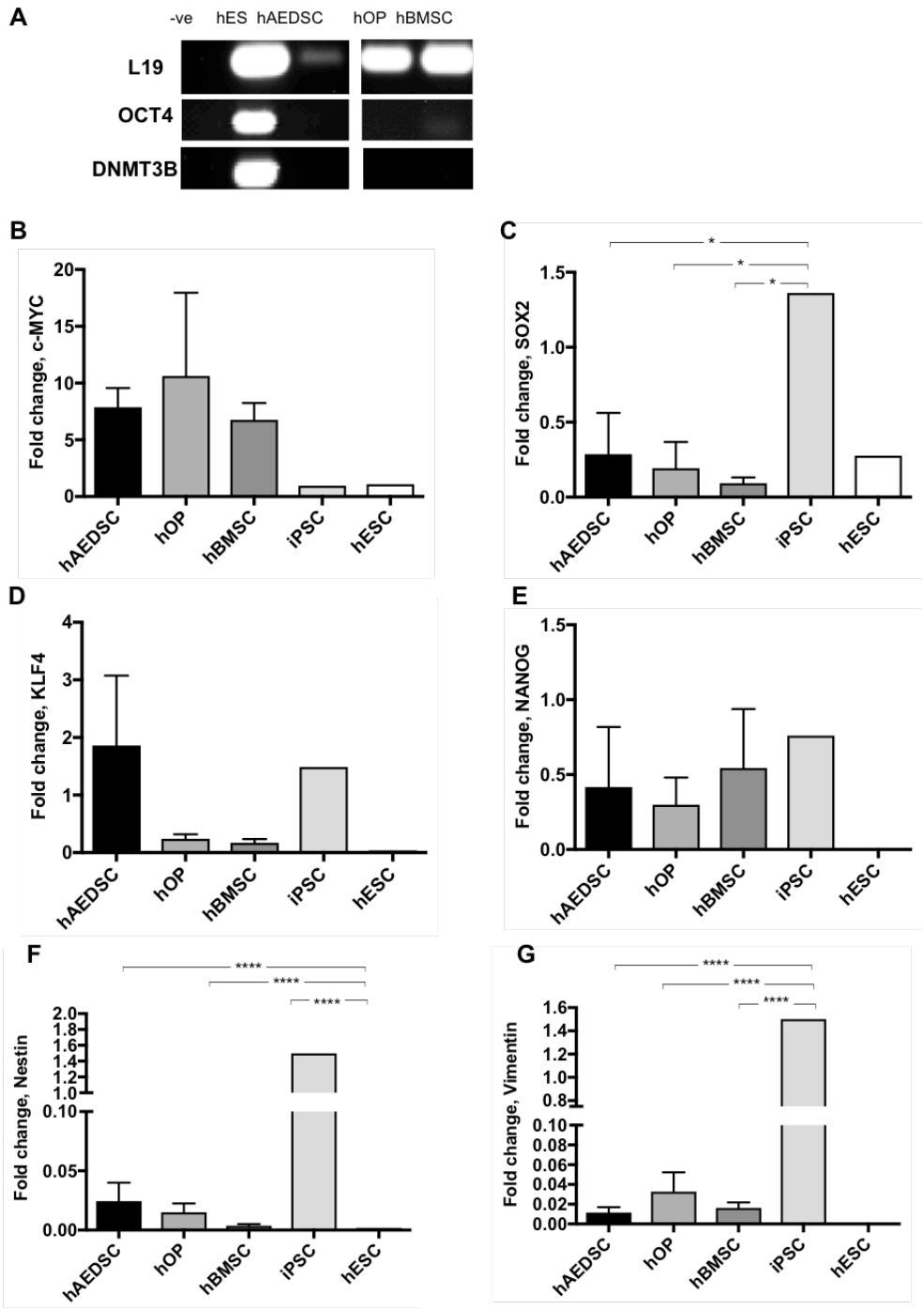

Figure 4.8: Comparison of pluripotency of different osteoprogenitor cell types by gene expression analysis.

A) Expression of OCT4 and DNMT3B by hAEDSC, hOP and hBMSC (representative result from three different cell lines) with human embryonic stem cell (n=1) as positive control and L19 as housekeeping gene. **B-G)** Relative quantification PCR result of expression of pluripotency markers for hAEDSC (n=3), hOP (n=5) and hBMSC (n=5) presented as fold change relative to iPSC (n=2) positive controls. hES; human embryonic stem cells, iPSC; induced pluripotent stem cells, all data are expressed as mean ± SEM, statistical significance; *p<0.05, ****p<0.0001.

was down regulated by 2 fold in hOP when compared with hAEDSC and hBMSC although this difference was not statistically significant. All three cell types did however demonstrate significantly lower levels of vimentin when compared with positive control (Figure 4.8 G). Previous studies have shown expression of vimentin in murine iPSC is similar to that of embryonic fibroblasts but higher than embryonic stem cells whereby the latter upregulated cytoskeletal genes on differentiating (Boraas et al., 2016).

4.2.4.5 Mesenchymal and Skeletogenic Protein expression

Undifferentiated osteoprogenitor cell lines from hAEDSC (n=2), hOP (n=3) and hBMSC (n=3) were analysed for proteins associated with mesenchymal and early osteogenic phenotypes using immunocytochemistry (Figure 4.9).

Stro-1 is a mesenchymal surface marker that has been extensively studied in BMSC. It is associated with stem cell populations which have greater growth and colony forming capacity (Samsonraj et al., 2015). None of the osteoprogenitor cells convincingly exhibited positive staining for STRO-1 (Figure 4.9).

As previously discussed, collagen 1 is the main extracellular matrix protein in bone whilst alkaline phosphatase (ALP) is required for osteoblast mediated mineralisation. The existence of both of these proteins was analysed in undifferentiated osteoprogenitor cells to establish whether there was any baseline expression hinting at osteogenic lineage restriction. Whilst collagen 1 protein expression as seen in all osteoprecursor types (Figure 4.9), not every cell stained positively and the protein was intracellular in distribution. None of the cell types expressed ALP.

Vimentin is recognised as a mesenchymal stem cell marker with proteomic analysis suggesting that it is associated with porcine BMSC migration (Huang et al., 2015) whilst a lack of vimentin was shown to restrict endothelial differentiation of mouse embryonic stem cells (Boraas and Ahsan, 2016). Beyond its original discovery as a neuroepithelial marker (Lendahl et al., 1990), Nestin has also been shown to be expressed in hBMSC (Tondreau et al., 2004). Recently, nestin expression was suggested to correspond with a proangiogenic, multipotent population of BMSC, which are capable of self-renewal and osteochondral differentiation in a mouse model (Méndez-Ferrer et al., 2010). Both nestin and vimentin were co-expressed on hAEDSC, hOP and hBMSC (Figure 4.9). This is in keeping with previous in vitro studies on adipose derived stem cells (Guasti et al., 2012) although to date, there has not been any work published analysing concomitant expression of both these proteins in human osteoblast precursors and bone marrow derived stem cells.

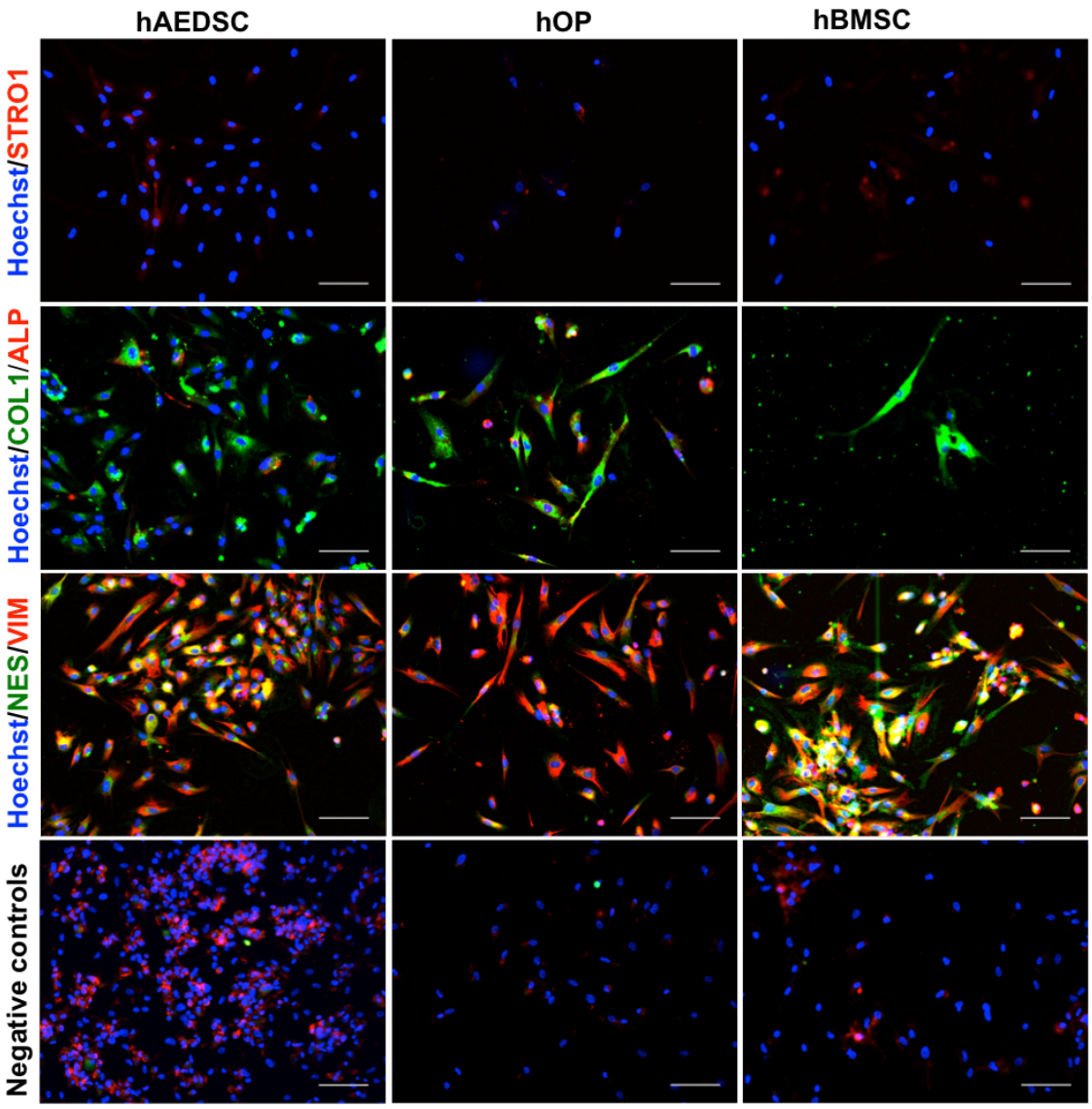

Figure 4.9: Protein expression in osteoprogenitor cells detected by immunocytochemistry.

Immunoflourescent staining for STRO1, COL1, ALP. NES and VIM protein expression by hAEDSC, hOP and hBMSC cells on monolayer culture in expansion media. Images representative of staining from different areas on coverslip and cell lines from hAEDSC (n=2), hOP (n=3) and hBMSC (n=3), Nuclei counterstained with Hoechst (blue), negative controls (no primary antibody) for alexa 488nm anti rabbit (green) and Alexa 594nm anti mouse (red), scale bars; 100um, STRO1; stromal precursor antigen 1, ALP; alkaline phosphatase, Col 1; collagen 1, NES; nestin, VIM; vimentin.

4.2.4.6 Trilineage differentiation potential of osteoprogenitor cells

Osteoprogenitor cell lines (n=3 different lines per group in experimental triplicates) were cultured in control, adipogenic, chondrogenic or osteogenic media to compare differentiation potential (Figure 4.10).

Adipogenesis was achieved on differentiated hAEDSC compared with controls. Oil droplets were also seen on differentiated hOP and hBMSC albeit smaller in quantities when compared with adipogenically-differentiated hAEDSC (Figure 4.10 A). Extraction of Oil red O and subsequent absorbance quantification shows significant increase in relative adipogenic measurement between hAEDSC control and differentiated cells ($p=0.023$). Relative adipogenic measurement was also higher in differentiated hAEDSC compared with hOP ($p=0.021$) and hBMSC ($p=0.0093$).

Alcian blue staining was used to detect chondroid matrix as evidence of chondrogenic differentiation. Staining was stronger in differentiated cells compared with undifferentiated controls amongst all groups (B). Differentiated hOP and hBMSC also produced a deeper blue colour when compared with hAEDSC. Unfortunately, it was not possible to extract the alcian blue in order to quantify the relative chondrogenic measurement.

Osteogenesis was verified using Alizarin red staining (Figure 4.10 C). The morphology of controls (spindle-shaped cells) differed from osteogenically differentiated cells, which aggregated in clusters (Figure 4.10 C). Alizarin staining was stronger and in a dense pattern in differentiated cells consistent with mineral deposition by osteogenically differentiated cells. Extracted Alizarin was quantified and presented as a fold change relative to undifferentiated hAEDSC (Figure 4.10 C). Relative osteogenic measurement showed non-significant differences in baseline measurement in control hOP, hBMSC and hAEDSC. There was a 5.8-fold increase in relative osteogenic measurement in differentiated hAEDSC compared with controls ($p=0.0006$). Relative osteogenic measurement in differentiated hAEDSC was significantly higher than hBMSC ($p=0.0026$) but not hOP ($p=0.1058$). Relative osteogenic measurement in differentiated hOP was 5.7 times higher than control hOP ($p=0.547$) whereas differentiated hBMSC had a 3.2 fold increase compared with control ($p=0.9268$).

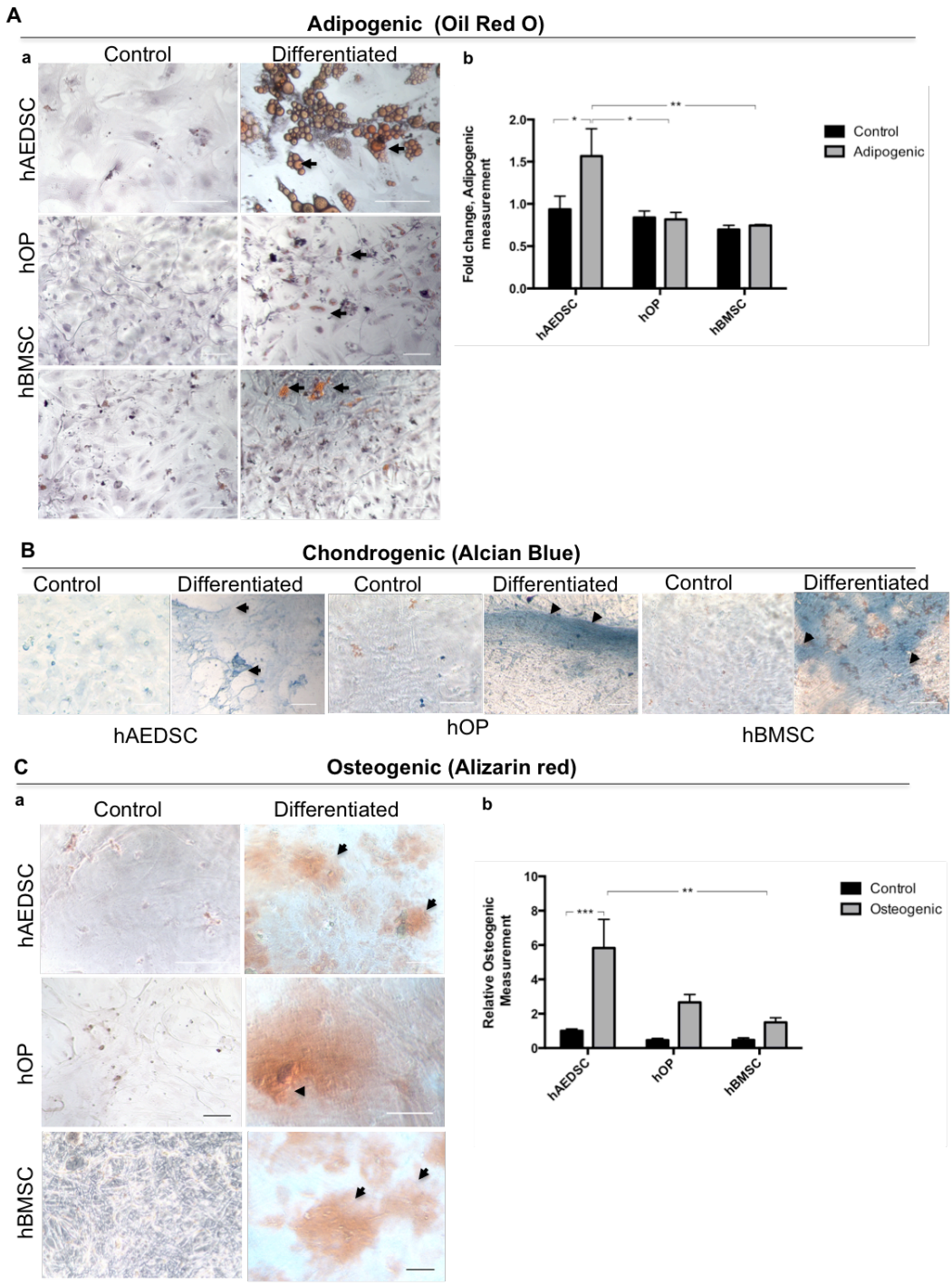

Figure 4.10: Verification of trilineage differentiation on monolayer culture of different osteoprogenitor cell types.

A) Adipogenic differentiation detected using Oil Red O and nuclear counterstaining with haematoxylin (arrows denote oil droplets). Relative adipogenic measurement expressed as fold change compared to undifferentiated hAEDSC (g). **B)** Alcian blue staining to detect chondroid matrix deposition (arrows). **C)** Osteogenic differentiation verified by Alizarin red staining qualitatively (a) and quantitatively (expressed as fold change relative to undifferentiated hAEDSC) (b). Scale bars; 100um, data expressed as mean ± SEM, statistical significance; * $p<0.05$; ** $p<0.01$; *** $p<0.0001$.

4.2.5 Comparison of different osteoprogenitor cells for bone tissue engineering

4.2.5.1 Capacity for osteogenesis on monolayer by osteoprogenitor cells

To compare osteogenic differentiation capability, osteoprogenitor cells were cultured in control or osteogenic differentiation media on plastic monolayer (for 3 weeks Figure 4.11). All differentiated osteoprogenitor cells demonstrated a change in organization and mineral deposition when compared with controls (Figure 4.11 A). Undifferentiated cells maintained a fibroblastic morphology and were organized in a uniform multilayer with little or no mineral deposition whilst differentiated cells aggregated to form multi-layered structures with widespread mineralized nodules (Figure 4.11 A).

Collagen 1 protein was expressed by undifferentiated hAEDSC in an intracellular (cytoplasmic) pattern with differentiated cells demonstrating an extracellular Fibrin meshwork pattern (Figure 4.11 B). This difference in location and pattern of distribution was similarly demonstrated in hOP and hBMSC (Figure 4.11 B).

A key feature of osteoblast maturation is change in cellular appearance from an elongated to a cuboidal shape before finally acquiring a stellate appearance (osteocyte formation). This change in morphology was shown to occur from as early as 15 days in a 3D culture system of immortalised mouse calvarial osteoblast precursor cells (Krishnan et al., 2010). Additionally, nuclear structure has been shown to influence osteogenic differentiation of murine MSC through upregulation of intranuclear actin (Sen et al., 2015). Through analysis of bovine MSC, rearrangement of nuclear architecture through the LAMIN A/C network appeared to be affected by extracellular differentiation cues such as mechanical loading which resulted in changes to nuclear aspect ratio and deformation (Heo et al., 2016b). Whilst it was not possible to assess the appearance of differentiated cells due to 3D clustering and mineralisation, analysis of nuclear shape and size was used to monitor osteogenesis based on evidence that nuclear morphology is influenced by cellular geometry through actin reorganisation in fibroblasts (Li et al., 2014). Nuclei counterstained with Hoechst were segmented analysed for circularity as well as area in ImageJ using the

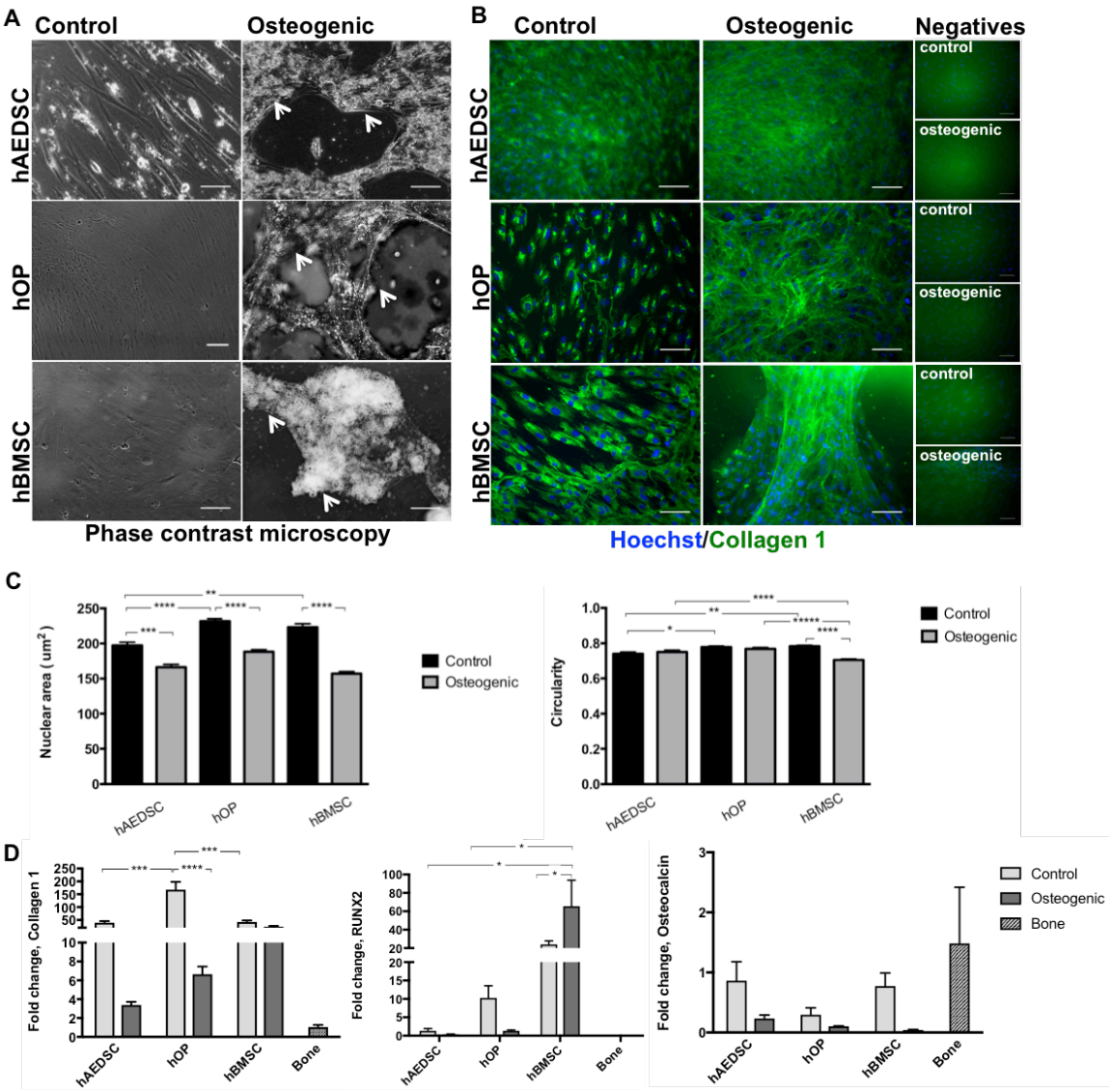

Figure 4.11: Osteogenic differentiation of monolayer cultures of hAEDSC, hOP and hBMSC.

A) Phase contrast imaging illustrating cell aggregation and mineral nodule formation (white arrows) in differentiated cells. **B)** Immunocytochemistry of Collagen (green) expression in control and differentiated cells. **C)** Nuclear morphometry comparing area and circularity of control and differentiated cells. **D)** qPCR for gene expression of collagen 1 and osteocalcin (expressed as fold changes relative to calvarial bone positive control) as well as RUNX2 (expressed as fold changes relative to hAEDSC control as none detected in bone). Nuclei counterstained with Hoechst (blue, negative controls for alexa 488nm anti rabbit, scale bars; 100um, data expressed as mean ± SEM, statistical significance; * $p<0.05$; ** $p<0.01$; *** $p<0.001$, ****$p<0.0001$.

ParticleAnalyzer plugin (Figure 4.11 C). The average nuclear area of undifferentiated hAEDSC was significantly lower than that of control hOP ($p<0.0001$) and hBMSC ($p=0.0011$). Osteogenically differentiated cells exhibited significantly reduced nuclear size (area) compared with their control counterparts in hAEDSC ($p=0.0002$), hOP ($p<0.0001$) and hBMSC ($p<0.0001$) groups. Differentiated cell nuclear size was also greater in hOP compared with hAEDSC ($p=0.035$) and hBMSC ($p<0.0001$). Nuclear circularity was also analysed using ImageJ where roundness is measured from 0-1 (1=perfect circle).

Nuclei of undifferentiated hAEDSC exhibited reduced circularity compared with hOP ($p=0.0439$) and hBMSC ($p=0.006$). Osteogenic differentiated did not significantly affect nuclear circularity compared with controls in hAEDSC ($p=0.964$) and hOP (0.937) but there was a reduction in circularity between differentiated hBMSC and their controls ($p<0.0001$). Differentiated hBMSC had significantly lower nuclear circularity compared with the other differentiated cell types ($p<0.0001$).

Collagen 1 and osteocalcin gene expression were analysed using qPCR with samples normalized to calvarial bone cDNA and expressed as fold changes relative to this positive control (Figure 4.11 D). Whilst collagen 1 protein was upregulated and expressed in an extracellular pattern, gene expression of collagen 1 was down regulated in differentiated samples. Collagen 1 baseline expression was significantly lower in control hAEDSC ($p=0.0002$) and hBMSC ($p=0.0002$) when compared with undifferentiated hOP. Differentiated cells exhibited collagen 1 downregulation when compared to undifferentiated controls in hOP ($p=0.0001$). There was little change in *COL1* expression between control and differentiated hBMSC ($p=0.0759$). Osteocalcin gene expression was similarly downregulated in differentiated cells compared with undifferentiated controls although this was not significantly different (Figure 4.11 D). Whilst collagen 1 was upregulated in control hOP compared with bone ($p<0.0001$), there was no significant difference between the remaining (control and differentiated) cells and bone with regards to *COL1* and *OSC* expression. Taken together, these results could suggest that the early stage of osteogenic differentiation (whereby *COL1* is upregulated then suppressed) may have been

surpassed and immature bone formed since at the more mature stage osteocalcin is expected to be upregulated (Açil et al., 2016). *RUNX2* which is increased in early and late stage osteoblast maturation (Rutkovskiy et al., 2016) was not expressed in the bone control but was significantly upregulated in differentiated hBMSC compared with hAEDSC and hOP.

4.2.5.2 The impact of 3D culture on extracellular matrix deposition and maturation by different osteoprogenitor cells

Osteoprogenitor cells were encapsulated in Fibrin scaffolds and cultured in either control or osteogenic differentiation media for three weeks to compare osteoinductive capacity in 3D culture (Figure 4.12). Osteogenic differentiation was achieved using three-cell types (n=3 different cell lines cultured in experimental triplicates), which were immunoflourescently stained for COL1 then imaged as whole mount specimens (Figure 4.12 A). COL1 protein expression was more evident on osteogenically differentiated samples although the difference between control and osteogenic differentiated samples was not as impressive in hOP and hBMSC as is evident in hAEDSC. COL1 was detected in all osteoprecursor cell types in both control and osteogenic culture conditions. The COL1 expressed by control hAEDSC appeared cytoplasmic compared with extracellular staining evident on the osteogenic. COL1 staining appeared extracellular in hOP and hBMSC cultured in control or osteogenic conditions. The networks of collagen fibres were more easily visualised in osteogenic hOP and hBMSC compared with controls.

Alizarin red staining demonstrated mineralization in control and osteogenic cellularised scaffolds amongst all osteoprogenitor groups (Figure 4.12 B). Whilst Alizarin staining appeared more dense in hBMSC (control and osteogenic) compared with hAEDSC and hBMSC, this was not reflected when alizarin was extracted and quantified (Figure 4.12 C). Relative osteogenic measurement was analysed by extracting alizarin red from samples (n=3 different cell lines, experimental triplicates) then expressed as a fraction of control hAEDSC to compare fold change in alizarin quantification. There is no difference in relative osteogenic measurement between differentiated cells compared with controls in hAEDSC ($p=0.92$), hOP ($p=0.96$) and hBMSC ($p=0.92$). There was also no significant difference in relative osteogenic measurement amongst the different cell groups. This contrasts with the results seen on plastic monolayer (C) and could suggest an osteoinductive effect inferred by Fibrin and a 3D culture system, which are both known to stimulate osteogenic differentiation (Catelas et al., 2006, Vielreicher et al., 2015) or that alizarin extraction from the Fibrin gels was incomplete.

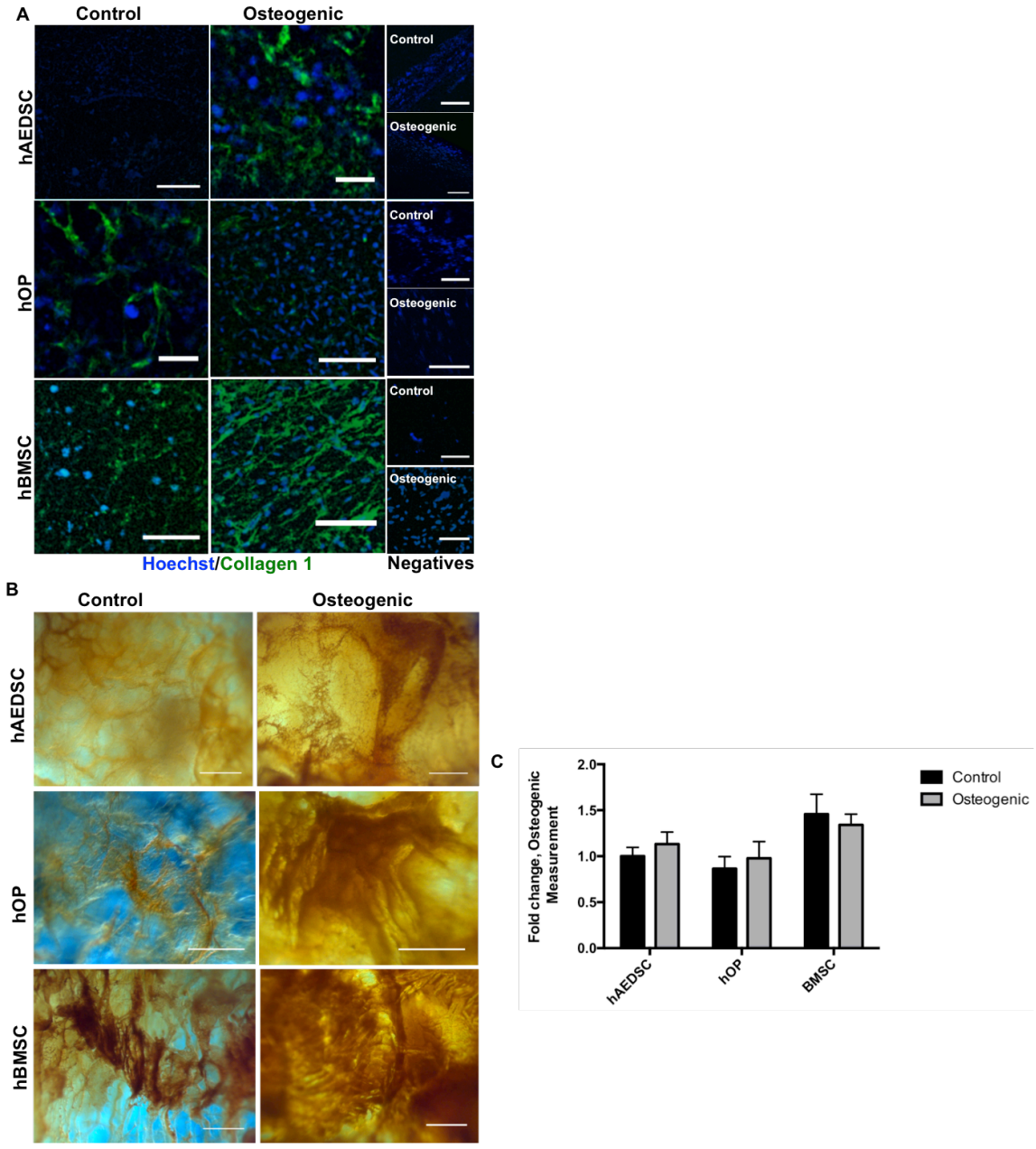

Figure 4.12: Comparison of extracellular matrix formation and mineralisation by hAEDSC, hOP and hBMSC osteogenically differentiated on Fibrin scaffolds.

A) Immunofluorescence of Collagen (green) expression of 3D cultures in control and osteogenic differentiation conditions. **B)** Alizarin red staining of cellularised gels C) Quantification of extracted alizarin red (results expressed as fold change relative to control hAEDSC). Scale bars; 100um, nuclei counterstained with Hoechst; negative controls for alexa 488nm anti rabbit, data expressed as mean ± SEM.

To further analyse the extracellular collagen produced by differentiated cells, OrientationJ was used to assess orientation and coherency of fibres. The protocols used to measure collagen directionality derived from SHG scans were adapted to analysed immunoflourescently stained samples by modifying adjustable parameters (minimum coherency and energy) in OrientationJ to take into account image quality as detailed in Chapter 2. Collagen networks were easily seen in bone samples with S-colour-surveys and histograms showing a relatively high amount of isotropy as evidenced by appearance of bundles of fibres and a single histogram peak (Figure 4.13, Figure 4.14).

The effect of Fibrin3D culture on collagen network formation was assessed by comparing cells cultured on plastic monolayer compared with Fibrin (A). As discussed in the previous section, collagen distribution appeared extracellular and fibrillar after osteogenic differentiation on plastic as can be seen in the circular segmented particles on S-colour images of controls compared with the longer fibrils seen in differentiated samples (Figure 4.13 B). Differentiated hAEDSC show disordered orientations of Fibrin as evidenced by wide distributions on the histogram plot whilst there was no evidence of fibre formation in the hAEDSC controls (Figure 4.14 A). Control hOP in contrast have an isotropic orientation which is visible on the immunoflourescent image (parallel arrangement of cells) and a sharp narrow histogram peak. Osteogenic dififerentiation of these cells results in extracellular collagen expression with a more isotropic distribution. Whilst hBMSC, appear to express some extracellular collagen as can be seen on the grey and S-colour-surverys, this changes to organised isotopic thick bundles after osteogenic differentiation.

Culture in Fibrin gels appears to induce extracellular collagen formation even in the absence of osteogenic differentiation media (Figure 4.13 A). This is however associated with a wide distribution of orientation as evidenced by the S-colour-survey maps and histogram plots (Figure 4.13 B, Figure 4.14 A). Osteogenically differentiated cells appear to contain collagen networks with greater isotropy than their undifferentiated controls with hOP and hBMSC plots more closely resembling that of bone.

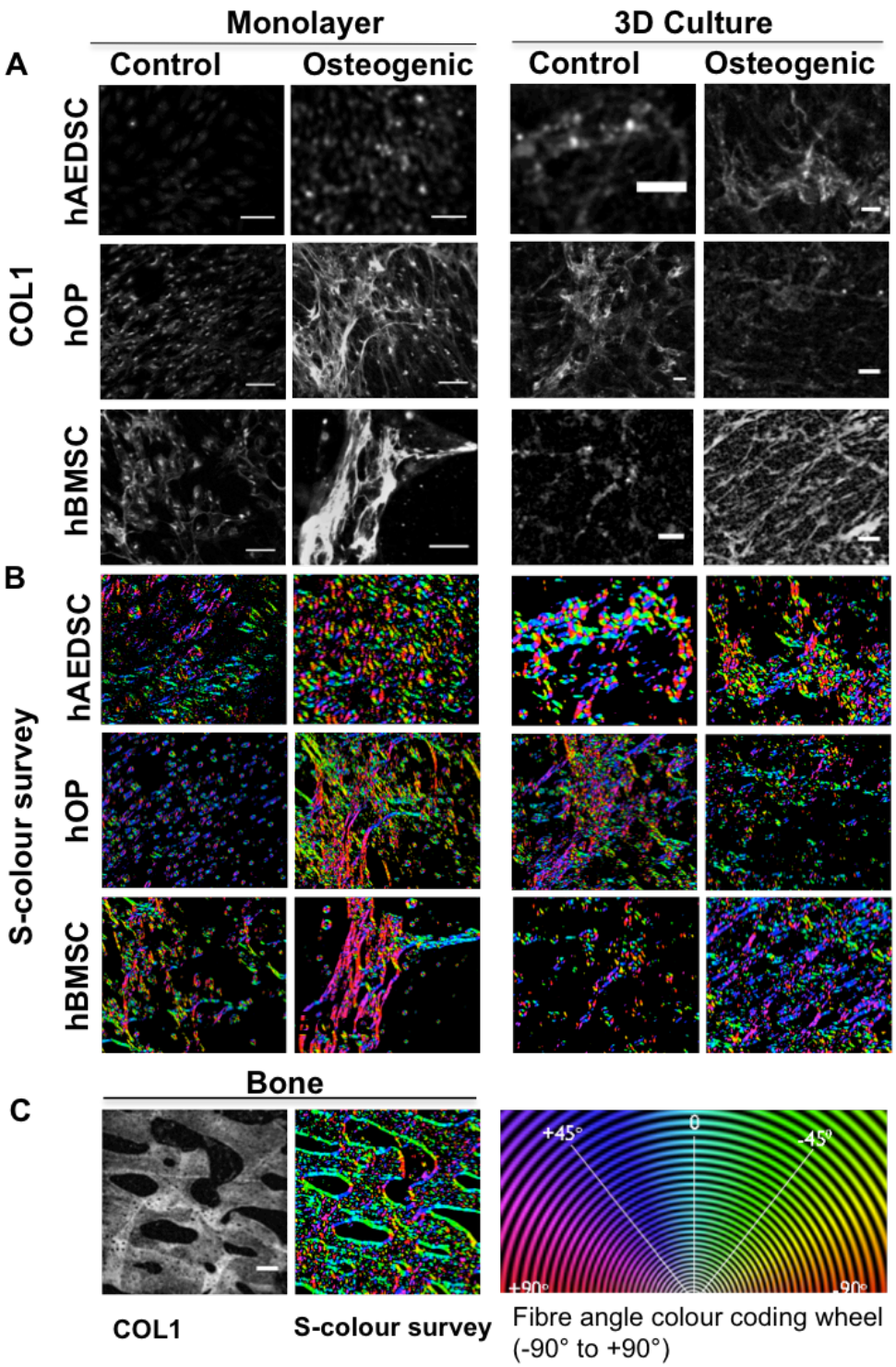

Figure 4.13: Comparison of collagen fibre arrangement by osteogenically differentiated osteoprogenitor cells in monolayer and 3D culture.

A) Immunoflourescent staining for Collagen protein (grey) in hAEDSC, hOP, and hBMSC cultured in monolayer or Fibrin gels in control or osteogenically differentiated media. **B)**. S-colour-surveys demonstrate local collagen fibre orientations as represented by the colour wheel. **C)** Collagen fibre orientation in bone positive control. Scale bar; 100um.

The coherency coefficient was also isolated from OrientationJ using uniform weights to further quantify directionality of collagen fibres in 3D culture (Figure 4.14 B). Control and differentiated hAEDSC and hOP as well as undifferentiated. hBMSC all had significantly lower coherency values than bone positive controls ($p<0.0001$) suggesting lower isotropy. Control hBMSC also demonstrated lower coherency than undifferentiated hAEDSC ($p<0.05$). Osteogenic differentiation prompted increased coherency in HBMSC when compared to controls ($p<0.0001$) and differentiated hAEDSC ($p<0.0001$).

Taken together, these results demonstrate that whilst 3D culture has osteoinductive properties on osteoprogenitor cells, osteogenic differentiation medium is still required to generate organised extracellular collagen. This echoes work by Vielreicher et al who analysed extracellular collagen network formation using second harmonic generation imaging to demonstrate the importance of media composition and 3D culture systems on osteogenic differentiation by way of analysing.

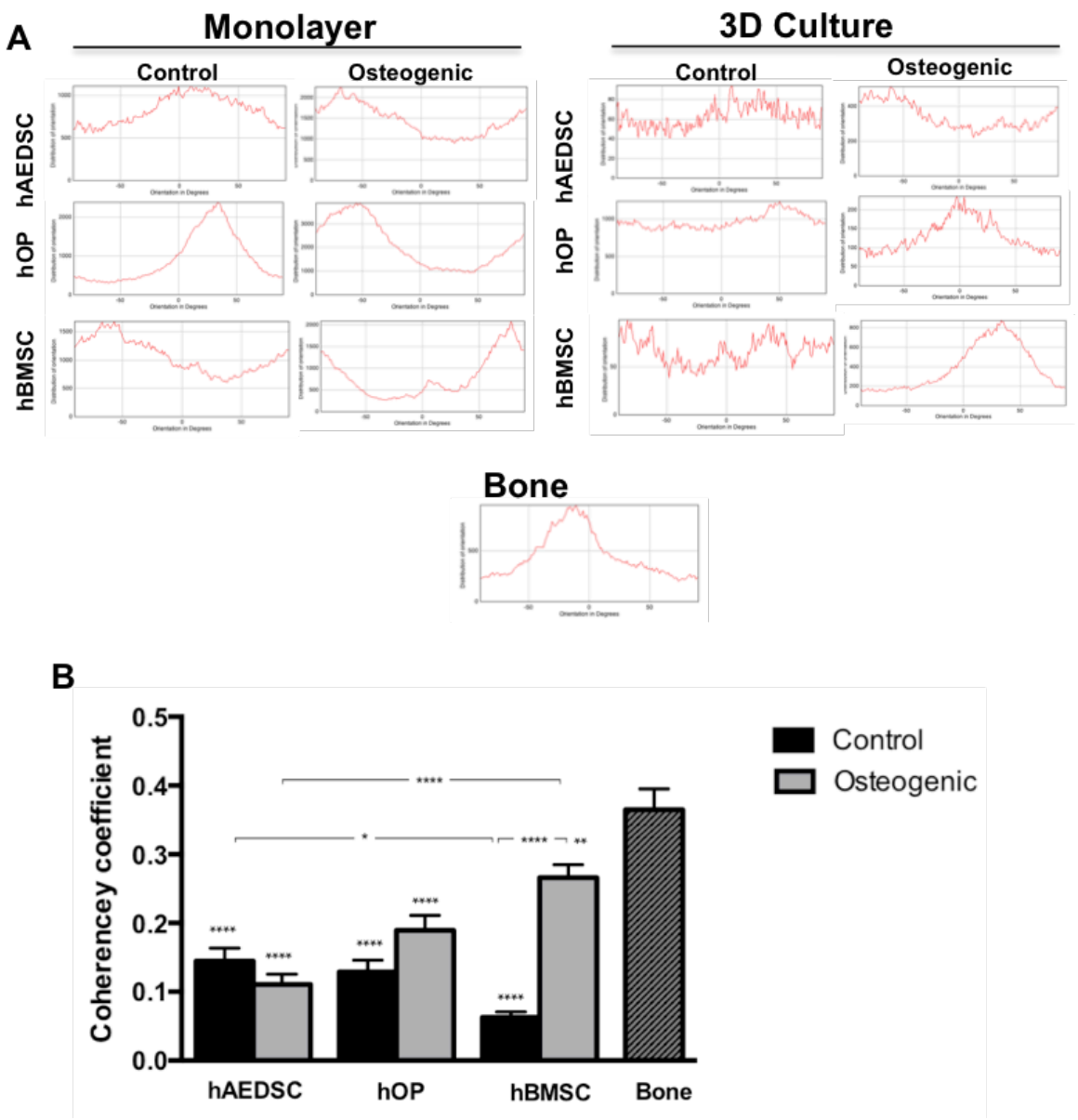

Figure 4.14: Analysis of collagen fibre orientation in extracellular protein deposited by osteoprogenitor cells osteogenically differentiated in monolayer or 3D culture as detected by immunoflourescent staining.

A) Histograms plot the distribution of the collagen fibre orientations in protein deposited by hAEDSC, hOP and hBMSC cultured in control or osteogenic media for 3 weeks either in monolayer or fibrin gels (3D culture). Paediatric calvarial bone section is provided as a positive control. **B)** Coherency coefficient as a measure of collagen directionality in hAEDSC, hOP and hBMSC cultured in fibrin compared with bone positive control. Data represented as mean ± SEM, statistically significant difference compared to bone expressed as * over bar whilst difference between groups is denoted with a line spanning both; **p<0.01; ***p<0.001; ****p<0.0001.

collagen fibre arrangement in rat BMSC (Vielreicher et al., 2015).

4.2.5.3 Impact of in vivo culture on behaviour of osteoprogenitor cells

Vascularisation is key to bone formation and survival. To assess viability and osteogenic differentiation of 3D hAEDSC, hOP and hBMSC cultures, samples were engrafted onto the chick chorioallantoic membrane (CAM) for 7 days after a period of 3 weeks in control or osteogenic differentiation media (n=4 per condition, one cell line per lineage used).

At harvest, all cellularised Fibrin constructs were encased by the CAM vasculature with evidence of neoangiogenesis into the engineered tissues (Figure 4.15 A). Fixed frozen sections were stained with Lamin A/C and Hoechst nuclear dye to distinguish between human and chick cells (do not stain for Lamin A/C). There appears to presence of both human (double-labelled) and chick cells in control and differentiated samples (Figure 4.15 B). This suggests a degree of host cell infiltration from the CAM that maybe related to the neoangiogensis as reflected in the stereoscopic images of the ex ovo samples or could be an inflammatory response.

MacNeal's tetrachrome with Von Kossa counterstain were then used to verify bone formation and assess the impact of vascularisation on maturity on Osteoprogenitor cells (Figure 4.15 C). All samples stained for MacNeal's/Von Kossa to varying degrees. Generally, undifferentiated control pre implanted samples ("Pre CAM") expressed predominantly immature osteoid (blue) with fewer mature mineralised (black) nodules compared with osteogenically differentiated cells. After incubation in ovo ("post CAM"), osteoid formation seemed to be increased (deeper blue staining) with a larger density of mineralised nodule deposition. To quantify this, bone volume to total volume ratio was calculated on binarized stained sections using ImageJ (Figure 4.15 D). In ovo implantation shows a significant increase in BV:TV in osteogenic hAEDSC when compared with Pre CAM control hAEDSC ($p=0.037$). Whilst osteogenic media produced a significant increase in differentiated hOP compared with controls ($p=0.023$) prior to implantation and an increase in BV:TV in Post CAM control compared with Pre CAM control ($p=0.0029$), there was no significant difference due to culture medium amongst Post CAM samples. Similarly, the impact of in ovo culture on hBMSC was to Significantly increase BV:TV in Post CAM undifferentiated ($p=0.0026$) and differentiated

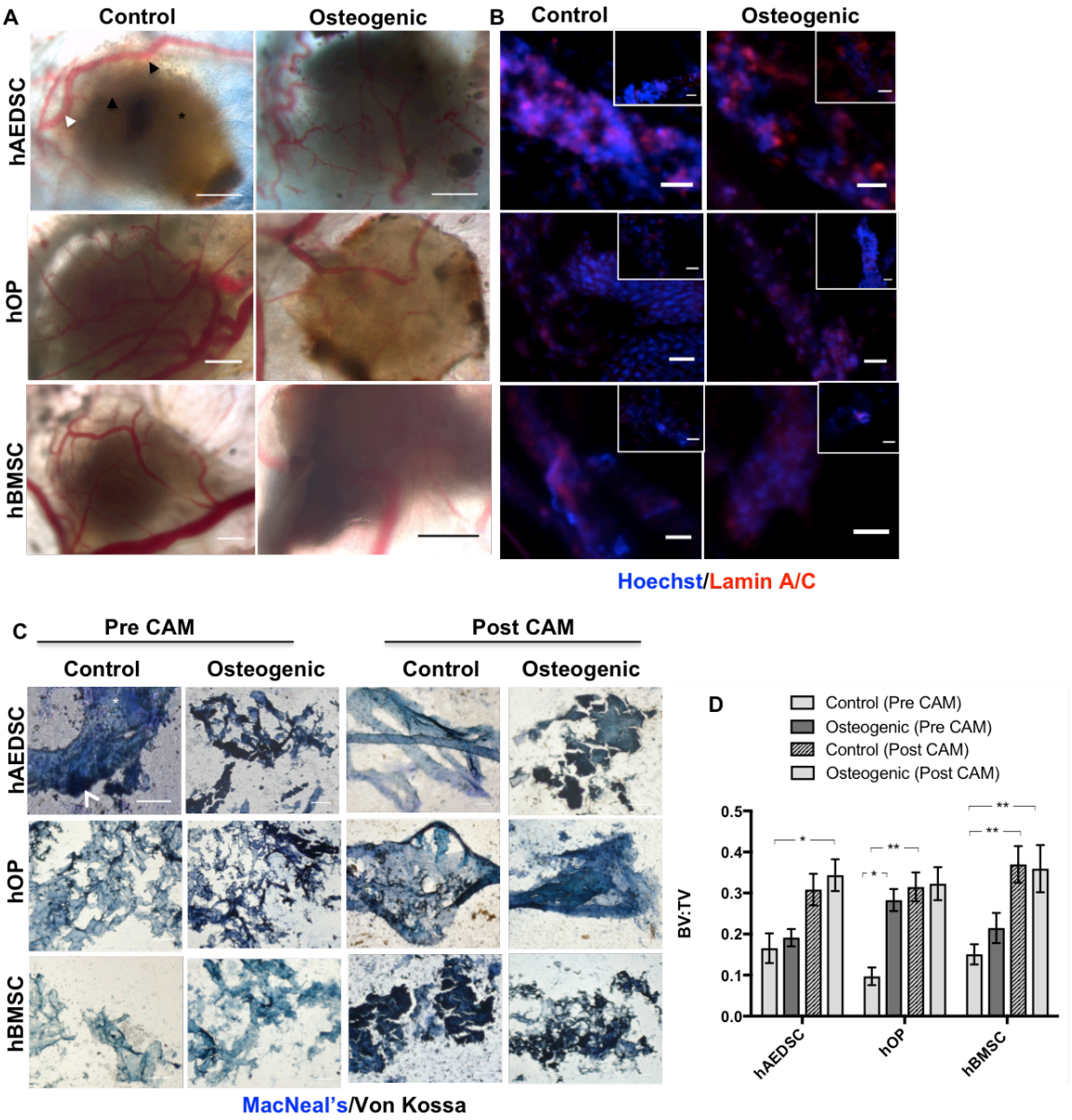

Figure 4.15: Vascularisation and mineral density formation by osteoprogenitor cells on Fibrin after chorioallantoic membrane (CAM) grafting.

A) In ovo images of vascularisation of hAEDSC, hOP and hBMSC cultured on Fibrin for 3 weeks in control or osteogenic media then CAM grafted for 7 days cultures (white arrow demonstrates blood vessel) **B)** Differentiating between chick and human cells by immunoflourescent staining of fixed sections with Lamin A/C (red) and nuclei counterstained with Hoechst (blue). **C)** Mineralisation and osteoid formation of control and osteogenically differentiated 3D cultures pre and post CAM grafting verified with MacNeal's tetrachrome stain (blue corresponds with osteoid) and Von Kossa (black corresponds with mineralisation). **C)** Bone volume fraction **(**Bone volume to total volume ratio (BV:TV)) of pre and post CAM cellularised gels. Negative controls for alexa 488nm anti rabbit (inset), scale bars; A (0.5mm); B (20um); C (100um), data expressed as mean ± SEM, statistical significance; *p<0.05; **p<0.01.

(p=0.0054) samples compared with pre CAM controls. Thus, irrespective of tissue source or medium, BV:TV increased after in vivo implantation. Furthermore, there was no significant difference in mineralisation between the different differentiated Osteoprogenitor cell types Pre or Post CAM.

4.3 Discussion

Whilst the structure and composition of adult bones (in particular those concerning weight-bearing) has been well studied, there is much less information available regarding paediatric craniofacial bone. As such, there is no defined reference by which researchers and clinicians can use to design or evaluate tissue engineered craniofacial bones. To date, there has also not been a comprehensive comparison of paediatric somatic osteoprogenitor cells for the purposes of bone regeneration and tissue engineering. Furthermore, whilst human bone marrow and adipose derived mesenchymal stem cells have been characterized, this has not been the case for human osteoprecursor cells resident within paediatric bone. This study is the first to use non-syndromic paediatric calvarial bone samples to define the biological properties of what is currently the “gold-standard” autologous graft for facial reconstruction. Additionally, this is the first comparison of three of the most accessible tissue-specific paediatric osteoprogenitor cell types (hAEDSC, hOP and hBMSC) with regards to “stemness” and osteoregenerative potential.

4.3.1 Characterization of calvarial bone grafts provides reference of paediatric intramembranous bone biology and maturity

In order for tissue engineering to generate clinically relevant craniofacial bone, it is important to clearly characterise the biomolecular properties of the target tissue and define markers to evaluate the success of any bioengineered constructs. Until now, studies tend to use generic markers of differentiation such as early and late osteogenic gene expression, extracellular matrix protein secretion and mineralization, which verify osteoinduction at a molecular level. Furthermore, differentiated samples are not usually assessed against a positive bone control but simply compared against undifferentiated controls or unseeded biomaterials depending on the nature of the experiment. Whilst this approach may provide an overview of osteogenic potential and induction, it fails to establish maturity of bone or reflect even the basic differences in bone properties due to embryological origin, age and function. In section 4.2.1, I assessed and defined a specific set of markers that would provide a meaningful reference for generating bone substitutes for craniofacial reconstruction.

Calvarial bone grafts are commonly used as autologous implants for reconstruction of midfacial defects in both adults and children with an established safety and efficacy profile (Tessier et al., 2005, Smolka et al., 2005) thus, they potentially represented a reasonable reference for bioengineering midface bones. The samples used in this thesis were obtained from sagittal bone sections from children undergoing spring-assisted cranioplasty for non syndromic sagittal suture craniosynostosis (NSSC) and as such analysis aimed to verify whether these bones could be a suitable reference for normal paediatric cancellous bone.

Study of bone at the macro and microscopic level can provide important information regarding its architecture and composition. Mineralisation is routinely used as a marker of osteogenesis. Whilst both Von Kossa and Alizarin red staining revealed widespread deposition of minerals in the extracellular matrix, this does not differentiate between mature and immature bone alone. For this reason, MacNeal's tetrachrome/Von Kossa staining proved useful in that it revealed widespread osteoid deposition and mineralization foci. Additionally, uCT scanning demonstrated trabecular architecture to bones, comprising a diploë sandwiched between an inner and outer cortex, and a mineral density of around 48% that did not relate to age. Cellular composition is also important in maintaining the balance between osteogenesis and remodelling. It is not usually considered in papers assessing osteogenic differentiation but is probably important in achieving functionally competent bone. Through routine histology, it was shown that distinct cell populations (osteoblasts, osteocytes and osteoclasts) can be clearly identified on histology and were able to determine the density of these cells in the calvarial bone samples. Whilst such an extensive structural and histomorphometric analysis has not been previously reported on paediatric calvarial bone, together these findings are in keeping with previously characterisation of calvarial bone architecture (Rühli et al., 2007) although that study used an adult dry skull. Similarly, an analysis of bone thickness and density using clinical paediatric CT scans did not find a correlation with age in the area corresponding to where the bone samples originated from (Smith et al., 2012). The measurements of cell composition revealed greater osteocyte and osteoclast density than in a

previous study of cellular composition in parietal bone samples although this was in a much older population (aged 16-79) (Torres-Lagares et al., 2010).

Organisation of collagen fibrils and mineral in human cortical bone has been shown to determine its mechanical properties in a combined model of intracortical porosity and apatite crystal orientation which related these variables to the elastic properties of bone (Baumann et al., 2012). Based on this structure-function relationship, it was suspected that ultrastructural analysis of bone maybe a useful indirect measure of biomechanics and could provide a useful marker of mature mesenchymal craniofacial bone. A larger number of imaging techniques exist for analysis of these properties of which uCT, second harmonic generation scanning and confocal laser scanning were used due to availability, application to tissue engineered samples and potential for generating qualitative and quantitative data (Georgiadis et al., 2016). In the calvarial bone samples, collagen expression and orientation were analysed using both Immunoflourescent staining for collagen 1 and SHG scanning. Both these techniques showed abundance of this protein in the bone extracellular matrix but the detail of collagen fibres were more apparent using the latter. Computational analysis of orientation and arrangement of these collagen fibrils shows increased isotropy in the cortices of the bone and disorder of fibres in the middle. Interestingly, this arrangement of aligned collagen fibres interspersed with disordered collagen and ground substance has been demonstrated in human femoral (cortical) bones (Georgiadis et al., 2016). The key difference, however is whilst in that study the organised fibres were arranged as a grid with disordered collagen occupying the spaces between them, the samples appear to possess aligned fibres lining the lacunae with the anisotropic fibres located within the lacunar matrix.

Bone was also characterised using gene expression for osteogenic markers in order to evaluate their usefulness in verifying mature bone formation. The samples expressed collagen 1, osteocalcin and osterix in keeping with previously published characterisation of mouse calvarial bone which showed that these genes are osteoblast specific and required for extracellular matrix deposition by osteoblasts (Nakashima and de Crombrugghe, 2003).

A major limitation of this work is the use of calvarial non-syndromic craniosynostotic bone as a positive control. Whilst some of the results seem to echo findings of normal bone previously published, Stamper et al found differences in fibroblast growth factor and extracellular matrix mediated adhesion between control osteoblasts and those from non syndromic sagittal craniosynostotic patients that maybe related to vascularisation (Stamper et al., 2011). More recently, a study comparing osteoblasts from sagittal craniosynostotic bone with controls found higher alkaline phosphatase activity and reduced proliferation in the former suggesting enhanced differentiation capacity (Park et al., 2015). Together these data suggest a difference at the cellular level in craniosynostotic bone, which may impact its suitability as a normal reference. Future work should aim to compare these samples with calvarial bone from a control population, which is likely to be biopsies or excisional samples from neoplastic lesions given that it is not ethically possible to obtain such specimens from completely healthy children.

Biomolecular characterisation of the paediatric bone tissue has provided important information on the properties of calvarial bone from non-syndromic craniosynostotic patients and indicates that this bone maybe normal compared with published findings. As bone is a hierarchical tissue composed of multiple subunits of organic and inorganic matrix containing cellular elements, I have established references, which could be used to verify osteogenesis at a macroscopic, microstructural and ultrastructural level (Figure 4.16).

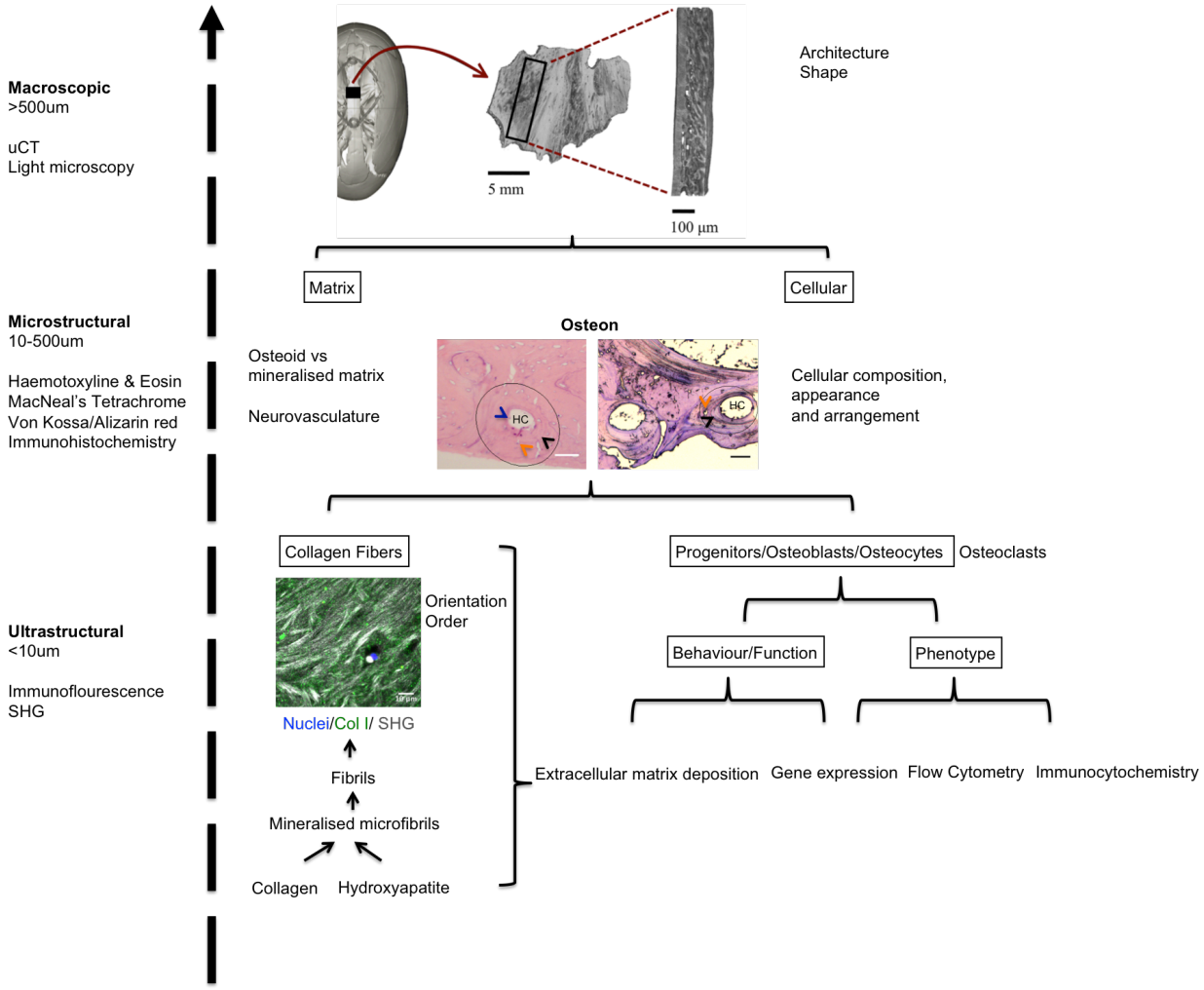

Figure 4.16: Hierarchy based calvarial bone analysis.

Representation of the main structures defining bone composition at a macroscopic, microstructural and ultra structural level and which markers may be useful in verifying these. Outlined boxes represent features investigated in this chapter. Blue arrow represents blood vessel, black arrow points to lamella, and orange arrow to osteocyte. uCT; micro CT, HC; Haversian canal, COL1; collagen 1, SHG; second harmonic generation scanning.

4.3.2 Paediatric adipose and bone are home to tissue-specific stem cells.

It was possible to isolate hAEDSC and hOP from explant culture of very small amounts of fat and bone tissue respectively. Additionally, hBMSC were derived from the bone samples by flushing the bone marrow cavities and culturing the supernatant. To the best of my knowledge, this is the first time, these tissues have been characterised and compared in parallel with regards to their clinical suitability as a stem cell source for paediatric bone tissue engineering.

My dataset revealed that there was no significant difference in how many cells could be isolated from wet tissue. Given the outcomes of the analysis of cellular composition of bone and evidence that a minimum seeding density maybe required to optimise tissue engineering on a biomaterial scaffold in human and rat BMSC (Wu et al., 2015, Holy et al., 2000), the results suggest that the number of cells obtained from small amounts of tissue by any of the osteoprogenitor stem cell sources is potentially large enough to generate bone tissue and as such enhances the potential for clinical application.

As expected, both hAEDSC and hBMSC expressed similar surface marker profiles consistent with that which is expected of mesenchymal stem cells (Lv et al., 2014) and had previously been demonstrated in paediatric hAEDSC and hADSC by our group (Guasti et al., 2012, New et al., 2015). Interestingly, in my dataset, the hOP also displayed similar profiles for mesenchymal and non-mesenchymal surface markers suggesting that these cells display either some characteristics of mesenchymal stem cells or the lack of specificity of these surface markers with regards to identification of somatic stem cells.

To further characterise these cells, analysis of pluripotent genes against iPSC and hESC controls was performed and found that all of the osteoprogenitor cells expressed *c-MYC, SOX2, KLF4* and *NANONG* as shown in previous studies on paediatric hAEDSC (Guasti et al., 2012, New et al., 2015) and adult hBMSC (Adegani et al., 2013). Both *OCT4* and *NANOG* have been shown to be important in maintaining self renewal of MSC through DNA methyltransferase 1 (*DNMT1*) whereby knock down of either results in inhibited proliferation and trilineage differentiation capacity in vitro (Tsai et al., 2012). This difference could indicate that only the hBMSC in my dataset were capable of self-renewal or that

the hOP and hAEDSC maintain pluripotency through another mechanism as previously described in a study of hADSC and hBMSC which displayed proliferative and differentiation capabilities despite absence of *OCT4* and *SOX2* and independently of *NANOG* (Pierantozzi et al., 2011). DNA methyltransferase 3B (*DNMT3B*) was previously shown to be expressed in similar adipose derived stem cell populations by our group (Guasti et al., 2012), it was absent in all of the Osteoprogenitor cell lines analysed in this study. Previously deficiency of *DNMT3B* in mouse embryonic stem cells resulted in disruption of methylation of both *OCT4* and *NANOG* gene expression thus suggesting a key role in differentiation and proliferation (Li et al., 2007). However, more recent work on *DNMT1/DNMT3A/DNMT3B* knock out mouse embryos has shown that ESC from these models still retained self renewal and survival during differentiation into extra embryonic lineages (Sakaue et al., 2010). Furthermore, absence of *DNMT3A* and *DNMT3B* did not affect nuclear reprogramming of mouse embryonic fibroblasts (Pawlak and Jaenisch, 2011), hence, the importance of *DNMT3B* on somatic stem cell survival, self renewal and differentiation may vary according to the cell type and thus its absence in my cells might not be significant with regards to characterisation of their “stemness”.

Regardless of tissue origin, all cells expressed Nestin and Vimentin genes on qPCR (at levels significantly lower than hESC/iPSC controls) and proteins as evidenced by immunoflourescent staining. Both of these cytoplasmic filaments have previously been shown to be expressed in mouse ESC and iPSC albeit downregulated when compared to embryonic fibroblasts thus suggesting that less differentiated cells are associated with a less developed cytoskeleton (Boraas et al., 2016). Collagen 1 protein expression was visualised to further characterise the cells and only found positive intracellular staining in a minority of cells, which may indicate spontaneous differentiation. This is supported by the fact that the majority of these cells exhibit similar staining after 3 weeks in vitro culture in control media. Worthy of note, is the absence of STRO-1 expression in these cells which is associated with increased growth and ectopic bone formation capacity in hBMSC (Samsonraj et al., 2015).

A key defining feature of mesenchymal stem cells is the ability to undergo trilineage differentiation (Dominici et al., 2006). All three cell types underwent

adipogenic, chondrogenic and osteogenic differentiation when cultured in relevant media for three weeks although hAEDSC showed significantly increased adipogenic differentiation which supports previous studies that MSC derived from adipose tissue displayed superior adipogenesis than bone marrow derived cells due to increased upregulation of late stage adipogenic genes (Liu et al., 2007). There was also a significant increase in alizarin red quantification in osteogenically differentiated hAEDSC compared with hBMSC contradicting previous comparative analysis of MSC derived from rat adipose, periosteum and bone marrow tissues which found enhanced osteogenesis in vitro and in vivo of cells derived from the periosteum and bone marrow (Hayashi et al., 2008). Alizarin red alone is however a poor indicator of mineral nodule formation as it can also detect non specific mineralisation caused by reduced cell viability rather than bone formation (Orriss et al., 2014).

A major limitation of this study is the use of tissues from patients with pre-existing diseases such as non-syndromic sagittal craniosynostosis and Craniofacial Microsomia. Since healthy children do not normally undergo these procedures, it maybe of use to compare these cells from tissues acquired from children undergoing biopsies for infection or trauma that could provide a closer control to normal cells. The cells used were at a relatively early passage but greater information regarding self renewal, proliferation and differentiation could be achieved from repeating this analysis on different stages of early and late passages. Additionally, analysis of a larger number of cell lines would be useful in distinguishing between patient-specific factors and clonal analysis would control for the heterogeneity of cell populations to allow direct comparison between these cell types.

Taken together these results indicate that in my dataset of paediatric patients, the fat, bone and bone marrow are home to three cell types with pluripotent potential. There does however exist a difference in expression of genes associated with pluripotency and the extent of trilineage differentiation between my osteoprogenitor cells and from results found in similar cell types by other research groups. Possible explanations for this maybe that due to the heterogeneous nature of MSC populations, these differences maybe due to patient-specific factors, culture conditions or the fact that these cells were

derived from paediatric tissues which have been less well characterised than adult or animal sources in the literature. Further analysis is required to compare these cells and assess generalizability of this data.

4.3.3 Potential for osteogenic maturation by paediatric osteoprogenitor cells derived from different tissue sources

Osteogenic differentiation was achieved on plastic in all three Osteoprogenitor cell types although differences in extracellular matrix appearance, nuclear morphology and gene expression suggest differences in maturity of bone formation.

Qualitatively, all differentiated cells appeared to deposit mineral nodules in a trabecular pattern and collagen 1 extracellularly as expected in the osteoblast maturation stage (Orriss et al., 2014, Rutkovskiy et al., 2016). Analysis of fibre morphology did however reveal that only differentiated hOP and hBMSC demonstrated collagen fibre networks on monolayer. Further differences were detected between the different osteoprogenitor cells with regards to nuclear size and circularity with all differentiated cells representing smaller nuclei but only hBMSC exhibiting a corresponding reduction in circularity. These ultrastructural findings are important in characterising osteogenic differentiation as nuclear morphometry has been shown to correspond with mesenchymal stem cell differentiation. Not only has intranuclear actin filament formation been shown to correspond with osteogenic gene upregulation in vitro in mouse BMSC and hBMSC (Sen et al., 2015) but deformation of nuclei through culture of rat MSC on a micro patterned surface resulted in loss of nuclear area and regularity and enhanced osteogenesis (Liu et al., 2016a).

The stages of osteoblast maturation involve a sequence of up/downregulation of specific genes as the cells progress from an early stage of proliferation to extracellular matrix deposition, matrix maturation and finally mineralisation (Owen et al., 1990). The gene expression analysis revealed downregulation of Collagen and Osteocalcin in all three cell types although this was only significantly reduced in differentiated hOP compared with controls. *RUNX2* expression was downregulated in differentiated hOP and hAEDSC but upregulated in differentiated hBMSC when compared with their controls

although none of these differences was significant. Previously, Owen et al identified a pattern of osteogenic gene expression which corresponds with stages of bone maturation in rat calvarial osteoblasts revealing that *COL1* expression peaks in early cultures and should reduce with increasing maturation whilst osteopontin, osteocalcin and *ALP* gene expression peaks between 15-20 days of culture before down regulating (Owen et al., 1990). A later study comparing human osteoblast cultures to this rat model of osteoblast maturation found a similar downregulation of collagen 1 and later downregulation of alkaline phosphatase (day 25) and no upregulation of osteocalcin and the absence of mineralisation although this failure to reach the mineralisation matrix phase may have been due to absence of β-glycerosphosphate in these cultures (Owen et al., 1990). *RUNX2* is the master regulator of osteogenic differentiation, is upregulated early on in differentiation of osteoprogenitors to pre-osteoblasts, and is required for late maturation. Absence of *RUNX2* in mice resulted in reduced expression of osteogenic genes such as *ALP*, osteocalcin and osteopontin, abnormal osteoblast morphology and failure of intramembranous and enchondral ossification of the embryonic skeletons (Komori et al., 1997). More recently, two isoforms of *RUNX2* have been shown to be expressed at different stages of foetal osteoblast differentiation, ”type 1” is upregulated in the early stage whilst “type 2” is expressed around day 14 in the rat foetal calvarial osteoblasts and 16 in mouse preosteoblast cell line (Banerjee et al., 2001). This could possibly explain the significantly increased expression of *RUNX2* in differentiated hBMSC compared with the other cell types despite the fact that all other markers of differentiation suggest a late stage of maturity in hBMSC.

In comparing the osteoprogenitor cells for osteogenic ability, I have shown that all cell types are capable of differentiating on monolayer as evidenced by simple and routinely used markers such as collagen 1 protein expression, alizarin red and mineralisation. More in depth ultrastructural analysis of collagen fibre networks and subcellular examination of nuclear morphometry has shown some differences in maturation of the extracellular matrix in favour of hBMSC and to a lesser extent hOP. Gene expression and mineralisation showed a similar pattern to the rat osteoblast maturation model. Together these results could be

used to build a more detailed picture of paediatric osteoprogenitor cell osteogenic differentiation, elucidate which markers maybe best to detect each stage and identify areas for optimisation if different differentiation time-points are analysed. A number of improvements could be made to this study in order to validate the results and further highlight the stages governing transition from MSC to mature osteoblast in my cells. The most important of these would be to repeat these experiments and analyse at multiple time-points (between day 0 and day 40) the different markers I have described. A crucial addition to this analysis should be Lamin A/C to monitor nuclear changes and an assay to detect alkaline phosphatase enzymatic activity. Cell cytoskeletal changes would also be of immense importance and as such analysis in the form of atomic force microscopy (to detail actin filament changes) and SEM would allow monitoring of these changes and relate them to any in nuclear morphology. Histological analysis would also be important to look for osteocytes and osteoid formation in order to gain an idea of the extent of maturation as the matrix mineralisation stage has been shown to stimulate osteocyte maturation in rat cells (Irie et al., 2008). I also only looked at collagen 1 protein but the extracellular matrix is also composed of other types of non-collagenous extracellular matrix proteins such as osteonectin, bone Sialoprotein and osteopontin. Measuring mineral nodule size and number would also be of immense use in that it would provide an overview of the architectural maturity of the differentiated cells. As ever, use of multiple cell lines from patients with different diagnoses could also help in assessing the generalizability of these results depending on the disease.

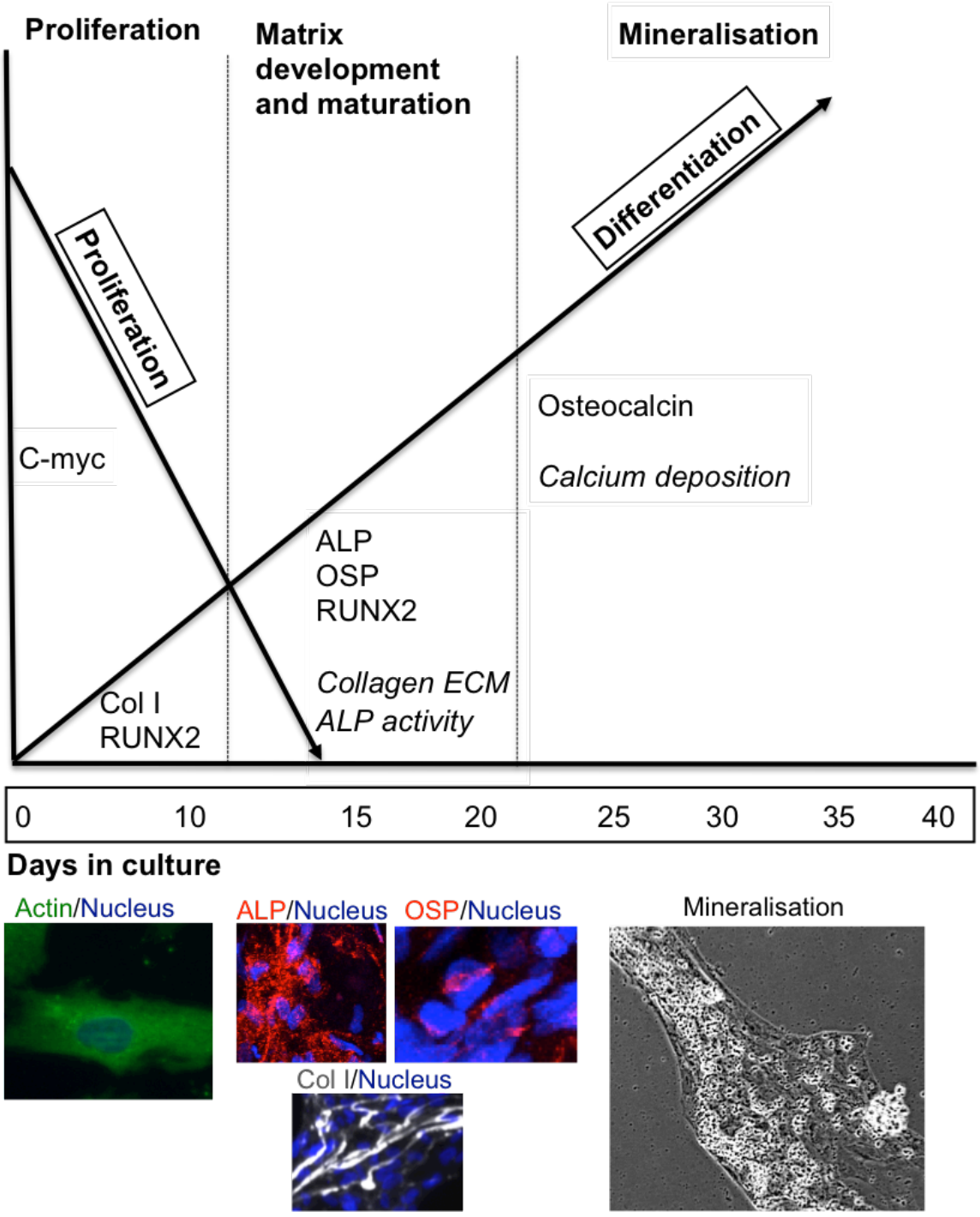

Figure 4.17: Proposed osteoprogenitor cell differentiation stages.

Osteoprogenitor cells derived from adipose and bone show osteogenic maturation in a similar manner to the rat osteoblast maturation model (Owen et al., 1990). I propose possible markers for monitoring the different stages of osteogenesis using gene expression, protein immunofluorescence, alkaline phosphatase activity and imaging of mineralisation and hypothesis the different stages at which these maybe most useful. Figure adapted from (Owen et al., 1990). Col1; collagen 1, ALP; alkaline phosphatase, OSP; osteopontin, RUNX2; runt-related transcription factor 2, ECM; extracellular matrix.

4.3.4 3D culture systems and vascularization promote osteoinduction but priming is required to achieve more mature osteogenesis

To ascertain the feasibility of using these cells for bone tissue engineering and in order to optimise osteogenic differentiation, I tested their behaviour in 3D culture and the impact of vascularisation.

The effect of 3D culture using Fibrin gels was to induce extracellular deposition of collagen 1 protein and mineralisation in undifferentiated cells as well as those cultured in osteogenic medium. This is unsurprising as MSC condensation is a key part of inducing differentiation and in on going osteoblast maturation as was evident by the nodular arrangement of differentiating cells in monolayer. In a study of craniofacial skeletogenesis in chick embryos it was revealed that condensation resulted in increasing of preosteoblast cell numbers which then progressed to maturation but it did not stimulate initial differentiation of MSC (Dunlop and Hall, 1995). Additionally, 3D pellet culture was previously found to accelerate human preosteoblast cell differentiation and maturation compared with monolayer culture (Jähn et al., 2010). This maybe relevant to these findings in that cells differentiated in osteogenic media still displayed collagen fibre networks with greater coherency values closer to bone controls. Furthermore, hBMSC once again displayed a more mature phenotype in the orientation and alignment of collagen networks compared with the other cell types and with similar cells grown on monolayer.

As blood supply is vital to bone formation and that previous work has demonstrated that human preosteoblast differentiation was most vulnerable to oxygen deprivation at the stage of matrix maturation (Nicolaije et al., 2013). The results indicate that in vivo culture (even for a short period) results in encasement and apparent vascular ingrowth of vessels into the engrafted cells. Whether this is due to the cells themselves or the fibrin (or both) is unclear but it also appears to promote bone formation and maturation as evidenced by increased density of mineral deposition. Lamin A/C staining was not only useful to distinguish human and chick cells but, as expression of this protein is also known to be important in osteogenic differentiation of hBMSC (Bermeo et al., 2015), it further supports evidence that 3D Fibrin culture stimulates some osteogenesis even in the absence of differentiation media. This also hints at the

potential pathway through which these cells differentiate through activation of Wnt/β-catenin signalling (Bermeo et al., 2015). Recently, vasculature has also been shown to provide a template and guide bone morphogenesis in mouse embryo (Ben Shoham et al., 2016). Although these findings related to long bone was during enchondral ossification, the in vivo experiment could be repeated using cells at earlier stages of differentiation to assess in detail the impact of vascularisation on maturation.

The stimulatory effect of vascularisation on mineralisation and bone maturation demonstrated by these results is also in keeping with current knowledge on osteogenesis. A recent study demonstrated that co-culture of hBMSC with peripheral blood mononuclear cells and vascular endothelial growth factor (VEGF) increased ALP activity and mineralisation in vitro (Joensuu et al., 2015). This is also supported by an earlier in vitro co-culture model of hOP and hBMSC with human vascular endothelial cells (HUVEC) or progenitor derived endothelial cells (PDEC) resulted in enhanced mineralisation (Thébaud et al., 2012). Interestingly, hADSC were shown to simultaneously contribute and respond to vascularisation in a study using murine cells. Najdanovic et al differentiated ADSC into endothelial like cells and showed that when combined with a bone matrix carrier this stimulated vascularisation and yielded an increased number of osteoblast-like cells as well as organised appearing extracellular collagen deposition when implanted subcutaneously in mice compared with the biomaterial alone (Najdanović et al., 2015).

Taken together these results indicate that both 3D culture and vascularisation enhance osteogenic differentiation of the osteoprogenitor cells but osteoinductive media is still required to produce mature bone formation. Whilst hBMSC exhibit enhanced osteogenesis compared with hOP and hBMSC, this advantage is somewhat small as they, still lack the architectural ultrastructural architecture associated displayed by the positive calvarial bone controls. The key limitation of this analysis was the use of only one cell line for each patient for the vascularisation study and as such the results can only be used to make a cautious statement with more cell lines required for a concrete conclusion. In order to fully appreciate the impact of 3D culture, it would be of use to visualise cell-cell interactions and changes in cytoskeletal morphology then compare with

those in monolayer and in the differentiated nodules. Whilst I analysed collagen fibres using collagen 1 immunoflourescent staining which is a verified method, SHG would provide greater detail and future studies should use this method. In addition to Von Kossa/MacNeal's, a Goldener's trichrome stain and uCT could provide further detail regarding the extent and pattern of matrix maturation. The vascularisation study would also benefit from performing at multiple time points (for instance after 1, 2 and 3 weeks of differentiation) to fully appreciate the impact of vascularisation in accelerating osteogenesis. It may also be useful to stain for any osteoclasts that may have infiltrated the samples from the chick circulation and whether this might have had an effect on these results.

4.3.5 Implications for bone tissue engineering

The results have demonstrated that three easily accessible osteoprogenitor cell sources can be derived from paediatric adipose and bone tissues. These cells display pluripotent features and late stage osteogenic differentiation can be achieved with all of them although further work is required to achieve the complex architecture of calvarial bone. I have also demonstrated that cell differentiation can be guided by the physical environment by way of 3D culture and through a simple in vivo culture system that I can further accelerate the maturity of these bioengineered tissues. A key limitation of this study is the assumption, albeit tentative, that these tissues are normal and the lack of osteoprogenitor cells from Treacher Collins Syndrome patients. As the disease is rare, I have not yet been able to obtain tissue samples from these patients in order to isolate cells and verify their suitability for bone tissue engineering. Given that Craniofacial microsomia and Treacher Collins Syndrome are both diseases affecting neural crest patterning rather than bone biology, I have for now assumed that the behaviour of hAEDSC in CM patients may be similar to that of TCS. Clearly, analysis of cells from TCS will be required to validate this.

The clinical relevance of this work is that bone bioengineering for paediatric patients can be tailored to the patient by harvesting osteoprogenitor cells at the time of resection of adipose or bone tissue depending on the clinical presentation and management of the patient. As hAEDSC showed promise as an osteoprogenitor cell source and because I have access to a relatively large volume of adipose tissue from a variety of patients including those with CM,

these cells were further investigated with regards to bone bioengineering in the rest of this thesis to discover an appropriate scaffold and the impact of in vivo implantation.

4.4 Conclusions

This chapter has provided an extensive characterization of calvarial bone grafts previously not available and provides a reference of bone biology and maturity relevant to paediatric craniofacial tissue. I have also confirmed previous findings that paediatric adipose and bone are home to populations of tissue-specific stem cells and that these are capable of a mature stage of osteogenic differentiation further enhanced by 3D culture and vascularisation.

In the next chapter, hAEDSC will be investigated for their osteogenic differentiation capabilities on a bioabsorbable scaffold in order to find a suitable cell-scaffold combination to bioengineer bone.

Chapter 5 Biomaterials For Bioengineering Paediatric Bones

5.1 Introduction

The highly complex mechanical and physiological functions of bone means it is virtually impossible to replace with foreign body implants alone. Additionally, bone is heavily dependent on a vascular supply for its growth and survival meaning that autologous bone grafts are limited to reconstructing small defects. Vascularised bone flaps are also limited to smaller sized defects as they generate a significant donor site morbidity, which must be offset by the benefits of reconstruction. Tissue engineering offers the potential to fabricate autologous bone implants that bypass the limitations of traditional reconstructive methods. Whilst there exists a number of easily accessible osteoprogenitor cell sources that have been shown to undergo osteogenic differentiation, there is also a need for a scaffold to directly or indirectly support osteoinduction and maturation of these cells. In Chapter 4, I demonstrated that osteoprogenitor cells from paediatric bone and adipose tissues can be osteogenically differentiated and that 3D culture and vascularisation can be used to achieve a more mature phenotype. In this section of the thesis, I design a bioabsorbable scaffold specifically for use in bone tissue engineering.

Several studies have attempted to identify the optimal physiochemical and structural properties of biomaterials required to promote osteogenesis (Terheyden H et al., 2001b, Terheyden H et al., 2001a). The most basic requirement for a scaffold is to promote cell adhesion, survival and differentiation. In the case of bone, the ability to support vascularization is also critical. Additionally, bioabsorbable scaffolds are more desirable in children whose skeleton continues to grow, as multiple surgeries are required to remove and/or replace permanent implants. Historically, a wide-variety of different scaffolds have been proposed for bone tissue engineering ranging from natural materials such as collagen (Weisgerber et al., 2015) and fibrin (Machado et al., 2015) to synthetic biomaterials in the form of polymers (Rossi et al., 2013), all of which have highlighted distinct advantages and disadvantages (Table 5.1). Increasingly, biomaterials that attempt to recreate and stimulate the extracellular matrix and stem-cell niche are being generated with the aim of enhancing cell adhesion, proliferation and differentiation (Nii et al., 2013, Minardi et al., 2015).

Table 5.1: Commonly used scaffolds for tissue engineering

Category	Scaffold	Advantages	Disadvantages
Natural	Alginate (polysaccharide derived from seaweed)	Licensed for clinical use. Hydrogel or microparticle. Easy functionalization and combined with other scaffolds.	Rapid degradation Low mechanical strength
	Collagen (extracellular matrix component)	Easily incorporates growth factors. Licensed for clinical use. Easily combined with other scaffolds.	
	Fibrin (protein involved in clotting)	Licensed for clinical use. Osteoinductive properties. Mass producible.	
	Gelatin (proteins/peptides derived from collagen)	Available in many forms including hydrogels	
	Silk (protein polymer)	Low immunogenicity. Controlled degradation.	No long term degradation data
	Decellularised matrix (fabricated by decellularisation of tissues)	Frequently used in preclinical and clinical research. Low inflammation. Preserves extracellular architecture and components.	Lengthy fabrication. Immunogenicity. Not easily reproducible.
Synthetic	Polygcolic acid (polyester porous scaffold)	Biodegradable. Mass producible. Easily modified to alter topography or functionalise.	Degradation products induce inflammation
	Polyethylene glycol (polyether compound)	Licensed for clinical use. Mass producible. Low toxicity. Biodegradable.	Low mechanical strength Rapid degradation
	Polycaprolactone (biodegradable polymer)	Mass producible. Easily modified. Provides mechanical strength.	Unstable degradation
	Poly-l-lactic acid (biodegradable polymer)	Mass producible. Easy surface modification to alter topography. Mechanical strength.	Rapid degradation
Natural-Synthetic composite scaffolds	Alginate/O-carboxymethyl chitosan (O-CMC) Biodegradable hydrogel	Mass producible. Mimics extracellular matrix. Easily injected into tissues.	Rapid degradation. Low mechanical strength.
	PLGA/hydrogel (biodegradable hydrogel)	Mass producible. Mechanical strength.	Rapid degradation.
	Alginate/poly vinyl alcohol (PVA) (biodegradable polymer)	Available as a hydrogel or porous scaffold. Mass producible Provides mechanical strength. Mimics extracellular matrix.	Unstable degradation.

The advantages and limitations of the most commonly used bioabsorbable biomaterials as applied to bone bioengineering. Adapted from (Ibrahim et al., 2016a).

5.1.1 The importance of scaffold microstructure in bone tissue engineering

It is well known that the migration, adherence, survival and differentiation of cells can be affected by the structural properties of scaffolds (Polo-Corrales et al., 2014, Ferlin et al., 2016). An increasingly popular approach to scaffold design has been to generate biomimetic materials in order to reproduce the impact of the extracellular matrix and tissue microenvironment that naturally direct cell fate (Marinkovic et al., 2016). Two key scaffold properties identified to date with regards to directing stem cell fate are topography and porosimtery.

Surface topography is known to influence MSC biology and behaviour with recent studies demonstrating that surface concavities on a calcium phosphate biomaterial can promote cell proliferation and osteogenic differentiation in a size-dependent manner (Urquia Edreira et al., 2016). Nanotopography has also been shown to drive osteogenic differentiation of MSC through manipulating cytoskeletal structure and intracellular signalling (Ahn et al., 2014). This effect has also been used to modify and optimise osteogenic differentiation and mineralisation of MSC on pre-existing scaffolds such as titanium in vitro (García-Gareta et al., 2015, Tan et al., 2014). In vivo studies have also provided evidence that nanotopography enhances osseointegration of calcium phosphate-coated titanium implants through increased osteoprogenitor and osteoclast cell activity (Jimbo et al., 2011). Further evidence of the effect of surface properties on hADSC behaviour was also demonstrated through plasma modification of a nanocomposite scaffold which resulted in enhanced cell adhesion, proliferation and preferentially directed osteogenic differentiation depending on the modification(Griffin et al., 2017).

Porosimetry is also an important determinant of osteoprogenitor cell behaviour and vascularisation (Sicchieri et al., 2012). Most recently, smaller pore sizes (200-300um) on calcium phosphate scaffolds have been shown to have increased osteoinductive and mechanical strength when used to repair bone defects in rabbits (Zhao et al., 2017). This relationship is likely to be more complex as Chang et al demonstrated that smaller pore sizes (188um) on titanium scaffolds promoted BMSC proliferation and differentiation in vitro but

larger pore sizes were associated with increased bone ingrowth in vivo (Chang et al., 2016). Larger pore size in hydroxyapatite scaffolds was also revealed to accelerate angiogenesis and the amount as well as pattern of bone formation when implanted heterotropically in dogs (Li et al., 2016). Greater porosity is also associated with increased mineralisation of MSC loaded b-tricalcium phosphate scaffolds in vivo (Kasten et al., 2008).

5.1.2 Biomaterials to induce osteogenesis of osteoprogenitor cells

Hydrogels such as fibrin present an attractive option for use as a scaffold in bone tissue engineering. Fibrin is bioabsorbable, already approved for use in clinical practice and has been known to promote MSC osteogenesis and vascularization (Lohse et al., 2012). Furthermore, fibrin can be decorated with osteoinductive components such as hydroxyapatite crystals or growth factors to stimulate osteogenesis when implanted in rat defects (Machado et al., 2015). The structural support afforded by hydrogels and the mechanical strength is a key limitation. Biomimetic scaffolds which combine fibrin and hydroxyapatite-β-tricalcium have been shown to harness the effect of hMSC proliferation and osteogenesis associated with fibrin with the additional benefit of increasing the mechanical strength (Linsley et al., 2016).

Nanotechnology permits the generation of customised scaffolds that combine the mechanical strength and biological molecules required to optimize cell differentiation. It also allows surface modification to alter nanotopography and architecture in order to direct cell behaviour. Scaffolds can also be generated in a reproducible manner with rapid-prototyping and mass-production possible (Gao et al., 2014a). The qualities that make nanomaterials particularly suited for use as a scaffold in bone tissue engineering include mechanical strength, biocompatibility, controlled biodegradation, an easily modifiable surface and porous structure which can promote cell proliferation and vascularisation (Rossi et al., 2013).

One such versatile nanomaterial is polyhedral oligomeric silsesquioxane-poly(Caprolactone-urea)urethane (POSS-PCL). POSS-PCL is a biodegradeable nanocomposite that can be fabricated into a flat disc-like scaffold (“cast”) that

supports monolayer cell growth or a porous (“coagulated”) form for 3D cell culture. It is an easily customisable scaffold whose structure can be modified to affect surface, mechanical and architectural properties.(Chawla et al., 2014, Griffin et al., 2017). A number of studies have shown that POSS-PCL can support growth of hMSC (Chawla et al., 2014) and even co-culture of epithelial and chondrogenically differentiated cells (New et al., 2016, Teoh et al., 2015).

The complexity of bone structure, function and physiology poses a number of challenges with regards to finding the ideal scaffold. This is further complicated by the fact that vascularisation is essential for bone survival and maturation. Given that there has not been a single biomaterial to date, which has fulfilled all these requirements, it is likely that a combination of available scaffolds may provide a better solution. Composite scaffolds could provide the biomimetic properties of the extracellular matrix bestowed by natural scaffolds such as hydrogels whilst possessing the mechanical strength, mass production and ease of surface modification that the synthetic scaffolds provide (Table 5.1).

In the previous chapter, I characterised paediatric calvarial bone grafts to establish a standard to assess bioengineered bone. In this section of the thesis, this data is used to design a biomimetic scaffold tailored for osteogenic differentiation of human adipose derived stem cells.

5.2 Results

5.2.1 Scaffold characterisation

5.2.1.1 Porosimetry

Coagulated POSS-PCL was compared with paediatric calvarial bone to evaluate architecture using µCT reconstructions from representatively sampled areas taken from the top, middle and bottom of the scanned region (n=6) (Figure 5.1). Volumetric representations of the µCT data show both bone and coagulated POSS-PCL are comprised of an inner lattice of solid struts and have a compact surface layer. Heat map representations of the interconnecting processes show a non-uniform spacing in both bone and the polymer also there appears to be greater heterogeneity in bone.

POSS-PCL scaffolds contained similar porosity to native bone samples. Pore size was however significantly reduced in the scaffolds ($p<0.0001$). Bone trabeculae are the network of interconnected calcified processes, which give rise to the spongy structure associated with bones commonly found in the craniofacial region. As demonstrated in the previous chapter, the cellular and protein components are also deposited on these trabeculae whilst bone marrow resides within the pores. I compared the biomaterial struts with bone trabeculae for “trabecular size” and ‘trabecular density’. The size of ‘trabeculae’ was significantly larger in bone ($p<0.00001$) but density was similar.

5.2.1.2 Material properties of cast and coagulated POSS-PCL

The two forms of POSS-PCL (cast and coagulated) were compared for surface and mechanical properties prior to sterilisation ascertain their base line (n=6 of each condition). Images acquired through reflections microscopy demonstrate differences in surface topography between the two forms as expected. Roughness was significantly greater in coagulated samples ($p<0.01$). Mechanical strength as defined by the Young’s modulus did not however differ between the two forms ($p=0.13$) (Figure 5.2).

A

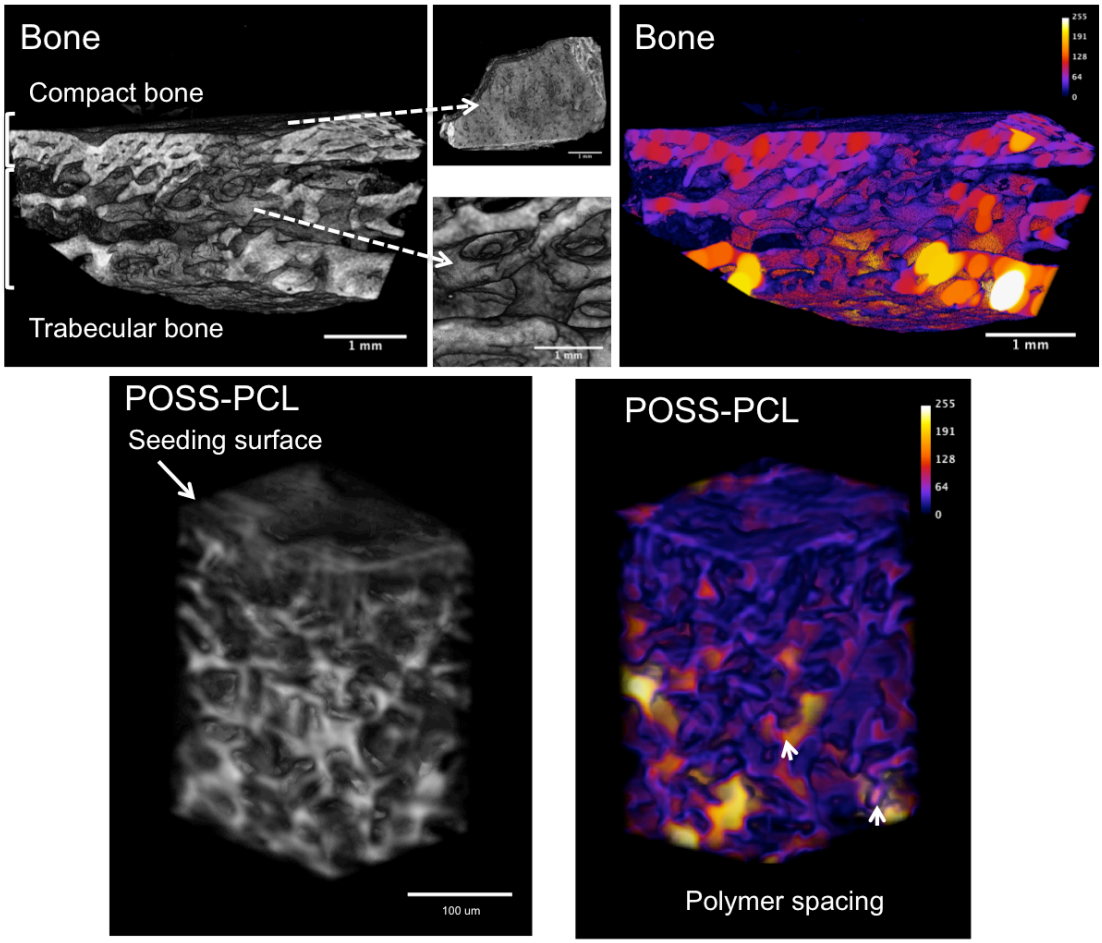

B

	Porosity (%)	Pore size (um)	Trabecular Size (um)	Trabecular density (um^-3)
Bone (n=6)	51.78 ± 3.2	437.67 ± 18.78	488.33 ± 93.06	0.009 ± 0.002
POSS-PCL (n=6)	63.5 ± 9	184.03 ± 5.35 ****	105.85 ± 3.81****	2.35^{-5} ± 2.0x10^{-6}

Figure 5.1: Comparison of porosimetry between coagulated POSS-PCL and paediatric calvarial bone by Commonly used scaffolds for tissue engineering by µCT analysis.

A) 3D reconstruction of bone and POSS-PCL showing trabecular structure of both. The difference between the compact outer layer of bone and the inner spongy layer (arrows) is replicated by the seeding surface and more porous core of POSS-PCL. Heat maps illustrate the trabecular density and (yellow is thickest) revealing thinner but similarly spaced trabeculae in the scaffold**. B)** Quantitative analysis demonstrates smaller pore and trabecular size in POSS-PCL. Statistical significance; ****p<0.00001.

5.2.2 Comparison of different sterilisation methods on biomaterial properties and cell behaviour

A key requirement for use of this scaffold in research and clinical application is a reproducible and safe sterilisation method. Four of the most common and readily available methods of sterilisation (autoclaving, UV light, de-contaminating agent (Decon 90) and ethanol) were compared for their suitability.

5.2.2.1 The impact of sterilisation on surface topography of cast and coagulated POSS-PCL

Topographic heat maps of the scaffold surface (n=6 of each) reveal visible differences, in particular for ethanol and autoclaving, in roughness between the different sterilisation techniques on both cast and coagulated POSS-PCL (Figure 5.3 A). This is further demonstrated on quantitative analysis of the root mean square deviation (Rq) to compare each sterilisation method against its unsterilized control. Surface roughness is significantly greater in coagulated POSS-PCL compared with cast ($p<0.0001$). Ethanol has the greatest effect on topography with surface roughness increasing in both cast ($p=0.0001$) and coagulated POSS-PCL ($p=0.003$). UV significantly reduces surface roughness in cast POSS-PCL ($p=0.0011$) whilst Decon treatment increases Rq ($p=0.0012$). Neither of these treatments significantly affects surface roughness on coagulated POSS-PCL. Autoclaving reduces roughness of cast scaffolds in that surface topography appears flattened and Rq is reduced ($p=0.0004$). Autoclaved coagulated surfaces have increased roughness ($p=0.039$).

5.2.2.2 Effect of sterilisation on mechanical properties of coagulated POSS-PCL

The effect of sterilisation on mechanical properties was compared in coagulated samples using uniaxial compression testing (Figure 5.3 C). There was no significant difference in the stiffness (Young's modulus) or the maximum capacity to elastically absorb energy (compressive strength) between the different sterilisation methods and the pre-sterilised control. Yield strength is the point where elastic behaviour ceases and after which deformation becomes

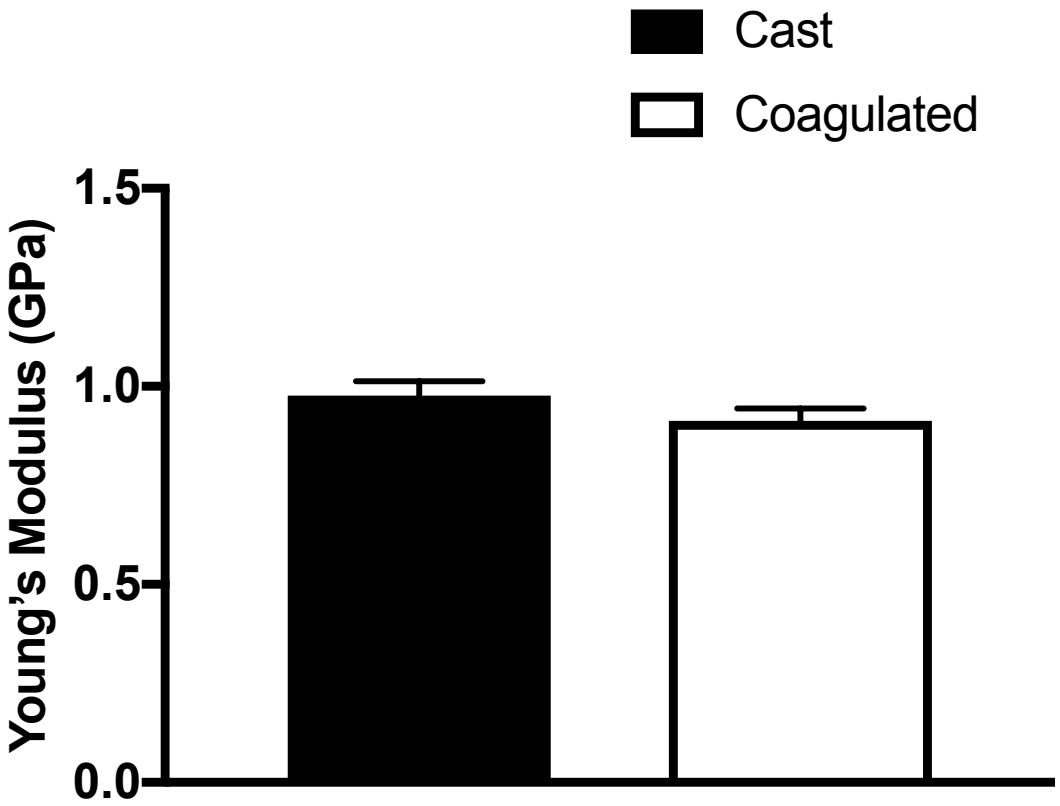

Figure 5.2: Compression testing of cast and coagulated POSS-PCL

Comparison of mechanical strength (as defined by Young's modulus) after uniaxial compression testing between unsterilized cast and coagulated POSS-PCL does not show any significant difference (p=0.13).

irrecoverable. Whilst there was no significant difference in the compressive force required to reach this point (yield stress), the corresponding deformation (yield strain) was significantly reduced by UV ($p=0.012$), ETOH ($p=0.0009$), Decon ($p=0.03$) and autoclaving ($p=0.01$) compared to controls.

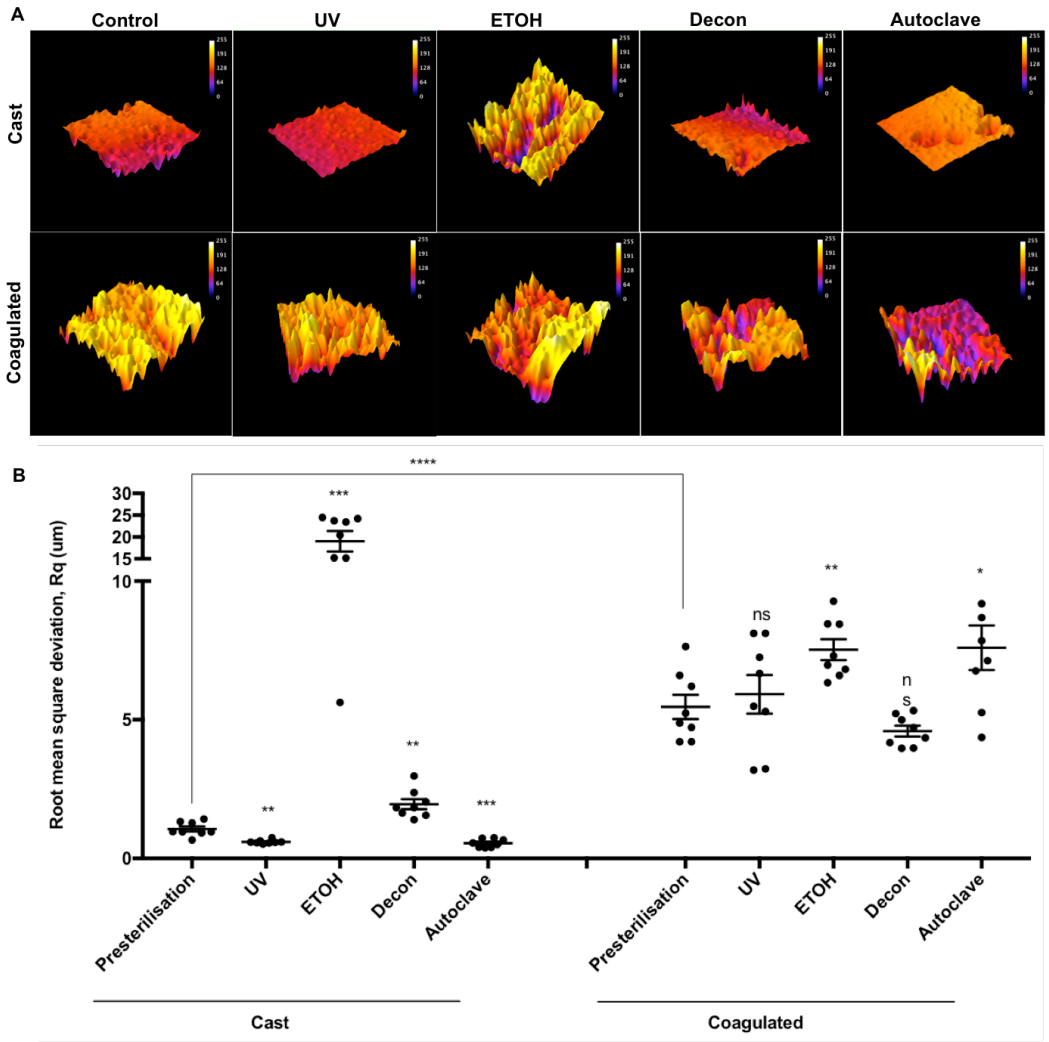

C

	Control (n=5)	UV (n=3)	ETOH (n=3)	Decon (n=3)	Autoclave (n=2)
E (GPa)	0.91 ± 0.01	0.98 ± 0.01	0.99 ± 0.003	0.96 ± 0.01	0.96
U_{el}^{Max} (kJ/m^3)	0.27 ± 0.19	0.10 ± 0.04	0.05 ± 0.02	0.07 ± 0.02	0.02
Yield strain, σmax (mm/mm)	2.16 ± 0.55	1.03 ± 0.29**	0.65 ± 0.11****	1.20 ± 0.34*	0.79**
Yield stress, εmax (MPa)	0.29 ± 0.15	0.26 ± 0.12	0.14 ± 0.04	0.12 ± 0.02	0.06

Figure 5.3: Analysis of the effect of different sterilisation techniques on porous POSS-PCL surface topography and mechanical properties.

A) Heat maps representing pixel height of scaffold surfaces (yellow is highest peak and blue is lowest) to visualise topography. ETOH treatment increases roughness in both forms of scaffold whereas autoclaving flattens topography. **B)** Quantitative analysis of surface roughness. **C)** Uniaxial compression of coagulated scaffolds shows reduced yield strain by all sterilisation methods. UV; ultraviolet light, ETOH; 70% ethanol, Decon; Decon 90, statistical significance; *p<0.05; **p<0.01; ***p<0.001; ****p<0.0001.

5.2.2.3 Effect of different sterilisation methods on cell behaviour on POSS-PCL

Paediatric hADSC were cultured on sterilised cast and coagulated for 14 days in culture control culture medium with cultured cells on plastic serving as a control using n=1 hADSC cell line performed on at least n=3 experimental replicates (Figure 5.4). There was evidence of bacterial contamination in only one of the autoclaved coagulated POSS-PCL scaffolds (1 out of 6) and as such, efficacy of sterilisation was broadly similar (Figure 5.4 A).

Alamar blue dye was used to assess cell viability at day 14 with values expressed as a percentage of the values from controls (cells cultured on plastic) (Figure 5.4 B). Cell viability was significantly reduced on cast scaffolds sterilised using ethanol ($p=0.016$) and Decon ($p=0.008$). There was also a significant reduction in viability for cells cultured on coagulated POSS-PCL treated with UV ($p=0.012$), ethanol ($p=0.02$) and Decon ($p=0.02$). Autoclaving did not seem to affect cell viability on either cast or coagulated POSS-PCL.

To determine whether the different sterilisation techniques affected cell morphology, F-actin staining was performed at day 14 of culture on cells cultured on the cast scaffolds (Figure 5.4 C). The hADSC grown on UV, ethanol and Decon appeared spread out, in contact with each other and have a filamentous cytoskeletal distribution of the actin in line with the controls grown on plastic (please refer to previous chapter for actin distribution in hADSC grown on plastic). The cells grown on autoclaved cast POSS-PCL appeared abnormal. They had irregularly shaped nuclei and F-actin staining was not filamentous. The cells also had an irregular and elongated outline and did not appear to be in contact with each other.

Based on all of the results of the of the sterilisation studies, I chose to proceed with UV sterilisation for all aliphatic POSS-PCL scaffolds used in the rest of the experiments.

A

Sterilisation Method	Scaffold Type	Contamination
UV	Cast	0/5
	Coagulated	0/5
ETOH	Cast	0/3
	Coagulated	0/6
Decon	Cast	0/3
	Coagulated	0/6
Autoclave	Cast	0/4
	Coagulated	1/6

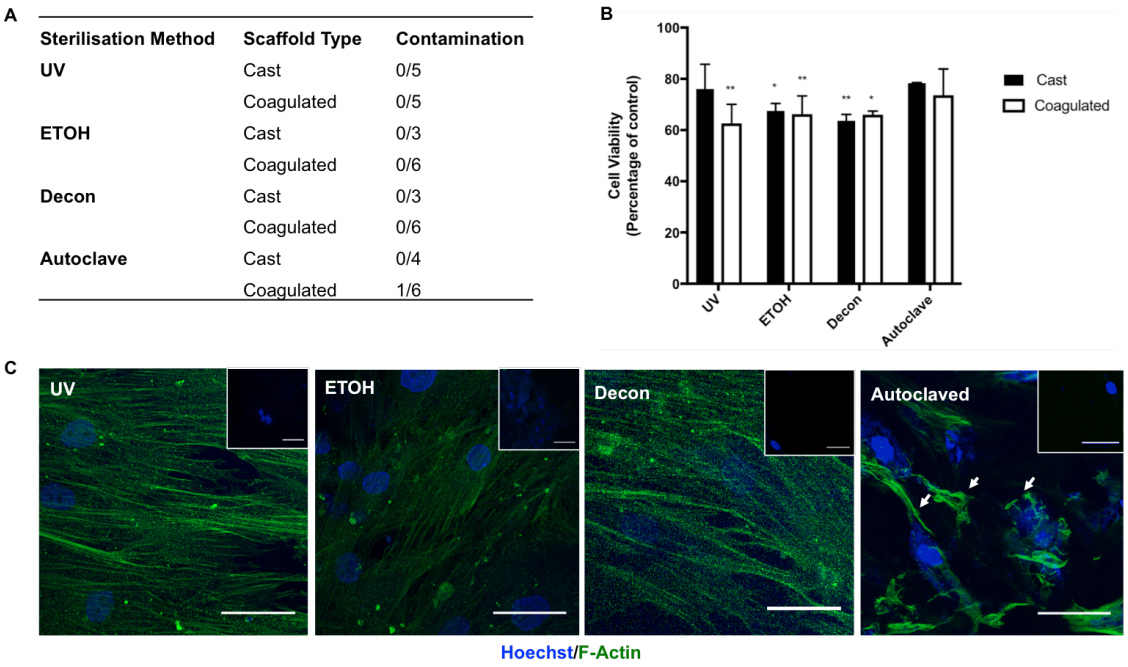

Figure 5.4: Efficacy of different sterilisation methods for POSS-PCL and impact on hADSC behaviour.

A) Visible contamination of culture media assessed using light microscopy was only evident in one autoclaved coagulated scaffold after 14 days of cell culture. **B)** Alamar blue assay of cultured cells expressed as a percentage of cells grown on plastic reveals reduced viability in all but UV sterilised cast and both forms of POSS-PCL after autoclaving. **C)** Confocal microscopy of F-Actin immunoflourescent staining of cells grown on cast scaffolds reveals abnormal cellular morphology (arrows point to irregular cytoskeleton) on autoclaved scaffolds. Scale bars; 100um, negative controls (labelled with 488 secondary antibody and Hoechst) inset at corner of each relevant image; UV; ultraviolet light, ETOH; 70% ethanol, Decon; Decon 90. Statistical significance; *p<0.05, **p<0.01.

5.2.3 Cell growth and differentiation of on POSS-PCL

5.2.3.1 Trilineage differentiation of hADSC on cast POSS-PCL

Paediatric hADSC from at least three different cell lines were seeded onto cast aliphatic POSS-PCL and differentiated using adipogenic, chondrogenic and osteogenic media in experimental triplicates for three weeks (Figure 5.5).

Differentiated cells in all conditions underwent a change in morphology compared with undifferentiated controls (Figure 5.5 A). Control hADSC maintained a spindle-like shape and continued to grow in monolayer with little evidence of clustering. Cells cultured in adipogenic media acquired a more rounded adipocyte-like morphology and were laden with multiple lipid droplets in their cytoplasm. The chondrogenically differentiated cells formed spherical aggregates whilst osteogenically differentiated cells coalesced in formed clusters of multi-layered nodules.

To further verify chondrogenic and osteogenic differentiation I used Alcian blue and Alizarin red staining (Figure 5.5 B). Alizarin red staining on the osteogenic samples was strongest in the nodular aggregates suggesting mineralisation. Both controls and chondrogenically-differentiated cells were also positive for alizarin red but the staining was cellular and non-specific hence not indicative of positive staining for mineral nodule formation. Chondrogenically differentiated cells strongly stained for alcian blue whilst both control and osteogenic samples had non-specific cellular staining. It was not possible to stain adipogenic cells with oil red O as the isopropranolol reacted with the scaffold causing opacity.

5.2.3.2 Osteogenic differentiation on cast and coagulated POSS-PCL

The biomaterial's ability to support osteogenic differentiation of hADSC for both monolayer and 3D culture was further analysed using immunoflourescent staining of cellularised scaffolds after a 3-week differentiation culture (Figure 5.5 C). Osteogenically differentiated cells on cast POSS-PCL, expressed Osteopontin. Differentiated hADSC on coagulated POSS-PCL expressed both Collagen 1 and Osteopontin. Collagen matrix was visible on osteogenically differentiated scaffolds on both the surface and within the pores.

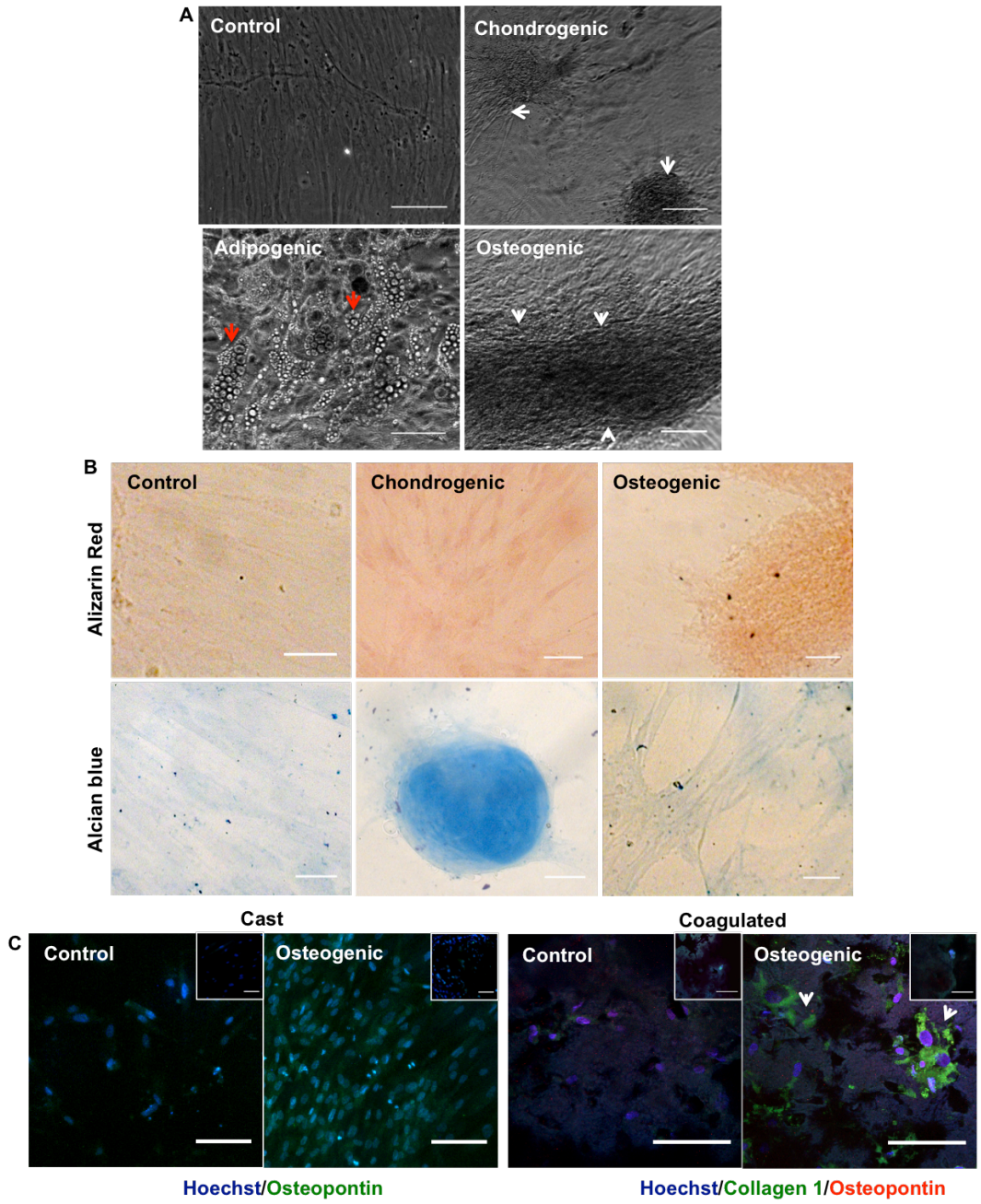

Figure 5.5: Multi-lineage differentiation of hADSC on POSS-PCL scaffold.

A) Phase contrast microscopy of cell morphology after 3 weeks differentiation of hADSC on cast POSS-PCL. Adipogenesis evidenced by oil droplets (red arrows), clustering of cells after chondrogenesis (white arrows) and multi-layered cell aggregates form (white arrows) after osteogenic differentiation**. B)** Alizarin red staining for mineral nodules and alcian blue staining for chondroid matrix on cast POSS-PCL. **C)** Immunoflourescent staining for osteopontin on osteogenically differentiated cells on cast POSS-PCL. Collagen 1 is deposited extracellularly (white arrows) by osteogenically differentiated hADSC on coagulated POSS-PCL. Scale bars; 100um, negative controls (488 and 594 secondary antibody staining only) inset within image.

5.2.4 Optimisation of POSS-PCL for 3D osteogenic culture

To optimise the scaffold for bone tissue engineering, modifications were made to POSS-PCL to improve cell adherence, differentiation and vascularisation.

5.2.4.1 The effect of surface modification on scaffold properties

Surface modification using sodium bicarbonate porogens (105um diameter) during the salt leaching coagulation process was used to generate scaffolds with rougher topography on the seeding surface ("sprinkled" POSS-PCL), which was then compared with controls ("plain" POSS-PCL). The effect of surface modification on the material properties of the scaffolds was analysed using roughness analysis, porosimetry and uniaxial compression testing (Figure 5.6).

Whilst the reflected surfaces and corresponding heat maps appear "rougher" on sprinkled samples, quantitative analysis of surface roughness did not show significant change by of this parameter (Figure 5.6 A-B). Modified scaffolds did however have significantly reduced porosity ($p<0.0001$) and pore size ($p=0.014$) (Figure 5.6 C) suggesting that the fabrication process disrupts the porogen-leaching step and thus alters the architecture of the scaffold.

The mechanical properties of POSS-PCL were also affected by surface modification. Sprinkled scaffolds exhibited reduced compressive strength ($p<0.0001$) and lower yield strength ($p<0.0001$) than plain POSS-PCL (Figure 5.6 D).

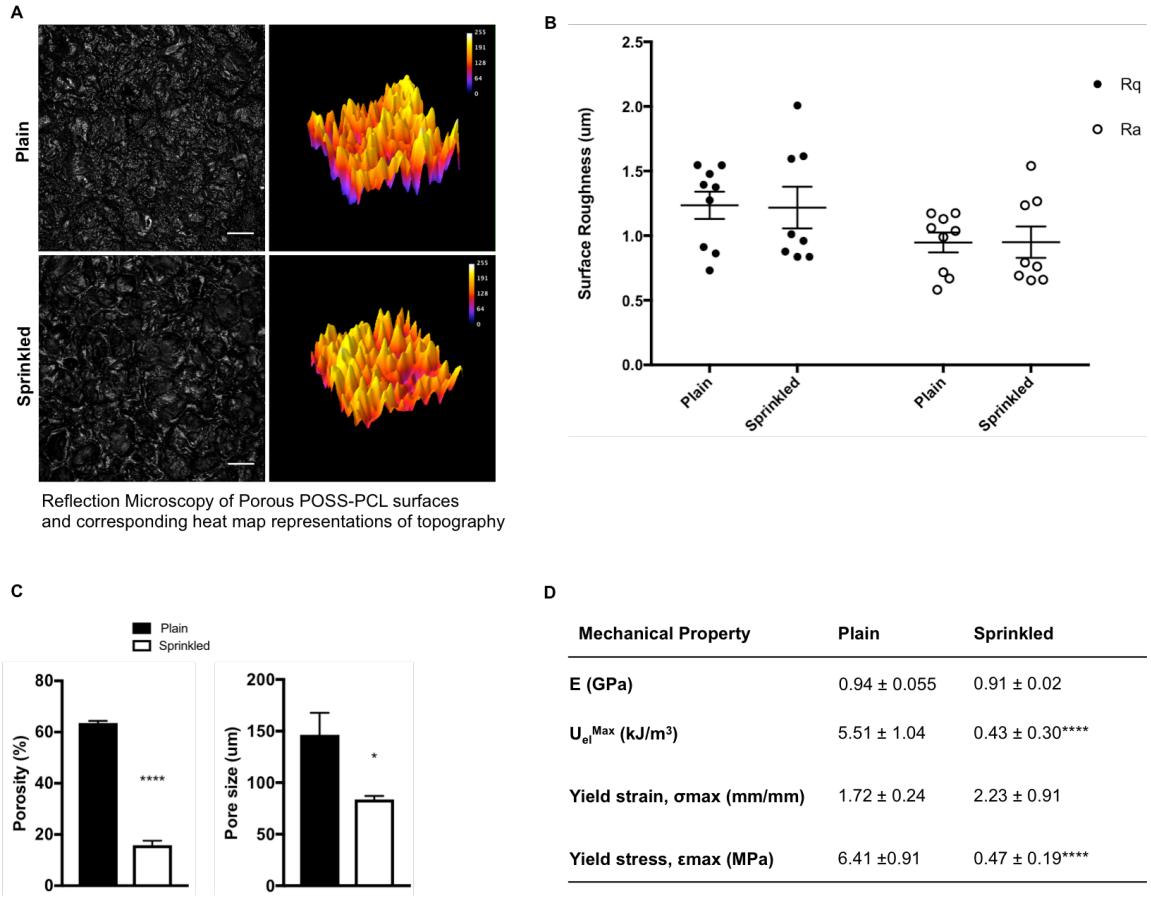

Reflection Microscopy of Porous POSS-PCL surfaces and corresponding heat map representations of topography

D

Mechanical Property	Plain	Sprinkled
E (GPa)	0.94 ± 0.055	0.91 ± 0.02
U_{el}^{Max} (kJ/m^3)	5.51 ± 1.04	0.43 ± 0.30****
Yield strain, σmax (mm/mm)	1.72 ± 0.24	2.23 ± 0.91
Yield stress, εmax (MPa)	6.41 ±0.91	0.47 ± 0.19****

Figure 5.6: Analysis of the effect of surface modification of coagulated POSS-PCL on topography, porosimetry and uniaxial compression testing.

A) Qualitative analysis of reflected surfaces of plain and sprinkled POSS-PCL and heat map representations (yellow represents highest pixel and corresponds with increased height) show increased roughness of the sprinkled surfaces. **B)** Quantitative analysis of roughness using Rq and Ra does not show any significant differences. **C)** Pore size and porosity analysed using µCT are significantly reduced in sprinkled POSS-PCL. **D)** Uniaxial compression testing demonstrates significant reduction in U_{el}^{Max} and Yield stress on sprinkled scaffolds. Scale bars; 100um, Ra; Arithmetical mean deviation, Rq; Root mean square deviation, E; Young's modulus, U_{el}^{Max}, compressive strength (maximum capacity to elastically absorb energy), Statistical significance; *p<0.05, ****p<0.0001.

5.2.4.2 Comparison of sprinkled and plain POSS-PCL on hADSC behaviour and biocompatibility

Although there was no significant difference in topography of sprinkled scaffolds, the effect of reduced porosity and pore size were evaluated to ascertain whether these conferred any benefit for cell culture or vascularisation (Figure 5.7).

Cells from 3 different cell lines that were cultured in experimental triplicates for 3 weeks in control media could be seen to infiltrate into the scaffold and appear to reside within small and large pores of plain and sprinkled POSS-PCL (Figure 5.7 A). The cells stained positively for Vimentin and cell morphology appeared elongated. There was no significant difference in the number of cells adhering to the scaffold but the size of cells on plain POSS-PCL was significantly larger (Figure 5.7 B) although this did not impact on cell morphology.

Vascularisation and biocompatibility were assessed by grafting unseeded scaffolds (n=6 of each) on the chorioallantoic membrane (CAM) of chick embryos for 7 days (Figure 5.7 C). On the day of harvest, both scaffolds appeared to be encased by blood vessels from the CAM. Immunoflourescent staining with Hoechst and Laminin of whole mount samples revealed infiltration of both scaffolds by chick cells on the scaffold and within the pores. Positive Laminin staining could also be seen around the spines of the sprinkled POSS-PCL scaffold and within the pores indicating vascularisation of the biomaterial.

Taken together these results suggest that whilst sprinkling did not alter topography, it affected the structure and mechanical strength of the scaffold. Whilst, there was no impact on attachment, cell size was significantly reduced. Additionally, sprinkling enhanced vascularisation. Despite the benefit of vascularisation by sprinkling, based on the reduced strength and non-reproducible fabrication method, plain POSS-PCL was chosen for further optimisation.

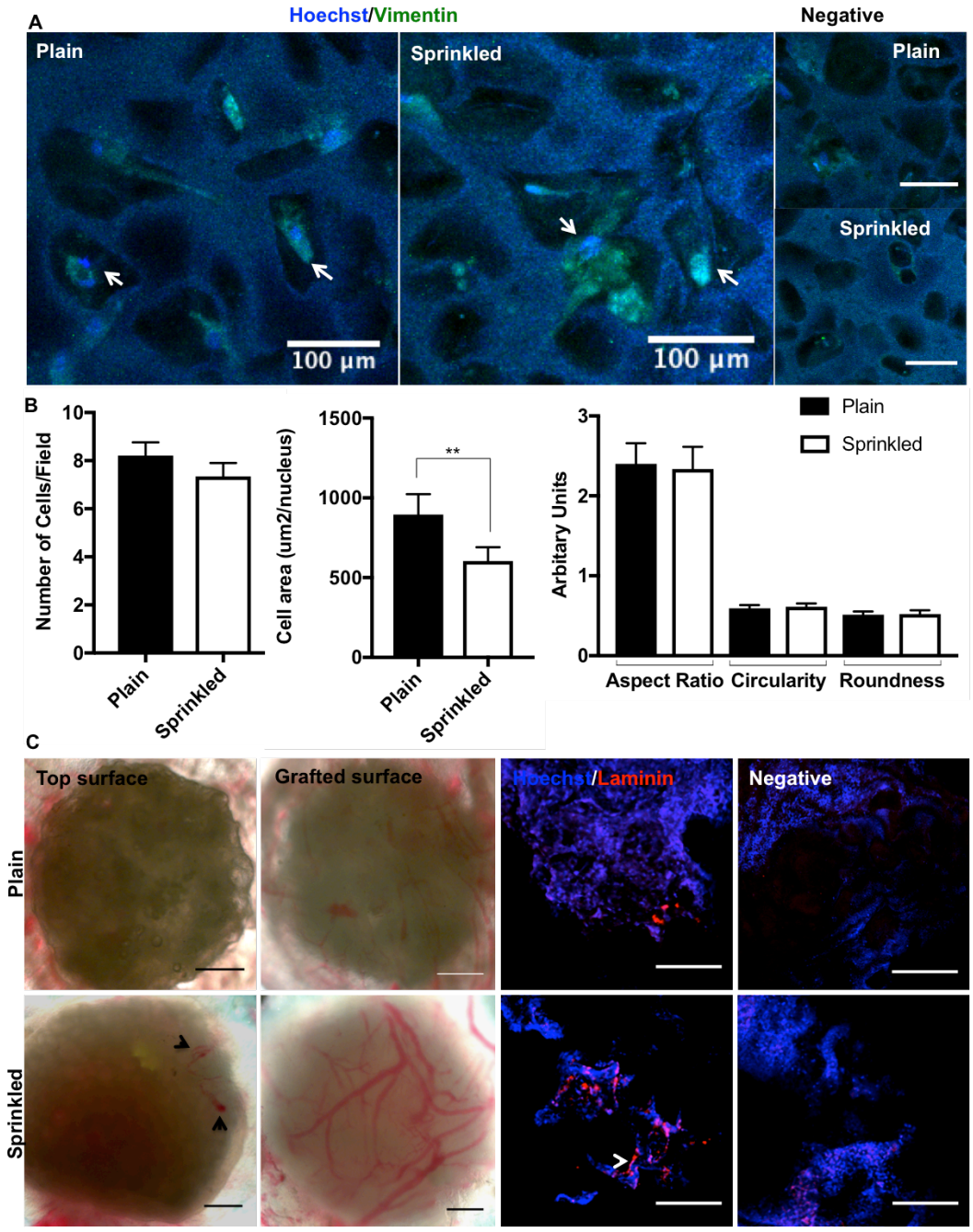

Figure 5.7: Immunoflourescent analysis of the effect of surface topography on hADSC behaviour and vascularisation.

A) Vimentin positive hADSC populate the pores of the scaffolds (white arrows). **B)** Cells cultured on sprinkled scaffolds are significantly smaller but both scaffolds produce elongated cells (low circularity and roundness). **C)** Chorioallantoic membrane grafting of scaffolds shows increased vessel encasement of sprinkled scaffolds (black arrows). There is infiltration of both types of un-seeded scaffolds by chick cells (Hoechst stained nuclei) but strong laminin expression evident on the sprinkled scaffolds (white arrows). Scale bars; 100um, negative control; 594 secondary antibody staining only, statistical significance; **p<0.01.

5.2.4.3 Analysis of the effect of POSS-PCL composition with fibrin on cell behaviour and vascularisation.

Fibrin was used as a cell carrier to seed hADSC onto plain coagulated POSS-PCL-Fibrin and comparison was made with plain POSS-PCL alone (Figure 5.8). After a 3 week period of culture in control media of cells from 3 different cell lines cultured in experimental triplicates, cells were visible on both scaffold types and expressed vimentin Figure 5.8 A). Cells on the POSS-PCL-Fibrin scaffold appeared to be widely distributed throughout the scaffold whilst the cells on POSS-PCL were mostly aggregated on the seeding surface and some of the pores. There was no overall difference however in the overall density of adherent cells found between the scaffolds (Figure 5.8 B).

Comparison was made between collagen 1 expression of osteogenically differentiated cells cultured on POSS-PCL and the fibrin hybrid scaffold using immunoflourescent staining (Figure 5.8 C). Collagen I was deposited in an extracellular pattern on both types of scaffolds although fibrin-containing scaffolds appeared to contain a greater density of collagen fibres.

Analysis of the orientation and distribution of collagen fibres was undertaken using OrientationJ (Figure 5.8 D-E). The s-colour surveys reveal a relatively high amount of isotropy as evidenced by appearance of bundles of fibres. The extracellular collagen fibre networks appeared to have a more organised orientation and the arrangement of the collagen bundles was more distinct in appearance on the fibrin hybrid scaffold.

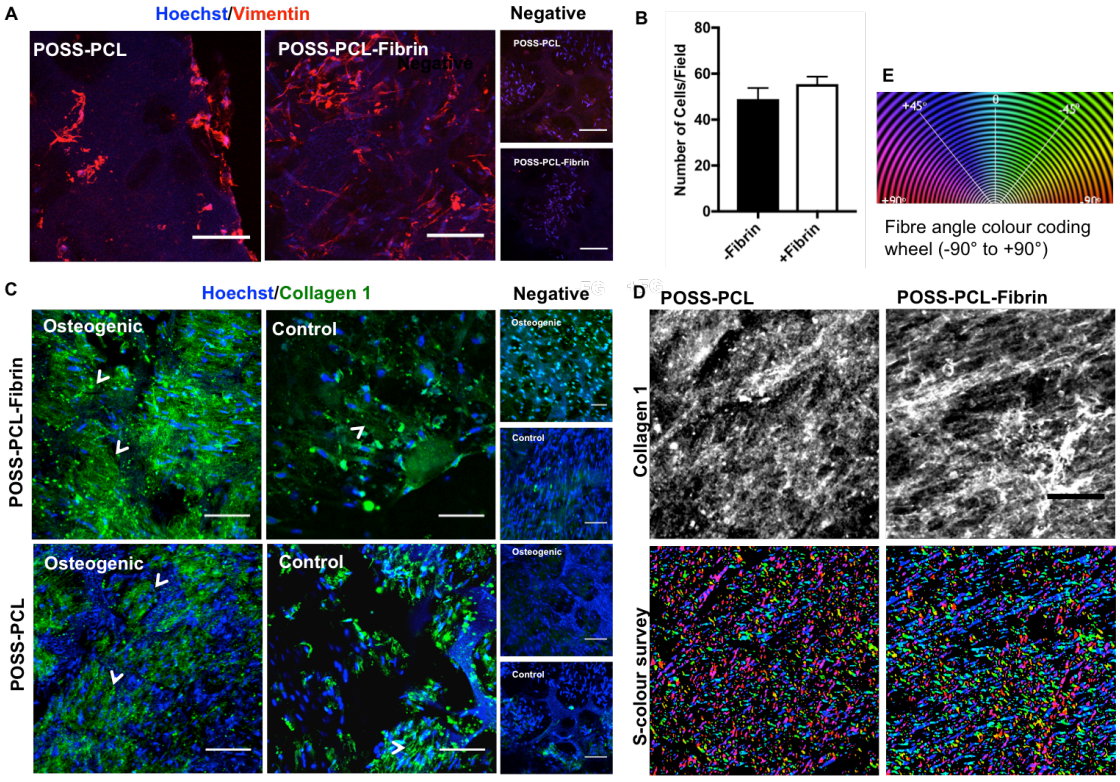

Figure 5.8: Comparison of fibrin-POSS-PCL composition on hADSC morphology and osteogenic differentiation by immunoflourescent staining and qPCR.

A) Vimentin staining of hADSC cultured on POSS-PCL with and without fibrin show elongated morphology. **B)** The addition of fibrin did not affect cell density. **C)** Collagen 1 immunoflourescent staining is widespread and extracellular in both types of scaffolds (white arrows) in osteogenically differentiated samples. Control cells also express collagen 1 although this appears less fibrous and less dense. **D-E)** Analysis of collagen fibre orientation of the fluorescently stained osteogenic samples is represented as a heat map (S-colour survey) (D) with the corresponding colour wheel showing the correlation between colour and orientation (**E).** Fibrin-containing scaffolds appear to produce more ordered collagen fibres as evidenced by the orientation, which is mostly between (0-45 degrees). Scale bars; 100um, negative control; 488 (green) anti-rabbit or 594 (red) anti-mouse secondary antibody staining only.

5.2.4.4 Comparison of biocompatibility and vascularisation in POSS-PCL and POSS-PCL-Fibrin scaffolds.

Unseeded POSS-PCL scaffolds with and without fibrin (n=6) were grafted onto the chorioallantoic membrane of the chick embryo to assess whether this modification could improve the ability of the scaffold to support vascularisation (Figure 5.9).

After a 7-day engraftment period, both scaffolds showed evidence of encasement and infiltration by CAM vessels. Scaffolds coated with fibrin appeared to be encapsulated by large and numerous blood vessels compared with uncoated scaffolds on visual inspection.

Immunoflourescent staining of whole mount samples with Von Willebrand Factor (VWF) and Hoechst revealed infiltration of both scaffolds by chick cells as evident by Hoechst nuclear staining. Fibrin modified scaffolds also stained positively for VWF in a pattern consistent with blood vessel lumens. The unmodified scaffolds did not display any convincing VWF positive staining suggesting limited vascularisation.

Taken together these results suggest that the limitation of plain POSS-PCL with regards to vascularisation can be overcome with the addition of fibrin.

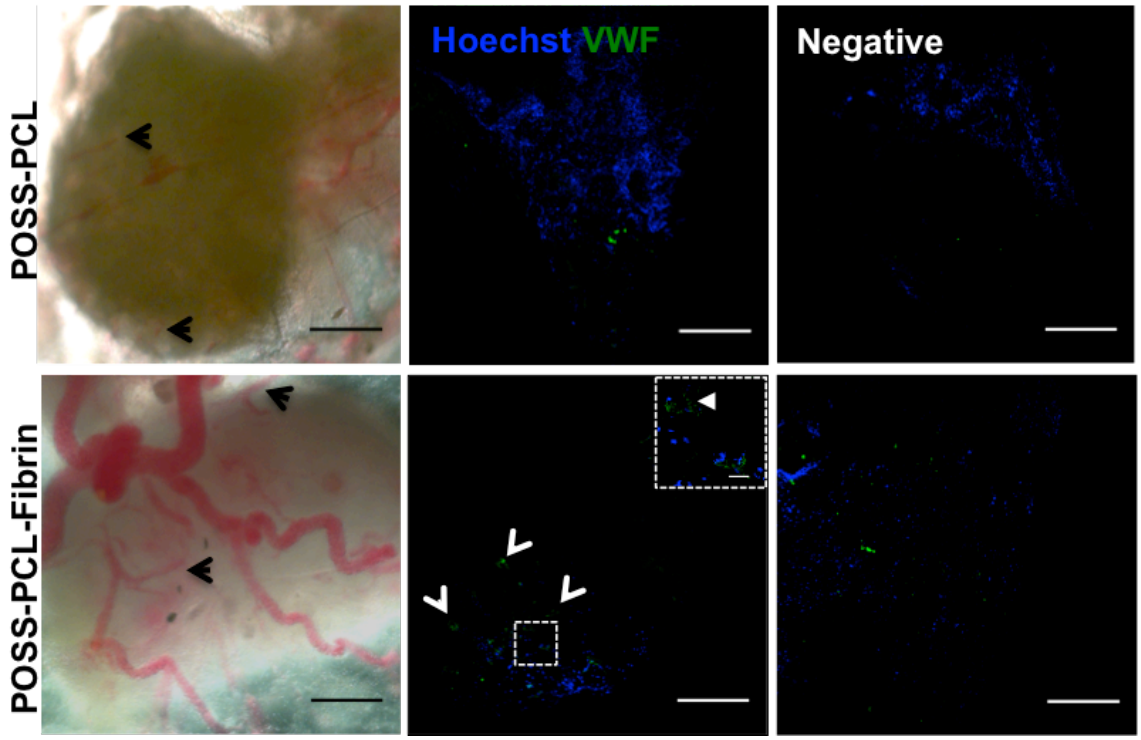

Figure 5.9: Comparison of vascularisation in non-cellularised POSS-PCL-Fibrin with POSS-PCL using the chick chorioallantoic membrane (CAM) graft model.

Blood vessels from the CAM could be seen to surround and infiltrate both types of scaffold. Both scaffolds appear to be infiltrated by chick cells as evidenced by Hoechst staining for nuclei but VWF staining was only seen on the fibrin based scaffold. VWF distribution is luminal (white arrows on main and expanded inset image) consistent with blood vessel staining. Scale bars; 100um (except for inset image which is 10um), VWF; Von Willebrand Factor, negative control; 488 (green) secondary antibody staining only.

5.3 Discussion

The tissue microenvironment has been previously shown to play a crucial role in directing and regulating stem cell survival, proliferation and differentiation (Yu et al., 2017, Paul et al., 2016). This effect is dependent on cell type and as such has resulted in tissue engineers trying to move from the use of generic scaffolds towards recreating the niche specific to the stem cell population being studied (Marinkovic et al., 2016, Lee et al., 2016). For bone bioengineering, the 3D microenvironment has been shown to be vital in maintenance of osteogenic differentiation capacity and inducing extracellular matrix deposition by MSC (Kittaka et al., 2015, Rakian et al., 2015). In this chapter I used the characterisation of paediatric bone structure and biology data described in Chapter 4 to design a scaffold capable of simulating the bone tissue microenvironment. The biomaterial I generated was structurally similar to bone controls and capable of supporting hADSC attachment, proliferation and trilineage differentiation. Furthermore, the nanocomposite scaffold was readily modifiable and alteration of surface properties enhanced its biocompatibility. Using fibrin as a cell carrier to generate a hybrid biomimetic scaffold further optimised the osteogenic and vascularisation capabilities of the scaffold.

5.3.1 Design and fabrication of a novel biomimetic scaffold to replicate the structural properties of native paediatric calvarial bone

Nanotechnology can be used to mimic the biophysical properties of native bone extracellular matrix to direct osteogenic differentiation of osteoprogenitor cells (Ibrahim et al., 2016a, Gulseren et al., 2015). This is the first study focusing on the characterisation and optimisation of POSS-PCL for bone tissue engineering.

The scaffolds showed similar porosity and trabecular/biomaterial density to trabecular bone suggesting that seeded cells would be cultured in a 3D physical environment akin to that found in native bone. The importance of the microenvironment on directing cell behaviour was most recently shown by Sonomoto et al who showed that 3D culture on nanofibrous plugs alone can induce early osteogenic and chondrogenic differentiation of human MSC in the absence of any other stimulation by influencing cell-cell interactions (Sonomoto et al., 2016). Scaffold architecture was also shown to affect mouse osteoblast

and rat MSC migration, adhesion and mineralisation through regulating interactions between cell surface integrins and the extracellular matrix ligands in a phenotype-dependent manner (Murphy et al., 2016). I was able to mimic the bone extracellular matrix environment to design a scaffold customised for bone tissue engineering using human adipose derived stem cells. Additionally I also optimised the scaffold for vascularisation, which is key to bone bioengineering.

The issue of the effect of sterilisation on a biomaterial's properties and particularly the effect on cellular responses is often overlooked. Although only the coagulated form of POSS-PCL was of interest in my attempt to design a biomimetic scaffold for bone tissue engineering, I used the cast form to perform preliminary studies for rapid initial assessment of the biomaterial's impact on cell adhesion and survival. When I first started to use aliphatic POSS-PCL, there was no information regarding the optimal sterilisation protocol for this scaffold. I investigated four commonly used and readily available methods for their efficacy of sterilisation and impact on the material's physical characteristics and decided on using UV light as it was the least disruptive to the scaffold and behaviour of cells cultured on it. The findings are in conflict with previously published sterilisation study by Ahmed et al who found that ethanol was not associated with any material degradation although they recommended gamma radiation as the optimal protocol (Ahmed et al., 2013). A more recent study concurred with my results on ethanol and found that UV sterilisation does not result in significant material deformation but was ineffective at sterilisation and recommended slow-chlorine releasing molecules instead (Naderi et al., 2016). The relevance of this variation is potentially significant as all three used POSS-PCL fabricated in the same laboratory using the seemingly similar protocols. Clearly, it is important to establish a reproducible method prior to consideration of clinical application.

5.3.2 Cell survival and trilineage differentiation are achieved on a versatile bioabsorbable nanocomposite scaffold

Using defined tissue culture protocols I found that paediatric hADSC grown on cast POSS-PCL adhered and survived culture in control medium and could undergo differentiation along the 3 mesenchymal lineages. This suggests that

cast POSS-PCL could be useful for routine culture of hADSC as it promotes survival and phenotype but does not direct cell differentiation in its basic form without the presence of a differentiation stimulus (osteogenic culture medium in the case of this work).

Cells cultured on coagulated POSS-PCL did however express a small amount of osteopontin, which is an early maker of osteogenic differentiation suggesting that the structure of coagulated POSS-PCL may exert an osteoinductive effect on hADSC. The impact of 3D culture on providing biophysical stimulation for osteogenesis in hADSC was demonstrated in chapter 4 of this thesis. A recently published study by Lo et al elegantly modelled how 3D culture alters spatial boundary conditions for MSC to cause cytoskeletal reorganisation and integrin expression resulting in preferential osteogenic differentiation (Lo et al., 2016). As expected, culture in osteogenic differentiation media expressed collagen 1 protein that was deposited in an extracellular pattern within pores indicating maturity of the differentiated cells as evident by the deposition of their own osteoid matrix.

5.3.3 Towards recreating the bone tissue microenvironment with a hybrid hydrogel-nanocomposite scaffold

Coagulated POSS-PCL can be easily modified to alter its material properties. I sought to optimise it for hADSC adhesion and osteogenic differentiation through surface modification. Addition of sodium bicarbonate 105um porogens to the surface of the scaffold results in dispersion leaching which alters the seeding surface by increasing its porosity and surface roughness. Although I did not find that this process significantly altered the roughness of the scaffold it did reduce porosity, mean pore size and the mechanical strength of the scaffolds, which was associated with a reduction in the size of hADSC. There was also a clear improvement in vascularisation of POSS-PCL associated with sprinkling. Previously, this surface modification technique was used on a related non absorbable scaffold (“POSS-PCU”) which similarly did not show any alteration to surface roughness but enhanced neovascularisation of scaffolds after in vivo implantation (Crowley et al., 2016).

Sprinkling presented a dichotomy in that it provided an obvious advantage regarding vascularisation but the effect on porosimetry seemed to restrict cell growth of hADSC. It is widely known that pore size and porosity influence cell growth and extracellular matrix deposition capabilities. Smaller pore sizes are thought to inhibit cell growth and differentiation with a pore diameter of 100-150um considered to have greatest effect on osteogenic differentiation (Kiziltay et al., 2015, Lo et al., 2016). Another limitation of sprinkling is the non-reproducible fabrication method.

The current trend in biomaterial design for bone tissue engineering leans towards creating bioactive scaffolds complexed with extracellular matrix components, which have been shown to enhance osteoinduction. More recently a number of studies have shown that use of cell-derived extracellular matrices further optimise osteogenesis by MSC by helping recreate the bone cell niche (Kim et al., 2015). Based on the results of Chapter 4 and evidence that fibrin culture increases proliferation and osteogenesis in murine osteoprecursor cells (Oh et al., 2014), I investigated whether using fibrin as a cell carrier could optimise the osteogenic and angiogenic properties of POSS-PCL. The hADSC cultured on these scaffolds maintained their morphological appearance and addition of fibrin did not reduce cell density. I did however find that cells cultured on fibrin-POSS-PCL scaffolds deposited collagen extracellular matrix in a pattern that was more indicative of mature osteogenic differentiation suggesting that fibrin confers a additional osteoinductive benefit.

Vascularisation is critical to the survival of any tissue but in particular bone, which relies on a rich blood supply for its survival and functions (Auger et al., 2013, Tomlinson and Silva, 2013). In addition, vascularisation of bone grafts have shown improved osteogenesis and neoangiogensis in rabbit studies (Yao et al., 2010). The addition of fibrin to POSS-PCL improved vascularisation and vessel infiltration of the scaffolds. This is in keeping with studies which found that addition of fibrin to a mineralised scaffold not only enhanced osteogenesis but also induced secretion of vascular factors by hBMSC (Lohse et al., 2012). Fibrin based matrices were also shown to induce secretion of angiogenic factors and lead to hADSC vasculogenesis in vitro (Chung et al., 2015).

5.3.4 Limitations

A key limitation of this study is that mechanical properties of the cellularised scaffolds were not evaluated due to constraints with regards to access to the uniaxial compression apparatus. This is important for evaluation of the clinical applicability of the bioengineered bone. Whilst little data exist regarding the mechanical properties of non weight bearing craniofacial bone such as the object of this study, I have evaluated the, mechanical strength of the calvarial bone samples which I have used as controls in a collaborative study unrelated to this thesis (not yet published). In future, this data can be used to evaluate bioengineered constructs developed using these protocols.

Degradation studies have been published for aliphatic POSS-PCL whereby cast polymer was tested using different in vitro degradation buffers including collagenase for a period of 6 months and coagulated scaffolds were subcutaneously implanted in rats for up to 12 weeks (Yildirimer et al., 2015). Whilst this study demonstrated that the addition of the POSS nanocage to PCL stabilised degradation kinetics and maintained mechanical properties during the degradation of the scaffolds, it did not show the influence of cellularisation or even culture media on the degradation kinetics of POSS-PCL. Additionally, despite the study being performed by our collaborators, given the variation that I have had with regards to the sterilisation data, it would be necessary in future to perform degradation studies for my scaffolds in vitro and in vivo with and without hADSC.

Further data is also required with respect to long term maintenance of osteogenic differentiation of the cells and as such repeating these experiments over a longer period with analysis at different time points will provide invaluable information on the mechanism of osteoinduction on these scaffolds.

5.3.5 Future direction

A number of modifications can be considered in order to optimise the osteogenic and vasculogenic properties of these scaffolds. Whilst fibrin has proved useful in increasing vascularisation, decoration of the fibrin or POSS-PCL with extracellular matrix components could enhance the osteoinductive

process. Addition of glycosaminoglycan peptide nanofibers have been recently shown to enhance mineral matrix deposition by rabbit MSC in vitro and in vivo (Tansik et al., 2016). Whilst surface modification using sprinkling altered the overall structure of the scaffolds, it did improve vascularisation. One possible method that could be used to optimise the surface could be plasma treatment which was found to direct osteogenic differentiation of our hADSC on a related scaffold ("POSS-PCU") (Griffin et al., 2017).

Whilst I have not characterised the mechanical properties of the cellularised scaffolds, based on comparison with bone samples upon handling these constructs, it is likely that they will require strengthening biomechanically. This could be achieved by modification of the POSS-PCL by altering its chemical structure to include a harder segment but this has been shown to also affect degradation and could be detrimental to cell survival, which I have found to be favourable on the structure that I designed. A more desirable approach could however, be to enhance maturation of the osteogenically induced cells more efficiently so that cells can lay down a mineral matrix in a similar pattern to that of native bone which confers mechanical strength. This may be achieved with the use of a bioreactor capable of providing compressive strain which has been previously shown to enhance mineralisation and mechanical strength of cultured bovine bone specimens in vitro compared with unloaded samples (David et al., 2008). An additional reason for considering further research using a bioreactor is the ability to perfuse larger scale constructs and have the additional benefit of enhancing expansion and osteogenic differentiation as previously shown on ovine MSC and human dental pulp stem cells (Ding et al., 2016, Ji et al., 2014).

Ultimately, the aim will be to assess whether 3D printing could be used to generate shaped scaffolds based on the output of the model described in Chapter 3. 3D printing could also prove useful in making the scaffold fabrication process more reproducible. Furthermore, 3D printing could also be used to optimise POSS-PCL architecture for cell survival and differentiation based on recent evidence that pore geometry increased osteogenic activity of hBMSC (Ferlin et al., 2016).

5.4 Conclusions

This work sought to create a scaffold tailored for osteogenic differentiation of hADSC. Using native bone analysis, the criteria required for emulating the bone-specific tissue microenvironment was used to fabricate a novel hybrid fibrin-nanocomposite scaffold, which supports hADSC adhesion, growth, differentiation and vascularisation. The biomaterial created is bioabsorbable, easily manufactured and will enable further modification of its structure. Additional work is required to ensure that the manufacturing process is reproducible and enhancement of the mechanical strength of the cellularised constructs should be evaluated and optimised if necessary.

In the following chapter the impact of early vascularisation on osteoinduction of hADSC is explored. The behaviour of the cellularised hybrid scaffolds is also evaluated for survival, neovascularisation and osteogenesis in an in vivo mouse model.

Chapter 6 Effect Of Vascularisation On hADSC Osteogenesis

6.1 Introduction

Vascularisation and perfusion are integral to the development, survival and function of bone tissue (Auger et al., 2013, Tomlinson and Silva, 2013). In vitro, oxygen deprivation has been shown to impair matrix maturation of preosteoblast cells (Nicolaije et al., 2013). Furthermore induction of hypoxia inducible factor-1α (HIF-1α) under normoxic conditions promotes angiogenesis and osteogenesis in rat BMSC in vitro (Zou et al., 2011a) whilst increasing blood vessel formation as well as bone mineralisation of critical sized calvarial defects in rats in vivo (Zou et al., 2012, Zou et al., 2011b). This relationship between vascularisation and osteogenic differentiation of MSC is illustrated by evidence that *VegfA* is required for *Bmp-2* activation and osteogenic maturation of murine BMSC in vitro whilst *Bmp-2* knockout mice exhibit reduced osteoblast activity and micro blood vessel formation (Yang et al., 2013). The nature of this interdependence is further demonstrated by impaired blood vessel formation in mice with disrupted Notch signalling which leads to impaired angiocrine signalling by endothelial cells that results in reduced osteogenesis, skeletal abnormalities and decreased bone mass (Ramasamy et al., 2014).

The vasculature could also play a crucial role in providing a template to guide bone morphogenesis. In mouse embryos the bone vasculature lacks a basement membrane and has been shown to provide the patterning for mineral distribution by serving as a template during endochondral bone development (Ben Shoham et al., 2016). The pattern of vascular blood flow is also thought to regulate bone formation which if disrupted leads to down regulation of Notch activity in endothelial cells and resulting decrease in neoangiogenesis as well as osteogenesis in murine long bones (Ramasamy et al., 2016b).

Bone is a highly functional tissue whose structure is well adapted to its purpose (Clarke, 2008). This is especially evident in its mechanical roles whereby the difference of extracellular matrix organisation in highly organised weight-bearing cortical long bones can be contrasted with the disordered arrangements seen in the flat cancellous bones of the mid face which have a structural and protective but not load-bearing purpose (Rho et al., 1998). Bone vasculature plays a key role in regulating remodelling (Sims and Martin, 2014, Lafage-Proust et al.,

2015) which has also been shown to response to mechanosensory signalling in rat long bone defects in vivo (Boerckel et al., 2011). The key metabolic function of bone is in the regulation of calcium and phosphate whereby it acts as a reservoir for these minerals and releases or stores them in response to systemic cues. Reduced vascular supply to bone has been linked with metabolic diseases such as osteoporosis in humans (Vogt et al., 1997). Bone is also the main site of haemopoesis in adults and children, which occurs in the bone marrow cavities and thus is responsible for maintenance and differentiation of haemopoeitic stem cells in response to systemic signalling and is regulated by the bone vasculature. A distinct blood vessel network formed by bone marrow endothelial blood cells has been shown to differentially direct leucocyte and haemopoeitic stem cell mobilisation, differentiation and maintenance in mice (Itkin et al., 2016).

Vascularisation plays an important role in regulating bone survival, regeneration and function through its roles in transporting oxygen and nutrients as well as providing signals to direct growth, development and stem cell behaviour (Ramasamy et al., 2016a). Clearly, bone tissue engineering strategies should seek to replicate vascularization in order to simulate the native bone microenvironment as it not only affects the function of the bone but also the size of tissue that can be generated.

In the previous two chapters, I analysed the structure of paediatric calvarial bone grafts and the impact of 3D culture as well as short periods (7 days) of vascularisation to define optimal osteogenic differentiation conditions and generate a biomimetic scaffold to support bone tissue engineering using hADSC. In this chapter, I seek to investigate the impact of short-term early vascularisation on the osteogenic maturation of hADSC. I also assess the results of long-term in vivo implantation of osteogenically differentiated hADSC on a biomimetic scaffold with regards to maturation, integration and survival.

6.2 Results

6.2.1 The impact of differentiation culture period and early vascularisation on osteogenic maturation of hADSC

Fibrin scaffolds were cellularised with hADSC and cultured in control or osteogenic differentiation media for 2, 3, 4 or 5 weeks to assess the influence of differentiation period on ostegenesis. In parallel, cellularised scaffolds were also implanted for 7 days in the CAM after 2, 3 or 4 weeks of differentiation to analyse whether early vascularisation could drive further maturation compared with a longer culture period. All experiments were performed in experimental triplicates using cells derived from 3 different patients.

6.2.1.1 Analysis of extracellular matrix deposition and maturation in hADSC cultured in osteogenic medium at different in vitro differentiation end points

To assess the impact of in vitro differentiation period on maturity of osteogenic differentiation of the hADSC, immunoflourescent staining for COL1 and OSTP was performed in the first instance (Figure 6.1). COL1 expression was more visible in osteogenically differentiated cells from all culture periods when compared to their undifferentiated controls (Figure 6.1 A). The pattern of expression of COL1 was extracellular and could be seen to progress from a tight organisation surrounding individual cells after 2 weeks of osteogenic differentiation to a more extensive fibrous network arrangement after 4 weeks in differentiation media.

Both control and osteogenic cells expressed OSTP in all culture periods but with differing immunostaining patterns and expression was greatest in differentiated cells. Whilst OSTP in control cells appeared intracellular, osteogenically differentiated samples expressed OSTP in an extracellular pattern (Figure 6.1 B). Although the pattern of OSTP expression was localised to the spindle-shaped cell outlines in the 2 and 3-week differentiation protocols, cells cultured for 4 and 5 weeks exhibited a more compact cuboidal or cobblestone like appearance as is consistent with more mature osteoblasts.

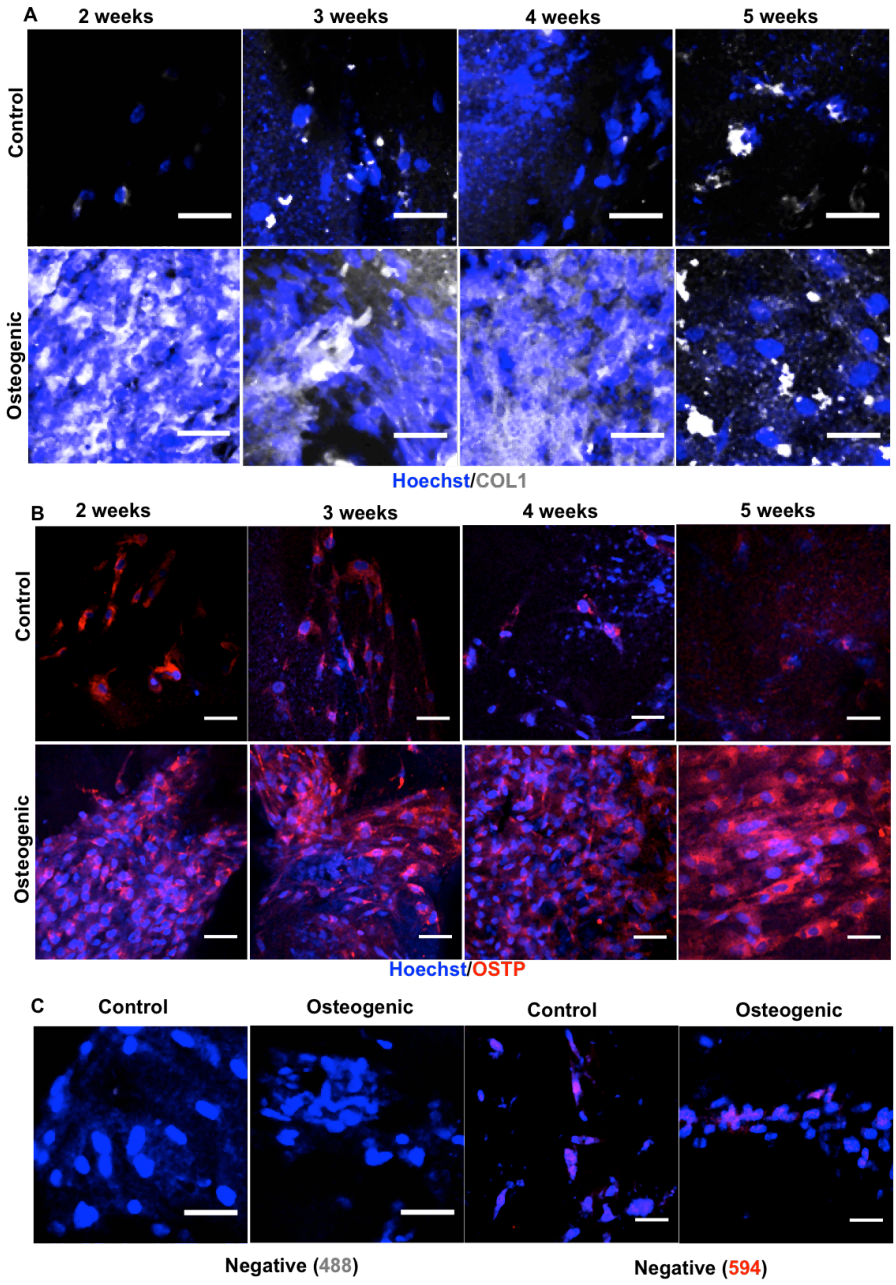

Figure 6.1: Effect of different in vitro differentiation times on osteogenesis of cellularised Fibrin scaffolds assessed by extracellular matrix deposition.

A) Immunoflourescent staining for COL1 reveals widespread staining under differentiation culture conditions. Longer differentiation in osteogenic media is associated with extensive extracellular matrix deposition with a fibrous network distribution. **B)** OSTP expression is more evident in osteogenically differentiated samples compared with controls at every time period. Longer differentiation period was associated with more widespread OSTP distribution and extracellular pattern of protein expression. C) Negative antibody control staining for COL1 staining (grey) and OSTP staining (red). COL1; collagen 1, OSTP; osteopontin, scale bar; 50 µm/100 µm (A/B), negative controls; 488nm anti rabbit and 594nm anti mouse secondary antibody only.

6.2.2 Effect of early vascularisation on osteogenic differentiation of hADSC in comparison with longer differentiation culture period.

Cells encased in Fibrin were cultured in control or osteogenic media for a period of either 2, 3 or 4 weeks in vitro. Each condition was performed in experimental replicates and repeated using cells from 3 different cell lines. After each differentiation end-point, samples were harvested and processed either for immediate analysis (3-5 weeks differentiation only)‘ pre CAM’ (n=3 per condition) or implantation in CAM for 7 days (2-4 weeks only) then analysed (n=6 per condition) and thus represent the ‘post CAM’ group. As such the CAM experiments compare samples that were cultured in control or differentiation media in vitro for 2, 3, 4 or 5 weeks then immediately analysed with cellularised scaffolds that were cultured in vitro for 2, 3 or 4 weeks then CAM grafted for 7 days prior to analysis. This was performed to assess whether vascularisation after a shorter in vitro culture period (e.g. 3 weeks in vitro + 1 week in CAM) enhanced osteogenesis compared with simply leaving cellularised in vitro for a longer culture period (e.g. 5 weeks). Hence, the control for 2 weeks in vitro followed by 7 days CAM grafting would be 3 weeks in vitro culture only and so forth.

Cellularised scaffolds were surrounded and encased by blood vessels from the CAM (Figure 6.2 A). There was not a statistically significant difference in vessel diameter between cells initially cultured in control or osteogenic differentiation media under all culture periods. Blood vessel diameter on average was however greater in cells that had been cultured in control media for 2 weeks before grafting compared to those that were cultured for 3 weeks in control ($p=0.0007$) or osteogenic ($p=0.0017$) differentiation media. This was also the case for osteogenically differentiated cells cultured for 2 weeks prior to CAM grafting whose blood vessel diameter was significantly higher than those that were cultured for 3 weeks in control ($p=0.0038$) or osteogenic ($p=0.008$) differentiation media prior to CAM grafting. There was no significant difference in blood vessel diameter between cellularised scaffolds cultured for 4 weeks prior to CAM grafting compared with 2 or 3 weeks. Although not significant. There is a trend to reduction at 4 weeks compared with 2 weeks.

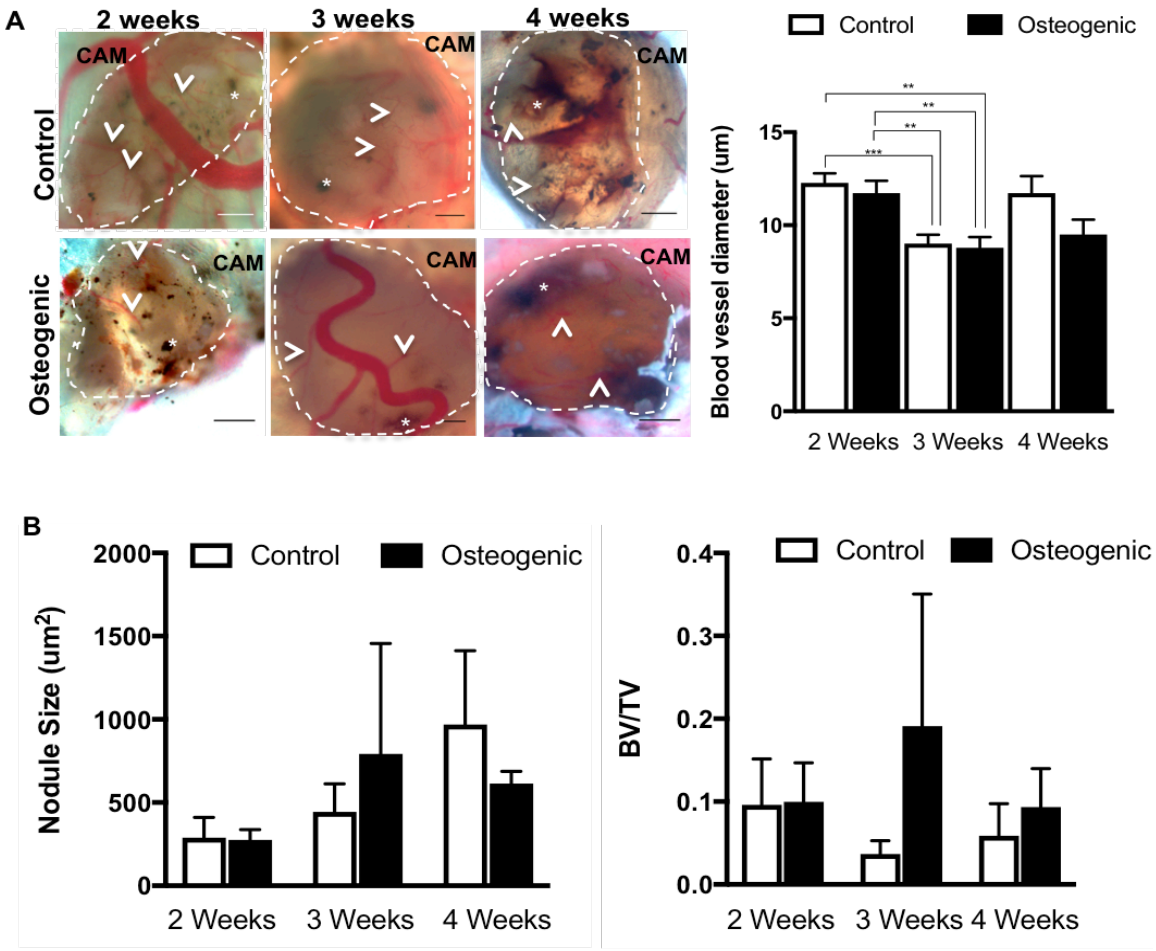

Figure 6.2: Vascularisation of cellularised Fibrin scaffolds osteogenically induced for different times prior to grafting onto the chorioallantoic membrane (CAM) for 7 days.

A) Stereoscopic images of ex ovo cellularised scaffolds cultured in either control or osteogenic media for 2, 3 or 4 weeks prior to CAM grafting. Small vessels from the CAM can be seen to encase and surround the samples (arrowheads) with evidence of calcified nodule formation (asterix). Quantification of blood vessel diameter (right panel) shows reduction in diameter with increased differentiation culture period. **B)** Analysis of mineral nodule size and bone fraction volume (BV/TV) after different differentiation times in culture reveals no significant difference in either. Scale bars; 100 μm, BV; bone volume, TV; total volume, **p<0.01, ***p<0.001.

Analysis of the bone volume fraction (BV/TV) and average mineral nodule size was performed on segmented 2D images to assess the impact of vascularisation and in vitro culture period on mineralisation of the cellularised scaffolds (Figure 6.2 B). Whilst mineralisation was observed in all experimental conditions, the average calcium nodule size and bone fraction volume were not significantly changed by length of differentiation or even whether cells were cultured in control or osteogenic media beforehand suggesting that vascularisation in itself provided an osteoinductive stimulus.

Immunoflourescent analysis of whole mount specimens was used to verify whether human cells were retained within the scaffold, if differentiation was maintained and accelerated and to confirm angiogenesis (Figure 6.3). The staining demonstrated that at least some of the human cells remained within the scaffold (evidenced by LMN and Hoechst co-staining) although there is also evidence of invasion by chick cells (lamin-/Hoechst+) (Figure 6.3 A). Additionally, VWF staining was positive and displayed a pattern consistent with the presence of blood vessel lumens suggesting vascularisation of the cellularised scaffold by the CAM for all differentiation times prior to CAM grafting. OSTP staining was evident in cells cultured in both differentiated and control conditions (Figure 6.3 B). The pattern of expression was clearly extracellular and widespread only in cells that were osteogenically differentiated prior to CAM grafting. There was no visible difference in OSTP staining between cells differentiated for 3 or 4 weeks.

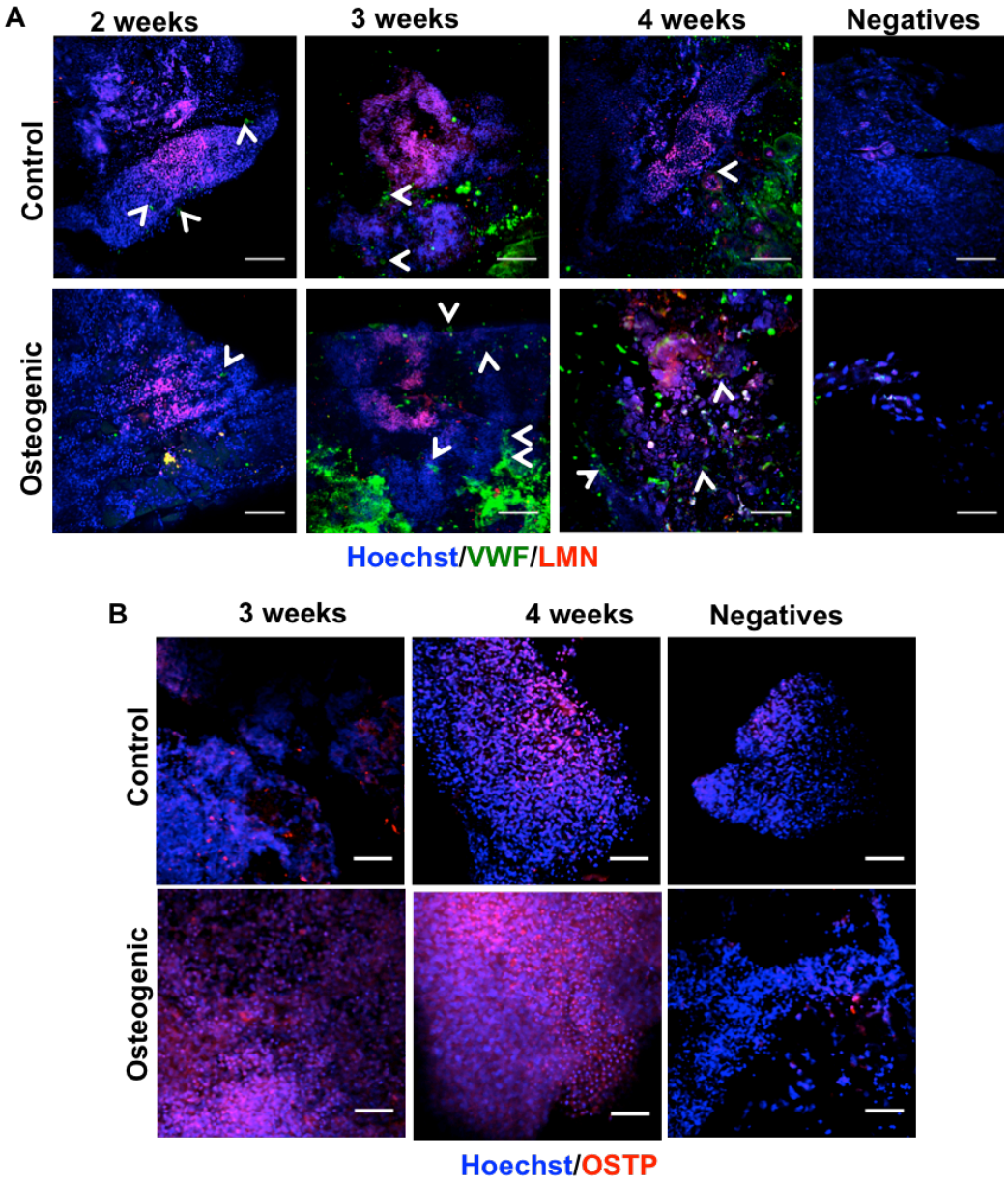

Figure 6.3: Analysis of angiogenesis, cellular survival and extracellular matrix formation by immunoflourescent staining in CAM-grafted cellularised Fibrin scaffolds following osteogneic induction *in vitro* for 2, 3 or 4 weeks.

A) Immunoflourescent staining of whole mount samples reveals presence of blood vessels evidenced by VWF expression (arrowheads) and presence of human cells within samples depicted by hoechst and LMN co-staining. **B)** Immunoflourescent staining for OSTP is more evident in osteogenically differentiated cells although longer period in control media prior to CAM grafting appears to generate more widespread OSTP expression. There is no visible difference in OSTP expression between 3 and 4 weeks of osteogenic differentiation. CAM; Chorioallantoic membrane, VWF; von Willebrand factor, LMN, lamin, OSTP; osteopontin, scale bars; 100 µm, negative controls; 488 and 594 secondary antibody only.

6.2.2.1 Comparison of 3, 4 or 5 weeks of in vitro culture with vascularisation for 7 days in CAM after 2, 3 or 4 weeks of in vitro culture

Cellularised Fibrin scaffolds were cultured in vitro then analysed immediately or CAM grafted for 7 days prior to analysis as described in 6.2.2. 3D volume rendering of segmented μCT reconstructions of samples reveals calcium nodule formation in control and differentiated conditions in all groups before and after CAM grafting (Figure 6.4).

Surface models of calcification do not show increased mineralisation with prolonged periods in culture prior to CAM grafting (pre CAM) (Figure 6.4 A). CAM grafted specimens exhibit more surface calcification in cells that are vascularised earlier rather than left longer in differentiation media.

Analysis of mineralisation using bone volume fraction (BV/TV) suggests increased BV/TV with longer differentiation and early vascularisation (Figure 6.4 B). Pre CAM grafting, bone fraction volume was higher in undifferentiated cells compared with osteogenically differentiated cells at 3 weeks ($p<0.0001$) and 4 weeks ($p<0.0001$) of culture. BV/TV was however increased by longer time in culture for both control and osteogenically differentiated cells. Undifferentiated samples cultured for 3 weeks showed lower bone volume fraction compared with undifferentiated cells left for 4 weeks ($p<0.0001$) and 5 weeks ($p<0.0001$) in culture media. Osteogenically differentiated samples also exhibited increased BV/TV when cultured for 4 weeks ($p<0.0001$) and 5 weeks ($p<0.0001$) in osteogenic media compared with those incubated for 3 weeks in the same condition. Interestingly, there was no added advantage to longer culture period after 4 weeks with regards to BV/TV that was significantly lower after 5 weeks of culture in undifferentiated media ($p<0.0001$) or osteogenic media ($p<0.0001$) when compared with 4 weeks in the same condition.

Cellularised scaffolds grafted onto the CAM for 7 days showed increased BV/TV when osteogenically differentiated for 3 weeks ($p<0.0001$) and 4 weeks ($p<0.0001$), as compared to scaffolds maintained in culture for total corresponding time, 4 or 5 weeks. There was no significant difference in BV/TV between undifferentiated scaffolds cultured for 2 weeks then CAM grafted compared with leaving in vitro in control media for 3 weeks ($p=0.64$). BV/TV

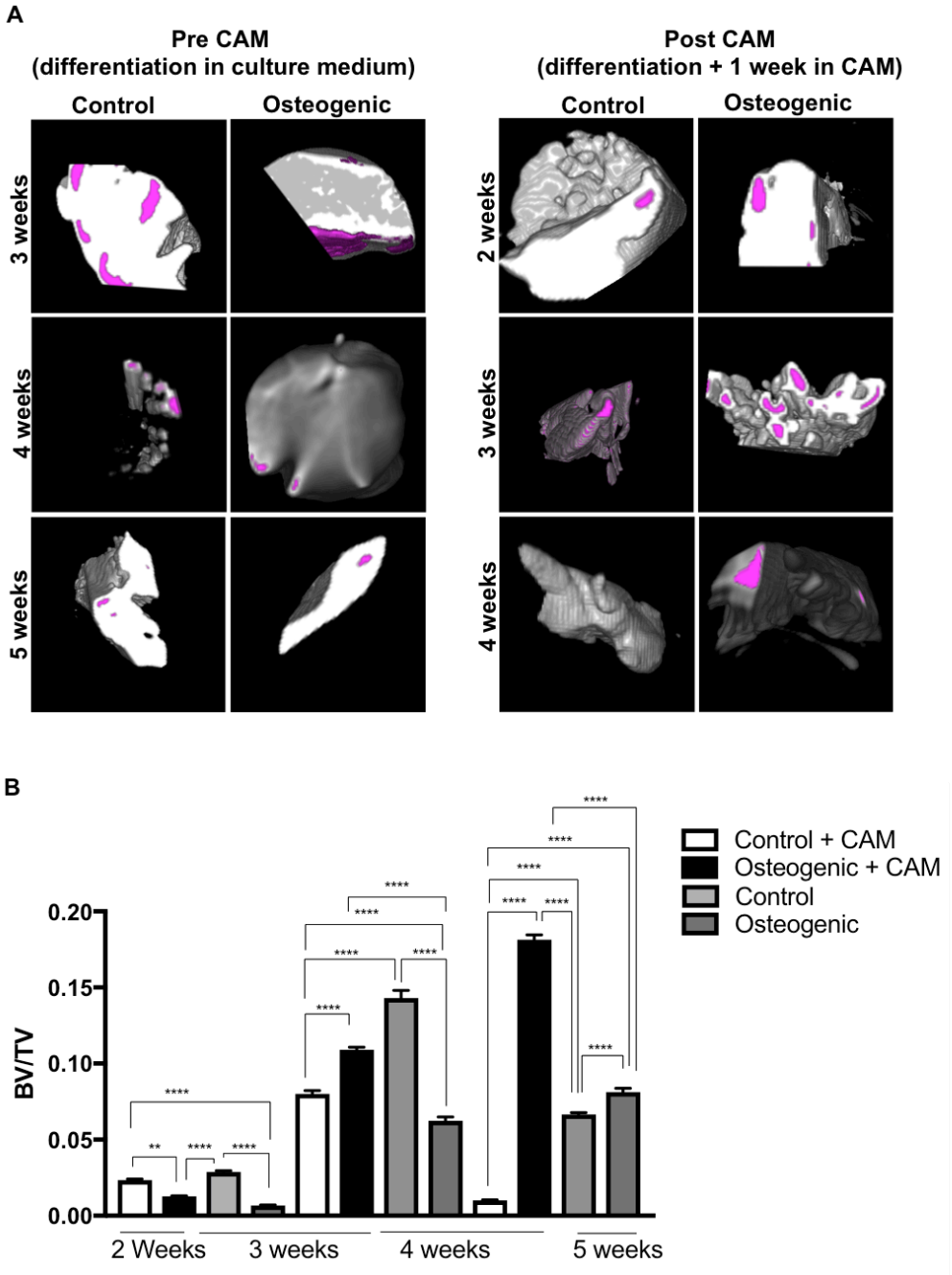

Figure 6.4: 3D models of µCT reconstructions comparing the impact of 3, 4, or 5 weeks in vitro differentiation with 7 day CAM grafting following 2, 3 or 4 weeks of in vitro culture on surface mineralisation.

A) 3D models of surface mineral nodule formation (magenta) on cellularised Fibrin scaffolds from differentiation time points before (pre) and after (post) CAM grafting for 7 days. **B)** Bone volume fraction (BV/TV) reveals greatest mineralisation density with longer differentiation period combined with CAM grafting. Early vascularisation is associated with accelerated mineralisation compared with longer differentiation culture period in vitro. CAM; chorioallantoic membrane, BV; bone volume, TV; total volume, **p<0.01, ***p<0.001, ****p<0.0001.

was however higher then undifferentiated cells cultured for 4 weeks ($p<0.0001$) or 5 ($p<0.0001$) weeks compared with those cultured in control media for 3 or 4 weeks respectively then CAM grafted. Overall the highest BV/TV was achieved after 4 weeks of osteogenic differentiation followed by CAM grafting for 7 days.

6.2.3 Evaluation of hADSC osteogenic differentiation in hybrid POSS-PCL-Fibrin scaffolds *in vitro* and following subcutaneous *grafting*

To evaluate the impact of the hybrid hydrogel nanocomposite scaffold (POSS-PCL-Fibrin) that was designed in Chapter 5 for supporting hADSC osteogenic differentiation on 3D cultures, I analysed osteogenic maturation in vitro in comparison with Fibrin alone. I then studied the impact of long term in vivo implantation of these scaffolds on extracellular matrix deposition and mineralisation. All experiments were performed in experimental triplicates using cell lines from 3 different patients for the in vitro work.

For the in vivo studies, hADSC from a single patient were grown on Fibrin alone or POSS-PCL-Fibrin scaffolds then differentiated for 3 weeks in control or osteogenic differentiation media in experimental replicates (n=6) prior to subcutaneous implantation on the flanks of nude mice (n=3 scaffolds per flank) for 4 months. The mouse engrafted with unseeded scaffolds did not survive (cause of death unknown).

6.2.3.1 Comparison of hADSC in POSS-PCL-Fibrin and Fibrin scaffolds on extracellular matrix formation

Deposition of the extracellular matrix was analysed using immunoflourescent staining for COL1 and OSTP as well as SHG (second harmonic generation) scanning to analyse collagen fibre orientation (Figure 6.5). COL1 was expressed in osteogenically differentiated cells on both Fibrin and POSS-PCL-Fibrin but not controls after 3 weeks of in vitro culture (Figure 6.5 A). The pattern of expression was extracellular but appeared more extensive and fibrous in the POSS-PCL-Fibrin biomaterial. OSTP was expressed by all samples but was most evident in cells cultured on POSS-PCL-Fibrin. SHG scanning demonstrated the formation of collagen fibre networks in osteogenically differentiated cells grown on Fibrin alone or POSS-PCL-Fibrin.

Analysis of collagen fibre orientation (using OrientationJ) from the SHG generated images shows a greater degree of anisotropy in extracellular fibres deposited by cells cultured on Fibrin scaffolds with orientation between -90 to +90 degrees (Figure 6.5 B-C). Osteogenically differentiated cells on Fibrin

appeared to produce the most disorganised collagen fibres. Cells cultured on POSS-PCL-Fibrin deposited collagen fibres that were aligned in a more polarised fashion suggesting a more organised arrangement. Whilst there was a bimodal distribution of orientation by undifferentiated cells on Fibrin, those cultured in osteogenic media tended to have an alignment tilted towards -90 degree suggesting a more uniform distribution.

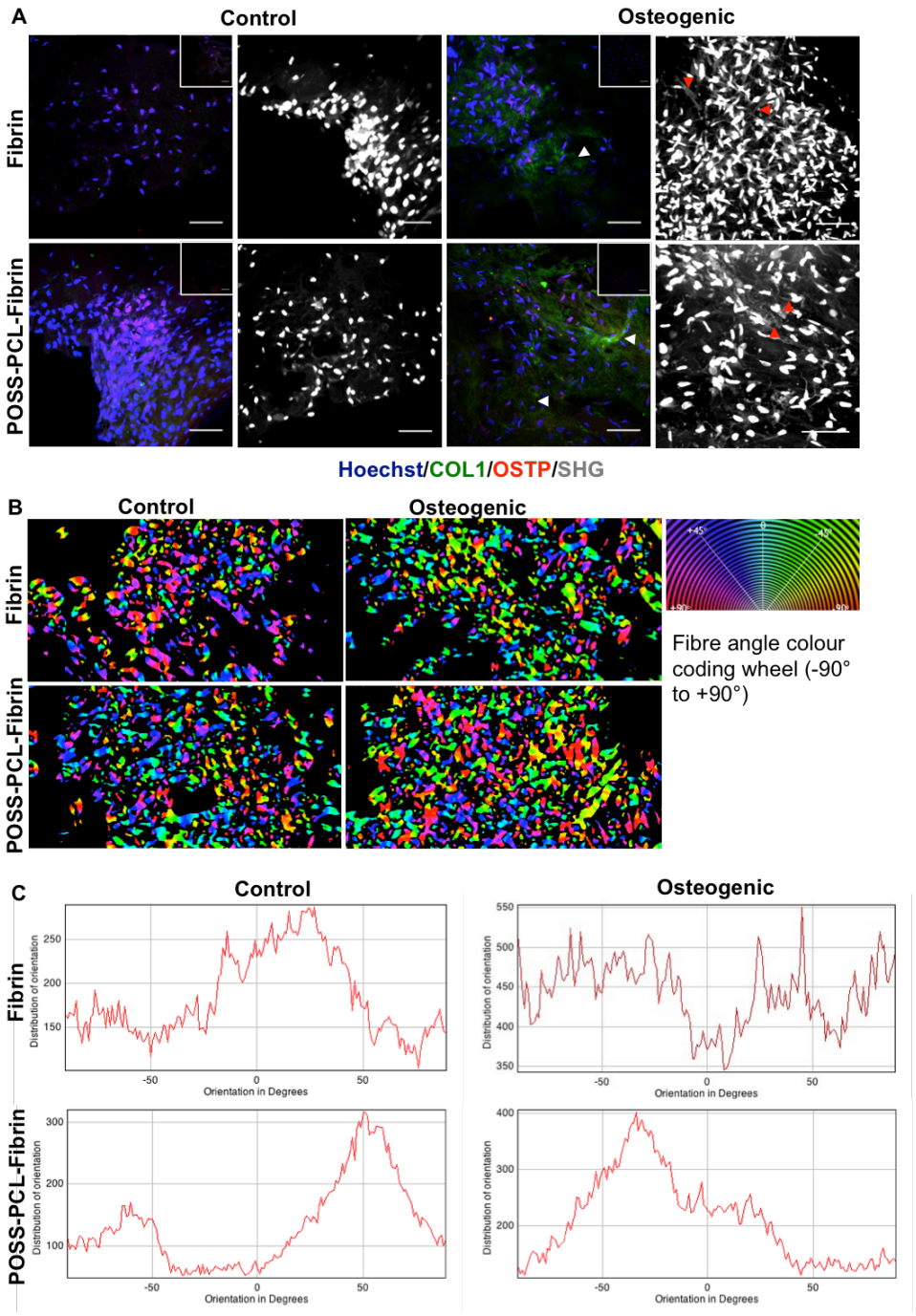

Figure 6.5: Analysis of extracellular matrix formation by hADSC on Fibrin and POSS PCL-Fibrin by immunoflourescent staining and second harmonic generation (SHG) scanning.

A) There is extracellular COL1 (white arrowheads) on osteogenically differentiated scaffolds and evidence of scant OSTP expression in control and osteogenic samples. SHG shows collagen fibres (red arrows) on all osteogenically differentiated scaffolds. **B-C)** Collagen fibre orientation analysis from SHG reveal more polarised orientation on POSS-PCL-Fibrin. COL1; collagen 1, OSTP; osteopontin, scale bar; 100 µm, negative controls (inset); 488 nm anti rabbit and 594 nm anti mouse secondary antibody only.

6.2.3.2 Histological analysis of cellularised scaffolds implanted in vivo for 4 months in athymic mice

Subcutaneously grafted scaffolds were retrieved surgically after 4 months with overlying skin and subcutaneous tissue as well as underlying membrane in order to analyse their integration and not disrupt the scaffold architecture (Figure 6.6).

Images were taken on the operating table to macroscopically determine vascularisation, which demonstrated encasement and vessel growth onto the surface of scaffolds (Figure 6.6 A). Paraffin embedded samples were sectioned into 4 μm thick slices and stained using H&E and alcian blue to analyse angiogenesis, integration, histomorphometry and extracellular matrix deposition (Figure 6.6 A). H&E staining of sections showed soft tissue growth in and around the scaffolds without evidence of inflammation or fibrosis (defined as absence of leucocyte invasion and fibrous tissue formation respectively). Whilst all scaffolds appeared cellularised, not all the POSS-PCL pores were populated with cells. Blood vessels were also readily identifiable within the mouse tissues and the scaffolds.

To further analyse the proteoglycan composition of the extracellular matrix deposited within the scaffolds, periodic acid Schiff (PAS) and alcian blue (AB) staining was performed on sections (Figure 6.6 A). Blood vessel lumens were easily visible and conformed the findings on H&E. Additionally, the pattern of proteoglycan staining of the cellularised scaffolds appeared to confirm a predominance of acid-complex connective tissue mucins (PAS-/AB+) and acid simple mucins (PAS+/AB+) which is expected in skeletogenic and stromal tissues.

Osteoblast, osteocyte and osteoclast like cells could be seen on H&E staining within the POSS-PCL-Fibrin and Fibrin scaffolds (Figure 6.6 A) with similar appearance and pattern of distribution to the native bone cellular constituents characterised in Chapter 4. Histomorphometric analysis was performed on the H&E sections to assess density of these populations (Figure 6.6 B). Whilst pre in vivo culture in control or osteogenic media was not associated with a difference in osteoblast density between cells grown on Fibrin, there was a

A

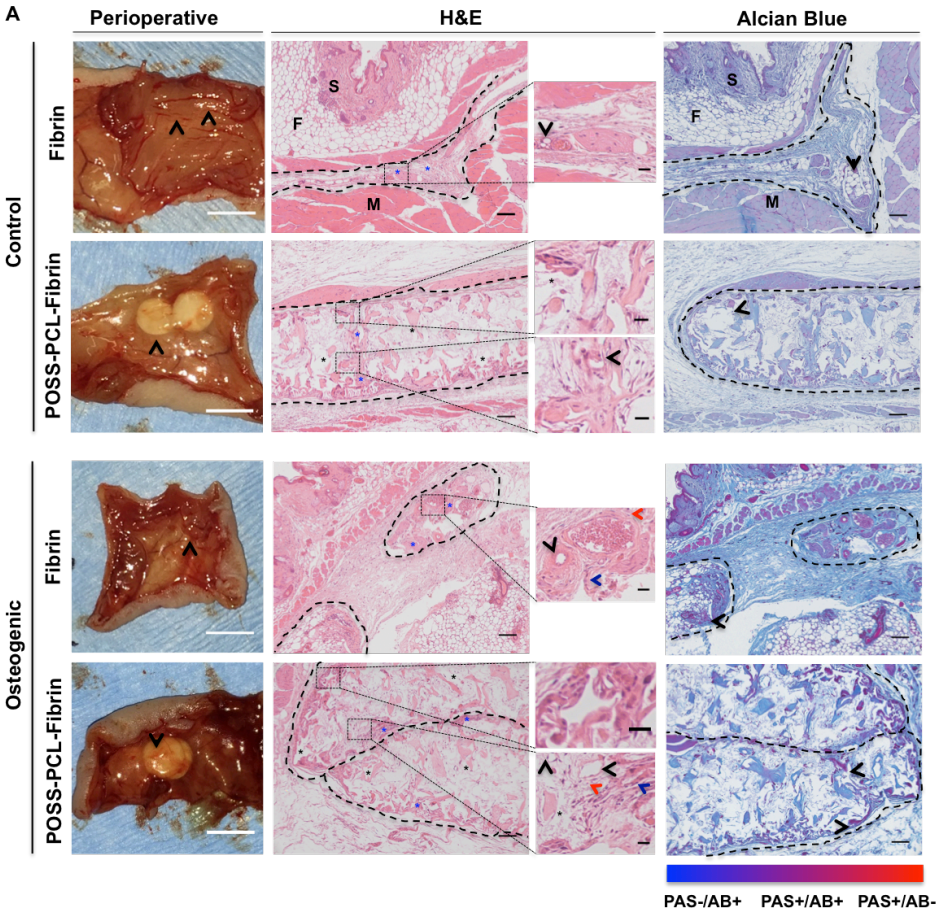

B

		Osteoblasts (cells/mm²)	Osteocytes (cells/mm²)	Osteoclasts (cells/mm²)
Fibrin	Control	138.22 ± 22.92	48.22 ± 6.26	2.22 ± 0.52
	Osteogenic	225.44 ± 24.05	105.22 ± 13.04*	5.44 ± 0.82*
POSS-PCL-Fibrin	Control	120.50 ± 32.10	44.50 ± 2.41	3.71 ± 0.68
	Osteogenic	309.22 ± 27.54***	188.11 ± 18.70****	7.75 ± 1.28*

Figure 6.6: Histological analysis of angiogenesis and osteogenic maturation of cellularised Fibrin and POSS-PCL-Fibrin after *in vivo* implantation for 4 months in nude mice.

A) Vessels surround scaffolds (black arrowheads) in the perioperative images. H&E staining shows integration of cellularised scaffolds (enclosed by black lines) and soft tissue growth (blue asterix) but some POSS-PCL-Fibrin pores remain acellular (black asterix). Blood vessels (black arrowhead), osteocytes (red arrowhead) and osteoblasts (blue arrow) are identifiable. PAS/AB staining reveals proteoglycan within scaffolds and angiogenesis (black arrowhead) with predominance of acid-complex connective tissue mucins (PAS-/AB+) and acid simple mucins (PAS+/AB+). **B)** Quantitative analysis of osteoblast, osteocyte and osteoclast density comparing osteogenically differentiated cells and their corresponding controls on the same scaffold. H&E; haematoxylin and eosin, AB; alcian blue, PAS; periodic acid Schiff, scale bars; 5mm (perioperative)/100 µm (large windows)/25 µm (small windows), *p<0.05, ***p<0.001, ****p<0.0001.

significant increase in osteoblast density in osteogenically differentiated hADSC grown on POSS-PCL-Fibrin when compared with undifferentiated cells cultured on Fibrin alone ($p=0.0002$) or POSS-PCL-Fibrin ($p=0.0003$).

Differentiation culture media prior to in vivo implantation was also related to osteocyte density. The number of osteocytes was higher in the osteogenically differentiated POSS-PCL-Fibrin group compared with the undifferentiated cells grown on the same scaffold ($p<0.0001$). Osteocyte density was also higher in osteogenically differentiated cells grown on Fibrin compared with their undifferentiated controls ($p=0.015$).

The density of osteoclast like cells was again increased in osteogenically differentiated cells compared with their undifferentiated controls in both Fibrin ($p=0.0469$) and POSS-PCL-Fibrin ($p=0.0191$) scaffolds.

6.2.3.3 Analysis of angiogenesis and mineralisation of cellularised scaffolds after subcutaneous grafting for 4 months in nude mice

3D models were generated using segmented μCT reconstructions of cellularised Fibrin and POSS-PCL-Fibrin scaffolds that were cultured in control or osteogenic media prior to subcutaneous implantation in athymic mice for 4 months (n=6) (Figure 6.7). The 3D models show a widespread vascular network surrounding each scaffold regardless of culture conditions pre-grafting and scaffold. There is evidence of infiltration and ingrowth of blood vessels into the POSS-PCL-Fibrin scaffolds as represented by vessels visible within the pores of the scaffold. Quantitative analysis of blood vessel diameter shows the smallest blood vessels are associated with cells cultured in control media for 3 weeks on a Fibrin scaffold. The size of these vessels was significantly smaller than those found in osteogenically differentiated cells grown on Fibrin ($p<0.0004$), undifferentiated cells on POSS-PCL-Fibrin ($p<0.0001$) or osteogenically differentiated cells on POSS-PCL-Fibrin ($p<0.0001$). Blood vessel size did not significantly differ between osteogenically differentiated cells grown on Fibrin and undifferentiated or osteogenically differentiated hADSC grown on POSS-PCL-Fibrin.

Analysing reconstructed μCT images assessed mineralisation of the extracellular matrix. Segmented μCT images were used to build 3D models of mineralisation (magenta) and overlay these onto the scaffold (grey). There appears to be patchy calcification of all scaffolds (Figure 6.8 A) and quantitative analysis of the bone volume fraction shows no significant difference in mineral density amongst all groups regardless of culture condition or scaffold type (Figure 6.8 B). Analysis of nodule size (Figure 6.8 C) shows that large calcium nodules are formed in Fibrin scaffolds compared with those on POSS-PCL-Fibrin in both control ($p<0.0001$) and osteogenically differentiated ($p<0.0001$) samples. There is however, no statistically significant difference in bone nodule size between cells (grown on the same scaffold type) cultured in control or osteogenic media grown. There was a large amount in variation between samples hence it would be important to repeat this experiment with a larger sample size.

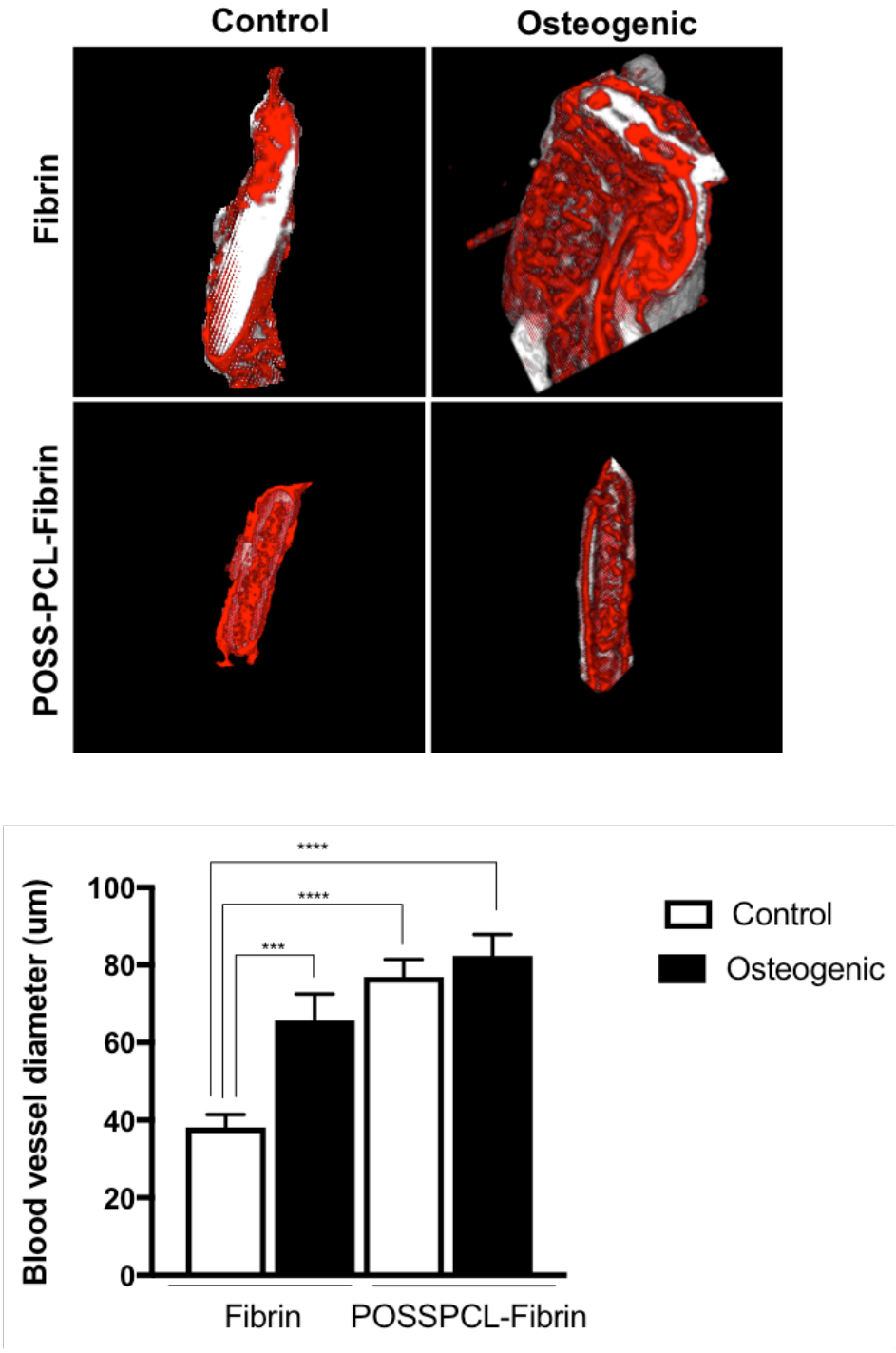

Figure 6.7: µCT analysis of vascularisation of cellularised scaffolds after 4 months of in vivo subcutaneous implantation in athymic mice.

3D models of segmented µCT reconstructed scans show blood vessels (red) surrounding and growing into each scaffold (grey). Analysis of blood vessel diameter shows significant increase in vessel size of vessels surrounding and growing into POSS-PCL-Fibrin compared with Fibrin scaffold alone. There was also increased vessel diameter in Fibrin scaffolds when specimens were cultured in osteogenic media compared with in undifferentiated media prior to implantation. Statistical significance ***p<0.001, ****p<0.0001.

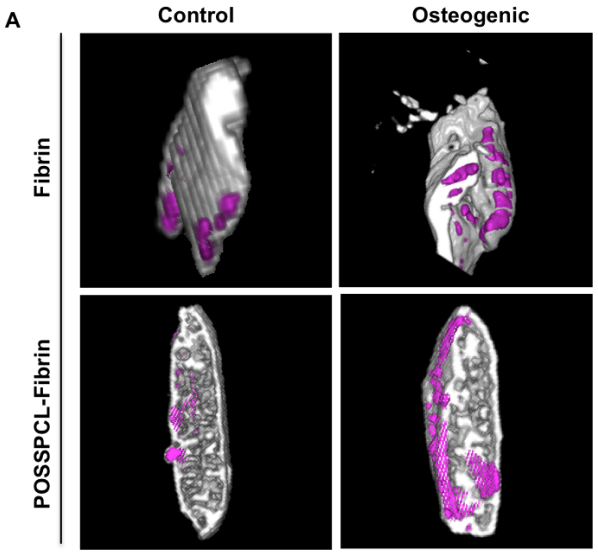

B Bone Fraction (BV/TV)

	Control (mean ± SEM)	Osteogenic (mean ± SEM)
Fibrin	0.34 ± 0.20	0.094 ± 0.053
POSSPCL-Fibrin	0.048 ± 0.014	0.019± 0.018

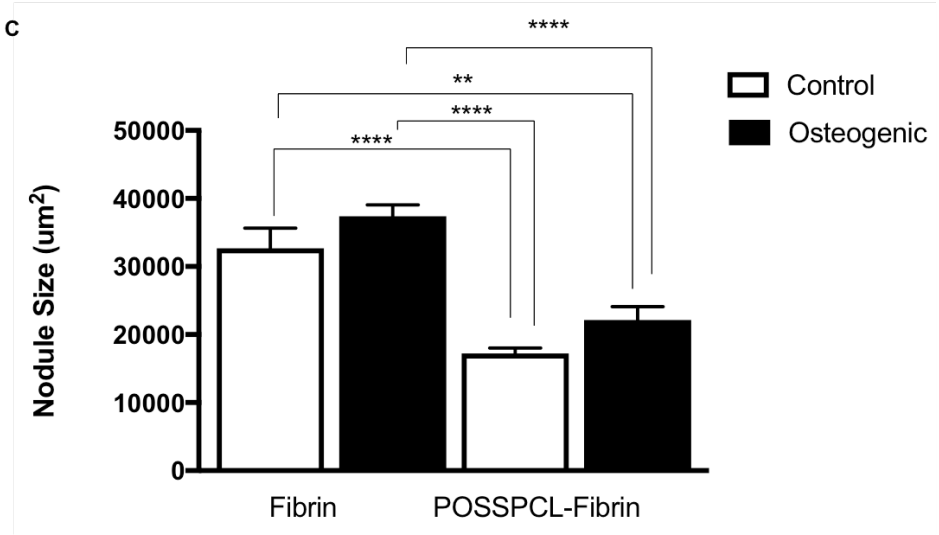

Figure 6.8: µCT analysis of mineralisation of cellularised scaffolds after 4 months of in vivo subcutaneous implantation in athymic mice.

A) 3D models of segmented scaffolds show calcium nodule formation (magenta) in cellularised scaffolds that were cultured in control or osteogenic media then implanted subcutaneously in vivo for 4 months. **B)** Bone volume fraction of samples does not show a significant difference between cells grown on either scaffold or differentiation culture condition. **C)** Bone nodule size is higher in cells grown on Fibrin rather than POSS-PCL-Fibrin but there is no difference in nodule size in control or osteogenic differentiated cells grown on the same scaffold type. SEM; standard error of mean, statistical significance **p<0.01, ****p<0.0001.

6.3 Discussion

In this chapter, the importance of vascularisation in driving osteogenic maturation of hADSC was demonstrated on a novel biomaterial. The ability of the POSS-PCL-Fibrin biomaterial to enhance osteogenic differentiation and maturation *in vitro* was also further demonstrated. This biomimetic scaffold was also shown to enable angiogenesis, the deposition of a skeletogenic extracellular matrix and recreate the cellular composition characteristic of native calvarial bone after *in vivo* implantation in an athymic mouse model.

The concept of the bone organ as defined by vasculature, the presence of an organic and inorganic extracellular matrix, bone niche and interplay between the osteogenic cells is an increasingly useful with regards to understanding bone development, regeneration, modelling disease and establishing the basis for bioengineering (Martine et al., 2017, Papadimitropoulos et al., 2011, Ramasamy et al., 2016a).

Recent work has suggested that bioengineering complex tissues like bone is possible if a multi-faceted approach that seeks to recreate the biophysical environment and metabolic demands of bone is employed. This is especially evident in studies that have mimicked the complex arrangement of osteoprogenitor cells and blood supply in native bone tissues by co-culture of human MSC and human umbilical vein endothelial cells (HUVEC) in a spatial pattern representative of the haversian system to bioengineer vascularised functional bone subunits in vitro (Cui et al., 2016). Recreating the bone blood supply by prevascularisation of tissue engineered bone grafts created using a bioceramic scaffold and rabbit MSC with the femoral blood vessels was shown to significantly enhance bone regeneration and angiogenesis in a critical bone defect in rabbit femurs (Wang et al., 2010). The importance of mimicking the spatial arrangement of cells found in native bone using bioprinted cellularised hydrogel bioinks was also shown to enhance bone regeneration in a computer model of large bone defect repair (Carlier et al., 2016). Similarly, understanding the process of bone development has also been previously used to engineer bone through a cartilage intermediate template by simulating the enchondral ossification process in vitro (Osinga et al., 2016).

6.3.1 Early vascularisation is associated with increased mineralisation by hADSC when compared with longer time in differentiation media in vitro

Using culture times of 2-5 weeks I have shown that longer periods in 3D culture were associated with increased mineralisation and extracellular matrix deposition by hADSC in vitro although this effect diminishes after 4 weeks of culture. Whilst these results are useful and compare most commonly used differentiation culture time (3 weeks) against shorter and longer periods of in vitro differentiation, they do not necessarily reflect the spatial-temporal evolution of bone development. An important consideration is the timing of adding osteoinductive stimuli during in vitro differentiation. There is evidence that replicating the patterns of signalling during bone development by modifying the spatiotemporal release of growth factors results in enhanced vasculogenesis and mineralisation by human endothelial colony forming cells and MSC in 3D culture (Barati et al., 2016). The in vitro system attempted to mimic this situation by adding control and differentiation media directly at the start of the experiment then replenishing media every 2-3 days. I was able to show that longer in vitro culture in my system was associated with more mature osteogenic differentiation between 2-4 weeks of culture. One major criticism is that I did not vary the composition of the differentiation media to replicate the signalling stimuli required during early and late osteogenesis.

In parallel, analysis of the effect of early vascularisation for 7 days compared with longer culture in vitro revealed that vascularisation was more important than longer differentiation period. Additionally, vascularisation enhanced mineralisation of undifferentiated cellularised constructs despite the absence of osteogenic pre-stimulation suggesting that vascularisation in itself has an osteoinductive effect on hADSC. This is supported by previous studies which shown that recreating vascularisation in vitro through co-culture of MSC with endothelial precursors prompted early vascularisation and osteogenic differentiation (Duttenhoefer et al., 2013). These findings were recently expanded in a study of human BMSC and HUVEC co-culture which also showed that these cells synergistically enhanced the osteogenic and angiogenic effects of each other (Böhrnsen and Schliephake, 2016).

Increasingly, the specific patterns and importance of perfusion and flow as a physical stimulus to osteoinduction has been simulated by bioreactors which have enabled optimisation of mineralisation and mechanical strength in animal and human MSC in vitro (David et al., 2008, Ding et al., 2016, Ji et al., 2014). To better appreciate the role played by the vasculature in bone development, computational modeling of perfusion patterns in native bone was previously used to produce micro-channel containing scaffolds that mimic the complex vascular networks and enabled bioengineering of vascularised bone grafts using human MSC in vitro (Holmes et al., 2016).

This data in addition to previous studies again confirm the importance of taking a whole organ based approach to bone tissue engineering with a particular emphasis on the crucial role played by the vasculature.

6.3.2 Extracellular collagen formation and orientation is preferentially directed by culture of hADSC on hybrid POSS-PCL-Fibrin scaffold in vitro

The hybrid hydrogel-nanocomposite biomaterial (POSS-PCL-Fibrin) that I designed to mimic the calvarial bone architecture in Chapter 5 was shown to support osteogenic differentiation of hADSC in vitro. When compared with cell-laden Fibrin, cellularised POSS-PCL-Fibrin enabled cells to deposit extracellular matrix containing organised collagen fibres. This provides further evidence that the physical environment directs MSC behaviour and further supports the rational for engineering a biomimetic scaffold based on the results of Chapter 5. The importance of the physical environment on influencing MSC behaviour and osteoinduction was also shown by using multi-walled carbon nanotube scaffolds which enhanced hADSC mineralisation in vitro and ectopic bone formation in vivo by enabling cell and protein adhesion as well as interactions similar to those found in bone extracellular matrix (Li et al., 2012).

Additionally mature bone exhibits isotropic collagen fibre orientation at the bone-forming surface as was shown in Chapters 4 and 5 and evident in the POSS-PCL-Fibrin collagen orientation analysis. Previous work has shown that deposition of isotropic collagen fibre networks by sheep MSC at the bone forming surface directed the pattern and size mineral particle formation which in turn resulted in reorganisation of collagen fibres to accommodate the dynamic

process of biomineralisation (Campi et al., 2015). Again whilst this combination of isotropic collagen fibre orientation at the osteoid and anisotropy at the mature bone in the medulla was observed in my calvarial bone analysis in earlier chapters and previous analysis of human long bone trabecular collagen distribution (Hua et al., 2016), this heterogeneic distribution was not observed in the POSS-PCL-Fibrin scaffolds indicating an earlier degree of maturation.

It is clear from this data and previous studies that the end-goal goal of generating autologous, anatomically accurate and functional bone grafts requires a better understanding of the biological, physical and mechanical environment of native bone to generate biomimetic materials and culture protocols that support the formation of complex bone tissues.

6.3.3 Long term subcutaneous implantation drives mineralisation, extracellular matrix formation and cellular maturation by hADSC

The in vivo study demonstrated a number of potentially promising findings. Not only did the POSS-PCL-Fibrin cellularised scaffolds show biocompatibility and integration with surrounding murine soft tissues but also enabled angiogenesis and extracellular matrix deposition independent of pre differentiation status in vitro.

Subcutaneous implantation of undifferentiated and osteogenically differentiated cellularised POSS-PCL-Fibrin revealed incorporation of biomaterial with surrounding tissue as evidenced by absence of inflammation and presence of vascular networks arising from the mouse and infiltrating the scaffold. Of particular significance is the diameter of these vessels that suggests the formation of microvasculature. This is important in that data from mapping of the vasculature in murine calvarial bone marrow has shown that the flow dynamics in these vessels directed haemopoeitic and progenitor cell homing (Bixel et al., 2017). It would be interesting to further analyse the local distribution of these microvascular channels and compare with bone since previous studies have shown that the thickness of bone tissue correlates with the pattern and organisation of the microvasculature in rat studies of long and flat bones (Pannarale et al., 1997). Equally important would be to assess whether the scaffold affects vascular patterning either positively or negatively.

Analysis of the in vivo samples revealed formation of an extracellular matrix comprised resembling mature skeletogenic connective tissue as evidenced by the histological staining and mineralisation. Significantly, there was presence of cells with an appearance similar to osteoblasts, osteocytes and osteoclasts suggesting establishment of a bone micro environment similar to that found in native tissues as described in Chapter 4. Although mineralisation density was not affected by osteogenic differentiation prior to in vivo implantation, the presence of bone related cells and an organised mature extracellular matrix was significantly enhanced by osteogenic priming of the cellularised scaffolds for 3 weeks prior to implantation. These results firstly confirm previous studies which have shown that osteogenic differentiation of human osteprogenitor cells can be significantly enhanced by culture on scaffolds which mimic the patterning of the extracellular matrix (Rakian et al., 2015) and even more so when combined with physical stimulation to reproduce the biomechanical environment of bone tissues (Zhou et al., 2016b) to direct cell behaviour. Whilst I found these cells in both control as well as osteogenically pre stimulated cells, they were significantly increased in cells that had been osteogenically differentiated. This would suggest that although modifying the biophysical environment is enough to enable osteoinduction, the presence of osteogenically primed cells is required to achieve a more mature degree of differentiation.

Taken together all of these findings provide a strong basis for taking an integrated approach to bone bioengineering. Whilst I demonstrated that my biomimetic scaffold could support hADSC osteogenesis and vascularisation in vitro and in vivo, it would be important to know whether specifically patterning the scaffold to direct microvessel formation could enhance or accelerate bone maturation. Studies which incorporated the key features of complex micro structures in the bone extracellular matrix including vascular microchannels were able to confer additional mechanical strength and facilitate osteogenesis and angiogenesis on their human amniotic fluid cell laden hydrogel/TCP/PCL-based biomaterial in vitro and in vivo (Kang et al., 2016).

6.3.4 Limitations

Whilst the CAM studies show hADSC retention after engraftment and vascularisation, the biggest imitation of this study is that it was unable to verify whether the differentiated cells populating the scaffold after in vivo implantation were derived from the host (mouse) or whether they were formed by the hADSC as the Lamin antibody staining of paraffin embedded sections did not work. This is important in that if the cells present were largely derived from the hADSC then it would be important to investigate whether starting with a higher density of hADSC could have increased the bone fraction volume or amount of extracellular matrix deposited. A possible and practical solution would have been to use labelled hADSC in order to monitor this.

In principle, μCT analysis of the scaffolds prior to implantation would have allowed assessment of any changes in terms of tissue growth and invasion and scaffold degradation. This is however not possible to do at present as the μCT scanning time for each sample was more than 4 hours and even if scaffolds were scanned in a sterile container, the absence of culture media and optimal culture temperature would have impacted cell survival and viability. As such, I could not measure pre implantation size of the cellularised scaffolds immediately prior to in vivo implantation and so were then unable to ascertain whether there was growth (or shrinkage) of the samples after in vivo implantation for 4 months. One possible solution is to compare them with the scanned scaffolds prior to cell seeding and culture although this would not help differentiate between how much of the tissue in growth was due to *in vitro* culture and how much due to *in vivo*.

Another key limitation is that the functional capacity of these bioengineered bones was not analysed. It would have been important to establish whether mechanical properties of the biomaterials were altered by longer differentiation protocols, vascularisation in the CAMS and importantly before and after in vivo implantation in mice. Furthermore, the haemopoeitic and metabolic functions of these bioengineered bones should have also been assessed. Equally important, the function of the cellular components of the bone tissue should be

studied to ascertain whether the complex interplay required for bone formation and remodelling is simulated.

The animal model was useful to characterise the biocompatibility of the cellularised biomaterials and effect of vascularisation on osteogenic maturation. This subcutaneous implantation model is however limited as it produces heterotopic bone formation. A more useful model would have been a critical bone defect model which would have allowed the scaffolds to benefit from an osteogenic environment and allowed assessment of whether this bioengineered bone could generate a viable replacement tissue.

6.3.5 Future direction

These results present an argument for the taking a multi-faceted approach to bone bioengineering in order to recreate the complexity of the bone-organ. In addition to addressing the limitations above, further work is required to fully characterise and utilise the effect of vascularisation on functional bone tissue formation.

Firstly, study of blood flow and vascular networks should be performed on craniofacial bone during embryonic and postnatal development as well as after injury and during regeneration. This data could be used to incorporate vascular networks into the scaffolds, which could serve as a template for neoangiogenesis. Furthermore, previous studies have shown that 3D culture of human MSC in a dynamic system using a bioreactor significantly enhanced osteogenic differentiation as evidenced by gene expression and extracellular matrix deposition (Stiehler et al., 2009). Further analysis of flow perfusion during craniofacial bone development could be simulated using a bioreactor to assess whether this would enhance and direct osteogenic differentiation and maturation.

Additionally, it would be important to study whether recreating the architecture of bone would help hADSC to differentiate into the cell populations that normally reside in them. This could potentially facilitate the interplay between the osteoprogenitor, osteoblasts and osteocyte populations found in native bone tissues. Cellularised constructs should include or be optimised to encourage the

migration of osteoclasts in order to establish the normal relationship between osteogenesis and remodelling.

3D modelling and bioprinting could enable the design and generation of such complex scaffolds. To date studies have provided protocols which allow bioprinting of high density MSC-laden hydrogels without loss of viability, enhancement of bioinks with bioactive particles and high resolution printing of constructs that recreate many of the structural and spacial arrangements in native bone (Costantini et al., 2016, Cui et al., 2016). In future, this technology could be used to build on the findings of this study by bioprinting constructs that replicate the different micro-niches and vascular networks found in bone as well as replicate the biophysical stimuli required for bone organogenesis.

Characterisation of the tissue-engineered bones will be required to assess biological and mechanical function. Additionally, the differentiated cells should be analysed with regards to regenerative capacity and signalling to assess whether their behaviour is similar to osteoblasts and osteocytes found in normal craniofacial bone.

To truly establish the clinical potential of these tissues, further long-term data using large-animal defect models will be necessary to ascertain safety, survival, functionality and maintenance of shape. Moreover, extensive evaluation of the bioengineered bone tissues is required to assess whether they also provide the metabolic and haemopoeitic functions required of native bones and when implanted in vivo, how they relate to the surrounding skeleton and systemic signalling.

6.4 Conclusions

In this chapter, the importance of vascularisation in directing osteogenic maturation of hADSC in 3D culture was demonstrated. Whilst longer osteogenic induction was associated with increased osteogenic differentiation in vitro, early vascularisation was shown to accelerate mineralisation and mature extracellular formation regardless of pre stimulation in osteogenic culture media. Furthermore, 3D culture and spatial arrangement was shown to enhance osteogenesis of hADSC on a biomimetic biomaterial echoing the findings of the previous two chapters.

In vivo studies using subcutaneous implantation in athymic mice revealed biocompatibility of the cellularised biomimetic scaffolds and enabled angiogenesis as well as population of scaffolds by osteoblast, osteocyte and osteoclast-like cells thus mimicking the bone micro-niche.

Despite the limitations associated with using a heterotopic bone model, inability to verify the origin of the cells populating the scaffolds and lack of functional assessment of the bioengineered tissues taken together, these results provide a promising basis for generating the bone-organ. Longer in vivo studies are needed in larger animal defect model to establish the possibility of bioengineering full-scale functional bone tissues.

Chapter 7 General Discussion

Congenital midface deformities can arise in conditions like Treacher Collins Syndrome and Craniofacial microsomia due to abnormal facial morphogenesis. Children born with these defects suffer from functional problems such as speech, vision or breathing as well as negative psychosocial outcomes. At present reconstructive surgery aims to restore form and function but frequently involves lengthy and invasive procedures based around autologous tissue transfer and/or foreign-body implants. In addition to risks of infection, extrusion and donor-site morbidity, the outcome of these procedures is difficult to predict and often requires repeat procedures throughout childhood and even into adulthood. Advances in computational biology and tissue engineering provide the potential to more accurately plan surgery and bioengineer personalised autologous replacement tissues to reconstruct the defect for a life-long solution. There are still many barriers to clinical translation including a paucity of information regarding normal postnatal midface growth and failure to achieve osteogenic maturation in differentiating paediatric mesenchymal stem cells on a vascularisable biomaterial. This thesis investigated whether combining morphometric analysis and bone tissue engineering could be used to lay the foundations for bioengineering bespoke autologous bone implants for reconstructing paediatric midface skeletal defects (Figure 7.1).

7.1 Morphometric analysis can be used to relate growth of the skeletal and soft tissues of the midface in normal and dysmorphic postnatal development and provide the basis for generating a surgical planning tool

In order to understand postnatal development of the midface I built the first combined soft and skeletal model of facial growth and morphology in healthy and dysmorphic children. This enabled us to relate the growth of soft and skeletal tissues during normal growth, accurately model the dysmorphology in TCS and CM as well as evaluate the outcomes of midface reconstruction in a child with TCS.

Whilst the combined model of postnatal midface development is novel, it also builds on findings from previous studies that showed significant coincidence between morphology of the midface skeleton and its overlying soft tissue envelope in children and adolescents (Young et al., 2016). My work furthers this

by using a wide range of age groups in children (1-16 years old) where previous work tends to use older patients (7 years onwards). I also showed that this relationship is also true in TCS and CM faces which was not previously known.

The model also analysed the difference in between midface morphology in TCS and CM compared with controls and echoed previous anthropometric and cephalometric findings (Kolar et al., 1985, Nikkhah et al., 2013, Herlin et al., 2013b, Herlin et al., 2013a, Claes et al., 2011, Ongkosuwito et al., 2013, Tuin et al., 2015). A significant advantage of this study is that it used a larger number of syndromic (TCS) patients, greater number of healthy controls and also analysed faces with severe dysmorphology compared with previous papers. Additionally, I showed that there is evidence of midfacial asymmetry in TCS which was not previously known but is an important consideration in operative planning (Dixon, 1996).

In using the combined model to evaluate the immediate and long-term efficacy of facial normalisation in a child with TCS. The observation that the correction is not maintained a year after surgery is validated by clinical studies that previously demonstrated that on-lay bone grafts resorb in the long-term (Fan et al., 2012). Hence, the model provides a potentially useful tool for quantitative surgical evaluation. I also established the foundations for developing the model into a surgical planning by using the age-matched controls for the same patient to virtually simulate surgery. Whilst this approach was very basic, provides proof of concept for the potential clinical applications of the model. Although computer models using 3D CT surfaces have been used to predict accurately plan soft tissue correction by virtually simulating maxillary and mandibular surgery (Liebregts et al., 2015b, Liebregts et al., 2015a), this has been limited by the use of non-syndromic adolescents and young adults.

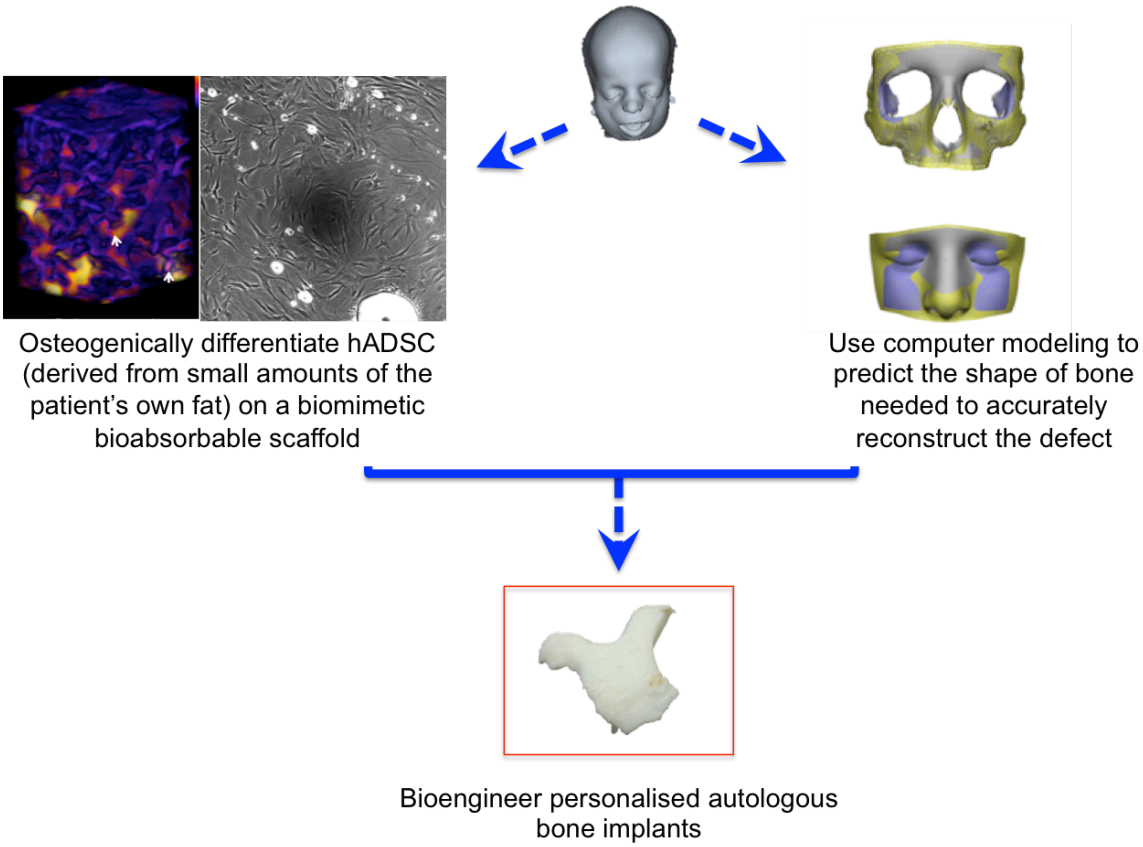

Figure 7.1: Overview of the aim to combine computational modelling and bone tissue engineering to create personalised facial bone implants.

Routine computed tomography scans from patients with skeletal midface defects could be used to evaluate the deformity and model the optimal bone shape required to reconstruct the defect. This can be used to bioengineer an autologous custom shaped bon implant using the patient's own hADSC and a biomimetic bioabsorbable scaffold.

7.2 Analysis of paediatric calvarial bones establishes a reference for craniofacial bone bioengineering in children

Prior to this study there was a paucity of information in the literature regarding the biomolecular characterisation of paediatric craniofacial bones. Since, calvarial bone grafts have long served as replacement tissues for facial bone defects (Tessier et al., 2005, Smolka et al., 2005), I analysed the structure of these tissues. Through this I described the composition and arrangement of the cellular as well as mineral and organic extracellular matrix components of paediatric calvarial bone tissues.

Previous attempts at bone characterisation often looked at physical and biological properties separately and were further limited by using older patient groups (Nakashima and de Crombrugghe, 2003). (Rühli et al., 2007, Torres-Lagares et al., 2010). As such, this is the first study to use non-syndromic paediatric calvarial bone samples to define the biological properties of craniofacial bone. I were also able to confirm that mature paediatric calvarial tissues bones expressed *COL1, OSC* and *OSX* which was previously only known from mouse studies (Nakashima and de Crombrugghe, 2003). In addition to showing that these genes were useful markers for mature osteogenesis, I also demonstrated that less commonly used techniques such as collagen orientation analysis could provide a useful measure of the extracellular matrix arrangement in mature calvarial bone. In defining the bone microenvironment and hierarchical structure at the macro and ultrastructural level, I was able to provide a meaningful standard against which bioengineered tissues can be compared.

7.3 Paediatric osteoprogenitor cells from different tissue sources can all be osteoinduced and are capable of undergoing osteogenic maturation using clinically acceptable protocols

This was the first study to characterise and compare osteoprogenitor cells derived from paediatric adipose, bone and bone marrow sources for the purposes of mature bone formation. In addition to confirming previously published results that the hAEDSC and hBMSC were capable of self-renewal and multi-lineage differentiation cells (Lv et al., 2014, Guasti et al., 2012, New

et al., 2015, Adegani et al., 2013), I also showed that hOP exhibited properties consistent with mesenchymal stem cell phenotype.

To continue the theme of integrating computational biology into analysis of cell behaviour and characterisation, I analysed the ultra cellular components, extracellular matrix arrangement alongside traditional analyses such as gene and protein expression. These methods enabled me to verify osteogenic maturation by all of the osteoprogenitor cells which deposited extracellular matrix in a pattern previously described as typical of mature osteoblasts (Orriss et al., 2014, Rutkovskiy et al., 2016).

Through this work I also supported the use of a whole-organ approach to bone bioengineering. I showed that 3D culture and vascularisation optimised osteoinduction and bone maturation of osteoprogenitor cells. Whilst previous studies have shown 3D culture accelerated osteogenic differentiation of human preosteoblast cells (Jähn et al., 2010), this work is the first to demonstrate this on different paediatric mesenchymal stem cell types and to comprehensively analyse and compare these results with human bone control tissues. The importance of vascularisation on osteogenic differentiation has been previously shown in co-culture studies of osteoprogenitor cells with blood-derived angiogenic cells and in vivo in mice studies (Joensuu et al., 2015, Thébaud et al., 2012, Najdanović et al., 2015). Uniquely, this work extensively compared three different sources of human osteoprogenitor cells. I demonstrated that even short periods (7 days) of vascularisation in the CAM model promote osteogenic maturation (as evidenced by increased mineral density) even in the absence of prior osteogenic stimulation in vitro.

A key advantage of this study is it uses in vitro culture and differentiation protocols that have been previously described and can easily lend themselves to GMP compliance and clinical translation at a later date (Lechanteur et al., 2016). I also show retention of the human cells, albeit for a short implantation period, in CAM grafted samples. This is also promising if eventual clinical use is attempted.

7.4 Increased knowledge of bone biology and structure enabled replication of the bone microenvironment by designing biomimetic scaffolds and culture conditions to optimise osteoinduction and osteogenic maturation of hADSC

I used data from the bone characterisation analysis to fabricate a novel biomimetic bioabsorbable scaffold that supports vascularisation and osteogenic differentiation of hADSC. This builds on previous studies, which have shown that the 3D microenvironment can be used to reproduce direct MSC behaviour (Yu et al., 2017, Paul et al., 2016, Marinkovic et al., 2016, Lee et al., 2016) and more specifically driving osteogenic differentiation (Kittaka et al., 2015, Rakian et al., 2015).

Unique to this study was the use of native bone tissue to reverse engineer the bone micro-niche with a bioabsorbable scaffold comprised of two biomaterials already licensed for clinical use. The POSS-PCL biomaterial showed immense potential for surface and structural modification to enhance cell survival and optimisation whilst combination with Fibrin enhanced vascularisation and osteoinduction. The results also further support the use of bioactive and biomimetic scaffolds which reproduce the extracellular matrix environment which were previously shown to enhance osteoinduction of MSC (Kim et al., 2015, Oh et al., 2014). My characterisation of the osteogenic maturation by the hADSC was however more extensive than previous studies and were able to show that the pattern of extracellular collagen deposition was comparable with mature bone.

7.5 Vascularisation promotes hADSC osteogenesis and accelerates bone maturation

Through the CAM grafting studies, I demonstrated that early vascularisation of hADSC enhanced bone maturation even more so than prolonged in vitro culture in osteoinductive media. This builds on previous work showing early transient vascularisation drives chondrogenic differentiation and maturation by hADSC (Takebe et al., 2014). In addition my findings build on previous studies that have shown that replication of vascularisation in vitro through co-culture of endothelial cells human MSC or use of bioreactors enhanced mineralisation

and mature bone formation (Barati et al., 2016, Duttenhoefer et al., 2013, Böhrnsen and Schliephake, 2016, David et al., 2008, Ding et al., 2016, Ji et al., 2014). Unlike previous studies, I assessed the effect of vascularisation at multiple time points to show that priming in osteoinductive media was still required to achieve more mature bone formation.

7.6 Tissue engineered bone from hADSC cultured on a biomimetic scaffold are biocompatible and capable of vascularization and survival in long term in vivo culture

In designing a biomimetic scaffold that sought to replicate the bone microenvironment and promote vascularisation, I were able to recreate the conditions previously described as important for bone organogenesis (Martine et al., 2017, Papadimitropoulos et al., 2011, Ramasamy et al., 2016a). This enabled me to demonstrate that mature osteogenic differentiation by hADSC could be achieved on a bioabsorbable scaffold in vitro and further driven in vivo.

Data from the in vivo samples also showed that long term (4 months) implantation of the cellularised scaffolds in an animal model preserved mineralisation and permitted the formation of a mature extracellular matrix consistent with bone tissue. I also demonstrated that the tissue engineered samples contained similar cell populations to paediatric calvarial bone tissues suggesting replication of the bone micro-niche. This is consistent with previous studies that osteogenic capability of hADSC can be optimised by using biomimetic scaffolds which replicate the extracellular matrix and biophysical environment in mature bone tissue (Rakian et al., 2015, Zhou et al., 2016b). I however further clarified this principle by showing that in addition to the important bone microenvironment in regulating hADSC behaviour, optimal mature bone formation is achieved with pre-stimulation of cells by osteogenic with differentiation media prior to in vivo implantation.

7.7 Towards bioengineering autologous personalised facial bone implants for reconstructing paediatric midface deformities by combining morphometric analysis and bone tissue engineering

The work in this thesis provides the foundations for creating custom-shaped bone implants. I propose a model approach that integrates midface modelling with bone tissue engineering using paediatric adipose derived stem cells. In an earlier case report, there has been published evidence of using tissue engineered (from hADSC) zygomatic bones to reconstruct midface deformity in an adolescent with TCS (Taylor, 2010). Although they provide evidence of lamellar bone formation at 6 months, the small sample size (n=1) and the absence of a follow up study since mean that the generalizability and success of this cannot be adequately confirmed in the long term.

There is already evidence for the use of an integrated approach that combines computer-aided design and biomimetic MSC culture protocols can be used to bioengineer custom-shaped facial bone tissue (Grayson et al., 2010, Temple et al., 2014). The work in this thesis is however unique in that it attempts to model the missing or hypoplastic bones and reproduce the biological and structural complexity of these bones to bioengineer mature bone tissues. Whilst the results are at an early stage, they provide proof of concept of the potential for combining morphometric analysis and bone tissue engineering to generate replacement tissues for complex treating paediatric midface deformities.

7.8 Further considerations

In order to build on the results of the morphometric analysis work (Chapter 3), an increased sample size is required for both control and dysmorphic patients. There is also a need for acquiring longitudinal data in the form of multiple CT scans from different time points of the same individual. This would help model individual growth trajectories for each child in order to allow simulation of midface growth and surgical reconstruction. As diseases like TCS are rare and since healthy children do not routinely undergo CT scanning, it is likely that either a large multi-centre study will be required.

One of the key limitations of this work is the use of calvarial non-syndromic craniosynostotic bone as a positive control. As such, future work will need to compare my findings with a healthy control population. Since healthy children do not undergo invasive procedures such as craniofacial bone biopsies, a suitable alternative may have to be samples from neoplastic lesions, trauma or

infection that are usually excised with a large healthy tissue margin to ensure adequate clearance.

To substantiate the findings of the osteoprogenitor cell characterisation, these studies will need to be performed on a larger number of cell lines from patients of different ages and with both craniofacial microsomia, Treacher Collins Syndrome and non syndromic controls. This would enable greater confidence in the generalisation of these findings and delineate any normal heterogeneity that could exist within patients with the same diagnosis.

To build on these results, I will also need to focus on gaining a deeper understanding of the spatial-temporal evolution of bone organogenesis and the role of the collagen matrix in the organic-mineral transition (Barati et al., 2016, Reznikov et al., 2014, Cedola et al., 2014). This would enable me to further optimise my differentiation protocols and bioactive scaffold to bioengineer mature bone tissues.

To capitalise on the effect of vascularisation on osteogenic maturation exhibited by the cells, I will need to explore whether a bioreactor can help replicate the biophysical and perfusion patterns in an in vitro culture system. This can also be used to attempt to bioengineer large tissues. I should also attempt to further modify my hybrid scaffold to optimise cell adhesion, osteogenesis and vascularisation by modifying the surface

Whilst my work employed multiple methods to verify the extent of osteogenic maturation, future studies should additionally assess the mechanical and functional properties of work. This would enable me to accurately evaluate the clinical application of these bioengineered tissues in that both the structural and functional properties of bones will be needed to provide an adequate replacement tissue.

Since the overall aim of this research is to generate personalised autologous facial bone tissues, 3D printing would help integrate the facial modelling work with the bone tissue engineering findings to design custom-shaped bones. This is an increasingly popular area of research that has been shown to enable simultaneous printing of multiple cell types, scaffolds and bioactive substances

fabricate complex bone tissues and their associated vascular networks (Costantini et al., 2016, Cui et al., 2016).

Finally, whilst the in vivo model enabled me to demonstrate the biocompatibility of the biomaterial and that osteogenic differentiation was maintained, it is limited by the fact that it is subcutaneous and therefore supports hetetrophic bone formation. If I generate larger pre-shaped bone constructs need I will need to consider a critical defect model in a larger animal. This would enable accurate evaluation of the regenerative capacity of my bioengineered bone tissues.

Chapter 8 Conclusions

This work provides a number of important and novel findings, which advance the aim of bioengineering, personalised autologous face bones for the reconstruction of paediatric craniofacial defects. New data regarding human postnatal midface growth and craniofacial bone biology was generated in addition to the formation of mature vascularised bone tissues by human adipose derived stem cells on a novel bioabsorbable scaffold.

In modelling midface growth and of the soft tissue and skeletal tissues I was able to, for the first time, show the relationship between these tissues in normal and dysmorphic postnatal development. The model also provides the potential to generate an operative planning and evaluation tool that could enable more accurate surgical outcomes for patients with midface deformities. Furthermore, I was able to characterise calvarial bone tissue to establish a useful reference for evaluating the maturity of engineered bone tissues. Through this I also demonstrated that a reverse engineering approach could be successfully adopted to fabricate a biomimetic scaffold and recreate the bone tissue microenvironment in order optimise osteogenic maturation by human adipose derived stem cells. Through my in vivo work I was able to show that my bioengineered constructs were biocompatible and that mature bone tissue with histological appearance of the cellular and extracellular composition of normal bone tissue was achieved.

Although at an early stage, the work in this thesis highlights the importance of taking a combined whole organ approach to generating autologous bones for the reconstruction of midface skeletal defects. Further research will be required to generate full-scale custom-shaped facial bones. Functional analysis and a larger animal critical defect model is also required to verify the regenerative potential for using these cells to reconstruct midface bone defects.

Bibliography

ADEGANI, F. J., LANGROUDI, L., AREFIAN, E., SHAFIEE, A., DINARVAND, P. & SOLEIMANI, M. 2013. A comparison of pluripotency and differentiation status of four mesenchymal adult stem cells. *Mol Biol Rep,* 40**,** 3693-703.

AHMED, M., PUNSHON, G., DARBYSHIRE, A. & SEIFALIAN, A. M. 2013. Effects of sterilization treatments on bulk and surface properties of nanocomposite biomaterials. *J Biomed Mater Res B Appl Biomater,* 101**,** 1182-90.

AHN, E. H., KIM, Y., KSHITIZ, AN, S. S., AFZAL, J., LEE, S., KWAK, M., SUH, K. Y., KIM, D. H. & LEVCHENKO, A. 2014. Spatial control of adult stem cell fate using nanotopographic cues. *Biomaterials,* 35**,** 2401-10.

ALT, E., YAN, Y., GEHMERT, S., SONG, Y. H., ALTMAN, A., VYKOUKAL, D. & BAI, X. 2011. Fibroblasts share mesenchymal phenotypes with stem cells, but lack their differentiation and colony-forming potential. *Biol Cell,* 103**,** 197-208.

AN, S., HUANG, X., GAO, Y., LING, J., HUANG, Y. & XIAO, Y. 2015. FGF-2 induces the proliferation of human periodontal ligament cells and modulates their osteoblastic phenotype by affecting Runx2 expression in the presence and absence of osteogenic inducers. *Int J Mol Med,* 36**,** 705-11.

ANH, D. J., DIMAI, H. P., HALL, S. L. & FARLEY, J. R. 1998. Skeletal alkaline phosphatase activity is primarily released from human osteoblasts in an insoluble form, and the net release is inhibited by calcium and skeletal growth factors. *Calcif Tissue Int,* 62**,** 332-40.

ARGANDA-CARRERAS, I., KAYNIG, V., RUEDEN, C., ELICEIRI, K. W., SCHINDELIN, J., CARDONA, A. & SEUNG, H. S. 2017. Trainable Weka Segmentation: a machine learning tool for microscopy pixel classification. *Bioinformatics*.

ASHBURNER, J. & FRISTON, K. J. 2000. Voxel-based morphometry--the methods. *Neuroimage,* 11**,** 805-21.

AUGER, F. A., GIBOT, L. & LACROIX, D. 2013. The pivotal role of vascularization in tissue engineering. *Annu Rev Biomed Eng,* 15**,** 177-200.

AYANDELE, E., SARKAR, B. & ALEXANDRIDIS, P. 2012. Polyhedral Oligomeric Silsesquioxane (POSS)-Containing

Polymer Nanocomposites. *nanomaterials,* 2**,** 445-475.

AÇIL, Y., GHONIEM, A. A., GÜLSES, A., KISCH, T., STANG, F., WILTFANG, J. & GIERLOFF, M. 2016. Suppression of osteoblast-related genes during osteogenic differentiation of adipose tissue derived stromal cells. *J Craniomaxillofac Surg*.

BAEK, W. Y., LEE, M. A., JUNG, J. W., KIM, S. Y., AKIYAMA, H., DE CROMBRUGGHE, B. & KIM, J. E. 2009. Positive regulation of adult bone formation by osteoblast-specific transcription factor osterix. *J Bone Miner Res,* 24**,** 1055-65.

BAINO, F., NOVAJRA, G. & VITALE-BROVARONE, C. 2015. Bioceramics and Scaffolds: A Winning Combination for Tissue Engineering. *Front Bioeng Biotechnol,* 3**,** 202.

BANERJEE, C., JAVED, A., CHOI, J. Y., GREEN, J., ROSEN, V., VAN WIJNEN, A. J., STEIN, J. L., LIAN, J. B. & STEIN, G. S. 2001. Differential regulation of the two principal Runx2/Cbfa1 n-terminal isoforms in response to bone morphogenetic protein-2 during development of the osteoblast phenotype. *Endocrinology,* 142**,** 4026-39.

BARATI, D., SHARIATI, S. R., MOEINZADEH, S., MELERO-MARTIN, J. M., KHADEMHOSSEINI, A. & JABBARI, E. 2016. Spatiotemporal release of BMP-2 and VEGF enhances osteogenic and vasculogenic differentiation of human mesenchymal stem cells and endothelial colony-forming cells co-encapsulated in a patterned hydrogel. *J Control Release,* 223**,** 126-36.

BASKIN, J. Z. & EPPELL, S. J. 2013. A selected review of the recent advances in craniomaxillofacial bone tissue engineering. *Curr Opin Otolaryngol Head Neck Surg,* 21**,** 389-95.

BAUMANN, A. P., DEUERLING, J. M., RUDY, D. J., NIEBUR, G. L. & ROEDER, R. K. 2012. The relative influence of apatite crystal orientations and intracortical porosity on the elastic anisotropy of human cortical bone. *J Biomech,* 45**,** 2743-9.

BELLOWS, C. G., HEERSCHE, J. N. & AUBIN, J. E. 1992. Inorganic phosphate added exogenously or released from beta-glycerophosphate initiates mineralization of osteoid nodules in vitro. *Bone Miner,* 17**,** 15-29.

BEN SHOHAM, A., ROT, C., STERN, T., KRIEF, S., AKIVA, A., DADOSH, T., SABANY, H., LU, Y., KADLER, K. E. & ZELZER, E. 2016. Deposition of collagen type I onto skeletal endothelium reveals a new role for blood vessels in regulating bone morphology. *Development,* 143**,** 3933-3943.

BERGMAN, R. T., WASCHAK, J., BORZABADI-FARAHANI, A. & MURPHY, N. C. 2014. Longitudinal study of cephalometric soft tissue profile traits between the ages of 6 and 18 years. *Angle Orthod,* 84**,** 48-55.

BERKOWITZ, S. 2013. *Cleft Lip and Palate: Diagnosis and Management*, Springer Berlin Heidelberg.

BERMEO, S., VIDAL, C., ZHOU, H. & DUQUE, G. 2015. Lamin A/C Acts as an Essential Factor in Mesenchymal Stem Cell Differentiation Through the Regulation of the Dynamics of the Wnt/β-Catenin Pathway. *J Cell Biochem,* 116**,** 2344-53.

BERNER, A., HENKEL, J., WOODRUFF, M. A., STECK, R., NERLICH, M., SCHUETZ, M. A. & HUTMACHER, D. W. 2015. Delayed minimally invasive injection of allogenic bone marrow stromal cell sheets regenerates large bone defects in an ovine preclinical animal model. *Stem Cells Transl Med,* 4**,** 503-12.

BINULAL, N. S., DEEPTHY, M., SELVAMURUGAN, N., SHALUMON, K. T., SUJA, S., MONY, U., JAYAKUMAR, R. & NAIR, S. V. 2010. Role of nanofibrous poly(caprolactone) scaffolds in human mesenchymal stem

cell attachment and spreading for in vitro bone tissue engineering--response to osteogenic regulators. *Tissue Eng Part A,* 16**,** 393-404.

BIRGFELD, C. B. & HEIKE, C. 2012. Craniofacial microsomia. *Semin Plast Surg,* 26**,** 91-104.

BIRGFELD, C. B., HEIKE, C. L., SALTZMAN, B. S., LEROUX, B. G., EVANS, K. N. & LUQUETTI, D. V. 2016. Reliable classification of facial phenotypic variation in craniofacial microsomia: a comparison of physical exam and photographs. *Head Face Med,* 12**,** 14.

BIRGFELD, C. B., LUQUETTI, D. V., GOUGOUTAS, A. J., BARTLETT, S. P., LOW, D. W., SIE, K. C., EVANS, K. N. & HEIKE, C. L. 2011. A phenotypic assessment tool for craniofacial microsomia. *Plast Reconstr Surg,* 127**,** 313-20.

BIXEL, M. G., KUSUMBE, A. P., RAMASAMY, S. K., SIVARAJ, K. K., BUTZ, S., VESTWEBER, D. & ADAMS, R. H. 2017. Flow Dynamics and HSPC Homing in Bone Marrow Microvessels. *Cell Rep,* 18**,** 1804-1816.

BLAZQUEZ-MARTINEZ, A., CHIESA, M., ARNALICH, F., FERNANDEZ-DELGADO, J., NISTAL, M. & DE MIGUEL, M. P. 2014. c-Kit identifies a subpopulation of mesenchymal stem cells in adipose tissue with higher telomerase expression and differentiation potential. *Differentiation,* 87**,** 147-60.

BLUESTONE, C. D., SIMONS, J. P. & HEALY, G. B. 2014. *Bluestone and Stool's Pediatric Otolaryngology*, People's Medical Publishing House-USA.

BOERCKEL, J. D., UHRIG, B. A., WILLETT, N. J., HUEBSCH, N. & GULDBERG, R. E. 2011. Mechanical regulation of vascular growth and tissue regeneration in vivo. *Proc Natl Acad Sci U S A,* 108**,** E674-80.

BONEWALD, L. F., HARRIS, S. E., ROSSER, J., DALLAS, M. R., DALLAS, S. L., CAMACHO, N. P., BOYAN, B. & BOSKEY, A. 2003. von Kossa staining alone is not sufficient to confirm that mineralization in vitro represents bone formation. *Calcif Tissue Int,* 72**,** 537-47.

BORAAS, L. C. & AHSAN, T. 2016. Lack of vimentin impairs endothelial differentiation of embryonic stem cells. *Sci Rep,* 6**,** 30814.

BORAAS, L. C., GUIDRY, J. B., PINEDA, E. T. & AHSAN, T. 2016. Cytoskeletal Expression and Remodeling in Pluripotent Stem Cells. *PLoS One,* 11**,** e0145084.

BREITSPRECHER, L., FANGHÄNEL, J., METELMANN, H. R., MLYNSKI, G., WÜRFEL, F., FREISE, K. & KNAPE, U. 1999. The influence of the muscles of facial expression on the development of the midface and the nose in cleft lip and palate patients. A reflection of functional anatomy, facial esthetics and physiology of the nose. *Ann Anat,* 181**,** 19-25.

BRENNAN, P. A., MAHADEVAN, V. & EVANS, B. T. 2015. *Clinical Head and Neck Anatomy for Surgeons*, CRC Press.

BRITTO, J. A., GREIG, A., ABELA, C., HEARST, D., DUNAWAY, D. J. & EVANS, R. D. 2014. Frontofacial surgery in children and adolescents: techniques, indications, outcomes. *Semin Plast Surg,* 28**,** 121-9.

BROWN, J. S. & SHAW, R. J. 2010. Reconstruction of the maxilla and midface: introducing a new classification. *Lancet Oncol,* 11**,** 1001-8.

BUDAI, M., FARKAS, L. G., TOMPSON, B., KATIC, M. & FORREST, C. R. 2003. Relation between anthropometric and cephalometric measurements and proportions of the face of healthy young white adult men and women. *J Craniofac Surg,* 14**,** 154-61; discussion 162-3.

BURR, D. B. & ALLEN, M. R. 2013. *Basic and Applied Bone Biology*, Elsevier Science.

BÖHRNSEN, F. & SCHLIEPHAKE, H. 2016. Supportive angiogenic and osteogenic differentiation of mesenchymal stromal cells and endothelial cells in monolayer and co-cultures. *Int J Oral Sci,* 8**,** 223-230.

CAMPI, G., FRATINI, M., BUKREEVA, I., CIASCA, G., BURGHAMMER, M., BRUN, F., TROMBA, G., MASTROGIACOMO, M. & CEDOLA, A. 2015. Imaging collagen packing dynamics during mineralization of engineered bone tissue. *Acta Biomater,* 23**,** 309-16.

CARLIER, A., SKVORTSOV, G. A., HAFEZI, F., FERRARIS, E., PATTERSON, J., KOÇ, B. & VAN OOSTERWYCK, H. 2016. Computational model-informed design and bioprinting of cell-patterned constructs for bone tissue engineering. *Biofabrication,* 8**,** 025009.

CATELAS, I., SESE, N., WU, B. M., DUNN, J. C., HELGERSON, S. & TAWIL, B. 2006. Human mesenchymal stem cell proliferation and osteogenic differentiation in fibrin gels in vitro. *Tissue Eng,* 12**,** 2385-96.

CECCARELLI, J. & PUTNAM, A. J. 2014. Sculpting the blank slate: how fibrin's support of vascularization can inspire biomaterial design. *Acta Biomater,* 10**,** 1515-23.

CEDOLA, A., CAMPI, G., PELLICCIA, D., BUKREEVA, I., FRATINI, M., BURGHAMMER, M., RIGON, L., ARFELLI, F., CHANG CHEN, R., DREOSSI, D., SODINI, N., MOHAMMADI, S., TROMBA, G., CANCEDDA, R. & MASTROGIACOMO, M. 2014. Three dimensional visualization of engineered bone and soft tissue by combined x-ray micro-diffraction and phase contrast tomography. *Phys Med Biol,* 59**,** 189-201.

CHAN, M. E., LU, X. L., HUO, B., BAIK, A. D., CHIANG, V., GULDBERG, R. E., LU, H. H. & GUO, X. E. 2009. A Trabecular Bone Explant Model of Osteocyte-Osteoblast Co-Culture for Bone Mechanobiology. *Cell Mol Bioeng,* 2**,** 405-415.

CHANG, B., SONG, W., HAN, T., YAN, J., LI, F., ZHAO, L., KOU, H. & ZHANG, Y. 2016. Influence of pore size of porous titanium fabricated by vacuum diffusion bonding of titanium meshes on cell penetration and bone ingrowth. *Acta Biomater,* 33**,** 311-21.

CHAUDHARY, L. R., HOFMEISTER, A. M. & HRUSKA, K. A. 2004. Differential growth factor control of bone formation through osteoprogenitor differentiation. *Bone,* 34**,** 402-11.

CHAWLA, R., TAN, A., AHMED, M., CROWLEY, C., MOIEMEN, N. S., CUI, Z., BUTLER, P. E. & SEIFALIAN, A. M. 2014. A polyhedral oligomeric

silsesquioxane-based bilayered dermal scaffold seeded with adipose tissue-derived stem cells: in vitro assessment of biomechanical properties. *J Surg Res,* 188**,** 361-72.

CHEN, H., SENDA, T. & KUBO, K. Y. 2015. The osteocyte plays multiple roles in bone remodeling and mineral homeostasis. *Med Mol Morphol,* 48**,** 61-8.

CHOI, J. W. & KIM, N. 2015. Clinical application of three-dimensional printing technology in craniofacial plastic surgery. *Arch Plast Surg,* 42**,** 267-77.

CHOUNG, P. H., NAM, I. W. & KIM, K. S. 1991. Vascularized cranial bone grafts for mandibular and maxillary reconstruction. The parietal osteofascial flap. *J Craniomaxillofac Surg,* 19**,** 235-42.

CHUNG, E., RYTLEWSKI, J. A., MERCHANT, A. G., DHADA, K. S., LEWIS, E. W. & SUGGS, L. J. 2015. Fibrin-based 3D matrices induce angiogenic behavior of adipose-derived stem cells. *Acta Biomater,* 17**,** 78-88.

CIGNONI, P., CALLIERI, M., CORSINI, M., DELLEPIANE, M., GANOVELLI, F. & RANZUGLIA, G. 2008. MeshLab: an Open-Source Mesh Processing Tool. *In:* ERRA, V. S. A. R. D. C. A. U. (ed.) *Eurographics Italian Chapter Conference* The Eurographics Association.

CLAES, P., WALTERS, M., VANDERMEULEN, D. & CLEMENT, J. G. 2011. Spatially-dense 3D facial asymmetry assessment in both typical and disordered growth. *J Anat,* 219**,** 444-55.

CLARKE, B. 2008. Normal bone anatomy and physiology. *Clin J Am Soc Nephrol,* 3 Suppl 3**,** S131-9.

COBB, A. R., GREEN, B., GILL, D., AYLIFFE, P., LLOYD, T. W., BULSTRODE, N. & DUNAWAY, D. J. 2014. The surgical management of Treacher Collins syndrome. *Br J Oral Maxillofac Surg,* 52**,** 581-9.

CONTE, C., D'APICE, M. R., RINALDI, F., GAMBARDELLA, S., SANGIUOLO, F. & NOVELLI, G. 2011. Novel mutations of TCOF1 gene in European patients with Treacher Collins syndrome. *BMC Med Genet,* 12**,** 125.

CONVERSE, J. M., COCCARO, P. J., BECKER, M. & WOOD-SMITH, D. 1973. On hemifacial microsomia. The first and second branchial arch syndrome. *Plast Reconstr Surg,* 51**,** 268-79.

CORRADETTI, B., TARABALLI, F., POWELL, S., SUNG, D., MINARDI, S., FERRARI, M., WEINER, B. K. & TASCIOTTI, E. 2015. Osteoprogenitor cells from bone marrow and cortical bone: understanding how the environment affects their fate. *Stem Cells Dev,* 24**,** 1112-23.

COSTANTINI, M., IDASZEK, J., SZÖKE, K., JAROSZEWICZ, J., DENTINI, M., BARBETTA, A., BRINCHMANN, J. E. & ŚWIĘSZKOWSKI, W. 2016. 3D bioprinting of BM-MSCs-loaded ECM biomimetic hydrogels for in vitro neocartilage formation. *Biofabrication,* 8**,** 035002.

COX, T. C., LUQUETTI, D. V. & CUNNINGHAM, M. L. 2013. Perspectives and challenges in advancing research into craniofacial anomalies. *Am J Med Genet C Semin Med Genet,* 163C**,** 213-7.

CROWLEY, C., KLANRIT, P., BUTLER, C. R., VARANOU, A., PLATÉ, M., HYNDS, R. E., CHAMBERS, R. C., SEIFALIAN, A. M., BIRCHALL, M. A. & JANES, S. M. 2016. Surface modification of a POSS-nanocomposite material to enhance cellular integration of a synthetic bioscaffold. *Biomaterials,* 83**,** 283-93.

CUI, H., ZHU, W., NOWICKI, M., ZHOU, X., KHADEMHOSSEINI, A. & ZHANG, L. G. 2016. Hierarchical Fabrication of Engineered Vascularized Bone Biphasic Constructs via Dual 3D Bioprinting: Integrating Regional Bioactive Factors into Architectural Design. *Adv Healthc Mater,* 5**,** 2174-81.

CURI, M. M., OLIVEIRA, M. F., MOLINA, G., CARDOSO, C. L., OLIVEIRA, L. E. G., BRANEMARK, P. I. & RIBEIRO, K. E. C. 2012. Extraoral implants in the rehabilitation of craniofacial defects: implant and prosthesis survival rates and peri-implant soft tissue evaluation. *J Oral Maxillofac Surg,* 70**,** 1551-7.

DAUWERSE, J. G., DIXON, J., SELAND, S., RUIVENKAMP, C. A., VAN HAERINGEN, A., HOEFSLOOT, L. H., PETERS, D. J., BOERS, A. C., DAUMER-HAAS, C., MAIWALD, R., ZWEIER, C., KERR, B., COBO, A. M., TORAL, J. F., HOOGEBOOM, A. J., LOHMANN, D. R., HEHR, U., DIXON, M. J., BREUNING, M. H. & WIECZOREK, D. 2011. Mutations in genes encoding subunits of RNA polymerases I and III cause Treacher Collins syndrome. *Nat Genet,* 43**,** 20-2.

DAVID, V., GUIGNANDON, A., MARTIN, A., MALAVAL, L., LAFAGE-PROUST, M. H., RATTNER, A., MANN, V., NOBLE, B., JONES, D. B. & VICO, L. 2008. Ex Vivo bone formation in bovine trabecular bone cultured in a dynamic 3D bioreactor is enhanced by compressive mechanical strain. *Tissue Eng Part A,* 14**,** 117-26.

DE PEPPO, G. M., MARCOS-CAMPOS, I., KAHLER, D. J., ALSALMAN, D., SHANG, L., VUNJAK-NOVAKOVIC, G. & MAROLT, D. 2013. Engineering bone tissue substitutes from human induced pluripotent stem cells. *Proc Natl Acad Sci U S A,* 110**,** 8680-5.

DE SOUZA, M. A., MCALLISTER, C., SUTTIE, M., PERROTTA, C., MATTINA, T., FARAVELLI, F., FORZANO, F., HOLLAND, A. & HAMMOND, P. 2013. Growth hormone, gender and face shape in Prader-Willi syndrome. *Am J Med Genet A,* 161**,** 2453-63.

DELLOYE-BOURGEOIS, C., RAMA, N., BRITO, J., LE DOUARIN, N. & MEHLEN, P. 2014. Sonic Hedgehog promotes the survival of neural crest cells by limiting apoptosis induced by the dependence receptor CDON during branchial arch development. *Biochem Biophys Res Commun,* 452**,** 655-60.

DENG, Y., ZHOU, H., YAN, C., WANG, Y., XIAO, C., GU, P. & FAN, X. 2014. In vitro osteogenic induction of bone marrow stromal cells with encapsulated gene-modified bone marrow stromal cells and in vivo implantation for orbital bone repair. *Tissue Eng Part A,* 20**,** 2019-29.

DENNY, A. D., KALANTARIAN, B. & HANSON, P. R. 2003. Rotation advancement of the midface by distraction osteogenesis. *Plast Reconstr Surg,* 111**,** 1789-99; discussion 1800-3.

DING, M., HENRIKSEN, S. S., WENDT, D. & OVERGAARD, S. 2016. An automated perfusion bioreactor for the streamlined production of engineered osteogenic grafts. *J Biomed Mater Res B Appl Biomater,* 104**,** 532-7.

DING, R., JIANG, X., HA, Y., WANG, Z., GUO, J., JIANG, H., ZHENG, S., SHEN, Z. & JIE, W. 2015. Activation of Notch1 signalling promotes multi-lineage differentiation of c-Kit(POS)/NKX2.5(POS) bone marrow stem cells: implication in stem cell translational medicine. *Stem Cell Res Ther,* 6**,** 91.

DIXON, M. J. 1996. Treacher Collins syndrome. *Hum Mol Genet,* 5 Spec No**,** 1391-6.

DOMINICI, M., LE BLANC, K., MUELLER, I., SLAPER-CORTENBACH, I., MARINI, F., KRAUSE, D., DEANS, R., KEATING, A., PROCKOP, D. & HORWITZ, E. 2006. Minimal criteria for defining multipotent mesenchymal stromal cells. The International Society for Cellular Therapy position statement. *Cytotherapy,* 8**,** 315-7.

DOUBE, M., KŁOSOWSKI, M. M., ARGANDA-CARRERAS, I., CORDELIÈRES, F. P., DOUGHERTY, R. P., JACKSON, J. S., SCHMID, B., HUTCHINSON, J. R. & SHEFELBINE, S. J. 2010. BoneJ: Free and extensible bone image analysis in ImageJ. *Bone,* 47**,** 1076-9.

DUNLOP, L. L. & HALL, B. K. 1995. Relationships between cellular condensation, preosteoblast formation and epithelial-mesenchymal interactions in initiation of osteogenesis. *Int J Dev Biol,* 39**,** 357-71.

DUTTENHOEFER, F., LARA DE FREITAS, R., MEURY, T., LOIBL, M., BENNEKER, L. M., RICHARDS, R. G., ALINI, M. & VERRIER, S. 2013. 3D scaffolds co-seeded with human endothelial progenitor and mesenchymal stem cells: evidence of prevascularisation within 7 days. *Eur Cell Mater,* 26**,** 49-64; discussion 64-5.

ESTEVE-ALTAVA, B. & RASSKIN-GUTMAN, D. 2014. Beyond the functional matrix hypothesis: a network null model of human skull growth for the formation of bone articulations. *J Anat,* 225**,** 306-16.

FAN, K. L., FEDERICO, C., KAWAMOTO, H. K. & BRADLEY, J. P. 2012. Optimizing the timing and technique of Treacher Collins orbital malar reconstruction. *J Craniofac Surg,* 23**,** 2033-7.

FARKAS, L. G., EIBEN, O. G., SIVKOV, S., TOMPSON, B., KATIC, M. J. & FORREST, C. R. 2004. Anthropometric measurements of the facial framework in adulthood: age-related changes in eight age categories in 600 healthy white North Americans of European ancestry from 16 to 90 years of age. *J Craniofac Surg,* 15**,** 288-98.

FARKAS, L. G., POSNICK, J. C. & HRECZKO, T. M. 1992. Growth patterns of the face: a morphometric study. *Cleft Palate Craniofac J,* 29**,** 308-15.

FARKAS, L. G., TOMPSON, B., PHILLIPS, J. H., KATIC, M. J. & CORNFOOT, M. L. 1999. Comparison of anthropometric and cephalometric measurements of the adult face. *J Craniofac Surg,* 10**,** 18-25; discussion 26.

FARKAS, L. G., TOMPSON, B. D., KATIC, M. J. & FORREST, C. R. 2002. Differences between direct (anthropometric) and indirect (cephalometric) measurements of the skull. *J Craniofac Surg,* 13**,** 105-8; discussion 109-10.

FARLEY, J. R., HALL, S. L., TANNER, M. A. & WERGEDAL, J. E. 1994. Specific activity of skeletal alkaline phosphatase in human osteoblast-line cells regulated by phosphate, phosphate esters, and phosphate analogs and release of alkaline phosphatase activity inversely regulated by calcium. *J Bone Miner Res,* 9**,** 497-508.

FERLIN, K. M., PRENDERGAST, M. E., MILLER, M. L., KAPLAN, D. S. & FISHER, J. P. 2016. Influence of 3D printed porous architecture on mesenchymal stem cell enrichment and differentiation. *Acta Biomater,* 32**,** 161-9.

FERNANDES, T. M., ADAMCZYK, J., POLETI, M. L., HENRIQUES, J. F., FRIEDLAND, B. & GARIB, D. G. 2015. Comparison between 3D volumetric rendering and multiplanar slices on the reliability of linear measurements on CBCT images: an in vitro study. *J Appl Oral Sci,* 23**,** 56-63.

FLORENCIO-SILVA, R., SASSO, G. R., SASSO-CERRI, E., SIMÕES, M. J. & CERRI, P. S. 2015. Biology of Bone Tissue: Structure, Function, and Factors That Influence Bone Cells. *Biomed Res Int,* 2015**,** 421746.

FRANCESCHI, R. T. & IYER, B. S. 1992. Relationship between collagen synthesis and expression of the osteoblast phenotype in MC3T3-E1 cells. *J Bone Miner Res,* 7**,** 235-46.

FRANCHI, G., KADLUB, N., DINER, P. A., BANDINI, M., VAZQUEZ, M. P. & PICARD, A. 2015. Orbital soft tissue surgery for patients with Treacher-Collins or Nager syndrome. A new surgical approach with early correction of soft tissue: prospective study. *Br J Oral Maxillofac Surg,* 53**,** 421-5.

FRISDAL, A. & TRAINOR, P. A. 2014. Development and evolution of the pharyngeal apparatus. *Wiley Interdiscip Rev Dev Biol,* 3**,** 403-18.

GANDHIMATHI, C., VENUGOPAL, J. R., THAM, A. Y., RAMAKRISHNA, S. & KUMAR, S. D. 2015. Biomimetic hybrid nanofibrous substrates for mesenchymal stem cells differentiation into osteogenic cells. *Mater Sci Eng C Mater Biol Appl,* 49**,** 776-85.

GAO, C., DENG, Y., FENG, P., MAO, Z., LI, P., YANG, B., DENG, J., CAO, Y., SHUAI, C. & PENG, S. 2014a. Current progress in bioactive ceramic scaffolds for bone repair and regeneration. *Int J Mol Sci,* 15**,** 4714-32.

GAO, S., CALCAGNI, M., WELTI, M., HEMMI, S., HILD, N., STARK, W. J., BÜRGISSER, G. M., WANNER, G. A., CINELLI, P. & BUSCHMANN, J. 2014b. Proliferation of ASC-derived endothelial cells in a 3D electrospun

mesh: impact of bone-biomimetic nanocomposite and co-culture with ASC-derived osteoblasts. *Injury,* 45**,** 974-80.

GARCÍA-GARETA, E., COATHUP, M. J. & BLUNN, G. W. 2015. Osteoinduction of bone grafting materials for bone repair and regeneration. *Bone,* 81**,** 112-121.

GASPAROTTO, V. P., LANDIM-ALVARENGA, F. C., OLIVEIRA, A. L., SIMÕES, G. F., LIMA-NETO, J. F., BARRAVIERA, B. & FERREIRA, R. S. 2014. A new fibrin sealant as a three-dimensional scaffold candidate for mesenchymal stem cells. *Stem Cell Res Ther,* 5**,** 78.

GEORGIADIS, M., MÜLLER, R. & SCHNEIDER, P. 2016. Techniques to assess bone ultrastructure organization: orientation and arrangement of mineralized collagen fibrils. *J R Soc Interface,* 13.

GHANBARI, H., COUSINS, B. G. & SEIFALIAN, A. M. 2011. A nanocage for nanomedicine: polyhedral oligomeric silsesquioxane (POSS). *Macromol Rapid Commun,* 32**,** 1032-46.

GIANNOTTI, S., TROMBI, L., BOTTAI, V., GHILARDI, M., D'ALESSANDRO, D., DANTI, S., DELL'OSSO, G., GUIDO, G. & PETRINI, M. 2013. Use of autologous human mesenchymal stromal cell/fibrin clot constructs in upper limb non-unions: long-term assessment. *PLoS One,* 8**,** e73893.

GRABER, L. W., VANARSDALL, R. L. & VIG, K. W. L. 2011. *Orthodontics: Current Principles and Techniques*, Elsevier Health Sciences.

GRANKE, M., GOURRIER, A., RUPIN, F., RAUM, K., PEYRIN, F., BURGHAMMER, M., SAÏED, A. & LAUGIER, P. 2013. Microfibril orientation dominates the microelastic properties of human bone tissue at the lamellar length scale. *PLoS One,* 8**,** e58043.

GRAY, H., STANDRING, S., ELLIS, H. & BERKOVITZ, B. K. B. 2005. *Gray's anatomy: the anatomical basis of clinical practice*, Elsevier Churchill Livingstone.

GRAYSON, W. L., FRÖHLICH, M., YEAGER, K., BHUMIRATANA, S., CHAN, M. E., CANNIZZARO, C., WAN, L. Q., LIU, X. S., GUO, X. E. & VUNJAK-NOVAKOVIC, G. 2010. Engineering anatomically shaped human bone grafts. *Proc Natl Acad Sci U S A,* 107**,** 3299-304.

GREEN, D. W., KWON, H. J. & JUNG, H. S. 2015. Osteogenic potency of nacre on human mesenchymal stem cells. *Mol Cells,* 38**,** 267-72.

GRIFFIN, M. F., IBRAHIM, A., SEIFALIAN, A. M., BUTLER, P. E., KALASKAR, D. M. & FERRETTI, P. 2017. Chemical group-dependent plasma polymerisation preferentially directs adipose stem cell differentiation towards osteogenic or chondrogenic lineages. *Acta Biomater,* 50**,** 450-461.

GRONTHOS, S., GRAVES, S. E., OHTA, S. & SIMMONS, P. J. 1994. The STRO-1+ fraction of adult human bone marrow contains the osteogenic precursors. *Blood,* 84**,** 4164-73.

GUASTI, L., PRASONGCHEAN, W., KLEFTOURIS, G., MUKHERJEE, S., THRASHER, A., BULSTRODE, N. & FERRETTI, P. 2012. High plasticity

of paediatric adipose tissue-derived stem cells: too much for selective skeletogenic differentiation? : UCL Institute of Child Health.

GUIBERT, M., FRANCHI, G., ANSARI, E., BILLOTET, B., DINER, P. A., CASSIER, S., VAZQUEZ, M. P., PICARD, A. & KADLUB, N. 2013. Fat graft transfer in children's facial malformations: a prospective three-dimensional evaluation. *J Plast Reconstr Aesthet Surg,* 66**,** 799-804.

GULSEREN, G., YASA, I. C., USTAHUSEYIN, O., TEKIN, E. D., TEKINAY, A. B. & GULER, M. O. 2015. Alkaline Phosphatase-Mimicking Peptide Nanofibers for Osteogenic Differentiation. *Biomacromolecules,* 16**,** 2198-208.

HALL, J. G. 2010. Importance of muscle movement for normal craniofacial development. *J Craniofac Surg,* 21**,** 1336-8.

HAMIDOUCHE, Z., HAŸ, E., VAUDIN, P., CHARBORD, P., SCHÜLE, R., MARIE, P. J. & FROMIGUÉ, O. 2008. FHL2 mediates dexamethasone-induced mesenchymal cell differentiation into osteoblasts by activating Wnt/beta-catenin signaling-dependent Runx2 expression. *FASEB J,* 22**,** 3813-22.

HAMMOND, P., FORSTER-GIBSON, C., CHUDLEY, A. E., ALLANSON, J. E., HUTTON, T. J., FARRELL, S. A., MCKENZIE, J., HOLDEN, J. J. & LEWIS, M. E. 2008. Face-brain asymmetry in autism spectrum disorders. *Mol Psychiatry,* 13**,** 614-23.

HAMMOND, P., HUTTON, T., MAHESWARAN, S. & MODGIL, S. 2003. Computational models of oral and craniofacial development, growth, and repair. *Adv Dent Res,* 17**,** 61-4.

HAND, A. R. & FRANK, M. E. 2014. *Fundamentals of Oral Histology and Physiology*, Wiley.

HARNET, J. C., LOMBARDI, T., MANIÈRE-EZVAN, A., CHAMOREY, E. & KAHN, J. L. 2013. Transversal craniofacial growth evaluated on children dry skulls using V2 and V 3 canal openings as references. *Surg Radiol Anat,* 35**,** 757-63.

HAYASHI, O., KATSUBE, Y., HIROSE, M., OHGUSHI, H. & ITO, H. 2008. Comparison of osteogenic ability of rat mesenchymal stem cells from bone marrow, periosteum, and adipose tissue. *Calcif Tissue Int,* 82**,** 238-47.

HAYWARD, R. 2004. *The Clinical Management of Craniosynostosis*, Wiley.

HEIKE, C. L., HING, A. V., ASPINALL, C. A., BARTLETT, S. P., BIRGFELD, C. B., DRAKE, A. F., PIMENTA, L. A., SIE, K. C., URATA, M. M., VIVALDI, D. & LUQUETTI, D. V. 2013. Clinical care in craniofacial microsomia: a review of current management recommendations and opportunities to advance research. *Am J Med Genet C Semin Med Genet,* 163C**,** 271-82.

HEO, J. S., CHOI, Y., KIM, H. S. & KIM, H. O. 2016a. Comparison of molecular profiles of human mesenchymal stem cells derived from bone marrow, umbilical cord blood, placenta and adipose tissue. *Int J Mol Med,* 37**,** 115-25.

HEO, S. J., DRISCOLL, T. P., THORPE, S. D., NERURKAR, N. L., BAKER, B. M., YANG, M. T., CHEN, C. S., LEE, D. A. & MAUCK, R. L. 2016b. Differentiation alters stem cell nuclear architecture, mechanics, and mechano-sensitivity. *Elife,* 5.

HERLIN, C., DOUCET, J. C., BIGORRE, M. & CAPTIER, G. 2013a. Computer-assisted midface reconstruction in Treacher Collins syndrome part 2: soft tissue reconstruction. *J Craniomaxillofac Surg,* 41**,** 676-80.

HERLIN, C., DOUCET, J. C., BIGORRE, M., KHELIFA, H. C. & CAPTIER, G. 2013b. Computer-assisted midface reconstruction in Treacher Collins syndrome part 1: skeletal reconstruction. *J Craniomaxillofac Surg,* 41**,** 670-5.

HOLMES, B., BULUSU, K., PLESNIAK, M. & ZHANG, L. G. 2016. A synergistic approach to the design, fabrication and evaluation of 3D printed micro and nano featured scaffolds for vascularized bone tissue repair. *Nanotechnology,* 27**,** 064001.

HOLY, C. E., SHOICHET, M. S. & DAVIES, J. E. 2000. Engineering three-dimensional bone tissue in vitro using biodegradable scaffolds: investigating initial cell-seeding density and culture period. *J Biomed Mater Res,* 51**,** 376-82.

HOPMAN, S. M., MERKS, J. H., SUTTIE, M., HENNEKAM, R. C. & HAMMOND, P. 2014. Face shape differs in phylogenetically related populations. *Eur J Hum Genet*.

HUA, W. D., CHEN, P. P., XU, M. Q., AO, Z., LIU, Y., HAN, D. & HE, F. 2016. Quantitative description of collagen fibre network on trabecular bone surfaces based on AFM imaging. *J Microsc,* 262**,** 112-22.

HUANG, L., NIU, C., WILLARD, B., ZHAO, W., LIU, L., HE, W., WU, T., YANG, S., FENG, S., MU, Y., ZHENG, L. & LI, K. 2015. Proteomic analysis of porcine mesenchymal stem cells derived from bone marrow and umbilical cord: implication of the proteins involved in the higher migration capability of bone marrow mesenchymal stem cells. *Stem Cell Res Ther,* 6**,** 77.

IBRAHIM, A., BULSTRODE, N. W., WHITAKER, I. S., EASTWOOD, D. M., DUNAWAY, D. & FERRETTI, P. 2016a. Nanotechnology for Stimulating Osteoprogenitor Differentiation. *Open Orthop J,* 10**,** 849-861.

IBRAHIM, A., SUTTIE, M., BULSTRODE, N. W., BRITTO, J. A., DUNAWAY, D., HAMMOND, P. & FERRETTI, P. 2016b. Combined soft and skeletal tissue modelling of normal and dysmorphic midface postnatal development. *J Craniomaxillofac Surg*.

IRIE, K., EJIRI, S., SAKAKURA, Y., SHIBUI, T. & YAJIMA, T. 2008. Matrix mineralization as a trigger for osteocyte maturation. *J Histochem Cytochem,* 56**,** 561-7.

ISHINO, T., YAJIN, K., TAKENO, S., FURUKIDO, K. & HIRAKAWA, K. 2003. Establishment of osteoblast culture from human ethmoidal sinus. *Auris Nasus Larynx,* 30**,** 45-51.

ITKIN, T., GUR-COHEN, S., SPENCER, J. A., SCHAJNOVITZ, A., RAMASAMY, S. K., KUSUMBE, A. P., LEDERGOR, G., JUNG, Y., MILO, I., POULOS, M. G., KALINKOVICH, A., LUDIN, A., KOLLET, O., SHAKHAR, G., BUTLER, J. M., RAFII, S., ADAMS, R. H., SCADDEN, D. T., LIN, C. P. & LAPIDOT, T. 2016. Distinct bone marrow blood vessels differentially regulate haematopoiesis. *Nature,* 532**,** 323-8.

JI, J., SUN, W., WANG, W., MUNYOMBWE, T. & YANG, X. B. 2014. The effect of mechanical loading on osteogenesis of human dental pulp stromal cells in a novel in vitro model. *Cell Tissue Res,* 358**,** 123-33.

JIMBO, R., XUE, Y., HAYASHI, M., SCHWARTZ-FILHO, H. O., ANDERSSON, M., MUSTAFA, K. & WENNERBERG, A. 2011. Genetic responses to nanostructured calcium-phosphate-coated implants. *J Dent Res,* 90**,** 1422-7.

JIN, Y., ZHANG, W., LIU, Y., ZHANG, M., XU, L., WU, Q., ZHANG, X., ZHU, Z., HUANG, Q. & JIANG, X. 2014. rhPDGF-BB via ERK pathway osteogenesis and adipogenesis balancing in ADSCs for critical-sized calvarial defect repair. *Tissue Eng Part A,* 20**,** 3303-13.

JOENSUU, K., UUSITALO, L., ALM, J. J., ARO, H. T., HENTUNEN, T. A. & HEINO, T. J. 2015. Enhanced osteoblastic differentiation and bone formation in co-culture of human bone marrow mesenchymal stromal cells and peripheral blood mononuclear cells with exogenous VEGF. *Orthop Traumatol Surg Res,* 101**,** 381-6.

JOHNSON, J. M., MOONIS, G., GREEN, G. E., CARMODY, R. & BURBANK, H. N. 2011. Syndromes of the first and second branchial arches, part 2: syndromes. *AJNR Am J Neuroradiol,* 32**,** 230-7.

JONES, N. C., LYNN, M. L., GAUDENZ, K., SAKAI, D., AOTO, K., REY, J. P., GLYNN, E. F., ELLINGTON, L., DU, C., DIXON, J., DIXON, M. J. & TRAINOR, P. A. 2008. Prevention of the neurocristopathy Treacher Collins syndrome through inhibition of p53 function. *Nat Med,* 14**,** 125-33.

JONSSON, K. B., FROST, A., NILSSON, O., LJUNGHALL, S. & LJUNGGREN, O. 1999. Three isolation techniques for primary culture of human osteoblast-like cells: a comparison. *Acta Orthop Scand,* 70**,** 365-73.

JÄHN, K., RICHARDS, R. G., ARCHER, C. W. & STODDART, M. J. 2010. Pellet culture model for human primary osteoblasts. *Eur Cell Mater,* 20**,** 149-61.

KADAKIA, S., HELMAN, S. N., BADHEY, A. K., SAMAN, M. & DUCIC, Y. 2014. Treacher Collins Syndrome: the genetics of a craniofacial disease. *Int J Pediatr Otorhinolaryngol,* 78**,** 893-8.

KANG, H. W., LEE, S. J., KO, I. K., KENGLA, C., YOO, J. J. & ATALA, A. 2016. A 3D bioprinting system to produce human-scale tissue constructs with structural integrity. *Nat Biotechnol,* 34**,** 312-9.

KASTEN, P., BEYEN, I., NIEMEYER, P., LUGINBÜHL, R., BOHNER, M. & RICHTER, W. 2008. Porosity and pore size of beta-tricalcium phosphate scaffold can influence protein production and osteogenic differentiation of

human mesenchymal stem cells: an in vitro and in vivo study. *Acta Biomater,* 4**,** 1904-15.

KATOWITZ, J. A., LINTON, A. & SRODULSKI, K. 2013. *Pediatric Oculoplastic Surgery*, Springer New York.

KELLY, M. P., VORPERIAN, H. K., WANG, Y., TILLMAN, K. K., WERNER, H. M., CHUNG, M. K. & GENTRY, L. R. 2017. Characterizing mandibular growth using three-dimensional imaging techniques and anatomic landmarks. *Arch Oral Biol,* 77**,** 27-38.

KEOGH, I. J., TROULIS, M. J., MONROY, A. A., EAVEY, R. D. & KABAN, L. B. 2007. Isolated microtia as a marker for unsuspected hemifacial microsomia. *Arch Otolaryngol Head Neck Surg,* 133**,** 997-1001.

KIM, I. G., HWANG, M. P., DU, P., KO, J., HA, C. W., DO, S. H. & PARK, K. 2015. Bioactive cell-derived matrices combined with polymer mesh scaffold for osteogenesis and bone healing. *Biomaterials,* 50**,** 75-86.

KIM, K. I., PARK, S. & IM, G. I. 2014. Osteogenic differentiation and angiogenesis with cocultured adipose-derived stromal cells and bone marrow stromal cells. *Biomaterials,* 35**,** 4792-804.

KITTAKA, M., KAJIYA, M., SHIBA, H., TAKEWAKI, M., TAKESHITA, K., KHUNG, R., FUJITA, T., IWATA, T., NGUYEN, T. Q., OUHARA, K., TAKEDA, K. & KURIHARA, H. 2015. Clumps of a mesenchymal stromal cell/extracellular matrix complex can be a novel tissue engineering therapy for bone regeneration. *Cytotherapy,* 17**,** 860-73.

KIZILTAY, A., MARCOS-FERNANDEZ, A., SAN ROMAN, J., SOUSA, R. A., REIS, R. L., HASIRCI, V. & HASIRCI, N. 2015. Poly(ester-urethane) scaffolds: effect of structure on properties and osteogenic activity of stem cells. *J Tissue Eng Regen Med,* 9**,** 930-42.

KOLAR, J. C., FARKAS, L. G. & MUNRO, I. R. 1985. Surface morphology in Treacher Collins syndrome: an anthropometric study. *Cleft Palate J,* 22**,** 266-74.

KOLAR, J. C., MUNRO, I. R. & FARKAS, L. G. 1987. Anthropometric evaluation of dysmorphology in craniofacial anomalies: Treacher Collins syndrome. *Am J Phys Anthropol,* 74**,** 441-51.

KOMORI, T., YAGI, H., NOMURA, S., YAMAGUCHI, A., SASAKI, K., DEGUCHI, K., SHIMIZU, Y., BRONSON, R. T., GAO, Y. H., INADA, M., SATO, M., OKAMOTO, R., KITAMURA, Y., YOSHIKI, S. & KISHIMOTO, T. 1997. Targeted disruption of Cbfa1 results in a complete lack of bone formation owing to maturational arrest of osteoblasts. *Cell,* 89**,** 755-64.

KOOK, S. H., HEO, J. S. & LEE, J. C. 2015. Crucial roles of canonical Runx2-dependent pathway on Wnt1-induced osteoblastic differentiation of human periodontal ligament fibroblasts. *Mol Cell Biochem,* 402**,** 213-23.

KOROLEVA, A., DEIWICK, A., NGUYEN, A., SCHLIE-WOLTER, S., NARAYAN, R., TIMASHEV, P., POPOV, V., BAGRATASHVILI, V. & CHICHKOV, B. 2015. Osteogenic differentiation of human mesenchymal stem cells in 3-D Zr-Si organic-inorganic scaffolds produced by two-photon polymerization technique. *PLoS One,* 10**,** e0118164.

KOUDELOVÁ, J., DUPEJ, J., BRŮŽEK, J., SEDLAK, P. & VELEMÍNSKÁ, J. 2015. Modelling of facial growth in Czech children based on longitudinal data: Age progression from 12 to 15 years using 3D surface models. *Forensic Sci Int,* 248**,** 33-40.

KRETLOW, J. D., SPICER, P. P., JANSEN, J. A., VACANTI, C. A., KASPER, F. K. & MIKOS, A. G. 2010. Uncultured marrow mononuclear cells delivered within fibrin glue hydrogels to porous scaffolds enhance bone regeneration within critical-sized rat cranial defects. *Tissue Eng Part A,* 16**,** 3555-68.

KRIMMEL, M., BREIDT, M., BACHER, M., MÜLLER-HAGEDORN, S., DIETZ, K., BÜLTHOFF, H., REINERT, S. & KLUBA, S. 2015. Three-Dimensional Normal Facial Growth from Birth to the Age of 7 Years. *Plast Reconstr Surg,* 136**,** 490e-501e.

KRISHNAN, V., DHURJATI, R., VOGLER, E. A. & MASTRO, A. M. 2010. Osteogenesis in vitro: from pre-osteoblasts to osteocytes: a contribution from the Osteobiology Research Group, The Pennsylvania State University. *In Vitro Cell Dev Biol Anim,* 46**,** 28-35.

KUBO, H., BERRETTA, R. M., JALEEL, N., ANGERT, D. & HOUSER, S. R. 2009. c-Kit+ bone marrow stem cells differentiate into functional cardiac myocytes. *Clin Transl Sci,* 2**,** 26-32.

KUMAR, G. S. 2014. *Orban's Oral Histology & Embryology*, Elsevier Health Sciences APAC.

KUMAR S, WAN C, RAMASWAMY G, CLEMENS TL & PONNAZHAGAN S 2010. Mesenchymal stem cells expressing osteogenic and angiogenic factors synergistically enhance bone formation in a mouse model of segmental bone defect. . *Molecular Therapy,* 18**,** 1026-1034.

KWAN, M. D., SELLMYER, M. A., QUARTO, N., HO, A. M., WANDLESS, T. J. & LONGAKER, M. T. 2011. Chemical control of FGF-2 release for promoting calvarial healing with adipose stem cells. *J Biol Chem,* 286**,** 11307-13.

LAFAGE-PROUST, M. H., ROCHE, B., LANGER, M., CLERET, D., VANDEN BOSSCHE, A., OLIVIER, T. & VICO, L. 2015. Assessment of bone vascularization and its role in bone remodeling. *Bonekey Rep,* 4**,** 662.

LANGENBACH, F. & HANDSCHEL, J. 2013. Effects of dexamethasone, ascorbic acid and β-glycerophosphate on the osteogenic differentiation of stem cells in vitro. *Stem Cell Res Ther,* 4**,** 117.

LAURENCIN, C., KHAN, Y. & EL-AMIN, S. F. 2006. Bone graft substitutes. *Expert Rev Med Devices,* 3**,** 49-57.

LECHANTEUR, C., BRIQUET, A., GIET, O., DELLOYE, O., BAUDOUX, E. & BEGUIN, Y. 2016. Clinical-scale expansion of mesenchymal stromal cells: a large banking experience. *J Transl Med,* 14**,** 145.

LEE, J., ABDEEN, A. A., TANG, X., SAIF, T. A. & KILIAN, K. A. 2016. Matrix directed adipogenesis and neurogenesis of mesenchymal stem cells derived from adipose tissue and bone marrow. *Acta Biomater,* 42**,** 46-55.

LEE, Y. B., POLIO, S., LEE, W., DAI, G., MENON, L., CARROLL, R. S. & YOO, S. S. 2010. Bio-printing of collagen and VEGF-releasing fibrin gel scaffolds for neural stem cell culture. *Exp Neurol,* 223**,** 645-52.

LENDAHL, U., ZIMMERMAN, L. B. & MCKAY, R. D. 1990. CNS stem cells express a new class of intermediate filament protein. *Cell,* 60**,** 585-95.

LEVI, B. & LONGAKER, M. T. 2011. Concise review: adipose-derived stromal cells for skeletal regenerative medicine. *Stem Cells,* 29**,** 576-82.

LEVINE, J. P., PATEL, A., SAADEH, P. B. & HIRSCH, D. L. 2012. Computer-aided design and manufacturing in craniomaxillofacial surgery: the new state of the art. *J Craniofac Surg,* 23**,** 288-93.

LEWANDROWSKI, K. U., GRESSER, J. D., WISE, D. L. & TRANTOL, D. J. 2000. Bioresorbable bone graft substitutes of different osteoconductivities: a histologic evaluation of osteointegration of poly(propylene glycol-co-fumaric acid)-based cement implants in rats. *Biomaterials,* 21**,** 757-64.

LI, C. J., MADHU, V., BALIAN, G., DIGHE, A. S. & CUI, Q. 2015. Cross-Talk Between VEGF and BMP-6 Pathways Accelerates Osteogenic Differentiation of Human Adipose-Derived Stem Cells. *J Cell Physiol,* 230**,** 2671-82.

LI, J., ZHI, W., XU, T., SHI, F., DUAN, K., WANG, J., MU, Y. & WENG, J. 2016. Ectopic osteogenesis and angiogenesis regulated by porous architecture of hydroxyapatite scaffolds with similar interconnecting structure in vivo. *Regen Biomater,* 3**,** 285-297.

LI, J. Y., PU, M. T., HIRASAWA, R., LI, B. Z., HUANG, Y. N., ZENG, R., JING, N. H., CHEN, T., LI, E., SASAKI, H. & XU, G. L. 2007. Synergistic function of DNA methyltransferases Dnmt3a and Dnmt3b in the methylation of Oct4 and Nanog. *Mol Cell Biol,* 27**,** 8748-59.

LI, Q., KUMAR, A., MAKHIJA, E. & SHIVASHANKAR, G. V. 2014. The regulation of dynamic mechanical coupling between actin cytoskeleton and nucleus by matrix geometry. *Biomaterials,* 35**,** 961-9.

LI, X., LIU, H., NIU, X., YU, B., FAN, Y., FENG, Q., CUI, F. Z. & WATARI, F. 2012. The use of carbon nanotubes to induce osteogenic differentiation of human adipose-derived MSCs in vitro and ectopic bone formation in vivo. *Biomaterials,* 33**,** 4818-27.

LIAO, J., HU, N., ZHOU, N., LIN, L., ZHAO, C., YI, S., FAN, T., BAO, W., LIANG, X., CHEN, H., XU, W., CHEN, C., CHENG, Q., ZENG, Y., SI, W., YANG, Z. & HUANG, W. 2014. Sox9 potentiates BMP2-induced chondrogenic differentiation and inhibits BMP2-induced osteogenic differentiation. *PLoS One,* 9**,** e89025.

LIEBERMAN, D. E. 2011. *The Evolution of the Human Head*, Harvard University Press.

LIEBREGTS, J., XI, T., TIMMERMANS, M., DE KONING, M., BERGÉ, S., HOPPENREIJS, T. & MAAL, T. 2015a. Accuracy of three-dimensional soft tissue simulation in bimaxillary osteotomies. *J Craniomaxillofac Surg,* 43**,** 329-35.

LIEBREGTS, J. H., TIMMERMANS, M., DE KONING, M. J., BERGÉ, S. J. & MAAL, T. J. 2015b. Three-dimensional facial simulation in bilateral sagittal split osteotomy: a validation study of 100 patients. *J Oral Maxillofac Surg,* 73**,** 961-70.

LINSLEY, C. S., WU, B. M. & TAWIL, B. 2016. Mesenchymal stem cell growth on and mechanical properties of fibrin-based biomimetic bone scaffolds. *J Biomed Mater Res A,* 104**,** 2945-2953.

LISBOA, C. E. O., MASTERSON, D., DA MOTTA, A. F. & MOTTA, A. T. 2015. Reliability and reproducibility of three-dimensional cephalometric landmarks using CBCT: a systematic review. *J Appl Oral Sci,* 23**,** 112-9.

LIU, B., WU, S., HAN, L. & ZHANG, C. 2015. β-catenin signaling induces the osteoblastogenic differentiation of human pre-osteoblastic and bone marrow stromal cells mainly through the upregulation of osterix expression. *Int J Mol Med,* 36**,** 1572-82.

LIU, T. M., MARTINA, M., HUTMACHER, D. W., HUI, J. H., LEE, E. H. & LIM, B. 2007. Identification of common pathways mediating differentiation of bone marrow- and adipose tissue-derived human mesenchymal stem cells into three mesenchymal lineages. *Stem Cells,* 25**,** 750-60.

LIU, X., LIU, R., CAO, B., YE, K., LI, S., GU, Y., PAN, Z. & DING, J. 2016a. Subcellular cell geometry on micropillars regulates stem cell differentiation. *Biomaterials,* 111**,** 27-39.

LIU, Y., LUO, D. & WANG, T. 2016b. Hierarchical Structures of Bone and Bioinspired Bone Tissue Engineering. *Small,* 12**,** 4611-32.

LO, Y. P., LIU, Y. S., RIMANDO, M. G., HO, J. H., LIN, K. H. & LEE, O. K. 2016. Three-dimensional spherical spatial boundary conditions differentially regulate osteogenic differentiation of mesenchymal stromal cells. *Sci Rep,* 6**,** 21253.

LOHSE, N., SCHULZ, J. & SCHLIEPHAKE, H. 2012. Effect of fibrin on osteogenic differentiation and VEGF expression of bone marrow stromal cells in mineralised scaffolds: a three-dimensional analysis. *Eur Cell Mater,* 23**,** 413-23; discussion 424.

LONGAKER, M. T. & SIEBERT, J. W. 1996. Microsurgical correction of facial contour in congenital craniofacial malformations: the marriage of hard and soft tissue. *Plast Reconstr Surg,* 98**,** 942-50.

LU, Z., ROOHANI-ESFAHANI, S. I., WANG, G. & ZREIQAT, H. 2012. Bone biomimetic microenvironment induces osteogenic differentiation of adipose tissue-derived mesenchymal stem cells. *Nanomedicine,* 8**,** 507-15.

LV, F. J., TUAN, R. S., CHEUNG, K. M. & LEUNG, V. Y. 2014. Concise review: the surface markers and identity of human mesenchymal stem cells. *Stem Cells,* 32**,** 1408-19.

LYSDAHL, H., BAATRUP, A., FOLDAGER, C. B. & BÜNGER, C. 2014. Preconditioning Human Mesenchymal Stem Cells with a Low Concentration of BMP2 Stimulates Proliferation and Osteogenic Differentiation In Vitro. *Biores Open Access,* 3**,** 278-85.

MACHADO, E. G., ISSA, J. P., FIGUEIREDO, F. A., SANTOS, G. R., GALDEANO, E. A., ALVES, M. C., CHACON, E. L., FERREIRA JUNIOR, R. S., BARRAVIERA, B. & CUNHA, M. R. 2015. A new heterologous fibrin sealant as scaffold to recombinant human bone morphogenetic protein-2 (rhBMP-2) and natural latex proteins for the repair of tibial bone defects. *Acta Histochem,* 117**,** 288-96.

MADEN, T. 2013 Mar 15 The BLAST Sequence Analysis Tool. 2nd edition. ed. The NCBI Handbook [Internet]. Bethesda (MD): National Center for Biotechnology Information (US); 2013-. Available from: http://www.ncbi.nlm.nih.gov/books/NBK153387/.

MAHDI, E. 2012. Assessment of facial and cranial development and comparison of anthropometric ratios. *J Craniofac Surg,* 23**,** e75-83.

MAHMOOD, A., HARKNESS, L., ABDALLAH, B. M., ELSAFADI, M., AL-NBAHEEN, M. S., ALDAHMASH, A. & KASSEM, M. 2012. Derivation of stromal (skeletal and mesenchymal) stem-like cells from human embryonic stem cells. *Stem Cells Dev,* 21**,** 3114-24.

MAILHOT, J. M. & BORKE, J. L. 1998. An isolation and in vitro culturing method for human intraoral bone cells derived from dental implant preparation sites. *Clin Oral Implants Res,* 9**,** 43-50.

MALEKI, M., GHANBARVAND, F., REZA BEHVARZ, M., EJTEMAEI, M. & GHADIRKHOMI, E. 2014. Comparison of mesenchymal stem cell markers in multiple human adult stem cells. *Int J Stem Cells,* 7**,** 118-26.

MANI, V. 2010. *Surgical Correction of Facial Deformities*, Jaypee Brothers,Medical Publishers Pvt. Limited.

MARINKOVIC, M., BLOCK, T. J., RAKIAN, R., LI, Q., WANG, E., REILLY, M. A., DEAN, D. D. & CHEN, X. D. 2016. One size does not fit all: developing a cell-specific niche for in vitro study of cell behavior. *Matrix Biol,* 52-54**,** 426-41.

MARTINE, L. C., HOLZAPFEL, B. M., MCGOVERN, J. A., WAGNER, F., QUENT, V. M., HESAMI, P., WUNNER, F. M., VAQUETTE, C., DE-JUAN-PARDO, E. M., BROWN, T. D., NOWLAN, B., WU, D. J., HUTMACHER, C. O., MOI, D., OUSSENKO, T., PICCININI, E., ZANDSTRA, P. W., MAZZIERI, R., LÉVESQUE, J. P., DALTON, P. D., TAUBENBERGER, A. V. & HUTMACHER, D. W. 2017. Engineering a humanized bone organ model in mice to study bone metastases. *Nat Protoc,* 12**,** 639-663.

MARTINEZ-MAZA, C., ROSAS, A. & NIETO-DÍAZ, M. 2013. Postnatal changes in the growth dynamics of the human face revealed from bone modelling patterns. *J Anat,* 223**,** 228-41.

MCINTYRE, G. T. & MOSSEY, P. A. 2003. Size and shape measurement in contemporary cephalometrics. *Eur J Orthod,* 25**,** 231-42.

MCMAHON, R. E., WANG, L., SKORACKI, R. & MATHUR, A. B. 2013. Development of nanomaterials for bone repair and regeneration. *J Biomed Mater Res B Appl Biomater,* 101**,** 387-97.

MEDELLÍN-CASTILLO, H. I., GOVEA-VALLADARES, E. H., PÉREZ-GUERRERO, C. N., GIL-VALLADARES, J., LIM, T. & RITCHIE, J. M. 2016. The evaluation of a novel haptic-enabled virtual reality approach for computer-aided cephalometry. *Comput Methods Programs Biomed,* 130**,** 46-53.

MEIJER GJ, DE BRUIJN JD, KOOLE R & CA, V. B. 2007. Cell-based bone tissue engineering. *PLoS Med,* 4**,** e9.

MELLION, Z. J., BEHRENTS, R. G. & JOHNSTON, L. E. 2013. The pattern of facial skeletal growth and its relationship to various common indexes of maturation. *Am J Orthod Dentofacial Orthop,* 143**,** 845-54.

MICHAEL MILORO, P. L. *Peterson's Principles of Oral and Maxillofacial Surgery, Volume 1*.

MILORO, M., GHALI, G. E., LARSEN, P. & WAITE, P. 2004a. *Peterson's Principles of Oral and Maxillofacial Surgery*, B C Decker.

MILORO, M., GHALI, G. E., LARSEN, P. & WAITE, P. 2004b. *Peterson's principles of oral and maxillofacial surgery,* Hamilton, Ont. ; London, B C Decker.

MINARDI, S., CORRADETTI, B., TARABALLI, F., SANDRI, M., VAN EPS, J., CABRERA, F. J., WEINER, B. K., TAMPIERI, A. & TASCIOTTI, E. 2015. Evaluation of the osteoinductive potential of a bio-inspired scaffold mimicking the osteogenic niche for bone augmentation. *Biomaterials,* 62**,** 128-37.

MITSUKAWA, N., SAIGA, A. & SATOH, K. 2014. Changing the facial features of patients with Treacher Collins syndrome: protocol for 3-stage treatment of hard and soft tissue hypoplasia in the upper half of the face. *Ann Plast Surg,* 73**,** 39-42.

MOODY, S. A. 2014. *Principles of Developmental Genetics*, Elsevier Science.

MORRISS-KAY, G. M. & WILKIE, A. O. 2005. Growth of the normal skull vault and its alteration in craniosynostosis: insights from human genetics and experimental studies. *J Anat,* 207**,** 637-53.

MURPHY, C. M., DUFFY, G. P., SCHINDELER, A. & O'BRIEN, F. J. 2016. Effect of collagen-glycosaminoglycan scaffold pore size on matrix mineralization and cellular behavior in different cell types. *J Biomed Mater Res A,* 104**,** 291-304.

MÉNDEZ-FERRER, S., MICHURINA, T. V., FERRARO, F., MAZLOOM, A. R., MACARTHUR, B. D., LIRA, S. A., SCADDEN, D. T., MA'AYAN, A., ENIKOLOPOV, G. N. & FRENETTE, P. S. 2010. Mesenchymal and haematopoietic stem cells form a unique bone marrow niche. *Nature,* 466**,** 829-34.

NADERI, N., GRIFFIN, M., MALINS, E., BECER, R., MOSAHEBI, A., WHITAKER, I. S. & SEIFALIAN, A. M. 2016. Slow chlorine releasing compounds: A viable sterilisation method for bioabsorbable nanocomposite biomaterials. *J Biomater Appl,* 30**,** 1114-24.

NAIR, M., NANCY, D., KRISHNAN, A. G., ANJUSREE, G. S., VADUKUMPULLY, S. & NAIR, S. V. 2015. Graphene oxide nanoflakes

incorporated gelatin-hydroxyapatite scaffolds enhance osteogenic differentiation of human mesenchymal stem cells. *Nanotechnology,* 26**,** 161001.

NAJDANOVIĆ, J. G., CVETKOVIĆ, V. J., STOJANOVIĆ, S., VUKELIĆ-NIKOLIĆ, M. Đ., STANISAVLJEVIĆ, M. N., ŽIVKOVIĆ, J. M. & NAJMAN, S. J. 2015. The Influence of Adipose-Derived Stem Cells Induced into Endothelial Cells on Ectopic Vasculogenesis and Osteogenesis. *Cellular and Molecular Bioengineering,* 8**,** 577-590.

NAKASHIMA, K. & DE CROMBRUGGHE, B. 2003. Transcriptional mechanisms in osteoblast differentiation and bone formation. *Trends Genet,* 19**,** 458-66.

NEW, S. E., ALVAREZ-GONZALEZ, C., VAGASKA, B., GOMEZ, S. G., BULSTRODE, N. W., MADRIGAL, A. & FERRETTI, P. 2015. A matter of identity - Phenotype and differentiation potential of human somatic stem cells. *Stem Cell Res,* 15**,** 1-13.

NEW, S. E., IBRAHIM, A., GUASTI, L., ZUCCHELLI, E., BIRCHALL, M., BULSTRODE, N. W., SEIFALIAN, A. M. & FERRETTI, P. 2016. Towards reconstruction of epithelialized cartilages from autologous adipose tissue-derived stem cells. *J Tissue Eng Regen Med*.

NICOLAIJE, C., VAN DE PEPPEL, J. & VAN LEEUWEN, J. P. 2013. Oxygen-induced transcriptional dynamics in human osteoblasts are most prominent at the onset of mineralization. *J Cell Physiol,* 228**,** 1863-72.

NIECHAJEV, I. 2012. Facial reconstruction using porous high-density polyethylene (medpor): long-term results. *Aesthetic Plast Surg,* 36**,** 917-27.

NIEMEYER, P., KORNACKER, M., MEHLHORN, A., SECKINGER, A., VOHRER, J., SCHMAL, H., KASTEN, P., ECKSTEIN, V., SÜDKAMP, N. P. & KRAUSE, U. 2007. Comparison of immunological properties of bone marrow stromal cells and adipose tissue-derived stem cells before and after osteogenic differentiation in vitro. *Tissue Eng,* 13**,** 111-21.

NII, M., LAI, J. H., KEENEY, M., HAN, L. H., BEHN, A., IMANBAYEV, G. & YANG, F. 2013. The effects of interactive mechanical and biochemical niche signaling on osteogenic differentiation of adipose-derived stem cells using combinatorial hydrogels. *Acta Biomater,* 9**,** 5475-83.

NIKKHAH, D., PONNIAH, A., RUFF, C. & DUNAWAY, D. 2013. Planning surgical reconstruction in Treacher-Collins syndrome using virtual simulation. *Plast Reconstr Surg,* 132**,** 790e-805e.

O'CONNELL, D. A. & FUTRAN, N. D. 2010. Reconstruction of the midface and maxilla. *Curr Opin Otolaryngol Head Neck Surg,* 18**,** 304-10.

ODENT, S., ATTI-BITACH, T., BLAYAU, M., MATHIEU, M., AUG, J., DELEZO DE, A. L., GALL, J. Y., LE MAREC, B., MUNNICH, A., DAVID, V. & VEKEMANS, M. 1999. Expression of the Sonic hedgehog (SHH) gene during early human development and phenotypic expression of new mutations causing holoprosencephaly. *Hum Mol Genet,* 8**,** 1683-9.

OH, J. H., KIM, H. J., KIM, T. I. & WOO, K. M. 2014. Comparative evaluation of the biological properties of fibrin for bone regeneration. *BMB Rep,* 47**,** 110-4.

ONGARO, A., PELLATI, A., BAGHERI, L., FORTINI, C., SETTI, S. & DE MATTEI, M. 2014. Pulsed electromagnetic fields stimulate osteogenic differentiation in human bone marrow and adipose tissue derived mesenchymal stem cells. *Bioelectromagnetics,* 35**,** 426-36.

ONGKOSUWITO, E. M., VAN NECK, J. W., WATTEL, E., VAN ADRICHEM, L. N. & KUIJPERS-JAGTMAN, A. M. 2013. Craniofacial morphology in unilateral hemifacial microsomia. *Br J Oral Maxillofac Surg,* 51**,** 902-7.

ORRISS, I. R., HAJJAWI, M. O., HUESA, C., MACRAE, V. E. & ARNETT, T. R. 2014. Optimisation of the differing conditions required for bone formation in vitro by primary osteoblasts from mice and rats. *Int J Mol Med,* 34**,** 1201-8.

OSINGA, R., DI MAGGIO, N., TODOROV, A., ALLAFI, N., BARBERO, A., LAURENT, F., SCHAEFER, D. J., MARTIN, I. & SCHERBERICH, A. 2016. Generation of a Bone Organ by Human Adipose-Derived Stromal Cells Through Endochondral Ossification. *Stem Cells Transl Med,* 5**,** 1090-7.

OWEN, T. A., ARONOW, M., SHALHOUB, V., BARONE, L. M., WILMING, L., TASSINARI, M. S., KENNEDY, M. B., POCKWINSE, S., LIAN, J. B. & STEIN, G. S. 1990. Progressive development of the rat osteoblast phenotype in vitro: reciprocal relationships in expression of genes associated with osteoblast proliferation and differentiation during formation of the bone extracellular matrix. *J Cell Physiol,* 143**,** 420-30.

PACINI, S., BARACHINI, S., MONTALI, M., CARNICELLI, V., FAZZI, R., PARCHI, P. & PETRINI, M. 2016. Mesangiogenic Progenitor Cells Derived from One Novel CD64(bright)CD31(bright)CD14(neg) Population in Human Adult Bone Marrow. *Stem Cells Dev,* 25**,** 661-73.

PACINI, S. & PETRINI, I. 2014. Are MSCs angiogenic cells? New insights on human nestin-positive bone marrow-derived multipotent cells. *Front Cell Dev Biol,* 2**,** 20.

PAIVA, K. B. & GRANJEIRO, J. M. 2014. Bone tissue remodeling and development: focus on matrix metalloproteinase functions. *Arch Biochem Biophys,* 561**,** 74-87.

PANNARALE, L., MORINI, S., D'UBALDO, E., GAUDIO, E. & MARINOZZI, G. 1997. SEM corrosion-casts study of the microcirculation of the flat bones in the rat. *Anat Rec,* 247**,** 462-71.

PANSKY, B. 1982. *Review of Medical Embryology,* Inc 1301 Harbor Bay Parkway, Alameda, CA, 94502, Macmillan USA

PAPADIMITROPOULOS, A., SCHERBERICH, A., GÜVEN, S., THEILGAARD, N., CROOIJMANS, H. J., SANTINI, F., SCHEFFLER, K., ZALLONE, A. & MARTIN, I. 2011. A 3D in vitro bone organ model using human progenitor cells. *Eur Cell Mater,* 21**,** 445-58; discussion 458.

PARK, S. S., BEYER, R. P., SMYTH, M. D., CLARKE, C. M., TIMMS, A. E., BAMMLER, T. K., STAMPER, B. D., MECHAM, B. H., GUSTAFSON, J. A. & CUNNINGHAM, M. L. 2015. Osteoblast differentiation profiles define sex specific gene expression patterns in craniosynostosis. *Bone,* 76**,** 169-76.

PARLEE, S. D., LENTZ, S. I., MORI, H. & MACDOUGALD, O. A. 2014. Quantifying size and number of adipocytes in adipose tissue. *Methods Enzymol,* 537**,** 93-122.

PARTHASARATHY, J. 2014. 3D modeling, custom implants and its future perspectives in craniofacial surgery. *Ann Maxillofac Surg,* 4**,** 9-18.

PASQUALE, P., GAETANO, M., GIOVANNI, D. O., LUIGI, C. & GILBERTO, S. 2015. Autologous fat grafting in facial volumetric restoration. *J Craniofac Surg,* 26**,** 756-9.

PAUL, A., MANOHARAN, V., KRAFFT, D., ASSMANN, A., UQUILLAS, J. A., SHIN, S. R., HASAN, A., HUSSAIN, M. A., MEMIC, A., GAHARWAR, A. K. & KHADEMHOSSEINI, A. 2016. Nanoengineered biomimetic hydrogels for guiding human stem cell osteogenesis in three dimensional microenvironments. *J Mater Chem B Mater Biol Med,* 4**,** 3544-3554.

PAWLAK, M. & JAENISCH, R. 2011. De novo DNA methylation by Dnmt3a and Dnmt3b is dispensable for nuclear reprogramming of somatic cells to a pluripotent state. *Genes Dev,* 25**,** 1035-40.

PENG, W., GAO, T., YANG, Z. L., ZHANG, S. C., REN, M. L., WANG, Z. G. & ZHANG, B. 2012. Adipose-derived stem cells induced dendritic cells undergo tolerance and inhibit Th1 polarization. *Cell Immunol,* 278**,** 152-7.

PEREIRA, I. H., AYRES, E., AVEROUS, L., SCHLATTER, G., HEBRAUD, A., DE PAULA, A. C., VIANA, P. H., GOES, A. M. & ORÉFICE, R. L. 2013. Differentiation of human adipose-derived stem cells seeded on mineralized electrospun co-axial poly(ε-caprolactone) (PCL)/gelatin nanofibers. *J Mater Sci Mater Med*.

PHILIPS, B. J., MARRA, K. G. & RUBIN, J. P. 2012. Adipose stem cell-based soft tissue regeneration. *Expert Opin Biol Ther,* 12**,** 155-63.

PHILLIPS, J. E., GERSBACH, C. A., WOJTOWICZ, A. M. & GARCÍA, A. J. 2006. Glucocorticoid-induced osteogenesis is negatively regulated by Runx2/Cbfa1 serine phosphorylation. *J Cell Sci,* 119**,** 581-91.

PIERANTOZZI, E., GAVA, B., MANINI, I., ROVIELLO, F., MAROTTA, G., CHIAVARELLI, M. & SORRENTINO, V. 2011. Pluripotency regulators in human mesenchymal stem cells: expression of NANOG but not of OCT-4 and SOX-2. *Stem Cells Dev,* 20**,** 915-23.

PILL, K., HOFMANN, S., REDL, H. & HOLNTHONER, W. 2015. Vascularization mediated by mesenchymal stem cells from bone marrow and adipose tissue: a comparison. *Cell Regen (Lond),* 4**,** 8.

PITTAYAPAT, P., JACOBS, R., ODRI, G. A., VASCONCELOS, K. E. F., WILLEMS, G. & OLSZEWSKI, R. 2015. Reproducibility of the sella turcica landmark in three dimensions using a sella turcica-specific reference system. *Imaging Sci Dent,* 45**,** 15-22.

PLOMP, R. G., VAN LIESHOUT, M. J., JOOSTEN, K. F., WOLVIUS, E. B., VAN DER SCHROEFF, M. P., VERSNEL, S. L., POUBLON, R. M. & MATHIJSSEN, I. M. 2016. Treacher Collins Syndrome: A Systematic Review of Evidence-Based Treatment and Recommendations. *Plast Reconstr Surg,* 137**,** 191-204.

POLO-CORRALES, L., LATORRE-ESTEVES, M. & RAMIREZ-VICK, J. E. 2014. Scaffold design for bone regeneration. *J Nanosci Nanotechnol,* 14**,** 15-56.

POSNICK, J. C., AL-QATTAN, M. M., MOFFAT, S. M. & ARMSTRONG, D. 1995. Cranio-orbito-zygomatic measurements from standard CT scans in unoperated Treacher Collins syndrome patients: comparison with normal controls. *Cleft Palate Craniofac J,* 32**,** 20-4.

POSWILLO, D. 1973. The pathogenesis of the first and second branchial arch syndrome. *Oral Surg Oral Med Oral Pathol,* 35**,** 302-28.

PREMKUMAR, S. 2011. *Textbook of Craniofacial Growth*, Jaypee Brothers,Medical Publishers Pvt. Limited.

QUINLAN, E., THOMPSON, E. M., MATSIKO, A., O'BRIEN, F. J. & LÓPEZ-NORIEGA, A. 2015. Long-term controlled delivery of rhBMP-2 from collagen-hydroxyapatite scaffolds for superior bone tissue regeneration. *J Control Release,* 207**,** 112-119.

RADA, T., SANTOS, T. C., MARQUES, A. P., CORRELO, V. M., FRIAS, A. M., CASTRO, A. G., NEVES, N. M., GOMES, M. E. & REIS, R. L. 2012. Osteogenic differentiation of two distinct subpopulations of human adipose-derived stem cells: an in vitro and in vivo study. *J Tissue Eng Regen Med,* 6**,** 1-11.

RAGHUNATH, J., GEORGIOU, G., ARMITAGE, D., NAZHAT, S. N., SALES, K. M., BUTLER, P. E. & SEIFALIAN, A. M. 2009. Degradation studies on biodegradable nanocomposite based on polycaprolactone/polycarbonate (80:20%) polyhedral oligomeric silsesquioxane. *J Biomed Mater Res A,* 91**,** 834-44.

RAJAN, A., EUBANKS, E., EDWARDS, S., ARONOVICH, S., TRAVAN, S., RUDEK, I., WANG, F., LANIS, A. & KAIGLER, D. 2014. Optimized cell survival and seeding efficiency for craniofacial tissue engineering using clinical stem cell therapy. *Stem Cells Transl Med,* 3**,** 1495-503.

RAKIAN, R., BLOCK, T. J., JOHNSON, S. M., MARINKOVIC, M., WU, J., DAI, Q., DEAN, D. D. & CHEN, X. D. 2015. Native extracellular matrix preserves mesenchymal stem cell "stemness" and differentiation potential under serum-free culture conditions. *Stem Cell Res Ther,* 6**,** 235.

RAMASAMY, S. K., KUSUMBE, A. P., ITKIN, T., GUR-COHEN, S., LAPIDOT, T. & ADAMS, R. H. 2016a. Regulation of Hematopoiesis and Osteogenesis by Blood Vessel-Derived Signals. *Annu Rev Cell Dev Biol,* 32**,** 649-675.

RAMASAMY, S. K., KUSUMBE, A. P., SCHILLER, M., ZEUSCHNER, D., BIXEL, M. G., MILIA, C., GAMREKELASHVILI, J., LIMBOURG, A.,

MEDVINSKY, A., SANTORO, M. M., LIMBOURG, F. P. & ADAMS, R. H. 2016b. Blood flow controls bone vascular function and osteogenesis. *Nat Commun,* 7**,** 13601.

RAMASAMY, S. K., KUSUMBE, A. P., WANG, L. & ADAMS, R. H. 2014. Endothelial Notch activity promotes angiogenesis and osteogenesis in bone. *Nature,* 507**,** 376-80.

RAO, R. R. & STEGEMANN, J. P. 2013. Cell-based approaches to the engineering of vascularized bone tissue. *Cytotherapy,* 15**,** 1309-22.

REN, L., YANG, P., WANG, Z., ZHANG, J., DING, C. & SHANG, P. 2015. Biomechanical and biophysical environment of bone from the macroscopic to the pericellular and molecular level. *J Mech Behav Biomed Mater,* 50**,** 104-122.

REZNIKOV, N., SHAHAR, R. & WEINER, S. 2014. Three-dimensional structure of human lamellar bone: the presence of two different materials and new insights into the hierarchical organization. *Bone,* 59**,** 93-104.

RHO, J. Y., KUHN-SPEARING, L. & ZIOUPOS, P. 1998. Mechanical properties and the hierarchical structure of bone. *Med Eng Phys,* 20**,** 92-102.

RICHTSMEIER, J. T. & FLAHERTY, K. 2013. Hand in glove: brain and skull in development and dysmorphogenesis. *Acta Neuropathol,* 125**,** 469-89.

RODRÍGUEZ, J. P., GONZÁLEZ, M., RÍOS, S. & CAMBIAZO, V. 2004. Cytoskeletal organization of human mesenchymal stem cells (MSC) changes during their osteogenic differentiation. *J Cell Biochem,* 93**,** 721-31.

ROLFE, S. M., SHAPIRO, L. G., COX, T. C., MAGA, A. M. & COX, L. L. 2011. A landmark-free framework for the detection and description of shape differences in embryos. *Conf Proc IEEE Eng Med Biol Soc,* 2011**,** 5153-6.

ROORYCK, C., SOUAKRI, N., CAILLEY, D., BOURON, J., GOIZET, C., DELRUE, M. A., MARLIN, S., LACOMBE, F. D. & ARVEILER, B. 2010. Array-CGH analysis of a cohort of 86 patients with oculoauriculovertebral spectrum. *Am J Med Genet A,* 152A**,** 1984-9.

ROSALES-ROCABADO, J. M., KAKU, M., KITAMI, M., AKIBA, Y. & UOSHIMA, K. 2014. Osteoblastic differentiation and mineralization ability of periosteum-derived cells compared with bone marrow and calvaria-derived cells. *J Oral Maxillofac Surg,* 72**,** 694.e1-9.

ROSON-BURGO, B., SANCHEZ-GUIJO, F., DEL CAÑIZO, C. & DE LAS RIVAS, J. 2014. Transcriptomic portrait of human Mesenchymal Stromal/Stem Cells isolated from bone marrow and placenta. *BMC Genomics,* 15**,** 910.

ROSSET, A., SPADOLA, L. & RATIB, O. 2004. OsiriX: an open-source software for navigating in multidimensional DICOM images. *J Digit Imaging,* 17**,** 205-16.

ROSSI, F., SANTORO, M. & PERALE, G. 2013. Polymeric scaffolds as stem cell carriers in bone repair. *J Tissue Eng Regen Med*.

RUTKOVSKIY, A., STENSLØKKEN, K. O. & VAAGE, I. J. 2016. Osteoblast Differentiation at a Glance. *Med Sci Monit Basic Res,* 22**,** 95-106.

RÜHLI, F. J., KUHN, G., EVISON, R., MÜLLER, R. & SCHULTZ, M. 2007. Diagnostic value of micro-CT in comparison with histology in the qualitative assessment of historical human skull bone pathologies. *Am J Phys Anthropol,* 133**,** 1099-111.

SAGAR, N., PANDEY, A. K., GURBANI, D., KHAN, K., SINGH, D., CHAUDHARI, B. P., SONI, V. P., CHATTOPADHYAY, N., DHAWAN, A. & BELLARE, J. R. 2013. In-vivo efficacy of compliant 3D nano-composite in critical-size bone defect repair: a six month preclinical study in rabbit. *PLoS One,* 8**,** e77578.

SAKAUE, M., OHTA, H., KUMAKI, Y., ODA, M., SAKAIDE, Y., MATSUOKA, C., YAMAGIWA, A., NIWA, H., WAKAYAMA, T. & OKANO, M. 2010. DNA methylation is dispensable for the growth and survival of the extraembryonic lineages. *Curr Biol,* 20**,** 1452-7.

SAMSONRAJ, R. M., RAI, B., SATHIYANATHAN, P., PUAN, K. J., RÖTZSCHKE, O., HUI, J. H., RAGHUNATH, M., STANTON, L. W., NURCOMBE, V. & COOL, S. M. 2015. Establishing criteria for human mesenchymal stem cell potency. *Stem Cells,* 33**,** 1878-91.

SARTORI, R. & SANDRI, M. 2015. BMPs and the muscle-bone connection. *Bone*.

SCHAEFER, K. & BOOKSTEIN, F. L. 2009. Does geometric morphometrics serve the needs of plasticity research? *J Biosci,* 34**,** 589-99.

SCHLICHER, W., NIELSEN, I., HUANG, J. C., MAKI, K., HATCHER, D. C. & MILLER, A. J. 2012. Consistency and precision of landmark identification in three-dimensional cone beam computed tomography scans. *Eur J Orthod,* 34**,** 263-75.

SCHOENWOLF, G. C. 2009. *Larsen's Human Embryology*, Churchill Livingstone/Elsevier.

SCHROF, S., VARGA, P., GALVIS, L., RAUM, K. & MASIC, A. 2014. 3D Raman mapping of the collagen fibril orientation in human osteonal lamellae. *J Struct Biol,* 187**,** 266-75.

SEN, B., XIE, Z., UZER, G., THOMPSON, W. R., STYNER, M., WU, X. & RUBIN, J. 2015. Intranuclear Actin Regulates Osteogenesis. *Stem Cells,* 33**,** 3065-76.

SHAFIEE, A., SEYEDJAFARI, E., SOLEIMANI, M., AHMADBEIGI, N., DINARVAND, P. & GHAEMI, N. 2011. A comparison between osteogenic differentiation of human unrestricted somatic stem cells and mesenchymal stem cells from bone marrow and adipose tissue. *Biotechnol Lett,* 33**,** 1257-64.

SHINAGAWA, K., MITSUHARA, T., OKAZAKI, T., TAKEDA, M., YAMAGUCHI, S., MAGAKI, T., OKURA, Y., UWATOKO, H., KAWAHARA, Y., YUGE, L. & KURISU, K. 2015. The characteristics of human cranial bone marrow mesenchymal stem cells. *Neurosci Lett,* 606**,** 161-6.

SI, J., DAI, J., ZHANG, J., LIU, S., GU, J., SHI, J., SHEN, S. G. & GUO, L. 2015. Comparative investigation of human amniotic epithelial cells and mesenchymal stem cells for application in bone tissue engineering. *Stem Cells Int,* 2015**,** 565732.

SICCHIERI, L. G., CRIPPA, G. E., DE OLIVEIRA, P. T., BELOTI, M. M. & ROSA, A. L. 2012. Pore size regulates cell and tissue interactions with PLGA-CaP scaffolds used for bone engineering. *J Tissue Eng Regen Med,* 6**,** 155-62.

SIDDAPPA R, MARTENS A, DOORN J, LEUSINK A, OLIVO C, LICHT R & DE BOER J 2008. cAMP/PKA pathway activation in human mesenchymal stem cells in vitro results in robust bone formation in vivo. *Proceedings of the National Academy of Sciences,* 105**,** 7281-7286.

SIMS, N. A. & MARTIN, T. J. 2014. Coupling the activities of bone formation and resorption: a multitude of signals within the basic multicellular unit. *Bonekey Rep,* 3**,** 481.

SINN, D. P., BEDROSSIAN, E. & VEST, A. K. 2011. Craniofacial implant surgery. *Dent Clin North Am,* 55**,** 847-69.

SMITH, K., POLITTE, D., REIKER, G., NOLAN, T. S., HILDEBOLT, C., MATTSON, C., TUCKER, D., PRIOR, F., TUROVETS, S. & LARSON-PRIOR, L. J. 2012. Automated measurement of pediatric cranial bone thickness and density from clinical computed tomography. *Conf Proc IEEE Eng Med Biol Soc,* 2012**,** 4462-5.

SMOLKA, W., EGGENSPERGER, N., KOLLAR, A. & IIZUKA, T. 2005. Midfacial reconstruction using calvarial split bone grafts. *Arch Otolaryngol Head Neck Surg,* 131**,** 131-6.

SONOMOTO, K., YAMAOKA, K., KANEKO, H., YAMAGATA, K., SAKATA, K., ZHANG, X., KONDO, M., ZENKE, Y., SABANAI, K., NAKAYAMADA, S., SAKAI, A. & TANAKA, Y. 2016. Spontaneous Differentiation of Human Mesenchymal Stem Cells on Poly-Lactic-Co-Glycolic Acid Nano-Fiber Scaffold. *PLoS One,* 11**,** e0153231.

SONOWAL, H., KUMAR, A., BHATTACHARYYA, J., GOGOI, P. K. & JAGANATHAN, B. G. 2013. Inhibition of actin polymerization decreases osteogeneic differentiation of mesenchymal stem cells through p38 MAPK pathway. *J Biomed Sci,* 20**,** 71.

SPERBER, G. H., SPERBER, S. M. & GUTTMANN, G. D. 2010. *Craniofacial embryogenetics and development,* Shelton, CT, People's Medical Pub.

STAMPER, B. D., PARK, S. S., BEYER, R. P., BAMMLER, T. K., FARIN, F. M., MECHAM, B. & CUNNINGHAM, M. L. 2011. Differential expression of extracellular matrix-mediated pathways in single-suture craniosynostosis. *PLoS One,* 6**,** e26557.

STEIN, G. S., LIAN, J. B., VAN WIJNEN, A. J., STEIN, J. L., MONTECINO, M., JAVED, A., ZAIDI, S. K., YOUNG, D. W., CHOI, J. Y. & POCKWINSE, S. M. 2004. Runx2 control of organization, assembly and activity of the regulatory machinery for skeletal gene expression. *Oncogene,* 23**,** 4315-29.

STEINBACHER, D. M. 2015. Three-Dimensional Analysis and Surgical Planning in Craniomaxillofacial Surgery. *J Oral Maxillofac Surg,* 73**,** S40-56.

STEWART, K., MONK, P., WALSH, S., JEFFERISS, C. M., LETCHFORD, J. & BERESFORD, J. N. 2003. STRO-1, HOP-26 (CD63), CD49a and SB-10 (CD166) as markers of primitive human marrow stromal cells and their more differentiated progeny: a comparative investigation in vitro. *Cell Tissue Res,* 313**,** 281-90.

STIEHLER, M., BÜNGER, C., BAATRUP, A., LIND, M., KASSEM, M. & MYGIND, T. 2009. Effect of dynamic 3-D culture on proliferation, distribution, and osteogenic differentiation of human mesenchymal stem cells. *J Biomed Mater Res A,* 89**,** 96-107.

STRECKBEIN, P., JÄCKEL, S., MALIK, C. Y., OBERT, M., KÄHLING, C., WILBRAND, J. F., ZAHNER, D., HEIDINGER, K., KAMPSCHULTE, M., PONS-KÜHNEMANN, J., KÖHLER, K., SAUER, H., KRAMER, M. & HOWALDT, H. P. 2013. Reconstruction of critical-size mandibular defects in immunoincompetent rats with human adipose-derived stromal cells. *J Craniomaxillofac Surg,* 41**,** 496-503.

SUTTIE, M., FOROUD, T., WETHERILL, L., JACOBSON, J. L., MOLTENO, C. D., MEINTJES, E. M., HOYME, H. E., KHAOLE, N., ROBINSON, L. K., RILEY, E. P., JACOBSON, S. W. & HAMMOND, P. 2013. Facial dysmorphism across the fetal alcohol spectrum. *Pediatrics,* 131**,** e779-88.

SUZUKI, A., SANGANI, D. R., ANSARI, A. & IWATA, J. 2016. Molecular mechanisms of midfacial developmental defects. *Dev Dyn,* 245**,** 276-93.

SZABÓ, G., BARABÁS, J., BOGDÁN, S., NÉMETH, Z., SEBŐK, B. & KISS, G. 2015. Long-term clinical and experimental/surface analytical studies of carbon/carbon maxillofacial implants. *Maxillofac Plast Reconstr Surg,* 37**,** 34.

TAHIRI, Y. & TAYLOR, J. 2014. An Update on Midface Advancement Using Le Fort II and III Distraction Osteogenesis. *Semin Plast Surg,* 28**,** 184-92.

TAKEBE, T., KOBAYASHI, S., SUZUKI, H., MIZUNO, M., CHANG, Y.-M., YOSHIZAWA, E., KIMURA, M., HORI, A., ASANO, J., MAEGAWA, J. & TANIGUCHI, H. 2014. Transient vascularization of transplanted human adult–derived progenitors promotes self-organizing cartilage. *The Journal of Clinical Investigation,* 124**,** 4325-4334.

TAN, G., TAN, Y., NI, G., LAN, G., ZHOU, L., YU, P., LIAO, J., ZHANG, Y., YIN, Z., WANG, H. & NING, C. 2014. Controlled oxidative nanopatterning of microrough titanium surfaces for improving osteogenic activity. *J Mater Sci Mater Med,* 25**,** 1875-84.

TANSIK, G., KILIC, E., BETER, M., DEMIRALP, B., KIZILTAS SENDUR, G., CAN, N., OZKAN, H., ERGUL, E., GULER, M. O. & TEKINAY, A. B. 2016. A glycosaminoglycan mimetic peptide nanofiber gel as an osteoinductive scaffold. *Biomater Sci,* 4**,** 1328-39.

TAYLOR, J. A. 2010. Bilateral orbitozygomatic reconstruction with tissue-engineered bone. *J Craniofac Surg,* 21**,** 1612-4.

TEBER, O. A., GILLESSEN-KAESBACH, G., FISCHER, S., BÖHRINGER, S., ALBRECHT, B., ALBERT, A., ARSLAN-KIRCHNER, M., HAAN, E., HAGEDORN-GREIWE, M., HAMMANS, C., HENN, W., HINKEL, G. K., KÖNIG, R., KUNSTMANN, E., KUNZE, J., NEUMANN, L. M., PROTT, E. C., RAUCH, A., ROTT, H. D., SEIDEL, H., SPRANGER, S., SPRENGEL, M., ZOLL, B., LOHMANN, D. R. & WIECZOREK, D. 2004. Genotyping in 46 patients with tentative diagnosis of Treacher Collins syndrome revealed unexpected phenotypic variation. *Eur J Hum Genet,* 12**,** 879-90.

TEMPLE, J. P., HUTTON, D. L., HUNG, B. P., HURI, P. Y., COOK, C. A., KONDRAGUNTA, R., JIA, X. & GRAYSON, W. L. 2014. Engineering anatomically shaped vascularized bone grafts with hASCs and 3D-printed PCL scaffolds. *J Biomed Mater Res A,* 102**,** 4317-25.

TEOH, G. Z., CROWLEY, C., BIRCHALL, M. A. & SEIFALIAN, A. M. 2015. Development of resorbable nanocomposite tracheal and bronchial scaffolds for paediatric applications. *Br J Surg,* 102**,** e140-50.

TERHEYDEN H, KNAK C, JEPSEN S, PALMIE S & RUEGER DR 2001a. Mandibular reconstruction with a prefabricated vascularized bone graft using recombinant human osteogenic protein-1: an experimental study in miniature pigs. Part I: Prefabrication. *International journal of oral and maxillofacial surgery,* 30**,** 373-379.

TERHEYDEN H, WARNKE P, DUNSCHE A, JEPSEN S, BRENNER W, PALMIE S & RUEGER DR 2001b. Mandibular reconstruction with prefabricated vascularized bone grafts using recombinant human osteogenic protein-1: an experimental study in miniature pigs. Part II: transplantation. *International journal of oral and maxillofacial surgery,* 30**,** 469-478.

TESSIER, P., KAWAMOTO, H., MATTHEWS, D., POSNICK, J., RAULO, Y., TULASNE, J. F. & WOLFE, S. A. 2005. Autogenous bone grafts and bone substitutes--tools and techniques: I. A 20,000-case experience in maxillofacial and craniofacial surgery. *Plast Reconstr Surg,* 116**,** 6S-24S; discussion 92S-94S.

THÉBAUD, N. B., SIADOUS, R., BAREILLE, R., REMY, M., DACULSI, R., AMÉDÉE, J. & BORDENAVE, L. 2012. Whatever their differentiation status, human progenitor derived - or mature - endothelial cells induce osteoblastic differentiation of bone marrow stromal cells. *J Tissue Eng Regen Med,* 6**,** e51-60.

TOMLINSON, R. E. & SILVA, M. J. 2013. Skeletal Blood Flow in Bone Repair and Maintenance. *Bone Res,* 1**,** 311-22.

TONDREAU, T., LAGNEAUX, L., DEJENEFFE, M., MASSY, M., MORTIER, C., DELFORGE, A. & BRON, D. 2004. Bone marrow-derived mesenchymal stem cells already express specific neural proteins before any differentiation. *Differentiation,* 72**,** 319-26.

TORRES-LAGARES, D., TULASNE, J. F., POUGET, C., LLORENS, A., SAFFAR, J. L. & LESCLOUS, P. 2010. Structure and remodelling of the

human parietal bone: an age and gender histomorphometric study. *J Craniomaxillofac Surg,* 38**,** 325-30.

TRAINOR, P. A. 2010. Craniofacial birth defects: The role of neural crest cells in the etiology and pathogenesis of Treacher Collins syndrome and the potential for prevention. *Am J Med Genet A,* 152A**,** 2984-94.

TRAINOR, P. A. & ANDREWS, B. T. 2013. Facial dysostoses: Etiology, pathogenesis and management. *Am J Med Genet C Semin Med Genet,* 163C**,** 283-94.

TSAI, C. C., SU, P. F., HUANG, Y. F., YEW, T. L. & HUNG, S. C. 2012. Oct4 and Nanog directly regulate Dnmt1 to maintain self-renewal and undifferentiated state in mesenchymal stem cells. *Mol Cell,* 47**,** 169-82.

TUIN, A. J., TAHIRI, Y., PAINE, K. M., PALIGA, J. T., TAYLOR, J. A. & BARTLETT, S. P. 2015. Clarifying the relationships among the different features of the OMENS+ classification in craniofacial microsomia. *Plast Reconstr Surg,* 135**,** 149e-56e.

TUTKUVIENE, J., CATTANEO, C., OBERTOVÁ, Z., RATNAYAKE, M., POPPA, P., BARKUS, A., KHALAJ-HEDAYATI, K., SCHROEDER, I. & RITZ-TIMME, S. 2015. Age- and sex-related growth patterns of the craniofacial complex in European children aged 3-6 years. *Ann Hum Biol***,** 1-10.

URQUIA EDREIRA, E. R., HAYRAPETYAN, A., WOLKE, J. G., CROES, H. J., KLYMOV, A., JANSEN, J. A. & VAN DEN BEUCKEN, J. J. 2016. Effect of calcium phosphate ceramic substrate geometry on mesenchymal stromal cell organization and osteogenic differentiation. *Biofabrication,* 8**,** 025006.

VALE, F., SCHERZBERG, J., CAVALEIRO, J., SANZ, D., CARAMELO, F., MALÓ, L. & MARCELINO, J. P. 2016. 3D virtual planning in orthognathic surgery and CAD/CAM surgical splints generation in one patient with craniofacial microsomia: a case report. *Dental Press J Orthod,* 21**,** 89-100.

VALERI, G., MAZZA, F. A., MAGGI, S., ARAMINI, D., LA RICCIA, L., MAZZONI, G. & GIOVAGNONI, A. 2015. Open source software in a practical approach for post processing of radiologic images. *Radiol Med,* 120**,** 309-23.

VIELREICHER, M., GELLNER, M., ROTTENSTEINER, U., HORCH, R. E., ARKUDAS, A. & FRIEDRICH, O. 2015. Multiphoton microscopy analysis of extracellular collagen I network formation by mesenchymal stem cells. *J Tissue Eng Regen Med*.

VIGUET-CARRIN, S., GARNERO, P. & DELMAS, P. D. 2006. The role of collagen in bone strength. *Osteoporos Int,* 17**,** 319-36.

VINCENT, M., GENEVIÈVE, D., OSTERTAG, A., MARLIN, S., LACOMBE, D., MARTIN-COIGNARD, D., COUBES, C., DAVID, A., LYONNET, S., VILAIN, C., DIEUX-COESLIER, A., MANOUVRIER, S., ISIDOR, B., JACQUEMONT, M. L., JULIA, S., LAYET, V., NAUDION, S., ODENT, S., PASQUIER, L., PELRAS, S., PHILIP, N., PIERQUIN, G., PRIEUR, F., ABOUSSAIR, N., ATTIE-BITACH, T., BAUJAT, G., BLANCHET, P.,

BLANCHET, C., DOLLFUS, H., DORAY, B., SCHAEFER, E., EDERY, P., GIULIANO, F., GOLDENBERG, A., GOIZET, C., GUICHET, A., HERLIN, C., LAMBERT, L., LEHEUP, B., MARTINOVIC, J., MERCIER, S., MIGNOT, C., MOUTARD, M. L., PEREZ, M. J., PINSON, L., PUECHBERTY, J., WILLEMS, M., RANDRIANAIVO, H., SZAKSZON, K., SZASKON, K., TOUTAIN, A., VERLOES, A., VIGNERON, J., SANCHEZ, E., SARDA, P., LAPLANCHE, J. L. & COLLET, C. 2016. Treacher Collins syndrome: a clinical and molecular study based on a large series of patients. *Genet Med,* 18**,** 49-56.

VOGT, M. T., CAULEY, J. A., KULLER, L. H. & NEVITT, M. C. 1997. Bone mineral density and blood flow to the lower extremities: the study of osteoporotic fractures. *J Bone Miner Res,* 12**,** 283-9.

WALSH, S., JORDAN, G. R., JEFFERISS, C., STEWART, K. & BERESFORD, J. N. 2001. High concentrations of dexamethasone suppress the proliferation but not the differentiation or further maturation of human osteoblast precursors in vitro: relevance to glucocorticoid-induced osteoporosis. *Rheumatology (Oxford),* 40**,** 74-83.

WAN, D. C., KWAN, M. D., KUMAR, A., BRADLEY, J. P. & LONGAKER, M. T. 2009. Craniofacial surgery, from past pioneers to future promise. *J Maxillofac Oral Surg,* 8**,** 348-56.

WANG, L., FAN, H., ZHANG, Z. Y., LOU, A. J., PEI, G. X., JIANG, S., MU, T. W., QIN, J. J., CHEN, S. Y. & JIN, D. 2010. Osteogenesis and angiogenesis of tissue-engineered bone constructed by prevascularized β-tricalcium phosphate scaffold and mesenchymal stem cells. *Biomaterials,* 31**,** 9452-61.

WANG, S., MUNDADA, L., COLOMB, E., OHYE, R. G. & SI, M. S. 2016. Mesenchymal Stem/Stromal Cells from Discarded Neonatal Sternal Tissue: In Vitro Characterization and Angiogenic Properties. *Stem Cells Int,* 2016**,** 5098747.

WATSON, J., HATAMLEH, M., ALWAHADNI, A. & SRINIVASAN, D. 2014. Correction of facial and mandibular asymmetry using a computer aided design/computer aided manufacturing prefabricated titanium implant. *J Craniofac Surg,* 25**,** 1099-101.

WEISGERBER, D. W., CALIARI, S. R. & HARLEY, B. A. 2015. Mineralized collagen scaffolds induce hMSC osteogenesis and matrix remodeling. *Biomater Sci,* 3**,** 533-42.

WEN GUAN AND ZHAOBIN, Q. 2012. Isothermal Crystallization Kinetics, Morphology, and Dynamic Mechanical Properties of Biodegradable Poly(ε-caprolactone) and Octavinyl–Polyhedral Oligomeric Silsesquioxanes Nanocomposites. *Industrial \& Engineering Chemistry Research,* 51**,** 3203-3208.

WILKIE, A. O. & MORRISS-KAY, G. M. 2001. Genetics of craniofacial development and malformation. *Nat Rev Genet,* 2**,** 458-68.

WU, H., KANG, N., WANG, Q., DONG, P., LV, X., CAO, Y. & XIAO, R. 2015. The Dose-Effect Relationship Between the Seeding Quantity of Human

Marrow Mesenchymal Stem Cells and In Vivo Tissue-Engineered Bone Yield. *Cell Transplant,* 24**,** 1957-68.

XIAO, G., GOPALAKRISHNAN, R., JIANG, D., REITH, E., BENSON, M. D. & FRANCESCHI, R. T. 2002. Bone morphogenetic proteins, extracellular matrix, and mitogen-activated protein kinase signaling pathways are required for osteoblast-specific gene expression and differentiation in MC3T3-E1 cells. *J Bone Miner Res,* 17**,** 101-10.

XU, S., DE BECKER, A., VAN CAMP, B., VANDERKERKEN, K. & VAN RIET, I. 2010. An improved harvest and in vitro expansion protocol for murine bone marrow-derived mesenchymal stem cells. *J Biomed Biotechnol,* 2010**,** 105940.

YANG, J., LEI, J., WU, Y., LU, J., KE, R., YU, Q. & MU, X. 2015a. Skeleton first in surgical treatment of facial disharmony. *J Craniofac Surg,* 26**,** 336-9.

YANG, M., ZHOU, G., SHUAI, Y., WANG, J., ZHU, L. & MAO, C. 2015b. Ca(2+)-induced self-assembly of Bombyx mori silk sericin into a nanofibrous network-like protein matrix for directing controlled nucleation of hydroxylapatite nano-needles. *J Mater Chem B Mater Biol Med,* 3**,** 2455-2462.

YANG, W., GUO, D., HARRIS, M. A., CUI, Y., GLUHAK-HEINRICH, J., WU, J., CHEN, X. D., SKINNER, C., NYMAN, J. S., EDWARDS, J. R., MUNDY, G. R., LICHTLER, A., KREAM, B. E., ROWE, D. W., KALAJZIC, I., DAVID, V., QUARLES, D. L., VILLAREAL, D., SCOTT, G., RAY, M., LIU, S., MARTIN, J. F., MISHINA, Y. & HARRIS, S. E. 2013. Bmp2 in osteoblasts of periosteum and trabecular bone links bone formation to vascularization and mesenchymal stem cells. *J Cell Sci,* 126**,** 4085-98.

YAO, Y., HUA, C., TANG, X., WANG, Y., ZHANG, F. & XIANG, Z. 2010. Angiogenesis and osteogenesis of non-vascularised autogenous bone graft with arterial pedicle implantation. *J Plast Reconstr Aesthet Surg,* 63**,** 467-73.

YAREMCHUK, M. J., DOUMIT, G. & THOMAS, M. A. 2011. Alloplastic augmentation of the facial skeleton: an occasional adjunct or alternative to orthognathic surgery. *Plast Reconstr Surg,* 127**,** 2021-30.

YASSIN, M. A., LEKNES, K. N., PEDERSEN, T. O., XING, Z., SUN, Y., LIE, S. A., FINNE-WISTRAND, A. & MUSTAFA, K. 2015. Cell seeding density is a critical determinant for copolymer scaffolds-induced bone regeneration. *J Biomed Mater Res A,* 103**,** 3649-58.

YILDIRIMER, L., BUANZ, A., GAISFORD, S., MALINS, E. L., REMZI BECER, C., MOIEMEN, N., REYNOLDS, G. M. & SEIFALIAN, A. M. 2015. Controllable degradation kinetics of POSS nanoparticle-integrated poly(ε-caprolactone urea)urethane elastomers for tissue engineering applications. *Sci Rep,* 5**,** 15040.

YOUNG, N. M., SHERATHIYA, K., GUTIERREZ, L., NGUYEN, E., BEKMEZIAN, S., HUANG, J. C., HALLGRÍMSSON, B., LEE, J. S. & MARCUCIO, R. S. 2016. Facial surface morphology predicts variation in internal skeletal shape. *Am J Orthod Dentofacial Orthop,* 149**,** 501-8.

YOUREK, G., HUSSAIN, M. A. & MAO, J. J. 2007. Cytoskeletal changes of mesenchymal stem cells during differentiation. *ASAIO J,* 53**,** 219-28.

YU, C., KORNMULLER, A., BROWN, C., HOARE, T. & FLYNN, L. E. 2017. Decellularized adipose tissue microcarriers as a dynamic culture platform for human adipose-derived stem/stromal cell expansion. *Biomaterials,* 120**,** 66-80.

ZHAO, Y. N., FAN, J. J., LI, Z. Q., LIU, Y. W., WU, Y. P. & LIU, J. 2017. Effects of Pore Size on the Osteoconductivity and Mechanical Properties of Calcium Phosphate Cement in a Rabbit Model. *Artif Organs,* 41**,** 199-204.

ZHOU, N., LI, Q., LIN, X., HU, N., LIAO, J. Y., LIN, L. B., ZHAO, C., HU, Z. M., LIANG, X., XU, W., CHEN, H. & HUANG, W. 2016a. BMP2 induces chondrogenic differentiation, osteogenic differentiation and endochondral ossification in stem cells. *Cell Tissue Res,* 366**,** 101-11.

ZHOU, X., CASTRO, N. J., ZHU, W., CUI, H., ALIABOUZAR, M., SARKAR, K. & ZHANG, L. G. 2016b. Improved Human Bone Marrow Mesenchymal Stem Cell Osteogenesis in 3D Bioprinted Tissue Scaffolds with Low Intensity Pulsed Ultrasound Stimulation. *Sci Rep,* 6**,** 32876.

ZIELINS, E. R., TEVLIN, R., HU, M. S., CHUNG, M. T., MCARDLE, A., PAIK, K. J., ATASHROO, D., DULDULAO, C. R., LUAN, A., SENARATH-YAPA, K., WALMSLEY, G. G., WEARDA, T., LONGAKER, M. T. & WAN, D. C. 2015. Isolation and enrichment of human adipose-derived stromal cells for enhanced osteogenesis. *J Vis Exp***,** 52181.

ZOU, D., HAN, W., YOU, S., YE, D., WANG, L., WANG, S., ZHAO, J., ZHANG, W., JIANG, X., ZHANG, X. & HUANG, Y. 2011a. In vitro study of enhanced osteogenesis induced by HIF-1α-transduced bone marrow stem cells. *Cell Prolif,* 44**,** 234-43.

ZOU, D., ZHANG, Z., HE, J., ZHANG, K., YE, D., HAN, W., ZHOU, J., WANG, Y., LI, Q., LIU, X., ZHANG, X., WANG, S., HU, J., ZHU, C., ZHANG, W., ZHOU, Y., FU, H., HUANG, Y. & JIANG, X. 2012. Blood vessel formation in the tissue-engineered bone with the constitutively active form of HIF-1α mediated BMSCs. *Biomaterials,* 33**,** 2097-108.

ZOU, D., ZHANG, Z., HE, J., ZHU, S., WANG, S., ZHANG, W., ZHOU, J., XU, Y., HUANG, Y., WANG, Y., HAN, W., ZHOU, Y., YOU, S. & JIANG, X. 2011b. Repairing critical-sized calvarial defects with BMSCs modified by a constitutively active form of hypoxia-inducible factor-1α and a phosphate cement scaffold. *Biomaterials,* 32**,** 9707-18.

ZUK, P. A., ZHU, M., ASHJIAN, P., DE UGARTE, D. A., HUANG, J. I., MIZUNO, H., ALFONSO, Z. C., FRASER, J. K., BENHAIM, P. & HEDRICK, M. H. 2002. Human adipose tissue is a source of multipotent stem cells. *Mol Biol Cell,* 13**,** 4279-95.

Appendices

Appendix I Stills And Legends For Videos

Video 1

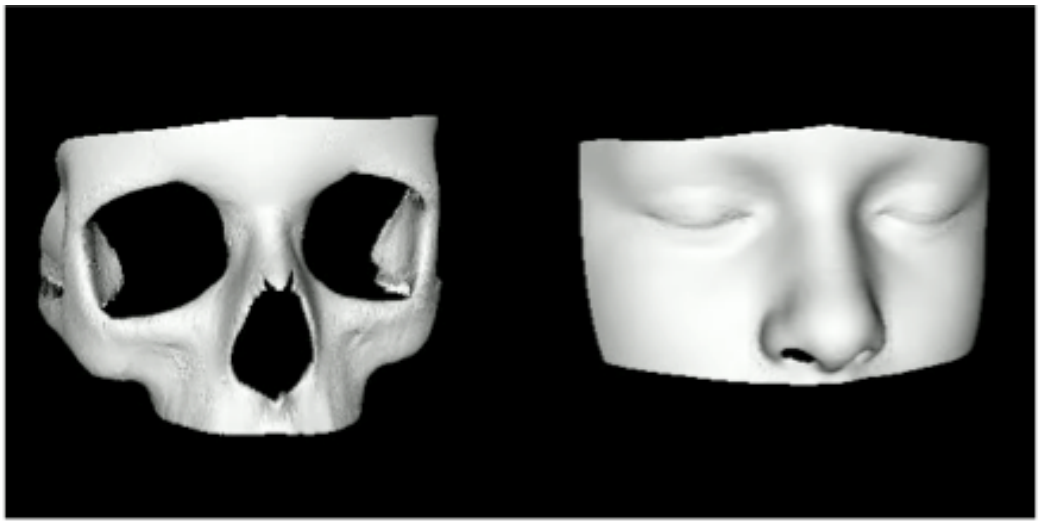

Principal Component 1. Dynamic morphs reveal the changes in midfacial appearance that are described by PC1 which relates to overall face size and is associated with age in our DSM (± 2 STD).

Video 2

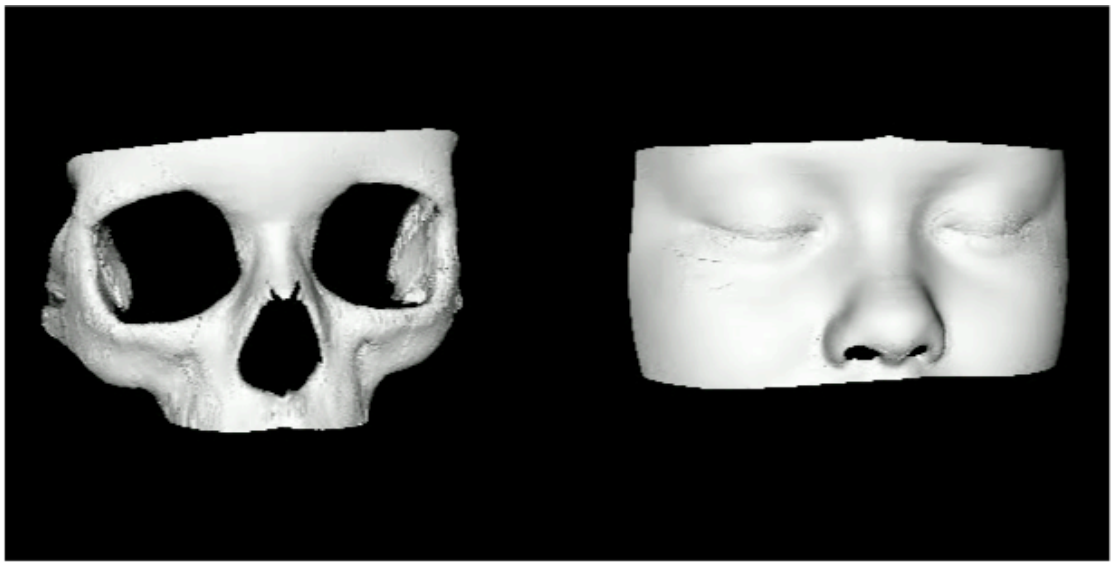

Principal Component 2. PC2 is associated with midface width and depth which is revealed by dynamic morphing of the surfaces in our model (± 2 STD).

Video 3

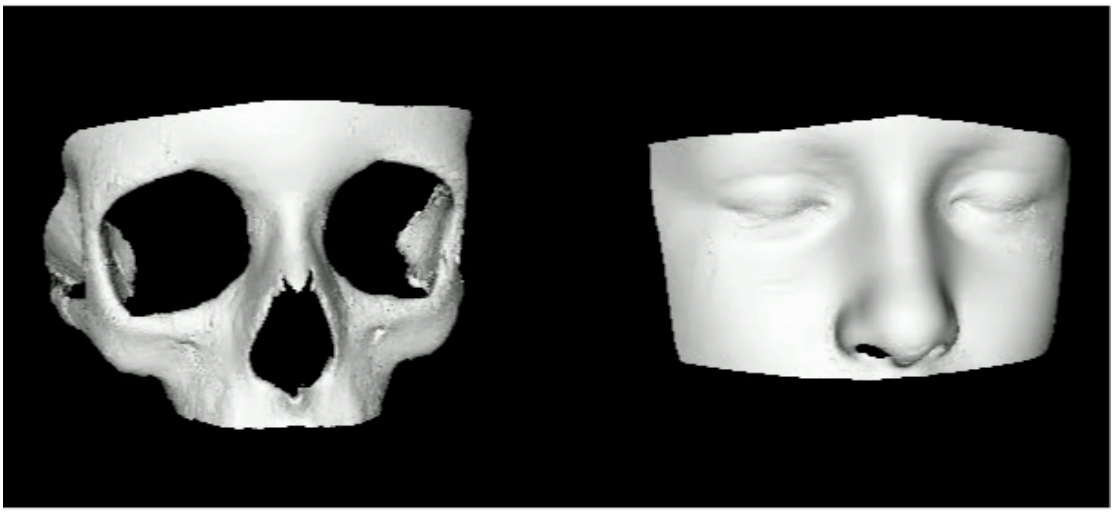

Principal component 3. Dynamic morphing of the midface surfaces reveals the association between midface width and length with PC3 (± 2 STD). There is also evidence of overlap between the changes described by all 3 PCs.

Appendix II *RUNX2* And *ALP* Expression In Calvarial Bone

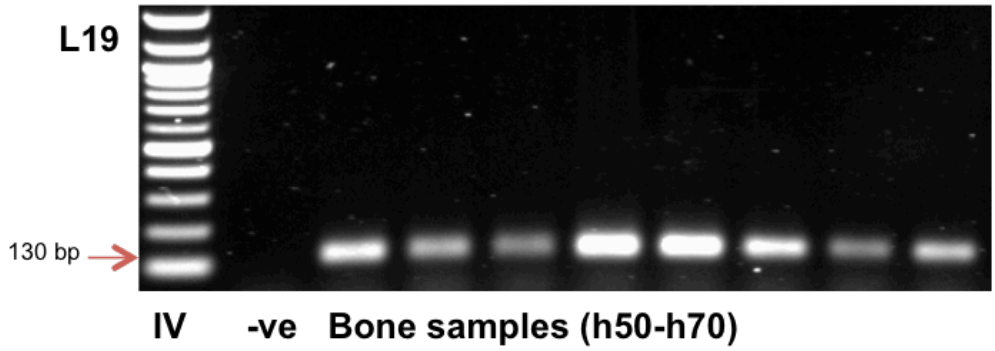

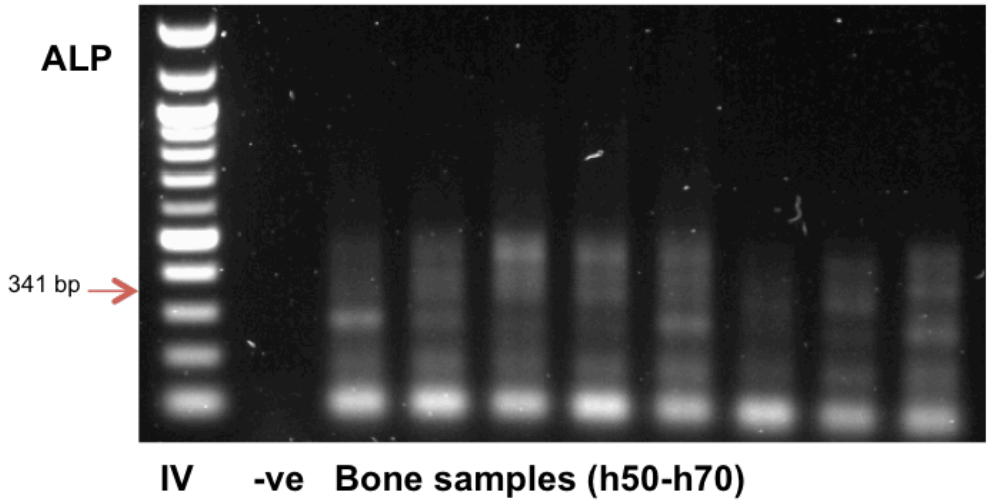

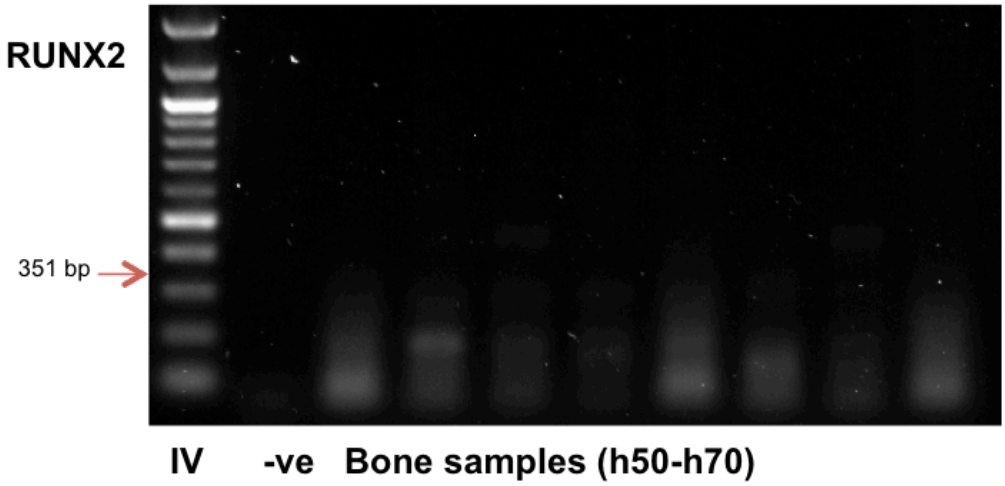

Paediatric calvarial bone samples did not express *RUNX2* or *ALP*. On PCR gene expression analysis. Above gels were loaded with hyperladder IV (IV), negative PCR water control (-ve) and samples (n=8).

Illustrative Material (attached to back cover)